HYDRODYNAMICS OF A ROTATING STRONGLY INTERACTING FERMI GAS

by

Bason Eric Clancy

Department of Physics
Duke University

Date:_____
Approved:

_____
Dr. John Thomas, Supervisor

_____
Dr. Steffen Bass

_____
Dr. Robert Behringer

_____
Dr. Alfred Goshaw

_____
Dr. David Skatrud

Dissertation submitted in partial fulfillment of the
requirements for the degree of Doctor of Philosophy
in the Department of Physics
in the Graduate School of
Duke University

2008

ABSTRACT

(Physics)

HYDRODYNAMICS OF A ROTATING STRONGLY INTERACTING FERMI GAS

by

Bason Eric Clancy

Department of Physics
Duke University

Date:_____
Approved:

_____
Dr. John Thomas, Supervisor

_____
Dr. Steffen Bass

_____
Dr. Robert Behringer

_____
Dr. Alfred Goshaw

_____
Dr. David Skatrud

An abstract of a dissertation submitted in partial fulfillment of
the requirements for the degree of Doctor of Philosophy
in the Department of Physics
in the Graduate School of
Duke University

2008

Abstract

Strongly interacting Fermi gases are unique quantum fluids that can be used to model other strongly interacting systems in nature, such as the quark-gluon plasma of the big bang, high temperature superconductors, and nuclear matter. This is made possible through the use of a collisional resonance, producing a gas in which the scattering length far exceeds the interparticle spacing. At the peak of the resonance, a strongly interacting Fermi gas is created which exhibits universal behavior, providing a test-bed for many-body theories in a variety of disciplines.

This dissertation presents an experimental study of the hydrodynamics of a strongly interacting Fermi gas with finite angular momentum in the superfluid and normal fluid regimes. The expansion dynamics of a rotating gas are modeled using a simple hydrodynamic theory based on the Euler equation and the equation of continuity. By including dissipative terms in the equations of motion, an estimate for the quantum viscosity η of an ultracold Fermi gas in the strongly interacting regime is produced.

In addition to the hydrodynamic results, the thermodynamics of a strongly interacting gas is investigated through a model independent measurement of the entropy S of the gas as a function of energy E. This study allows the superfluid transition temperature in the strongly interacting regime to be estimated from $T = \partial E/\partial S$. The hydrodynamic and thermodynamic results can be used in conjunction to provide an estimate of the ratio of the viscosity to the entropy density,

expressed as η/s. A fundamental lower bound on this ratio is conjectured using string theory methods. When the experimental measurements are compared to the string theory conjecture, the results provide evidence that a strongly interacting Fermi gas is a near-perfect fluid.

Acknowledgements

The realization that my graduate years are finally coming to an end has afforded me the opportunity to reflect back on how I actually reached this point. It has become more than obvious to me that I couldn't have come this far without the support and guidance of the many people that I have crossed paths with over the years. It is more than appropriate to begin with my parents who started me out on this journey, but unfortunately will not be able to see me complete it. My father is perhaps the kindest and most self-sacrificing person that I have ever known. His dedication to my sister and me is something I strive to replicate in my own life. His influence on me over the years has allowed me to remain humble during my accomplishments, and has given me the strength to remain confident even in the face of defeat. Thanks for everything Dad.

The next person to thank is my greatest competitor, my older sister Kim. While growing up with her everything became a competition. A simple thing like a relaxing bike ride would quickly escalate into a race to see who could get to the destination first. But the athletic challenges of our youth quickly transformed into academic challenges in high school after I began playing football, and races began to be highly skewed in my favor. So when my sister started bringing home perfect report cards, I, obviously, had to follow suit. In the process of striving to compete with my sister, I actually began to enjoy being academic, an aspect of my personality that has only intensified over the years. With the completion of my

Ph.D., I will have finally surpassed my sister in the total number of degrees each of us has earned. In turn, I am sure she will enroll back into school immediately after I receive my diploma. I would expect no less.

When I arrived at Duke I was a little apprehensive about finding people who I would relate to, and also become good friends with. But luckily I was fortunate enough to be put in an office with Matt Kiser and Matthew Blackston my first year, who helped my out immensely with my first year classes. Without their patience and help, I would have received far less sleep than I was able to get that year. No discussion about my first year at Duke would be complete without mentioning Dean Hidas and Andrew Dawes. I'll always remember all the great times we had in our favorite pub in downtown Durham. I especially have to thank Andy and his wife Leslie for having me over for all those Thanksgivings. Good luck to you guys and your recently expanded family.

I joined JETlab in the summer of 2003 after my first year of classes and briefly overlapped with Mike Gehm, who designed the main vacuum chamber, and Staci Hemmer who first showed me the ropes and helped me get the Zeeman slower working for the first time. When I became full time in the lab Joe Kinast was the senior graduate student and Andrey Turlapov was the postdoc. I always appreciated how Andrey was willing to sit down with me and work through a problem that I was stuck on. As for Joe, he and I started off as coworkers, but quickly became close friends. I would have to say that Joe knows me better than anyone I have met at Duke. He gave me huge amounts of advice and help while we were working together in the lab, and was always willing to listen to me whenever I was having trouble outside the lab. For that I owe him a debt of gratitude.

I was never alone in my scientific pursuits, for I always had my lab partner Le Luo to work with during all the experiments. There were many times during my graduate career in the lab when I could easily have slacked off and not made progress, but Le kept me motivated. We both pushed each other to become better experimentalists and it would have taken me a substantially longer time to graduate if it wasn't for him.

No discussion of my time at Duke would be complete without mentioning my mentor, John Thomas. I have no reservations when I say that he has had the largest impact on my academic career then anyone I have ever met. His enthusiasm for physics is infectious, and our daily discussions constantly remind me about how lucky I am to have the opportunity to do the research I have been able to do. The passion for science that he has shown me will continue to encourage me long after I have graduated, and will no doubt carry me through the rough patches I will face in my future career. After this summer our careers will diverge, but I am sure our friendship will continue for many years to come.

The future of the lab looks bright with James Joseph taking over the reigns of head graduate student after Le and I graduate. The attention to detail that he has shown thus far in his experiments will no doubt lead to exceptional results in the future. He will be accompanied by postdocs Xu Du and Jessie Petricka who have demonstrated that they are excellent researchers in their own right. In closing, I would also like to thank the members of my advisory committee who have followed my graduate career including Steffen Bass, Robert Behringer, Alfred Goshaw, and David Skatrud for taking the time out of their busy schedules to read my thesis and attend my defense.

Contents

List of Tables

List of Figures

Chapter 1

Introduction

The pace of scientific advancement tends to follow in step with the development of the scientific tools that make progress possible. The discovery of bacteria was made possible through the use of the microscope, and devices such as particle accelerators allow the predictions of the Standard Model to be tested. Without the initial development of the experimental tools, the resultant scientific advancements would not be possible. This dissertation presents a study of the hydrodynamics of a strongly interacting Fermi gas with finite angular momentum in the superfluid and normal fluid regimes. These experiments were made possible through the construction of a new cooling and trapping apparatus that is used to initially trap ^{6}Li fermions using all optical methods, and subsequently cool them down into the nano-Kelvin temperature regime where quantum effects become paramount.

In the hydrodynamic studies presented in this dissertation, experiments are performed to characterize the expansion dynamics of a rotating gas. These dynamics are subsequently modeled using a simple theory based on the Euler equation and the equation of continuity. Dissipative terms are then included in the equations of motion, allowing an estimate of quantum viscosity to be obtained in an strongly interacting ultracold Fermi gas. In addition to the hydrodynamic results, the thermodynamics of a strongly interacting gas is investigated through a

measurement of the entropy of the gas as a function of energy. The hydrodynamic and thermodynamic results can be used in conjunction to provide an estimate of η/s, the ratio of the viscosity, η, to the entropy density, s. A comparison of this estimate to the fundamental limit as conjectured using string theory methods provides evidence that a strongly interacting Fermi gas is a near-perfect fluid.

The history of the cooling and trapping of neutral atoms can be traced back to the 1980's with the development of the first atomic traps [1, 2]. The initial experiments focused on the trapping of atoms with integer spin known as bosons [3,4], which collectively follow Bose-Einstein statistics. One of the unique features of bosons is that more than one atom is allowed to occupy the same quantum state. It was proposed by Einstein that below a critical temperature, the ground state of a collection of bosons will begin to become macroscopically populated. This is known as Bose-Einstein condensation. A major triumph of the field of atom cooling and trapping came in 1995 with the experimental observation of a Bose-Einstein condensate in a dilute gas of atoms [5–7]. The work with bosons has continued, with future prospects for advancements in quantum computing and information technology.

It wasn't until 1999 that fermions, which have a half integer spin and follow Fermi-Dirac statistics, were cooled into the degenerate regime [8]. Fermions are pervasive in nature and include protons, neutrons, electrons, and quarks, which all follow Fermi statistics. In contrast to bosons, two or more fermions cannot simultaneously occupy the same quantum state as conveyed by the Pauli exclusion principle. Therefore, the condensation effects seen for bosonic atoms are absent in Fermi systems. But a paring can exist between two fermions of opposing spins, known as a Cooper pair [9], which allows them to behave like a boson and condense

into a Fermi superfluid at a low enough temperature [10]. Unfortunately, for a weakly interacting gas of fermions, the transition temperature is exceptionally small, making the formation of the condensate technically challenging to achieve [11].

Although a very small transition temperature is postulated in a *weakly* interacting gas of fermions, a much larger and experimentally attainable transition temperature is observed in a *strongly* interacting Fermi gas [11]. A gas is considered to be strongly interacting when the scattering length due to s-wave collisions between atoms becomes large in comparison to the interparticle spacing. In this regime, the superfluid transition temperature is substantially increased and a Fermi superfluid can be created using available cooling technology. An enhancement of the s-wave scattering length can be created through the use of a collisional Feshbach resonance [12]. At the peak of a Feshbach resonance the s-wave scattering length diverges to $\pm\infty$ and the gas is considered to be in the unitary regime. Since the scattering length diverges in the unitary regime, it can no longer be used to describe the interparticle interactions between colliding atoms. This results in the collisional properties becoming independent of the microscopic potentials between atoms. Therefore, a strongly interacting Fermi gas is considered to be *universal* [13], meaning that the experimentally measured properties of a strongly interacting Fermi gas in our system can be applied to any other strongly interacting Fermi system in nature. The connections between our gas of ^{6}Li atoms and other strongly interacting systems is presented in section Section 1.1.

1.1 Motivation for studies

As discussed in the previous section, the s-wave scattering length in the vicinity of a Feshbach resonance exceeds the interparticle spacing, leading to the unitary regime. In this regime, a strongly interacting Fermi gas can be used to model other Fermi systems in nature, while proving a test-bed for many-body theories. Examples of other strongly interacting Fermi systems are high temperature superconductors, neutron stars, and the quark-gluon plasma. This section will illuminate the connections between our collection of ultracold lithium atoms and other strongly interacting systems that prove difficult to access experimentally.

1.1.1 Quark-gluon plasma

According to the Standard Model, all of the elementary fermions in the universe can be categorized as either leptons or quarks, with gauge bosons mediating the interactions between them [14]. The leptons consist of the familiar electron, the heavier muon and tau, and their corresponding neutrinos. The photon is designated as one of the gauge bosons as well as the gluon. The gluon is responsible for binding quarks together and confining them within composite structures like protons and neutrons. The quarks themselves are fermions, having a spin quantum number of 1/2. Normally, the quarks are bound together through the exchange of gluons. But at extremely high temperatures and densities, the quarks and gluons can temporarily be liberated from each other, creating what has become known as a quark-gluon plasma. It has been proposed that such a plasma existed tens of μs after the Big Bang [15].

The quark-gluon plasma is considered to be a strongly interacting system, and

since quarks are fermions, the properties of the strongly interacting gases produced in our lab should also be correlated to the properties of the quark-gluon plasma. On the surface this may seem like an outlandish claim, since in our experiments the gas is cooled to hundreds of nK, while the quark-gluon plasma is expected to occur at temperatures exceeding 2×10^{12} Kelvin [16]. But even though these two systems are separated by almost 19 orders of magnitude in temperature, recent evidence suggests that they demonstrate similar hydrodynamic behavior.

At an experiment done at the Relativistic Heavy Ion Collider (RHIC) two gold nuclei were accelerated to 100 GeV per nucleon before a collision was produced at a glancing angle [17]. Since the collision was not head on, the nuclear reaction zone was deformed into an almond shape, similar to the cigar shaped distributions produced in our experiments. The resultant plasma produced from the collision exhibits nearly perfect hydrodynamics during the subsequent expansion. The same dynamics, termed "elliptic flow", is observed to occur in a strongly interacting Fermi gas produced in our laboratory [18]. Based on these observations, a quark-gluon plasma and a strongly interacting Fermi gas have been proclaimed to be nearly perfect fluids [19, 20].

1.1.2 High temperature superconductors

All natural materials which conduct electricity offer a certain amount of resistance to the flow of current. The resistance is caused by collisions between the electrons and atoms in the conductor, which leads to the generation of heat and the loss of power during the electrical transmission. However, there exists a class of man made materials, named superconductors, that can transmit electricity without dissipation and have a vanishing resistance below a critical temperature [21].

These materials are extremely important to modern life since they could potentially provide a means of transmitting power without dissipation, resulting in more efficient power delivery systems and smaller semiconductor devices.

The advent of superconductors began in 1911 when the Dutch physicist Heike Onnes observed that when liquid mercury was cooled below 4 Kelvin its resistance to the flow of electricity disappeared. In the subsequent decades, solid state materials were found to possess the same properties, but at temperatures very close to absolute zero. A major advancement in the field of superconductivity came in 1986 and 1987 when superconductors were produced with critical temperatures of 30 Kelvin and 90 Kelvin, respectively [22]. These breakthroughs instigated the search for the so called high temperature superconductors, which have a critical temperature, $T_c > 77$ Kelvin. Unfortunately, the ability to find superconductors with higher critical temperatures soon stagnated, with the highest critical temperature remaining about 160° C below room temperature.

A satisfactory theory to explain low temperature superconductivity arrived in 1957 with a paper by Bardeen, Cooper, and Schrieffer [23]. This paper presented the so called BCS theory of superconductivity after the surnames of the authors, and eventually lead to the Nobel prize in 1972. In the theory, a large collection of electrons, which are fermions, are allowed to couple together in spin up and spin down pairs, known as Cooper pairs. This pairing occurs in momentum space and allows the collection of electrons to make a transition into a superconducting state.

The same type of paring exhibited in the BCS theory of superconductivity is also found in dilute gases of fermionic atoms below a critical temperature, T_c. This critical temperature can be increased by enhancing the interactions between

atoms in the vicinity of a collisional Feshbach resonance. Recent theoretical estimates put the critical temperature of a strongly interacting Fermi gas at roughly $T_c/T_F = 0.30$ [24–29], where T_F is a density dependent characteristic temperature in the system, which is called the Fermi temperature. For a normal metal T_F is on the order of thousands of degrees Kelvin, meaning that if it were possible to scale the critical temperature for ultracold gases up to that of a superconductor, the superconducting properties would appear well above room temperature at thousands of Kelvin. As it stands right now, there is no satisfactory theory that can describe all the effects observed for high temperature superconductors. Therefore researchers are optimistic that studies of strongly interacting Fermi gases may shed light on the mechanisms behind high temperature superconductivity.

1.1.3 Many-body theories

Another unique and extremely useful feature of strongly interacting Fermi gases are their ability to act as test-beds for strongly interacting many-body theories. Recently, theorists have taken advantage of the wide tunability of the collisional properties afforded to degenerate Fermi gases in the vicinity of a Feshbach resonance to test their many-body theories. Although most of these theories were originally formulated to tackle the properties of high temperature superconductors [30] and nuclear matter [31], due to the universal properties of unitary Fermi gases they are equally applicable to our system.

The many-body problem of the ground state properties of a Fermi gas with an infinite scattering length was first formulated by Bertsch in 1998 [32]. It was further proposed by Heiselberg [33] that a dilute strongly interacting Fermi gas with an infinite s-wave scattering length can be used to model nuclear matter,

like the low density neutron gas in the inner crust of a neutron star. One method that is well suited for treating strongly correlated systems such as neutron stars and unitary Fermi gases is Quantum Monte Carlo techniques [34]. Since it is not feasible to perform experiments on neutron stars to validate the results of such a theory, experimentally accessible Fermi gases in atom traps are used instead. Recently, a Quantum Monte Carlo technique was used to predict the entropy of a strongly interacting Fermi gas as a function of energy [35]. The calculation of the entropy using the theory was preceded by the experimental measurement of the entropy as a function of energy as presented in Section 6.2. When the Monte Carlo theory is compared against the experimental data, excellent agreement is found between the data and the theory.

An additional technique that has been compared to the unitary entropy data is based on Nozières-Schmidt-Rink (NSR) theory [36]. In this work excellent agreement between experiment and theory is also found. In addition to the data presented in Section 6.2, the theory was compared to data from a group at Rice University also using ^{6}Li [37], and to a group at JILA using ^{40}K [38]. All of the data from each group was obtained in the unitary regime. It was found that the NSR model was able to predict the entropy as a function of energy for the conditions found in each experiment. This provides further evidence that the properties of fermions in the unitary regime are universal, since the same theoretical prediction can be used to model the thermodynamics of separate atomic species.

1.2 Significance of current work

The contributions I have made to the lab can be split into two separate but equally important and intimately related categories. The first is the design and construction of a new experimental apparatus that is detailed in Section 1.2.1. The apparatus consists of all the equipment and optics necessary to trap and cool the atoms during the experiments. The second category consists of the original experiments conducted on the newly constructed cooling and trapping apparatus. These experiments investigate the hydrodynamics and thermodynamics of a strongly interacting Fermi gas.

The hydrodynamic experiments presented in this dissertation involve an investigation into the expansion dynamics of a rotating unitary gas in the superfluid and normal fluid regimes. These experiments demonstrate that a strongly interacting Fermi gas has an exceptionally small viscosity not only in the superfluid state, but also at higher temperatures as a normal fluid. The thermodynamic experiments involve a measurement of the entropy as a function of energy in the strongly interacting regime. This data allows the first model independent measurement of the superfluid transition temperature in a strongly interacting Fermi gas. The significance of these experiments is discussed in Section 1.2.2.

1.2.1 Construction of a new experimental apparatus

Looking back at all the work I have done in the lab, I would have to say that the most challenging project I worked on was the construction of the new experimental apparatus. Our lab space consists mainly of two rooms that are connected together. All of the previous experiments that have been done in the lab before

my arrival were conducted in one of the rooms, now referred to as the "old lab". That room contains a fully functional cooling and trapping apparatus consisting of a dye laser, CO_2 laser, vacuum chamber with the atomic ^{6}Li source, and all the necessary optical and electronic equipment to run the experiments. When I first joined the lab, I was slightly intimidated by the obvious complexity of the experiment, and wondered how I would be able to understand the functionality of the seemingly infinite number of individual parts. It soon became clear that I would have the opportunity to intimately understand how every part of the experiment worked as my lab partner Le Luo and I began construction of the "new lab" in the room adjacent to the old lab.

While Le and I both worked on the construction of the experiment, we focused our design and manufacturing efforts on different aspects of the apparatus to speed up construction. Although we worked as efficiently as we could, the apparatus still took upwards of two years to complete. My main contributions came in the form of the design and production of many of the major components of the apparatus. In particular the design and construction of the locking region vacuum system, the magnet system, the construction of the main vacuum chamber and oven, the optical beam layout and alignment, and the development of numerous custom pieces of electronic equipment. All of these pieces of equipment, as well as an overall description of the new experimental apparatus is given in Chapter 4.

Although the design of the new lab closely mirrored that of the old lab, many improvements were made to make the apparatus more reliable. One of these improvements was the new design of the locking region vacuum system. The new design uses ultra-high vacuum technology and an ion pump to create a self contained chamber that eliminates the need for external mechanical pumps. Also,

for reasons explained in Chapter 4, the new locking region design can last for 3 to 4 years with normal use as opposed to a few months for the previous design. Due to these advantages, the old lab has recently upgraded to this design, and discarded the old locking region.

Another particularly substantial design change was undertaken with the main vacuum chamber and corresponding magnet system. It was decided that the main vacuum chamber should have a "pancake" geometry of a very short cylinder with almost all of the ports attached radially on the cylinder. This allowed the magnets, that are used to tune the interactions between the atoms, to be mounted on the top and bottom of the cylindrical chamber and brought very close to the center of the chamber where the atoms are trapped. This allows for an order of magnitude decrease in the power needed to create a particular magnetic field, when compared to the old lab. Not only does this allow larger fields to be generated, but it also makes it easier to cool the magnets, permitting experiments to be performed at higher fields for a longer period of time.

All of the improvements to the apparatus have lead to an efficient experimental system that has not had a major failure since its initial construction. This is quite impressive since a typical experimental sequence lasts less than 30 seconds, allowing upwards of 8000 experimental repetitions to be performed on a regular day.

1.2.2 Original studies of strongly interacting Fermi gases

After construction of the new experimental apparatus was completed, investigations into the properties of degenerate Fermi gases could commence. The experiments detailed in this thesis center around the hydrodynamics and ther-

modynamics of strongly interacting Fermi gases. The first experiment that was undertaken on the new experimental apparatus was a study on the entropy, S, as a function of energy, E of a strongly interacting Fermi gas [39]. The details of this experiment are given in Chapter 6. The entropy of a strongly interacting gas was determined by measuring S in a weakly interacting gas and employing an isentropic magnetic field sweep to link the two regimes. By parameterizing the $S(E)$ curve, the temperature, T, of a strongly interacting Fermi gas could be determined for the first time in a model independent way using the relation $1/T = \partial S/\partial E$. This experiment also provided a value for the superfluid transition temperature, which was concluded to occur at an abrupt slope change in the $S(E)$ data.

Once the entropy experiment was completed, investigations into the hydrodynamics of a strongly interacting Fermi gas began. In Chapter 5 a study of the rotational and irrotational flow dynamics of a strongly interacting Fermi gas is presented [40]. In these experiments, the gas is rotated prior to release from the trap and allowed to expand after the trap is turned off. The expansion dynamics can be monitored by measuring the angle of the principal axes of the cloud along with the aspect ratio. It was found that the dynamics of a superfluid gas near the ground state evolve according to the equations of ideal irrotational hydrodynamics, as expected. But it was also discovered that a normal strongly interacting Fermi gas can exhibit the same irrotational hydrodynamics at energies up to twice the expected superfluid transition energy. These dynamics can be understood as long as the viscosity of a normal gas is exceptionally small.

These experiments demonstrated that the viscosity of a normal strongly interacting Fermi gas must be smaller than previously thought. An exciting possibility

is that the viscosity may be as small as the theoretical limit of quantum viscosity as conjectured using string theory methods. It has been shown that the ratio of the shear viscosity, η, to the entropy density, s, has a universal minimum value [41]. In units of Plank's constant, $\hbar$, over Boltzmanns constant, k_B, the string theory prediction is

$$\frac{\eta}{s} \geq \frac{1}{4\pi}\frac{\hbar}{k_B}. \tag{1.1}$$

The entropy density in equation (1.1) can be calculated from the measurements of the entropy presented in Chapter 6. By including viscosity terms in the hydrodynamic theory developed in Chapter 5 for the rotation and expansion of a strongly interacting fermi gas, an estimate of the viscosity can be obtained. This procedure is given in detail in Chapter 6. Therefore, the entropy measurement and the viscosity estimate can be used to calculate the ratio of the viscosity to the entropy density, testing the string theory prediction for cold atomic gases.

1.3 Dissertation organization

Following the Introduction presented in this chapter, the dissertation continues with a discussion of the physics behind the Feshbach resonance in Chapter 2. The goal of this chapter is to introduce the concept of an s-wave scattering length and explain the mechanism that leads to a collisional Feshbach resonance. The energy level structure of the ground state and the first excited state are also included in this chapter since an understanding of the tuning of these energy levels with magnetic field is essential not only to explain the workings of the Feshbach resonance, but are needed to discern the operation of the optical traps as well.

Chapter 3 builds on the s-wave scattering length ideas presented in Chapter 2, and applies them to the process of evaporative cooling used in the lab. The methodology of forced evaporative cooling in the unitary regime is presented, along with a derivation of the specific trajectory of the trap potential as a function of time for a strongly interacting gas. This is preceded by a description of the two different types of optical traps used to perform the experiments in this dissertation.

A detailed account of the design and construction of the newly created experimental apparatus is given in Chapter 4. This includes the design of the vacuum system where the atom samples are created, the optical system that creates all the laser beams needed to trap and image the atoms, and the magnet system that is used to tune the interactions between atoms. The chapter ends with a description of a typical experimental sequence to illustrate how ultracold samples are prepared.

A presentation of an experiment that probes the hydrodynamic nature of a strongly interacting Fermi gas in the normal and superfluid regimes is given in Chapter 5. The chapter begins with a derivation of a simple hydrodynamic theory to describe the rotation and expansion of a superfluid Fermi gas. This is followed by a derivation of a ballistic theory for the same type of dynamics. Both theories are then compared to experimental data in the superfluid regime, as well as higher temperature data that is substantially above the superfluid transition temperature. It is found that both data sets closely follow the ideal hydrodynamic theory, and the consequences of the observed behavior are discussed.

The ideal superfluid theory presented in Chapter 5 is extended in Chapter 6 to include a simple model for viscosity. The viscosity model is incorporated into

the equations of motion, and the effects of viscosity on the resulting expansion dynamics are presented. This is followed by a description of an experiment that was done to measure the entropy of a strongly interacting Fermi gas as a function of energy. By combining the results obtained from the viscosity theory and the entropy experiment, an estimate for the ratio of the viscosity to the entropy density is given, and compared to the lower bound predicted by string theory methods.

The dissertation ends with a presentation of the conclusions in Chapter 7. This chapter includes an account of possible improvements that should be made to the experimental apparatus and ends with a discussion of the future outlook for experiments in the lab.

Chapter 2

Magnetically Tunable Interactions

Since the first degenerate Fermi gas was produced in a magnetic trap [8] and subsequently created using all optical methods [42], a substantial amount of progress has been made in the field of ultra-cold Fermi gases. The field has attracted many experimental and theoretical investigators, mainly due to the accessability of novel states of matter that can be created in degenerate Fermi systems. Arguably the most important and interesting system to study is the strongly interacting Fermi gas. After the first strongly interacting Fermi gas was produced in 2002 [18], an explosion of research has followed to investigate its properties. Strongly interacting Fermi gases have attracted a substantial amount of attention since they can model other strongly interacting systems in nature as discussed in Section 1.1.

A strongly interacting gas can be created by tuning the interactions between atoms through the use of a magnetic field. At a particular field, a so-called Feshbach resonance occurs, which is a collisional resonance between colliding atoms. In the vicinity of the Feshbach resonance, the zero-energy scattering length diverges, greatly exceeding the interparticle spacing. Under these conditions, the interactions become so strong that the collisional behavior of the gas is no longer dependent upon the microscopic details of the scattering potentials, but rather

becomes a function of the only relevant length scale, the interparticle spacing. A detailed review of the physics behind Feshbach resonances will be presented in Section 2.5 toward the end of the chapter.

This chapter begins with a discussion of the BEC-BCS crossover, which is the term given to describe the wide range of behavior exhibited in the vicinity of a Feshbach resonance. This is followed by a derivation of the collision cross section, σ_c, including quantum effects in Section 2.2. At the center of a Feshbach resonance where the scattering length diverges, the properties of a degenerate Fermi gas become universal and the gas is said to be in the unitary regime. The consequences of universality, including the effects of a unitary limited cross section, are described in Section 2.3. In order to understand the collisional properties of a Feshbach resonance presented in Section 2.5, it is instructive to provide an overview of the electronic states of ^{6}Li. A calculation of the energy eigenstates of ^{6}Li and how they tune with magnetic field is provided in Section 2.4. The chapter finishes with a discussion of the thermodynamic and hydrodynamic research that has been done in the unitary regime in Section 2.6.

2.1 The BEC-BCS crossover

At the heart of investigations into strongly interacting Fermi gases is the "BEC-BCS" crossover, where the character of a Fermi gas can be tuned from fermionic in nature to bosonic by simply changing a magnetic field. A natural starting point for describing the BEC-BCS crossover is a discussion of the acronym. BEC stands for Bose-Einstein condensation, which is a phenomenon first described by Einstein [43] and predicts how large numbers of bosonic particles will begin to populate

the ground state in a system if they are cooled below a critical temperature. On the other hand, BCS refers to the last names of the authors who first put forth BCS theory (Bardeen, Cooper, and Schrieffer) [23], which describes how superconductivity is achieved in a superconducting material through the paring of fermions.

These seem to be disparate subjects since they describe the properties of systems that follow completely different statistics. The beauty of the BEC-BCS crossover is that both types of behavior can be created in a Fermi gas through the use of a Feshbach resonance, which will be further discussed in Section 2.5. At the center of a Feshbach resonance, the zero-energy scattering length becomes infinite, but on either side of the resonance the scattering length is finite and opposite in sign. Below the resonance the scattering length is positive, producing a repulsive mean field and permitting the adiabatic formation of $^6Li_2$ molecules [44]. Since a molecule constructed of two fermions creates a composite boson, these molecules will follow Bose-Einstein statistics. When the gas is cooled below a critical temperature, a weakly interacting Bose-Einstein condensate can be created simply by tuning a magnetic field far below the resonance [45].

Alternately, above the Feshbach resonance the scattering length is negative, which does not favor the formation of molecules. Instead, if the magnetic field is tuned far above resonance a weakly interacting Fermi gas is created. At a cold enough temperature, paring can exist between the atoms in the gas that resemble the Cooper pairing of electrons in BCS theory. Therefore the BEC-BCS crossover describes the contrasting behaviors that are exhibited in the vicinity of a Feshbach resonance. These regimes are easily accessible to experimentalists due to the fact that the scattering length between two atoms can be tuned simply by

varying a magnetic field. Additionally, the gas is mechanically stable throughout the crossover region [46]. The wide tunability and stability features are unique to Fermi gases, since trapped Bose gases are unstable for negative scattering lengths [47]. The combination of these properties allows a multitude of unique studies to be performed on this novel system.

2.2 Collisional properties

Collisions between trapped atoms are of paramount importance for creating a degenerate, strongly interacting Fermi gas. By definition, a substantial amount of interactions must exist between atoms for a gas to be considered strongly interacting. These interactions are provided by collisions. One technique that is inherently a collisional process is the method of evaporative cooling, which reduces the temperature of the atom cloud and will be discussed in Section 3.4. During evaporative cooling, scattering events between atoms result in some of the particles gaining a sufficient amount of kinetic energy from the collision to escape from the trap, taking energy away with them. The remainder of the atoms in the trap can rethermalize to a lower temperature, providing a mechanism for cooling.

This section will focus on the theory that describes binary collisions between indistinguishable atoms. The major result will be a functional form for the scattering cross section, σ_c, which, qualitatively, describes the spatial extent of the atomic interactions. A derivation of this type can be found in most quantum mechanics texts [48, 49] and in previous theses [50, 51], so only the most relevant steps will be presented.

2.2.1 Scattering amplitude

The situation of a collision between two identical particles can be reduced to the equivalent scenario of a single particle of reduced mass μ_m colliding with a central potential $V(r)$ with momentum $\langle \mathbf{p} \rangle = \hbar \, \mathbf{k}$. Treating the atom as a wave packet and choosing the z-axis to be parallel to $\mathbf{k}$, after a collision with the potential the wavefunction that describes the atom, $\psi_{\mathbf{k}}$, can be written as

$$\psi_{\mathbf{k}} = e^{ikz} + \psi_{sc}(r, \theta, \phi), \tag{2.1}$$

where e^{ikz} is the original forward propagating plane wave and $\psi_{sc}(r, \theta, \phi)$ is a modification to the original wavefunction due to the interaction with the potential. Assuming that the potential vanishes as $r \to \infty$, the scattered part of the wavefunction far from the origin can be approximated by a spherical wave. Under these conditions the total wavefunction reduces to

$$\lim_{r \to \infty} \psi_{\mathbf{k}} = e^{ikz} + f(\theta, \phi) \frac{e^{ikr}}{r}, \tag{2.2}$$

where $f(\theta, \phi)$ is called the scattering amplitude. The scattering amplitude has units of length and is the only function in equation (2.2) that depends upon the potential $V(r)$. Since $V(r)$ is spherically symmetric, the scattering amplitude must be independent of ϕ, allowing the simplification $f(\theta, \phi) = f(\theta)$. But the scattering amplitude must also be a function of the energy $E = \hbar^2 k^2 / 2\mu_m$, leading to the final notational form of $f = f(\theta, k)$

One of the most important quantities to calculate in any scattering process in the collision cross section σ_c. An expression for the cross section can be obtained

through the use of the differential cross section, $d\sigma_c/d\Omega$, where $d\Omega$ is the solid angle. By calculating the ratio of the probability flowing into $d\Omega$ per second to the incident current density, the differential cross section can be shown to be [48]

$$\frac{d\sigma_c}{d\Omega} = |f(\theta, k)|^2 . \tag{2.3}$$

Based on the results of equation (2.3), a calculation of the differential cross section reduces to the calculation of $f(\theta, k)$. Any function of θ can be expanded in terms of the Legendre polynomials

$$P_l(\cos\theta) = \left(\frac{4\pi}{2l+1}\right)^{1/2} Y_l^0, \tag{2.4}$$

where Y_l^0 is the $m = 0$ spherical harmonic. Expanding $f(\theta, k)$ in terms of $P_l(\cos\theta)$ produces the partial wave expansion

$$f(\theta, k) = \sum_{l=0}^{\infty} (2l+1) f_l(k) P_l(\cos\theta), \tag{2.5}$$

where $f_l(k)$ are the partial wave amplitudes with corresponding angular momentum $\hbar\, l$. Since the assumed spherically symmetric form for the scattering potential conserves angular momentum, each one of the partial waves l scatter independently. The partial wave amplitudes are related to the scattering phase shifts, δ_l, by [48]

$$f_l(k) = \frac{e^{i\delta_l} \sin\delta_l}{k} = \frac{e^{2i\delta_l} - 1}{2ik}. \tag{2.6}$$

2.2.2 Identical particles

Up to this point the nature of the scattering particles has not been taken into account. In order to apply the results of Section 2.2.1 to a Fermi system, the statistics of the particles must be included. We are interested in equations that describe a collision between two identical fermions, which are *indistinguishable* particles. Therefore, the scattered part of the wavefunction, $\psi_{sc}(r, \theta)$, needs to be symmetrized in the center of mass frame of the colliding particles.

The total wavefunction for the collision is composed of a spatial component along with a spin component. Since we are considering the scattering of two fermions, the total wavefunction must be antisymmetric. An argument will be presented in Section 2.2.3 for the exclusive existence of s-wave collisions in the scattering of ultra-cold atoms. An s-wave collision requires a spatially *symmetric* spatial wavefunction. Therefore the spatial part of the scattered wavefunction must be symmetric leading to $\psi_{sc} \rightarrow [f(\theta, k) + f(\pi - \theta, k)]e^{ikr}/r$. This modifies equation (2.3) for the differential cross section to read

$$\frac{d\sigma_c}{d\Omega} = |f(\theta, k)|^2 + |f(\pi - \theta, k)|^2 + 2Re[f(\theta, k)f^*(\pi - \theta, k)], \tag{2.7}$$

where the asterisk in the last term represents the complex conjugate. The first two terms are valid for a collision between distinguishable particles and the last term accounts for the quantum interference that arises for scattering between identical particles. Since the entire θ dependence of the scattering amplitude is contained in the Legendre polynomial, where $P_l(-\cos\theta) = (-1)^l P_l(\cos\theta)$, the symmetrized

scattering amplitudes are described by

$$f(\pi - \theta, k) = \frac{1}{k} \sum_{l=0}^{\infty} (-1)^l (2l+1) e^{i\delta_l} \sin \delta_l P_l(\cos\theta) \tag{2.8}$$

$$f(\theta, k) = \frac{1}{k} \sum_{l=0}^{\infty} (2l+1) e^{i\delta_l} \sin \delta_l P_l(\cos\theta). \tag{2.9}$$

Since these two equations only differ by a factor of $(-1)^l$, the first two terms in equation (2.7) will be identical and positive definite, while the third term can either be positive or negative depending upon the order of the partial wave l.

2.2.3 Cross section and scattering length

An expression for the cross section can be acquired by inserting equations (2.8) and (2.9) for the scattering amplitudes into the differential cross section given by equation (2.7) and subsequently solving for σ_c. After performing the integral for the solid angle over 2π radians so as not to count each particle twice, the collision cross section can be shown to be

$$\sigma_c = \frac{4\pi}{k^2} \sum_{l=0}^{\infty} \left[1 + (-1)^l\right] (2l+1) \sin^2 \delta_l, \tag{2.10}$$

which is nonzero only for even values of l. This demonstrates that partial waves of even l will constructively interfere for indistinguishable particles with a symmetric spatial wavefunction, but will destructively interfere for odd l.

Although the formula for the collision cross section given by equation (2.10) seems to indicate that σ_c varies depending on the angular momentum of the incoming particles, a simple argument can be used to show that scattering is dominated by s-wave collisions in ultra-cold gases. A typical cloud of atoms produced during

experiments has a temperature of roughly 1 μK. For this temperature, a trapped atom has a de Broglie wavelength of approximately $\lambda_{dB} = 700$ nm and a corresponding maximum linear momentum of $p_{max} = h/\lambda_{dB} = 9.3 \times 10^{-28}$ kg m/s. Most scattering events of interested occur at high magnetic field where the atoms are interacting with a triplet molecular potential. For ^{6}Li the effective range of the potential is approximately $r_0 = 20$ Bohr. Therefore the maximum angular momentum that can be produced during a collision can be approximated by the equation $\hbar l_{max} = r_0 p_{max}$, which leads to a maximum l of

$$l_{max} = \frac{2\pi r_0}{\lambda_{dB}} \simeq .001 \tag{2.11}$$

essentially limiting the collisions to s-wave ($l = 0$).

When collisions are limited to s-wave in nature, the collision cross section in equation (2.10) can be greatly simplified. Neglecting all terms in the sum except the $l = 0$ term produces the s-wave collision cross section

$$\sigma_c = \frac{8\pi}{k^2} \sin^2 \delta_0 = \frac{8\pi}{k^2} \frac{\tan^2 \delta_0}{1 + \tan^2 \delta_0}, \tag{2.12}$$

where δ_0 is the s-wave scattering phase shift, and trigonometric identities were used to write σ_c in terms of $\tan \delta_0$. The s-wave phase shift can be calculated by solving the Schrödinger equation for a particle scattering off a central potential with $l = 0$

$$\frac{d^2\varphi}{dr^2} + \frac{2\mu_m}{\hbar^2} [E - V(r)] \varphi = 0, \tag{2.13}$$

where $\varphi(r)$ is the radial part of the scattering wavefunction and as before $E = \hbar^2 k^2 / 2\mu_m$. A qualitative plot of a solution to equation (2.13) is given in Figure 2.1.

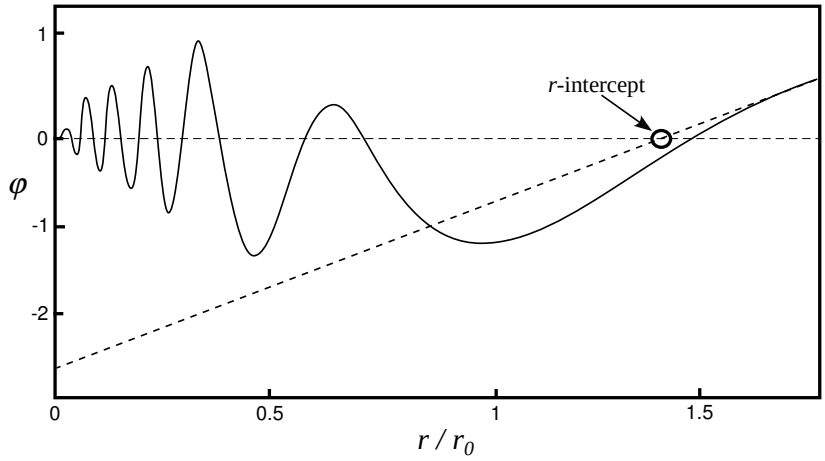

Figure 2.1: Illustration of the radial wavefunction, $\varphi(r)$, during a s-wave collision. The heavy dashed line shows the linear asymptotic form of $\varphi(r)$. The r-intercept gives the s-wave scattering length a_s, which in general can either be positive or negative.

The solution is highly oscillatory in the region within the range of the potential, $r < r_0$, where $kr_0 \ll 1$. For positions far from the influence of the potential, $r \gg r_0$, the solution is also oscillatory, but with a much larger spatial period of $1/k$, as will be shown below. Therefore, in the region $r_0 \ll r \ll 1/k$, the wavefunction φ can be approximated by a straight line, as shown in the figure.

The phase shift δ_0 can be calculated by solving the Schrödinger equation in the far field, $r \gg r_0$, where the potential is negligible. This reduces equation (2.13) to

$$\frac{d^2\varphi}{dr^2} + \frac{2\mu_m E}{\hbar^2}\varphi = 0, \tag{2.14}$$

which is easily solved to yield a solution of the form

$$\varphi(r) = A_0 \sin(kr + \delta_0), \tag{2.15}$$

where A_0 is a complex constant. The momentum, and hence the energy, of an s-wave collision is exceptionally small as demonstrated by equation (2.11). This allows the collisional properties to be determined under the condition of vanishing momentum. Using the condition $k \to 0$, equation (2.15) can be expanded about $k = 0$. Taking the expansion out to first order in k produces

$$\varphi(r) = (A_0 \sin \delta_0) \left(1 + \frac{k}{\tan \delta_0} r\right). \tag{2.16}$$

This is an equation of the form $\varphi(r) = A(1 + Br)$, which is also a solution of equation (2.14) for $E \to 0$. For the wavefunction in Figure 2.1, equation (2.16) is displayed as the linear dashed line that is tangent to the wavefunction φ for $r \gg r_0$. The r-intercept of this line defines the low energy s-wave scattering length a_s [4]. The case illustrated in Figure 2.1 is for a positive a_s, but the scattering length can either be positive or negative depending upon the nature of the scattering potential. By setting $\varphi(r) = 0$ in our simple formula, the s-wave scattering length is identified as $a_s = -1/B$. Comparing this simple expression to equation (2.16) generates the relation

$$\lim_{k \to 0} a_s = -\frac{\tan \delta_0}{k}. \tag{2.17}$$

The s-wave scattering length in this form qualitatively describes the spatial extent of the interactions. The larger the scattering length, the larger the effect of the interaction.

The expression for the s-wave scattering length in equation (2.17) allows the

collision cross section given in equation (2.12) to be written in terms of a_s as

$$\sigma_c = \frac{8\pi a_s^2}{1 + k^2 a_s^2}. \tag{2.18}$$

For very low collision energies the assumption $k \to 0$ can be applied to equation (2.18) to give the weak interaction limit for the cross section

$$\lim_{k \to 0} \sigma_c = 8\pi a_s^2, \tag{2.19}$$

which is *independent* of energy. This is a very important result since it states that the scattering process for low energies can be characterized by a single parameter a_s as long as the interactions are not too strong. In the weakly interacting limit the mean field interaction can be described as $U_{int} = gn$, where $g = 4\pi\hbar^2 a_s/m$ and n is the density. Since the sign of a_s can be negative or positive, a mean field can be produced that is either attractive ($a_s < 0$) or repulsive ($a_s > 0$). The effects of the mean field interaction will be discussed further is Section 2.3.1.

2.3 The Unitary regime

The expression given in equation (2.19) that relates the collision cross section to the s-wave scattering length is valid for the case of weak interactions. In general, the scattering length can vary between $-\infty \leq a_s \leq \infty$, rendering the expression $\sigma_c = 8\pi a_s^2$ unphysical as $a_s \to \pm\infty$. Rather, in this limit equation (2.18) reduces to

$$\lim_{a_s \to \pm\infty} \sigma_c = \frac{8\pi}{k^2}, \tag{2.20}$$

which is energy *dependent* since $k^2 = 2\mu_m E/\hbar^2$. This result can also be obtained from the scattering amplitude $f_0 = (e^{2i\delta_0} - 1)/2ik$. For a resonant collision $\delta_0 = \pi/2$ leading to $f_0 = i/k$. Plugging this into the equation for the cross section yields $\sigma_c = 8\pi|f_0|^2 = 8\pi/k^2$.

In this limit the interactions are no longer dependent upon the magnitude or sign of the scattering length, but rather are functions of the wavevector k, which is proportional to the interparticle spacing for a Fermi gas at zero temperature. Actually, the wavevector k defines the only relevant length scale in the system as $a_s \to \pm\infty$. In this so-called unitary regime, which occurs in the vicinity of a Feshbach resonance, a strongly interacting Fermi gas can be created. This section will detail the ground state properties of a Fermi gas in the unitary regime.

2.3.1 Universal parameters

In the unitary regime, the properties of a zero temperature gas can be shown to rely on a few universal parameters [13]. These parameters are universal, meaning they should be applicable for all unitary Fermi systems, since the collisional properties, such as σ_c, no longer depend upon the microscopic details of the scattering potentials. This is demonstrated by the absence of a_s, which is intimately related to $V(r)$, in equation (2.20). The unitary hypothesis is incredibly powerful since it allows the results of our experiments, obtained using ^{6}Li atoms, to be applied to other strongly interacting Fermi systems in nature, such as electrons or quarks, as described in Section 1.1.

The most relevant and experimentally accessible universal parameter is denoted as β and describes the ratio of the ground state energy per particle in the unitary regime to the Fermi energy in a noninteracting *homogenous* gas as

$E_0/E_F = 1 + \beta$, where $E_F = \hbar^2 k_F^2/2m$ [18]. For a harmonically *trapped* gas, the ratio can be shown to be $E_0/E_F = \sqrt{1+\beta}E_F$, where $E_F = \hbar(3N\omega_x\omega_y\omega_z)^{1/3}$ and the ω_i are the harmonic trap frequencies. The influence of β on the thermodynamics of a trapped Fermi gas in the unitary regime is best demonstrated by looking at the equation of state. The equation of state for a *noninteracting* spin polarized gas at zero temperature in a trapping potential $U(\mathbf{r})$ is [52]

$$\epsilon_F(\mathbf{r}) + U(\mathbf{r}) = E_F, \tag{2.21}$$

where $\epsilon_F(\mathbf{r})$ is the local Fermi energy that can be written as $\epsilon_F(\mathbf{r}) = \hbar^2 k_F^2(\mathbf{r})/2m$. The local Fermi wavevector, $k_F(\mathbf{r})$, is determined from the density $n(\mathbf{r})$ as

$$k_F(\mathbf{r}) = [6\pi^2 n(\mathbf{r})]^{1/3}. \tag{2.22}$$

The Fermi energy, E_F, is also equal to the global chemical potential, μ_{NI}, for a noninteracting gas. For a zero temperature harmonically trapped noninteracting Fermi gas with $N/2$ atoms per spin state, the Fermi energy is calculated to be

$$E_F = \hbar\bar{\omega}(3N)^{1/3}, \tag{2.23}$$

where $\bar{\omega} = (\omega_x\omega_y\omega_z)^{1/3}$ is the geometric mean of the trap frequencies.

If a model for a weakly interacting gas is desired, an additional term must be added to the left hand side of equation (2.21) to account for the interaction. For weak interactions, a mean field $U_{int} = gn(\mathbf{r})$ can be used, where the coupling constant is given by $g = 4\pi\hbar^2 a_s/m$. Since this expression is linearly proportional to the s-wave scattering length, it can not be used to describe the mean field

interaction in the unitary regime where $a_s \to \pm\infty$. In this limit the only length scale available is given by the Fermi wavevector $1/k_F$. Therefore, in the unitary regime, $g \propto 1/k_F$. It has been established by equation (2.22) that the density is proportional to k_F^3, requiring that the unitary mean field interaction follows $U_{int} = gn(\mathbf{r}) \propto k_F^2$ based purely on dimensional grounds. Since the local Fermi energy, $\epsilon_F(\mathbf{r}) = \hbar^2 k_F^2(\mathbf{r})/2m$, is also proportional to k_F^2, the relation

$$U_{int}(\mathbf{r}) = \beta\, \epsilon_F(\mathbf{r}) \tag{2.24}$$

can be used for the unitary mean field interaction potential. Inserting equation (2.24) into the equation of state given by equation (2.21) produces

$$(1+\beta)\epsilon_F(\mathbf{r}) + U(\mathbf{r}) = \mu \tag{2.25}$$

where μ is the global chemical potential for a unitary gas. Equation (2.25) is identical to the noninteracting equation of state, equation (2.21), if an effective mass $m^* = m/(1+\beta)$ is defined. Since the geometric mean of the trap frequencies, $\bar{\omega}$, is proportional to $\sqrt{1/m}$, the chemical potential for a zero temperature unitary Fermi gas differs from equation (2.23) by a factor of $\sqrt{1+\beta}$ resulting in

$$\mu = \sqrt{1+\beta}\, E_F, \tag{2.26}$$

with E_F given in equation (2.23).

An equation of state of the form of equation (2.25) is not unique to just trapped gases. The problem of calculating the ground state properties of a unitary Fermi gas was first posed by G. F. Bertsch in 1999 for the specific case of nuclear mat-

ter [53]. This was followed by the formulation of equation (2.24) to describe the unitary mean field interaction in a strongly interacting Fermi gas in 2002 [18]. Since β is a *universal* parameter, the interaction potential in equation (2.24) is applicable to all Fermi systems regardless of their microscopic structure. Measurements of β have been performed by many experimental groups using a myriad of methods. The most recent experimental measurements indicate that the value of β is between -0.54 [38] and -0.57 [54]. These measurements are consistent with recent quantum Monte Carlo calculations that predict $\beta = -.58$ [31, 34, 55] and $\beta = -.56$ [29].

2.3.2 Unitary gas total energy

In Section 2.3.1 it was shown that the chemical potential of a harmonically trapped strongly interacting Fermi gas assumes a universal form in the unitary regime. The same universal ideas can be extended to other thermodynamic quantities, such as the total energy of a trapped gas [56]. Consider a small volume ΔV of gas in the trap at a position $\mathbf{r}$ containing a number of particles ΔN with energy ΔE. Further, by assuming that the number of particles in the volume remains constant, a fixed value of $n = \Delta N/\Delta V$ results. In the unitary regime the total energy ΔE must be proportional to the local Fermi energy $\epsilon_F(n)$. As a result, the local energy can be written as

$$\Delta E = \Delta N \epsilon_F(n) f_E \left[\frac{T}{T_F(n)}\right], \tag{2.27}$$

where f_E is a function of the local Fermi temperature $T_F(n)$. Dividing both sides of equation (2.27) by ΔV yields the energy density

$$\frac{\Delta E}{\Delta V} = \mathcal{E}(n,T) = n\,\epsilon_F(n) f_E\left[\frac{T}{T_F(n)}\right], \tag{2.28}$$

where $f_E = 3/5$ for a zero temperature ideal Fermi gas and $f_E = 3(1+\beta)/5$ for a zero temperature unitary gas.

A similar expression to equation (2.27) can be written for the total entropy, ΔS. Through the use of the thermodynamic identity $P = -\partial\Delta E/\partial\Delta V$ at constant ΔS and ΔN, the pressure can be determined to be [13, 56]

$$P(\mathbf{r}) = \frac{2}{3}\,n\,\epsilon_F(n) f_E\left[\frac{T}{T_F(n)}\right], \tag{2.29}$$

leading to the identity $P = \frac{2}{3}\,\mathcal{E}(n,T)$. In mechanical equilibrium, the forces due to the pressure and the trap potential must be equal. Therefore, the Euler equation [57] for a trapped gas reduces to

$$\boldsymbol{\nabla} P(\mathbf{r}) + n(\mathbf{r})\boldsymbol{\nabla} U(\mathbf{r}) = 0, \tag{2.30}$$

where the expression for $P(\mathbf{r})$ is given in equation (2.29) and was also shown to equal $P = \frac{2}{3}\,\mathcal{E}(n,T)$. By multiplying both sides of equation (2.30) by $\mathbf{r}$ and integrating over the volume of the trap produces the relation

$$N\langle U\rangle = \frac{E}{2}, \tag{2.31}$$

where $\langle U\rangle$ is the average potential energy per particle for a harmonic trap. Equa-

tion (2.31) is an expression for the virial theorem in a harmonically trapped unitary Fermi gas. The potential for a harmonic oscillator has the form $U(\mathbf{r}) = m\left(\omega_x^2 x^2 + \omega_y^2 y^2 + \omega_z^2 z^2\right)/2$. Therefore, the average potential energy is proportional to the mean square size, $\langle U \rangle \propto \langle x^2 \rangle$. Based on this result, the desired expression for the total energy can be shown to be

$$\frac{E}{N} = 3m\omega_x^2 \langle x^2 \rangle, \tag{2.32}$$

where ω_x is the trap frequency in the x-direction.

The expression in equation (2.32) is a very powerful relation since it states that a value for the total energy of a strongly interacting gas in the universal regime can be obtained simply by measuring the mean square size of the atom cloud. In the strongly interacting regime thermometry is difficult, requiring the state of the gas to be described by a parameter other than temperature. Using equation (2.32), the state of the gas can be determined as a function of the total energy instead of the temperature, which is of paramount importance when characterizing the gas at finite temperatures.

2.4 Electronic states of ^{6}Li

Before discussing the collisional Feshbach resonance that facilitates the unitary regime, it is necessary to understand how the energy levels of ^{6}Li tune in an applied magnetic field. Lithium is an alkali metal, being found in group 1A in the leftmost column of the periodic table. What distinguishes the alkali metals from other atoms is a single unpaired valence electron. Neutral lithium atoms have 3 protons and 3 electrons yielding a ground state electronic configuration of $1s^2 2s^1$,

along with a first excited state configuration of $1s^2 2p^1$. Our experiments employ the ^{6}Li isotope, which is a fermion that contains 3 neutrons, as opposed to the 4 neutrons found in the more naturally abundant ^{7}Li.

A knowledge of the electronic structure of ^{6}Li is critical for the imaging and trapping methods employed in our lab. All the experiments performed in this thesis utilize the two lowest hyperfine ground states of ^{6}Li, and are executed at various magnetic fields. Therefore, a detailed knowledge of the Zeeman tuning of the ground state energy levels with magnetic field are essential. In Section 2.3 the ground state electronic properties of ^{6}Li are presented by including the effects of a magnetic field on the atomic Hamiltonian. This is followed by a discussion of the energy level configuration for first excited state of ^{6}Li, which can be coupled to the ground state through the use of near-resonant light.

2.4.1 ^{6}Li ground state

A ^{6}Li atom is a composite fermion, where the total atomic spin is made up of several different components. In the ground state, the valence electron of the ^{6}Li is in an s-state, which is spherically symmetric and has an orbital angular momentum quantum number of $L = 0$. Being a fermion, the spin quantum number of the valence electron is $S = 1/2$, whereas the total nuclear spin is $I = 1$. As a consequence of angular momentum addition, the total angular momentum, $F = I + L + S$, can be either $F = 3/2$ or $F = 1/2$.

The nuclear spin and the electron spin are coupled by a magnetic dipole interaction that takes the form

$$H_{hf} = \frac{a_{hf}}{\hbar^2} \mathbf{S} \cdot \mathbf{I}, \tag{2.33}$$

where $a_{hf}/\hbar = 152.14$ MHz is the magnetic dipole constant. The interaction described by equation (2.33) lifts the degeneracy of the $F = 3/2$ and $F = 1/2$ states producing a hyperfine doublet with an energy splitting of $\hbar \times 228.2$ MHz, with $F = 1/2$ being lower in energy. Each of the F states have angular momentum projections, m_F, that are degenerate at zero magnetic field. The degeneracy is lifted with the application of a magnetic field through the interaction

$$H_B = \frac{\mu_B}{\hbar}\left(g_J^{gnd}\,\mathbf{S} + g_I\,\mathbf{I}\right)\cdot\mathbf{B}, \tag{2.34}$$

where μ_B is the bohr magneton, $g_J^{gnd} = 2.002$ is the total electronic g-factor for the ^{6}Li ground state, $g_I = -0.000448$ is the total nuclear g-factor, and B is the external magnetic field.

The total interaction Hamiltonian is composed of the sum of the individual magnetic dipole and Zeeman Hamiltonians given by equations (2.33) and (2.34) respectively. Diagonalizing the total interaction Hamiltonian in the $|m_S\ m_I\rangle$ basis produces the six orthonormal eigenstates

$$|1\rangle = \sin\Theta_+\ |1/2\ 0\rangle - \cos\Theta_+\ |-1/2\ 1\rangle \tag{2.35}$$

$$|2\rangle = \sin\Theta_-\ |1/2\ -1\rangle - \cos\Theta_-\ |-1/2\ 0\rangle \tag{2.36}$$

$$|3\rangle = |-1/2\ -1\rangle \tag{2.37}$$

$$|4\rangle = \cos\Theta_-\ |1/2\ -1\rangle + \sin\Theta_-\ |-1/2\ 0\rangle \tag{2.38}$$

$$|5\rangle = \cos\Theta_+\ |1/2\ 0\rangle + \sin\Theta_+\ |-1/2\ 1\rangle \tag{2.39}$$

$$|6\rangle = |1/2\ 1\rangle\,, \tag{2.40}$$

where the kets $|m_S\ m_I\rangle$ give the electronic spin projection $m_S = \pm 1/2$ and the

nuclear spin projection $m_I = -1, 0, 1$. The states are in order of increasing energy, with state $|1\rangle$ being lowest in energy. States $|4\rangle$ through $|6\rangle$ are low field seeking, being drawn towards regions of low field when placed in a magnetic field gradient. Alternately, states $|1\rangle$ through $|3\rangle$ are high field seeking states, making them unfit for magnetic trapping and compelling the need for all-optical trapping methods. The coefficients in equations (2.35) through (2.40) are defined by

$$\sin\,\Theta_{\pm} = \frac{1}{\sqrt{1+\left(Z^{\pm}+R^{\pm}\right)^2/2}} \tag{2.41}$$

$$\cos\,\Theta_{\pm} = \sqrt{1-\sin^2\Theta_{\pm}} \tag{2.42}$$

$$Z^{\pm} = \frac{\mu_B\,B}{a_{hf}}(g_J^{gnd}-g_I)\pm\frac{1}{2} \tag{2.43}$$

$$R^{\pm} = \sqrt{(Z^{\pm})^2+2}, \tag{2.44}$$

which vary depending upon magnetic field strength. In addition to the eigenstates in equations (2.35) through (2.40), the diagonalization of the total interaction Hamiltonian also produces six magnetic field dependent energy eignevalues given in terms of coefficients (2.43) and (2.44) as

$$E_1 = -\frac{1}{4}\left(a_{hf}-2\,g_I\,\mu_B\,B+2\,a_{hf}\,R^{+}\right) \tag{2.45}$$

$$E_2 = -\frac{1}{4}\left(a_{hf}+2\,g_I\,\mu_B\,B+2\,a_{hf}\,R^{-}\right) \tag{2.46}$$

$$E_3 = \frac{a_{hf}}{2}-\frac{\mu_B\,B}{2}(2\,g_I+g_J^{gnd}) \tag{2.47}$$

$$E_4 = \frac{1}{4}\left(-a_{hf}-2\,g_I\,\mu_B\,B+2\,a_{hf}\,R^{-}\right) \tag{2.48}$$

$$E_5 = \frac{1}{4}\left(-a_{hf}+2\,g_I\,\mu_B\,B+2\,a_{hf}\,R^{+}\right) \tag{2.49}$$

$$E_6 = \frac{a_{hf}}{2}+\frac{\mu_B\,B}{2}(2\,g_I+g_J^{gnd}). \tag{2.50}$$

A plot of the energy eignevalues in equations (2.45) through (2.50) is given in Figure 2.2. As shown in the figure, states $|1\rangle$ through $|3\rangle$ decrease in energy with increasing magnetic field. As mentioned previously, these states are referred to as high field seeking states, and are incapable of being confined in a magnetic trap, where magnetic field gradients are used to trap the atoms. Since a local magnetic field maximum is impossible to create in free space, only the low field seeking states $|4\rangle$ through $|6\rangle$ can be used in a magnetic trap.

In the experiments presented in this thesis, an equal mixture of the two lowest energy states $|1\rangle$ and $|2\rangle$ are used. These states are allowed to be trapped since the experiments are performed using all-optical methods. A mixture of states $|1\rangle$ and $|2\rangle$ is used since a gas composed of a single spin state would be *non-interacting* due to Fermi statistics. It was shown in Section 2.2.2 that a symmetric spatial part of the scattering wavefunction is necessary for s-wave collisions. Since the total wavefunction for fermions must be antisymmetric, this must be reflected in the spin component. An antisymmetric wavefunction cannot be constructed out of a single spin state, therefore only p-wave collisions are allowed for a spin polarized mixture. Since p-wave collisions are highly suppressed in ultra-cold systems, the mixture will be essentially noninteracting. Therefore, since collisions are essential in order to cool a strongly interacting Fermi gas, a mixture of spin states must be used.

There are certain advantages of using states $|1\rangle$ and $|2\rangle$ in experiments. Collisions between some higher energy states are connected by inelastic collision channels, which release enough energy during the collision to eject an atom from the trap. It can be gathered from Figure 2.2 that at large magnetic fields a substantial energy gap exists between the three highest and lowest states. During s-wave

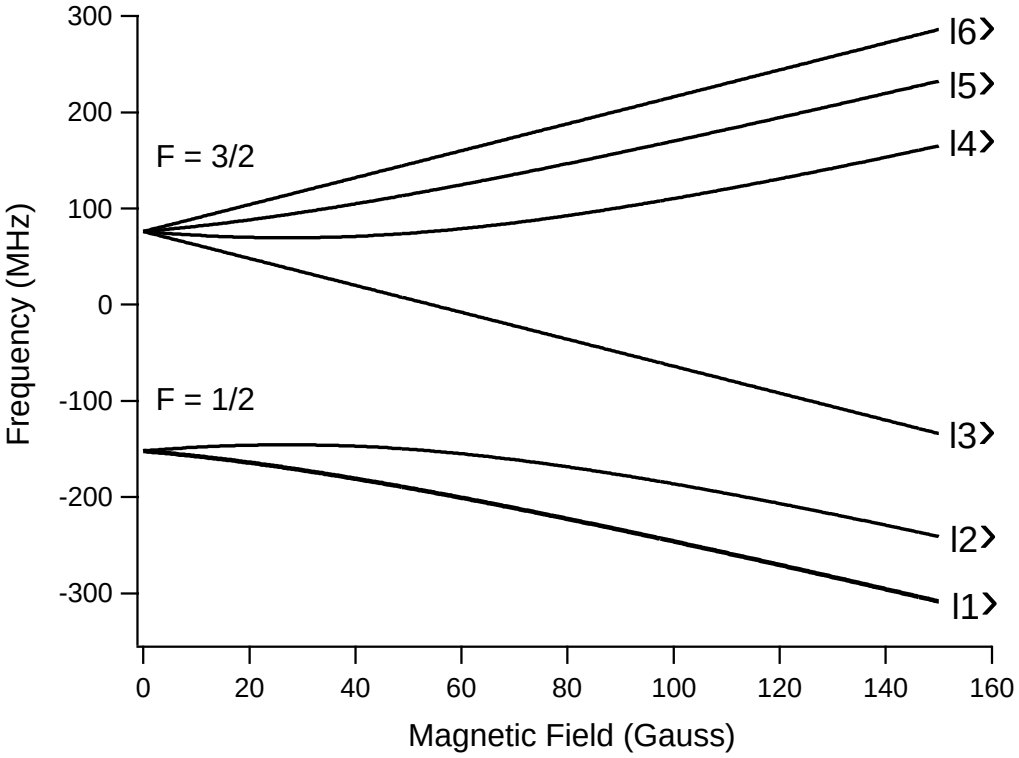

Figure 2.2: Tuning of the hyperfine ground state energy levels with magnetic field for ^{6}Li in frequency units. The states are identified by their respective eigenvalues $|1\rangle$ through $|6\rangle$. The total angular momentum quantum number at zero magnetic field, $F = 1/2$ and $F = 3/2$, is denoted at the left of the figure. An equal mix of the two lowest energy states, $|1\rangle$ and $|2\rangle$, are used in the experiments presented in this thesis.

collisions in the ^{6}Li ground state, the total angular momentum spin projection $m_F = m_S + m_I$ is conserved during a collision. Therefore, an inelastic collision between initial states $|1\rangle$ and $|4\rangle$, for example, can result in the final states $|1\rangle$ and $|2\rangle$. But the gap in energy between $|2\rangle$ and $|4\rangle$ is in the mK range in temperature units, whereas the temperature of the atoms in the trap is typically only hundreds of nK. If inelastic collisions are allowed to exist, the gas would quickly destroy itself through the creation of high energy particles. Since states $|1\rangle$ and $|2\rangle$ are the lowest lying states, these types of destructive inelastic collisions are forbidden.

2.4.2 $2P$ excited states

Although and understanding of the ground state properties of the ^{6}Li atom is sufficient to deduce the corresponding collisional properties, a knowledge of the energy level spacing for the $2P$ first excited state is necessary to discern the interactions created by a near-resonant laser field. This will be of paramount importance later in Chapter 3, which contains a description of the trapping methods used in the lab.

When a near-resonant laser field is incident on an atom in the ground state, an excited state can be populated through the absorbtion of a photon. The first excited state in ^{6}Li is the $2P$ level and has an orbital angular momentum quantum number of $L = 1$. Due to a $\mathbf{L} \cdot \mathbf{S}$ spin orbit coupling, the fine structure is split into a doublet of $2P_{1/2}$ and $2P_{3/2}$ levels, where the subscript refers to the total electronic angular momentum quantum number, $J = L + S$, for the level. The fine structure of the first excited state is shown in the energy level diagram in Figure 2.3. Also shown in the figure are the D_1 and D_2 lines (a notation that is a

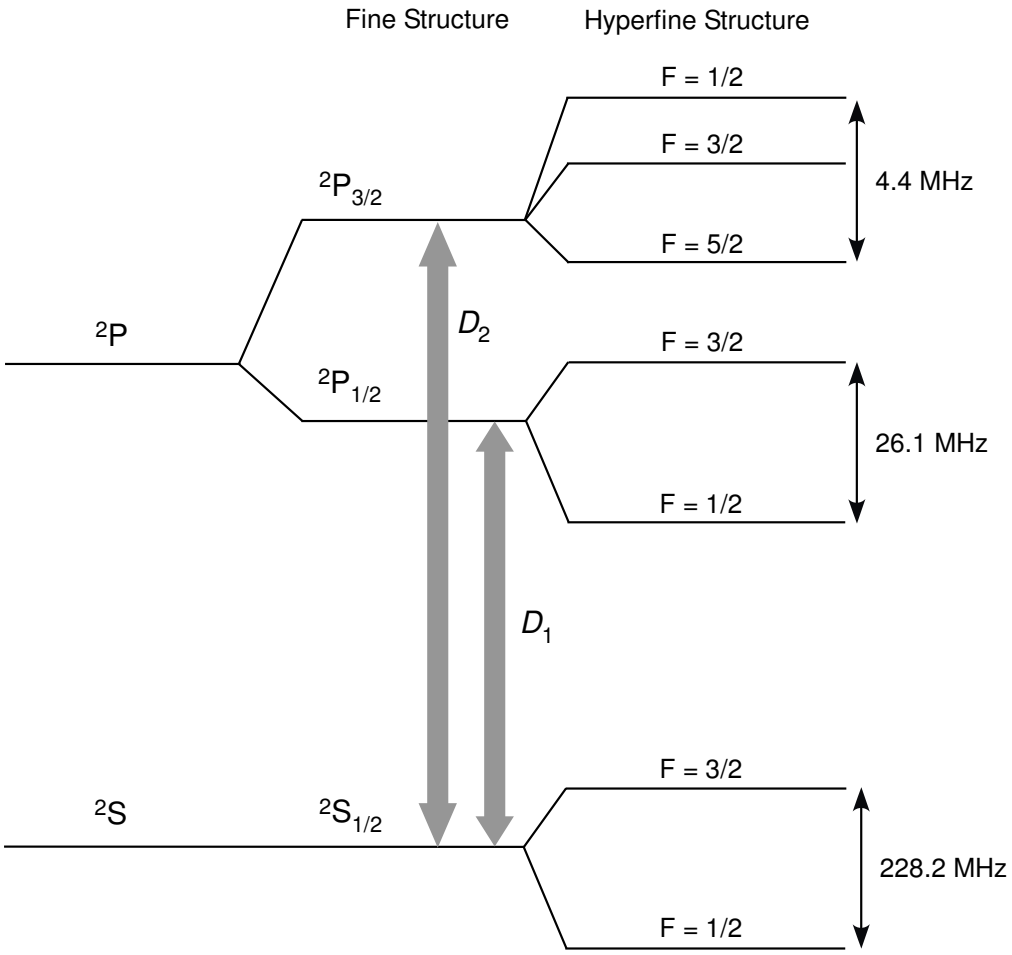

Figure 2.3: Energy level diagram of the ground and $2P$ excited states of ^{6}Li at zero magnetic field. The so-called D_1 and D_2 spectroscopic lines represent transitions between the ground and excited states due to a resonant laser field. The frequency gap between the two lines is $D_2 - D_1 = 10.056$ GHz. The diagram is not to scale.

vestige from spectroscopic studies) that denote two broad peaks that are observed when spectroscopy is performed on a sample of ^{6}Li. The frequency splitting between the the D_1 and D_2 lines is 10.056 GHz, which is large in comparison to the hyperfine splittings also shown in the figure. Due to an enhancement in transition strength [2, 50] and the presence of a cycling transition, the D_2 line is favored over the D_1 line for trapping and imaging procedures used during experiments.

2.5 Collisional Feshbach resonances

The unitary regime, as discussed in Section 2.3, is accessed through the use of a collisional Feshbach resonance. In the case of s-wave scattering in our lab, a Feshbach resonance occurs for collisions between ^{6}Li atoms of different internal states, notably states $|1\rangle$ and $|2\rangle$ from Section 2.3. For a binary collision between two atoms, the individual spins of the valence electrons, $\mathbf{s}_1$ and $\mathbf{s}_2$ are coupled to make a total spin $\mathbf{S}_{tot} = \mathbf{s}_1 + \mathbf{s}_2$. Since the individual spin quantum numbers are $s_1 = s_2 = 1/2$, the total spin quantum number can be $S_{tot} = 0$ or 1 as a result of angular momentum addition. The state $S_{tot} = 0$ is called the singlet state since it only has one angular momentum projection given by $m_S = 0$. The electrons must be antiparallel in this state since the sum of the spin projections is equal to zero. Likewise, the $S_{tot} = 1$ state is referred to as the triplet state since the angular momentum projections can be $m_S = -1, 0, 1$. In contrast to the singlet state, in the triplet state the electrons are parallel before the collision.

For a collision in the singlet state, the spin component of the scattering wavefunction is antisymmetric, leading to a symmetric spatial component since the

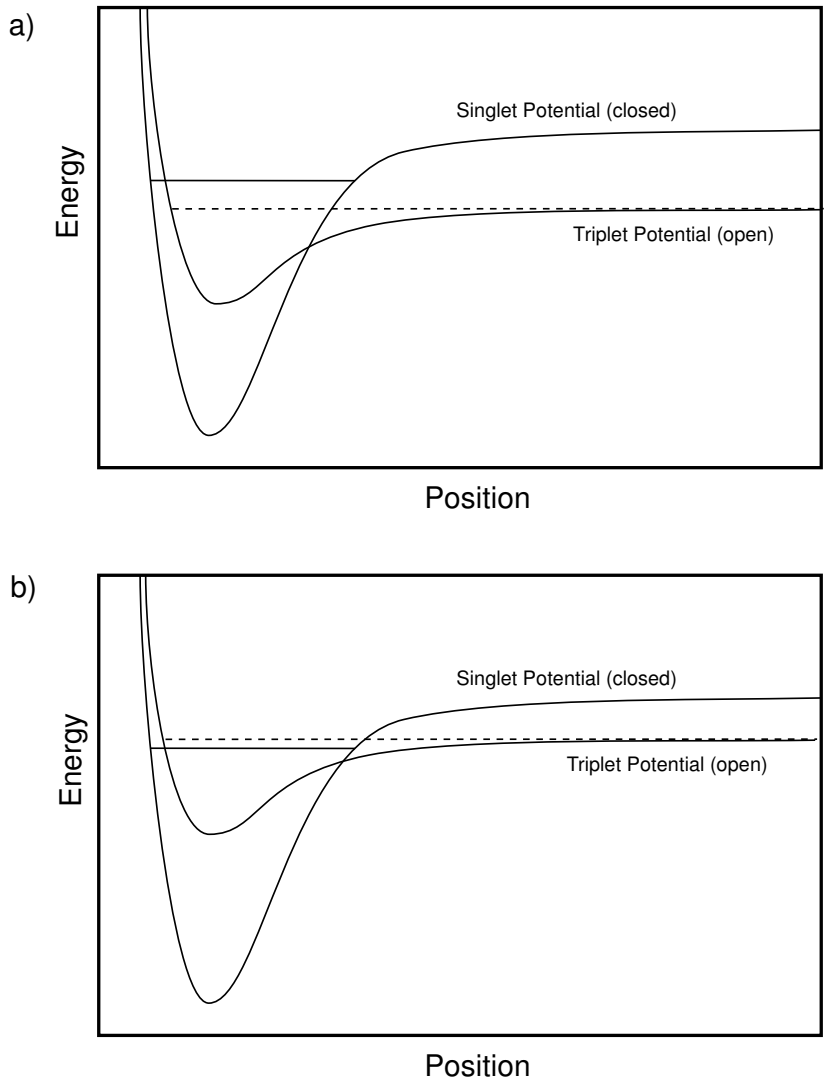

Figure 2.4: Illustration of the singlet and triplet molecular potentials for different magnetic fields. In plot a) the bound state in the singlet potential, indicated by the horizontal solid line, is above the dashed line representing the total energy of two incoming atoms with vanishing kinetic energy with respect to the triplet potential. By changing the magnitude of a magnetic field, the collisional energy in the triplet potential can be tuned above the bound state in the singlet potential as shown in plot b). At an intermediate field the bound state will be equal to the total energy of the collision, giving rise to a Feshbach resonance.

total wavefunction for fermions must be antisymmetric. A symmetric spatial wavefunction allows the electrons to be located at a position between the nuclei, producing a deep potential well. Conversely, the triplet state has an antisymmetric spatial wavefunction, excluding the electrons from the region between the nuclei and creating a shallow potential as shown in Figure 2.4.

Although two different potentials are possible, only scattering through the triplet potential is allowed based on energy considerations [12]. Therefore the triplet potential is referred to as an "open" channel, while the singlet potential is considered a "closed" channel. But a resonance can occur when the total energy of the collision, given as the dashed line in Figure 2.4, is equal to energy of a bound state in the closed channel, given by the solid line in the figure. Since the magnetic moments of states $|1\rangle$ and $|2\rangle$ from Section 2.3 tune differently for different magnetic field magnitudes, the open triplet channel bound state can be tuned relative to the closed singlet channel. This allows the resonance condition to be achieved by simply varying a bias magnetic field.

If the resonance condition occurs at a particular bias magnetic field B_0, the s-wave scattering length can be approximated by [4]

$$a_s = a_b \left(1 - \frac{\Delta}{B - B_0}\right) \tag{2.51}$$

where $a_b = -2240$ Bohr is the background scattering length and Δ is the width of the resonance. For s-wave collisions between states $|1\rangle$ and $|2\rangle$ the resonant magnetic field is 834 Gauss [58]. The width of the resonance for collisions between these states is roughly 100 Gauss, as shown in the plot of the scattering length in the vicinity of the Feshbach resonance in Figure 2.5. The large width of the

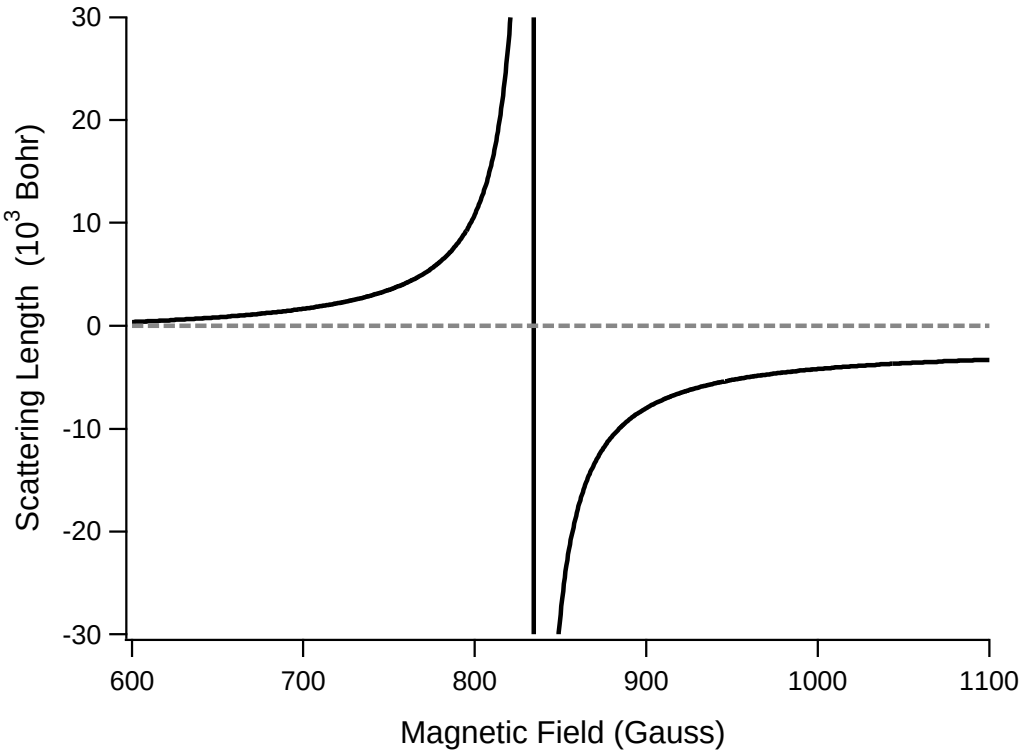

Figure 2.5: Plot of the scattering length a_s in the vicinity of a Feshbach resonance. The magnitude of the scattering length is positive at magnetic fields below the resonance, centered at 834 Gauss, and negative for fields above. Far above the resonance, a_s asymptotes to the background scattering length. The data in the plot is derived from the work presented in [58].

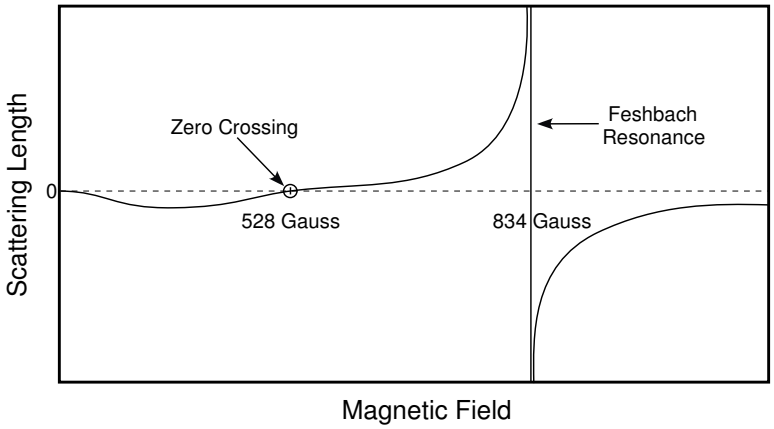

Figure 2.6: Comprehensive plot of the s-wave scattering length between states $|1\rangle$ and $|2\rangle$. The dashed line shows the location of zero a_s. The scattering length has a null value at zero magnetic field as well as at 528 Gauss. An attractive mean field due to a negative scattering length is found below 528 Gauss and above 834 Gauss, while a repulsive mean field only exists between these two fields.

resonance allows easy access to the BCS and BEC regions to the far right and left of the resonance, respectively. It also provides a wide area of strong interactions close to resonance. This allows the properties of the gas to be continuously tuned allows a great amount of control over the state of the gas.

There does exist an additional *narrow* Feshbach resonance at approximately 544 Gauss [42]. This resonance is not utilized during experiments since, as its name suggests, it is far to narrow to be of use. The narrow Feshbach resonance at 544 Gauss has a width of roughly 1 Gauss, which is technically challenging to reliably reproduce. Therefore, all of the experiments on strongly interacting gases described in this thesis are performed near the wide Feshbach resonance at 834 Gauss.

Although the scattering length in Figure 2.5 appears to asymptotically approach zero to the left of the resonance, it actually crosses zero at a magnetic

field of 528 Gauss [59] as shown in Figure 2.6. At this magnetic field the collision cross section vanishes according to equation (2.19), producing a *noninteracting* gas of the two states $|1\rangle$ and $|2\rangle$. This is extremely advantageous since it allows some experiments to be done in the ideal gas regime where the properties of the gas are well known. Therefore by simply tuning a magnetic field, a mixture of states $|1\rangle$ and $|2\rangle$ can go from noninteracting at 528 Gauss to strongly interacting at 834 Gauss, which is quite a remarkable experimental tool.

2.6 Unitary experiments

Since the first strongly interacting Fermi gas was produced in 2002 [18], a substantial amount of growth has been experienced in the field. One of the main motivations behind this progress was the so-called "race for superfluidity" that was reflected by many experimental groups providing evidence for a superfluid state in a degenerate Fermi gas. The first claim of evidence came in the form of a experiment where a fermionic condensate was projected onto a molecular condensate through the use of a fast magnetic field sweep [60]. The validity of the technique was first disputed [61], but was later confirmed when it was demonstrated that the formation time of the molecular condensate was long enough to affirm that the projection technique was accurate [62].

Evidence for superfluid hydrodynamics was provided in the form of exceptionally long lifetimes in collective mode experiments [63]. For a collisional gas, as the temperature goes to zero the collision rate, γ_c, also vanishes. Since the damping time is proportional to the collision rate, $\tau \sim \gamma_c/\omega^2$, the collective mode lifetime should decrease as the temperature is reduced. It was found, however, that at

lower temperatures the lifetime of the collective mode increased. This behavior can only be explained through the use of *superfluid* hydrodynamics as opposed to *collisional* hydrodynamics.

The supposed race reached a conclusion when a vortex lattice was observed to form in the equilibrium state of a stirred condensate [64]. A vortex lattice can only be supported in a superfluid system, and provides evidence for macroscopic coherence in the system. Although the qualitative proof of the existence of a condensate is a phenomenal achievement in its own right, it doesn't provide any *quantitative* information about the properties of the system. A substantial amount of information can be learned about a strongly interacting system by studying the corresponding thermodynamic and hydrodynamic properties.

The first experimental studies of the thermodynamics of a strongly interacting Fermi gas involved measuring the heat capacity [26]. This experiment resulted in a method of measuring the temperature of a strongly interacting Fermi gas, albeit in a model dependent way. These measurements supported a theoretical model based on pseudogap theory. The development of thermodynamic models was further advanced through the demonstration that a model independent measurement of the total energy of the gas can be obtained through a measurement of the mean square cloud size [56], as presented earlier in this chapter in Section 2.3.2. In that work, a method was proposed for measuring the entropy as a function of energy in the strongly interaction regime [56]. A little over a year later, the proposed entropy measurement experiment was executed by utilizing adiabatic magnetic field sweeps from the Feshbach resonance to a weakly interacting region, where the entropy is well known and easily measured [39]. The details of this experiment will be presented in Section 6.2. An understanding of the entropy as

a function of energy allowed the first model independent characterization of the thermodynamics and temperature of the gas in the unitary regime.

Various studies of the hydrodynamics in the unitary regime have been performed beginning in 2004. The bulk of the work centers around the measurement of collective modes. The first hydrodynamic experiments in the unitary regime involved characterizing the properties of radial breathing modes [63,65,66]. Breathing modes are characterized by the rhythmic vibration of the gas at specific frequency determined by the hydrodynamic properties of the system and will be discussed in Section 4.8.2. Other collective mode experiments have been performed in the unitary regime including investigations into the radial quadrupole mode [67] and scissors modes [68].

Most of the previous hydrodynamic experiments in the unitary regime focus on the dynamics of the gas at temperatures close to the ground state. Although these experiments probe the superfluid properties of the gas, interesting dynamics can also be observed in the strongly interacting normal fluid. In Chapter 5 a hydrodynamic experiment that is performed throughout the superfluid and normal regimes is presented. In this experiment, the expansion dynamics of a rotating atom cloud in the unitary regime is studied, and the results are compared to a model based on superfluid hydrodynamics. It is shown that the model closely follows the experimental data not only in the superfluid regime, but when the fluid is normal as well [40]. The implications of this observation are discussed and the superfluid model is extended to include non-ideal effects such as viscosity in Chapter 6.

Although substantial work has been performed in the strongly interacting regime, there is still potential for new discoveries. Work has begun on confining

fermions in an optical lattice [69], which may shed light on the mechanisms behind high temperature superconductivity in copper oxides. A very fruitful area of research can be found in strongly interacting systems in reduced dimensions [70, 71], which can also be produced in optical lattices. The ability of unitary Fermi gases to connect to other strongly interacting systems in nature guarantees that investigations in the field of strongly interacting Fermi gases will continue well into the future.

Chapter 3

General Cooling and Trapping Procedures

The cooling and trapping of neutral atoms began with the first magnetic traps becoming operational in 1985 [72] and the first successful magneto-optical traps being demonstrated in 1987 [73]. Since these humble beginnings, the available ways to trap and evaporatively cool atoms has grown to include all optical methods [42, 74, 75], which allowed experiments to be performed on atoms that could not previously be trapped magnetically. However, only incremental steps have been made in trapping technology and for the most part the basic physics behind atom trapping has not changed.

This chapter presents the basic physics behind the cooling and trapping technology using in our lab. The trapping procedure is a two stage process in which the atoms are initially trapped and pre-cooled in a Magneto-Optical Trap (MOT) and then transferred to a Far-Off Resonance Trap (FORT). The MOT consists of a combination of near resonant laser beams and a magnetic field gradient that, when used together, produce a viscous damping force as well as a spatially confining force. The FORT, on the other hand, consists of a single, focused laser beam that overlaps the ball of atoms created by the MOT and confines the atoms through a quasi-electrostatic dipole force. After the atoms are transferred to the FORT from the MOT, they can be cooled to degeneracy, and eventually into the

superfluid regime, through the use of forced evaporative cooling.

This chapter begins in Section 3.1 with a brief discussion of the lithium source used in the experiments. This is followed by Section 3.2, which details the basic physics behind a MOT and presents a discussion of the real world complications that arise when trying to trap ^{6}Li. After a description of the MOT is completed, the basic physics behind the FORT are presented in Section 3.3. This section describes how a single, focused laser beam can be used to confine the atoms in a potential that is approximately harmonic. The chapter continues with a model for forced evaporative cooling in Section 3.4. Scaling laws for the atom number and phase space density are derived, and used to determine the optimal trajectory for the trap potential as a function of time to produce a degenerate, strongly interacting Fermi gas.

3.1 Initial production of atoms

At room temperature ^{6}Li is a pliable, shiny metal that can easily be cut into pieces. This form is very different from the dilute, ultra-cold gas we use in our experiments. The first step in creating a steady source of atoms is to melt and partially vaporize the solid lithium inside of an oven as described later in Section 4.1.1. The oven is at one end of the experimental vacuum chamber, and produces a beam of lithium that is directed towards the main vacuum chamber where the atoms are eventually trapped. In order to create this atomic beam, the lithium is heated to temperatures nearing 420°C, producing a stream of very fast moving atoms. The thermal velocity of the atoms is too high for them to be captured by the atom traps employed in our lab. So in order to initially slow

these atoms, a counter-propagating laser beam is used in conjunction with a Zeeman slower to decelerate the atoms over a very short distance. The details of this process are given in Section 4.1.2. The slowing process involves Zeeman tuning the energy levels of the atoms to account for the Doppler shift they experience during deceleration.

Once the oven is brought up to the desired temperature, it remains on throughout all the experiments that are performed during a particular day. This provides a steady source of atoms to be used in the experiments. The stream of atoms that exit the Zeeman slower are traveling between 30 and 40 meters per second. This speed is substantially slower than the original velocity the atoms possessed when they left the oven, but far from the very low kinetic energies desired for experiments. In order to localize and further cool the slow moving atoms, a combination of laser beams and magnetic fields are used to create a Magneto-Optical Trap (MOT). The fundamental principles and operation behind a MOT are presented in Section 3.2.

3.2 Magneto-Optical Trap (MOT)

After emerging from the Zeeman slower, the atoms need to be localized in space and further cooled before they can be manipulated during an experiment. This function is provided by a Magneto-Optical Trap (MOT) [73]. The development of the MOT revolutionized the field of atom cooling and trapping and is used as the workhorse for the initial stage of cooling in all the experiments done in our lab. It is a very robust trapping method that produces high yields of atoms ($\simeq 10^6 - 10^9$) [50], at temperatures reaching 140μK. The MOT consists of a

combination of off-resonant laser beams and a magnetic field gradient that create a spatially restoring force and provide viscous damping. Therefore the MOT supplies the dual role of spatial confinement provided by the restoring force, as well as a method for cooling through the use of a damping force.

This section begins with a general discussion of the mechanisms behind the generation of forces in a MOT, which is detailed in Section 3.2.1. Here the process by which a two level atom can become confined and subsequently cooled in a MOT is developed using a one dimensional model. This is followed by Section 3.2.2, where a discussion of the real world complications involved with implementing a three dimensional MOT for ^{6}Li is presented.

3.2.1 Basic physics of the MOT

The MOT reduces the velocity and cools the atoms it has trapped through the use of Doppler cooling. The method of Doppler cooling can be understood through the phenomenon of optical molasses. In optical molasses the momentum of an atom is reduced through the use of off-resonant counterpropagating laser beams.

A one dimensional representation of optical molasses is given in Figure 3.1. In this figure the atom is assumed to have a single resonant frequency, ω_{atom}. If a laser beam at this frequency is incident on an atom at rest, the atom will experience a force in the direction of propagation of the laser beam through the absorbtion of a photon. But in the MOT, the atoms always have a non-vanishing resultant velocity due to thermal fluctuations. Therefore the frequency of the laser beams, ω_{phot}, are red-detuned from the atomic resonance ω_{atom}. When this is implemented, an atom within the field of the two counterpropagating laser beams will feel a force that opposes its motion since it will be closer in frequency to the

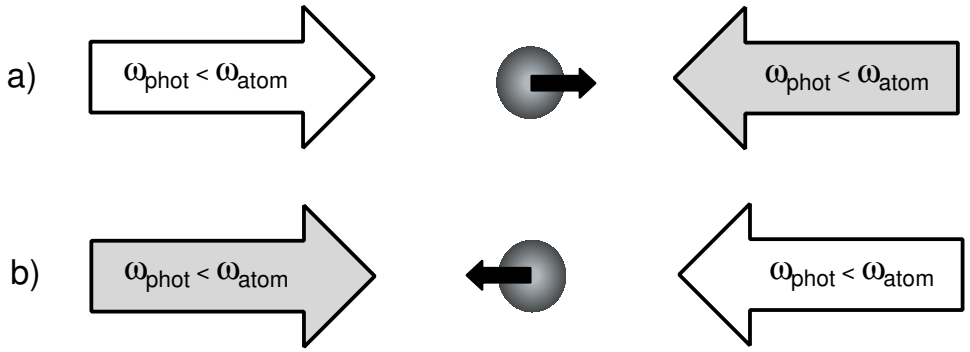

Figure 3.1: One dimensional schematic representation of optical molasses. An atom is represented as a circle, with its velocity direction denoted by a small solid arrow. The large white and grey block arrows represent the counterpropagating laser beams, which have a frequency ω_{phot} that is red-detuned from the resonant atom frequency ω_{atom}. The grey arrows denote the direction of the resultant force on the atom. In case a) the atom is moving to the right, bringing it closer in resonance with the laser beam propagating to the left due to the Doppler shift. Similarly, the atom becomes farther off resonance with the beam traveling in the same direction as the atom. This produces a preferential force opposing the motion of the atom. Case b) shows the opposite scenario for the atom traveling to the left, with the laser beams producing a net force to the right.

beam it is traveling towards, due to the Doppler shift. In case a) in Figure 3.1, the atom is moving to the right, bringing it closer in resonance with the laser beam traveling to the left and further off resonance with the beam traveling to the right. Since the atom will absorb more photons with the beam it is closer in resonance to, it will feel a force directed to the left, opposing its motion. This effect also works for the atom moving to the left, as given in case b) in the figure. Therefore an atom that is located in a red-detuned counterpropagating laser field will experience a reduction in momentum, regardless of the direction of its initial velocity.

The simple one dimensional scenario depicted in Figure 3.1 can be extended to three directions by introducing counterpropagating laser beams in all three orthogonal directions with a common intersection. This produces a force of the form

$$\mathbf{F}_{Doppler} = -a\mathbf{v}, \tag{3.1}$$

where a is a constant and $\mathbf{v}$ is the velocity of the atom [73]. Equation (3.1) is the equation for a viscus damping force, motivating the choice of the term "optical molasses" since the atoms are experiencing a force analogous to an object moving in a viscus fluid.

While optical molasses and Doppler cooling result in a confinement of the atoms to a region close to the origin in momentum space, it provides no confinement of the atoms in physical space. In the three dimensional scenario, after an atom absorbs a photon from one of the laser beams, it re-emits it in a random direction. Therefore the motion of the atom in the laser field can be described by a random walk. Since the force experienced by the atom due to to Doppler cooling given by equation (3.1) contains no spatial dependence, the atom can

easily follow a random walk out of the laser beams and be lost from the trap. Therefore another mechanism that provides a spatially dependent force must be used to confine the atoms to a specific region of space.

To create the spatially dependent force, the magnetic part of the magneto-optical trap is needed. The mechanism that provides a spatially dependent force through the application of a magnetic field can best be understood through the use of a simple model. Consider a two level atom with a total angular momentum of $F = 0$ in the ground state and $F' = 1$ in the excited state. In the ground state, the angular momentum projection is limited to the single value $m_F = 0$. However, in the excited state, the allowed values are $m_{F'} = 0, \pm 1$. If an eternal magnetic field is applied, the $m_{F'} = \pm 1$ sublevels will Zeeman tune in opposite directions since the angular momentum projections have opposite sign. Therefore, if an atom is placed in a magnetic field *gradient* with a vanishing field at the origin, the energy level spacing between the $m_{F'} = \pm 1$ sublevels will have a spatial dependence and diverge from each other as illustrated in Figure 3.2. In this figure, the Zeeman tuning of the energy sublevels with the applied magnetic field are depicted by thin solid lines.

The opposite Zeeman tuning of the $m_{F'} = \pm 1$ sublevels from the origin of the magnetic field can be utilized to create a spatially varying force through the use of circularly polarized light. Due to angular momentum selection rules, if an atom in the $F = 0$ ground state absorbs a σ_- photon, it can only make a transition to the $m_{F'} = -1$ sublevel. Correspondingly, the absorbtion of a σ_+ photon results in a transition to the $m_{F'} = +1$ sublevel. Since the $m_{F'} = \pm 1$ sublevels Zeeman tune below the $m_{F'} = 0$ sublevel on opposite sides of the origin of the magnetic field gradient, an atom will interact with σ_- and σ_+ beams differently depending upon

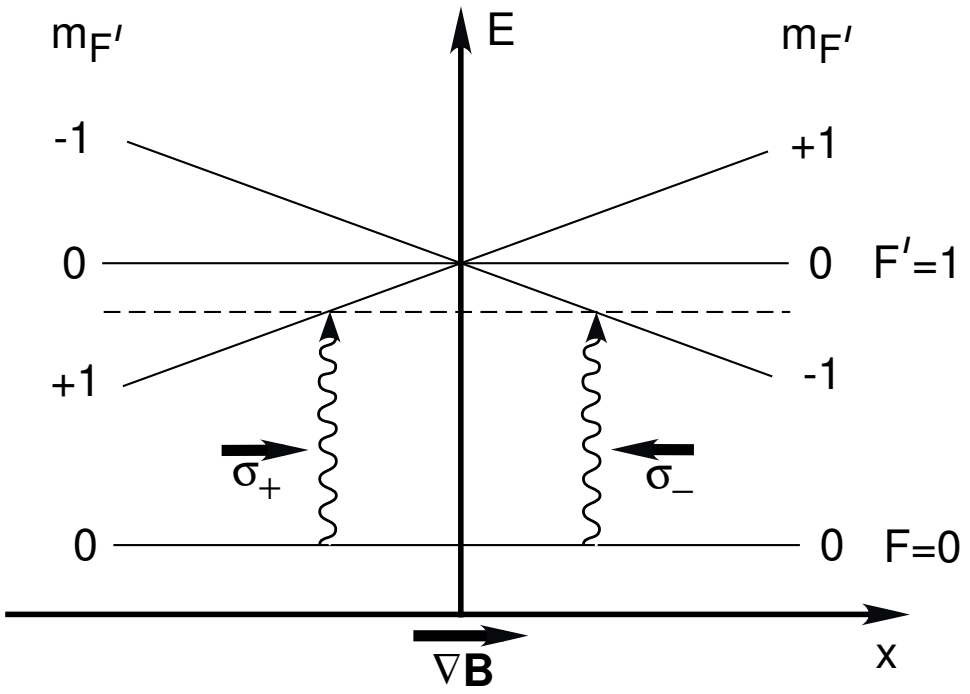

Figure 3.2: Schematic representation of the Zeeman tuning of the $m_{F'} = \pm 1$ sublevels for a two level atom due to an applied magnetic field gradient. The vertical axis is energy and the horizontal axis represents position. The magnetic field gradient is linear, with the field vanishing at the origin. If circularly polarized light that is red-detuned from the $F = 0$ to $F' = 1$ transition is incident on an atom located at $x > 0$, it will preferentially absorb a photon from the σ_- polarized beam. Similarly, a photon will be absorbed from the σ_+ polarized beam if the atom is located at $x < 0$. If these two beams are counterpropagating, a spatially dependent force is created.

its spatial position. A schematic representation of this process in one dimension is given in Figure 3.2. In the figure, the same counterpropagating beams that are red-detuned and used for optical molasses are σ_+ and σ_- polarized and propagate in opposite directions. The oscillating line in the figure represents the absorbtion of a photon that is red-detuned from the $m_{F'} = 0$ sublevel, as indicated by the dashed horizontal line. This will result in a transition to either the $m_{F'} = +1$ or $m_{F'} = -1$ sublevel, depending upon the spatial position of the atom. If the atom is located at a position $x < 0$, it will preferentially interact with the σ_+ beam, producing a force directed towards the origin. Alternately, an atom at $x > 0$ will strongly interact with the σ_- beam, again producing a force that pushes the atoms towards the origin. When this model is extended to three dimensions a force of the form

$$\mathbf{F}_{spatial} = -b\mathbf{x} \tag{3.2}$$

is produced, where b is a constant. When the spatial confinement force of equation (3.3) is used in conjunction with the viscous damping force from equation (3.1), the resultant total force localizes the atoms in space and simultaneously reduces their momentum. This combination of forces allows a large collection of cold atoms to be populated in a Magneto-Optical Trap.

3.2.2 The ^{6}Li MOT

A fairly simple model for the physics behind the forces produced by a MOT for a two level atom was presented in Section 3.2.1. Unfortunately the atom we are in need of trapping, ^{6}Li, has a complicated level structure that cannot be approximated by a simple two level system as seen in Section 2.4. The ground

state of ^{6}Li is split into a hyperfine doublet, allowing an atom in the excited state to fall into either hyperfine ground state after spontaneously emitting a photon as shown in Figure 2.3 in Section 2.4.2. The two hyperfine levels have a splitting of 228 MHz, so an atom that decays into the wrong hyperfine ground state will be completely off resonance with the MOT beams, and will quickly be lost from the trap. To prevent this from happening, an additional laser beam, termed the "repump" beam, co-propagates with the main MOT beam, but has a detuning equal to the spacing between the hyperfine levels. Therefore if an atom in the excited state makes a transition to the off-resonant hyperfine ground state, it will be pumped back into the excited state until it makes a transition back to the on-resonant ground state.

As discussed in Section 3.2.1, the Doppler cooling process can be considered a random walk process in momentum space where an interaction produces a bias in the motion in favor of steps to the origin of size $\hbar k$, where k is the wavevector of the absorbed photon. Since this cooling process inherently involves an exchange of momentum between the atoms and the laser field, there is a limit to how cold the atoms can become. This is referred to at the recoil limit to Doppler cooling and is defined to be

$$T_{Doppler} = \frac{\hbar\Gamma}{2k_B}, \tag{3.3}$$

where Γ is the linewidth of the optical transition [2]. For ^{6}Li the natural linewidth is $\Gamma/2\pi = 5.972$ MHz [50] leading to a limiting temperature of $T_{Doppler} = 140$ μK. On the surface this seems to be an extremely cold temperature, but the comparatively dilute nature of the MOT prohibits the atoms from achieving the degenerate regime where the density, n, multiplied by the cube of the thermal de Broglie wavelength, $\lambda_{dB} = h/\sqrt{2\pi m k_B T}$, is of order unity. Therefore, another method

of trapping that does not rely on direct momentum exchange in order to reach the degenerate regime, and ultimately, the superfluid regime, while increasing the phase space density of the trapped atoms must be used. This can be done through the use of a Far Off Resonance Trap (FORT) as presented in Section 3.3.

3.3 Far Off Resonance Trap (FORT)

The Magneto-optical trap described in Section 3.2 provides an excellent way of capturing large numbers of atoms and provides an initial cooling phase through the use of Doppler cooling. But as explained in Section 3.2.2, Doppler cooling has its limitations due to the random exchange of momentum between the atoms and the laser field. In order to achieve the densities and temperatures required for degeneracy and superfluidity, a method for trapping the atoms in a conservative potential is required.

Such a conservative potential can be supplied by a Far Off Resonance Trap (FORT) [76]. This type of trap does not confine atoms through momentum exchange as in a MOT, but rather traps the atoms through the electric polarizability. In order for a MOT to work, the laser beams are red-detuned from the ^{6}Li resonant frequency by only a few natural linewidths. In contrast, the CO_2 laser used to create the FORT in our lab has a wavelength of 10.6 μm, which is roughly 16 times longer than the wavelength used in the MOT beams. A FORT works by inducing a dipole moment in a trapped atom, and subsequently producing a force through an electric field gradient. Since the frequency of the laser used to produce the FORT is so far off resonance, the scattering rate of photons is negligibly small, allowing a conservative potential to be produced.

This section begins with a discussion of the origin of the force that is used to confine the atoms in a FORT in Section 3.3.1. This is followed by Section 3.3.2, which details the geometry of the FORT and provides a description of how the Gaussian trapping potential can be approximated by a harmonic oscillator.

3.3.1 Electric Dipole Potential

On a fundamental level, the laser radiation used to create a FORT consists of oscillating electric and magnetic fields. When a neutral atom is placed in an electric field, a dipole moment is induced. The magnitude of the induced dipole moment is proportional to the polarizability, α_d, of the atom. The interaction of an atom with an oscillating electric field of a laser is described by the interaction potential

$$U_{dipole} = -\frac{1}{2}\overline{\mathbf{p} \cdot \mathbf{E}}, \tag{3.4}$$

where $\mathbf{p} = \alpha_d \mathbf{E}$ is the induced dipole moment and $\mathbf{E}$ is the oscillating electric field [50]. The factor of one half in equation (3.4) is included to account for the fact that the dipole moment is induced by the electric field. In addition, the vector product of the dipole moment with the field is averaged over an optical cycle in the same equation. The inclusion of the definition for $\mathbf{p}$ in equation (3.4) leads to the potential

$$U_{dipole} = -\frac{1}{2}\alpha_d \overline{\mathbf{E}^2}. \tag{3.5}$$

Assuming that the magnitude of the slowly varying electric field is $\mathcal{E}$, equation (3.5) reduces to $U_{dipole} = -\alpha_d \mathcal{E}^2/4$. The square of the magnitude of the electric field, $\mathcal{E}^2$, is linearly proportional to the laser intensity, I. Using this relationship,

the potential produced by the laser in MKS units can be shown to be

$$U_{dipole} = -\frac{1}{2\epsilon_0 c}\alpha_d I, \tag{3.6}$$

where ϵ_0 is the permittivity of free space and c is the speed of light.

It is clear from equation (3.6) that the sign of α_d dictates whether the potential will be attractive or repulsive. If an atom is approximated by a two level system, a simple model for the atomic polarizability can be constructed [50, 77]. It can be concluded from this model that the sign of α_d is dependent upon the difference between the laser frequency, ω_{laser}, and the natural frequency of the atom, ω_{atom}. If $\omega_{laser} < \omega_{atom}$, then α_d will be positive, producing an attractive potential for the atoms to become trapped in. Therefore a red-detuned laser is needed to create a FORT. Likewise, if the laser frequency is blue-detuned, a repulsive potential is created.

If the atoms have a level structure that is more complicated than a two level system, a simple model may not accurately characterize the potential, leading to atoms in different states feeling slightly different potentials. This is an important consideration in our system, since a 50:50 mixture of the two lowest hyperfine states are needed to achieve the lowest temperatures and produce a superfluid. Fortunately, if the FORT laser is sufficiently detuned from the ^{6}Li resonant frequency, as it is with the CO_2 laser used in our lab, all the states have essentially the same atomic polarizability, producing the same potential regardless of the internal state of the atom. This is a result of the fact that the extreme detuning of the CO_2 laser from the atomic transitions essentially makes the hyperfine structure unresolveable. In turn, this allows the two level approximation to be

used for our system, permitting all the internal ground states of the atoms to experience the same potential described by equation (3.6), with a polarizability defined by the DC Stark effect, $\alpha_d = \alpha_0$.

3.3.2 Harmonic Approximation

The dipole potential produced by the FORT laser beam is proportional to the intensity of the beam, as described by equation (3.6). In order to trap atoms, the laser beam intensity must have a spatial variation since the force exerted on the atoms is proportional to the gradient of the potential, $\mathbf{F}_{dipole} = -\boldsymbol{\nabla} U_{dipole}$. A gradient in the potential can be created by simply focusing the CO_2 laser beam, resulting in a potential minimum at the beam focus where the atoms can become trapped.

In the case of cylindrical symmetry, the intensity of a focussed gaussian laser beam of wavelength λ propagating in the z-direction can be written in the form [78]

$$I(r,z) = \frac{I_0}{1+(z/z_0)^2} \exp\left[\frac{-2r^2}{r_0^2}\right], \tag{3.7}$$

where I_0 is the peak intensity at the focus, z_0 is the Rayleigh range ($z_0 = \pi r_0^2/\lambda$), r_0 is the $1/e^2$ radius of the intensity at the focus, and $r^2 = x^2 + y^2$. Inserting this form of the intensity into the expression for the induced dipole potential given by equation (3.6) yields the spatially varying potential

$$U(r,z) = -\frac{U_0}{1+(z/z_0)^2} \exp\left[\frac{-2r^2}{r_0^2}\right], \tag{3.8}$$

where the potential at the center of the trap is given by $U_0 = \alpha_0 I_0/(2\epsilon_0 c)$.

In most experiments, the potential at the center of the trap is much larger

than the Fermi energy, $U_0 \gg E_F$, meaning that the atoms are located in the trap at positions close to the origin. Under these conditions, the trap potential can be expanded in a Taylor series about the origin. Expanding equation (3.8) out to second order yields

$$U(r,z) \simeq -U_0 + \frac{U_0}{z_0^2} z^2 + 2\frac{U_0}{r_0^2} r^2, \tag{3.9}$$

which is the general form for the potential of a harmonic oscillator. Equating the expression given by equation (3.9) with that of a standard harmonic oscillator with mass m and frequencies ω_x, ω_y, and ω_z leads to the trap frequencies being identified as

$$\omega_r = \sqrt{\frac{4U_0}{mr_0^2}} \tag{3.10}$$

$$\omega_z = \sqrt{\frac{2U_0}{mz_0^2}}. \tag{3.11}$$

The equations that have been derived thus far are for a trap geometry where the z-direction is along the direction of propagation of the laser beam, the so called "axial" direction. Correspondingly, the x and y directions define the radial positions in the laser beam. This is the most natural definition for the trap geometry due to the inherent cylindrical symmetry of the laser beam and is also the most common coordinate system used in the literature. Since the Rayleigh length is much larger than the $1/e^2$ radius at the focus ($z_0 \gg r_0$), the frequencies in equations (3.10) and (3.11) describe a trap that is much softer in the axial direction compared to the radial direction. This produces an atom cloud in the shape of a prolate spheroid as illustrated in Figure 3.3.

Although the most common way of describing the trap geometry is by defining

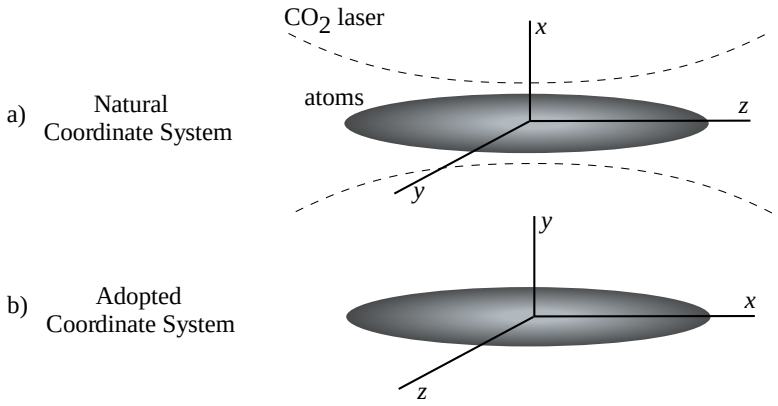

Figure 3.3: Illustration of the coordinate system used in this thesis. The atoms form a prolate spheroid when trapped at the focus of the CO_2 laser beam, which is given by the dashed lines in the figure. The weaker confinement of the FORT in the axial direction of the laser beam elongates the atom cloud in that direction. In the natural coordinate system, given by case a), the axial direction of the FORT is defined to be the z-direction. For the coordinate system that is adopted for this thesis and given by case b), the axial direction is considered to be the x-direction.

the soft axial direction as the z-direction, a slightly different notation is adopted for this thesis. In later sections (Chapter 5 and Chapter 6) it is advantageous to use a coordinate system where the long direction of the trap is defined as the x-direction as opposed to the z-direction. The alternate coordinate system is shown as case b) in Figure 3.3. This coordinate system simplifies the description of a long prolate cloud that is rotating about one of its short axes. By identifying the axial direction as the x-direction, the familiar scenario of a rotation occurring in the $x - y$ plane about the z axis can be constructed. This changes the definitions

in equations (3.10) and (3.11) to

$$\omega_{y,z} = \sqrt{\frac{4U_0}{mr_0^2}} \tag{3.12}$$

$$\omega_x = \sqrt{\frac{2U_0}{mz_0^2}}. \tag{3.13}$$

3.4 Evaporative cooling

After the ^{6}Li atoms are trapped in the MOT and subsequently loaded into the FORT, they can quickly be cooled to degeneracy through the use of evaporative cooling. Evaporative cooling is a collisional process where energy is removed from the system through the loss of high energy atoms from the trap. During a collision between two atoms in the trap, a majority of the energy from the collision can be transferred to one of the two atoms. If the total kinetic energy of the resulting energetic atom is greater than the potential energy of the trap, the atom can escape from the trap, removing energy. The remaining low energy atom can rethermalize, reducing the temperature of the gas.

There are two stages of evaporative cooling used in the lab, free and forced evaporation. During the preliminary cooling stage, the atoms are held in CO_2 beam at full power and the gas is allowed to freely evaporate so that the most energetic atoms are allowed to escape. After a certain amount of time this process stagnates as the gas cools. In order to facilitate further evaporation, the power in the CO_2 beam is reduced at a particular rate, reducing the trap depth and allowing atoms with smaller kinetic energies to escape. This process is very efficient, producing temperatures in the superfluid regime in less than a second with minimal atom loss.

This section begins with the development of a model for the scaling between the atom number and the trap potential as the trap depth is lowered during forced evaporation in Section 3.4.1. This model is based on energy conservation during the cooling process, when the trap depth is lowered and atoms are lost during evaporation. The scaling law model can be tested experimentally, an the results are given in Section 3.4.2. It is found that the model follows the data rather well, until the assumptions made in the model are no longer valid. In Section 3.4.3, the scaling law model is extended to derive a lowing curve trajectory for the trap potential as a function of time. This results in an explicit equation for the most efficient lowering curve for evaporative cooling in the unitary regime.

3.4.1 Scaling laws for forced evaporation

The easiest way to create a strongly interacting Fermi superfluid is to perform forced evaporation at a bias magnetic field of 834 Gauss, at the location of the broad Feshbach resonance. At this magnetic field, the scattering length diverges and the gas is said to be in the unitary regime, where the inverse of the Fermi wavevector, $1/k_F$, is equivalent to the interparticle spacing and sets the length scale at zero temperature. With $1/k$ supplying the only scale of length, the collision cross section becomes $\sigma_c = 8\pi/k^2$ as shown in equation (2.20) in Section 2.3. In the unitary regime, runaway evaporative cooling is possible since the collision rate increases as the trap depth is decreased. This occurs because the collision cross section increases with decreasing relative kinetic energy, $E = \hbar^2 k^2/2m$. By contrast, for a weakly interacting gas with an energy independent collision cross section, the collision rate always decreases as the trap is lowered [79].

In general, a time dependent optical trapping potential can be written as

$$V(\mathbf{x}, t) = -U(t)g(\mathbf{x}), \tag{3.14}$$

where $g(\mathbf{x})$ contains all the position dependence and describes the trap shape. This expression is equivalent to making U_0 in equation (3.8) time dependent. Efficient evaporation occurs when the ratio of the trap depth, U, to the average thermal energy $k_B T$ is large. This relationship is denoted as

$$\chi = \frac{U}{k_B T}. \tag{3.15}$$

A large value of χ assures that the evaporating atoms carry away a large amount of energy in comparison to the average thermal energy. For typical evaporation in optical traps, $\chi = 10$, although it may vary during the evaporation sequence. This is especially true if the lowering involves a time dependent potential, $U(t)$. But it is possible to tailor the trajectory of $U(t)$ in such a way that χ is *required* to remain constant and maintain a large value. This is precisely what is done in this section in order to obtain analytic results for the scaling laws and produce high efficiency evaporative cooling.

The scaling laws follow from energy conservation, with the assumption of keeping χ constant. During forced evaporation, work is done on the gas as the trapping potential is lowered, and energy is lost as energetic atoms evaporate from the gas. This produces a rate of energy loss, $\dot{E}$, as the gas is cooled during forced evaporation. Assuming the atoms are in a harmonic potential, the rate of energy loss is given by

$$\dot{E} = \frac{\dot{U}}{U}\frac{E}{2} + \dot{N}\left(U + \kappa k_B T\right), \tag{3.16}$$

where an escaping atom has an excess kinetic energy that is a factor κ smaller than the average thermal energy. The first term on the right hand side of equation (3.16) arises from the change in the potential energy as the trap is lowered. In the second term, $U + \kappa k_B T$ is the average energy carried away per particle. In general, $0 \leq \kappa \leq 1$. By using an energy independent s-wave collision cross section it can be shown that $\kappa = (\chi - 5)/(\chi - 4)$ [80, 81].

Equation (3.16) can be simplified by assuming the total energy in the harmonic trap can be approximated with the classical value, $E = 3Nk_BT$. This assumption should be valid until the gas begins to approach the degenerate regime, where quantum statistics will begin to contribute. The time derivative the total energy yields $\dot{E} = 3\dot{N}k_BT + 3Nk_B\dot{T}$. Assuming that χ is constant, the constraint given to U and T by equation (3.15) can be differentiated and rearranged to read $k_B\dot{T} = \dot{U}/\chi$. Putting these expressions together produces

$$\dot{E} = \frac{3\dot{N}U}{\chi} + \frac{3N\dot{U}}{\chi} \tag{3.17}$$

for the rate of change of the total energy in the trap. Using equations (3.16) and (3.17), an expression that depends solely on $\dot{N}/N$ and $\dot{U}/U$ can be constructed. The form of the resulting differential equation is

$$\frac{\dot{N}}{N} = \frac{\dot{U}}{U}\frac{3}{2(\chi + \kappa - 3)}. \tag{3.18}$$

By integrating the left had side of equation (3.18) from N_0 to N and the right hand side from U_0 to U, where N_0 and U_0 the initial values, a solution to equation

(3.18) can be obtained. This procedure yields the scaling law for the atom number

$$\frac{N}{N_0} = \left(\frac{U}{U_0}\right)^{\frac{3}{2(\chi'-3)}}, \tag{3.19}$$

where $\chi' = \chi + \kappa = \chi + (\chi - 5)/(\chi - 4)$.

Along with the number scaling, the scaling law for the phase space density, ρ, can also be formulated. For a 50-50 mixture of two spin states in a harmonic potential, the phase space density is essentially the total atom number in each state, $N/2$, divided by the number of accessible oscillator states or

$$\rho = \frac{N}{2}\left(\frac{\hbar\bar{\omega}}{k_B T}\right)^3, \tag{3.20}$$

where the geometric mean of the trap frequencies is defined as $\bar{\omega} \equiv (\omega_x\omega_y\omega_z)^{1/3}$. Using equation (3.15) for χ along with the equations that determine the trap frequencies (equations (3.12) and (3.13) from Section 3.3.2), the relations $k_B T \propto U$ and $\bar{\omega} \propto \sqrt{U}$ can be shown to result. Substituting these two relations into equation (3.20) gives $\rho \propto N/U^{3/2}$ for the phase space density. Inserting this into the scaling law for the atom number given by equation (3.19) produces the scaling for the phase space density

$$\frac{\rho}{\rho_0} = \left(\frac{U_0}{U}\right)^{\frac{3(\chi'-4)}{2(\chi'-3)}} = \left(\frac{N_0}{N}\right)^{\chi'-4}. \tag{3.21}$$

This equation demonstrates that if the typical value $\chi = 10$ is used, after lowering the trap depth by a factor of 100 the phase space density will have increased by over a factor of 400, while the atom number in the trap has only been reduced by a factor of 2.4.

For a gas in the unitary regime, the mean square size of the cloud, $\langle y^2 \rangle$ for example, does not change during forced evaporation if χ is held constant. This is counterintuitive since the gas would be expected to shrink in size as energy is removed, resulting in the atoms populating the lower lying vibrational energy states close to the center of the trap. The reason for the unvarying mean square size stems from the energy scaling in the unitary regime given by $E = 3Nm\omega_y^2 \langle y^2 \rangle$. This result follows from the fact that a unitary gas in a harmonic trap obeys the virial theorem as shown in Section 2.3.2. As previously stated, in the classical regime the total energy is also equal to $E = 3Nk_BT = 3NU/\chi$. Equating these two expressions for the total energy leads to

$$\langle y^2 \rangle = \frac{U}{m\omega_y^2 \chi}. \tag{3.22}$$

This equation can be simplified since the trap frequency ω_y can be written in terms of the trap potential, U, in equation (3.12). Using the expression for ω_y in equation (3.22), the mean square size of the trap during forced evaporation becomes

$$\langle y^2 \rangle = \frac{r_0^2}{4\chi}, \tag{3.23}$$

which remains constant as the trap is lowered since r_0 is the $1/e^2$ radius of the trapping beam at the focus, which remains fixed as the trap depth is lowered. Using the same logic, similar constant expressions result for the x and z directions in the trap.

3.4.2 Experimental test of number scaling

The validity of the scaling laws presented in Section 3.4.1 can be experimentally tested by measuring the atom number as a function of trap depth. After being loaded by the MOT, a 50-50 mixture of the two lowest hyperfine states of ^{6}Li are prepared in the FORT. Before proceeding with forced evaporation, free evaporative cooling is performed in the unitary regime at 834 Gauss to pre-cool the atoms. When free evaporation begins to stagnate, the trap depth is lowered in a precise trajectory such that $\chi = 10$ is maintained, allowing the scaling law in equation (3.19) to be experimentally validated.

An experimental test of the scaling laws requires a knowledge of the initial trap depth, U_0. At full trap depth, a parametric resonance experiment, described later in Section 4.8.2, can be used to determine the trap frequencies in the x, y, and z directions. An experiment of this type yields the frequencies $\omega_x = 2\pi \times 190$ Hz, $\omega_y = 2\pi \times 5500$ Hz, and $\omega_z = 2\pi \times 5400$ Hz. The power, P_0, in the CO_2 beam is measured by a power meter to be approximately 60 Watts under the same conditions. Using these parameters, the initial trap depth can be calculated from the expression

$$U_0 = \sqrt{\frac{\alpha_0 P_0 m \omega_y \omega_z}{c}}, \tag{3.24}$$

where c is the speed of light, and the ground state polarizability has been determined to be $\alpha_0 = 24.3 \times 10^{-30}$ m^3 [82]. Plugging in the values for full trap depth gives an initial potential of $U_0/k_B = 550$ μK. The initial atom number, N_0, can be measured from the absorbtion images taken of the cloud. A typical atom number measured for these experiments is $N_0 = 8 \times 10^5$ before the trap is lowered.

The experimental data for the atom number as a function of trap depth is

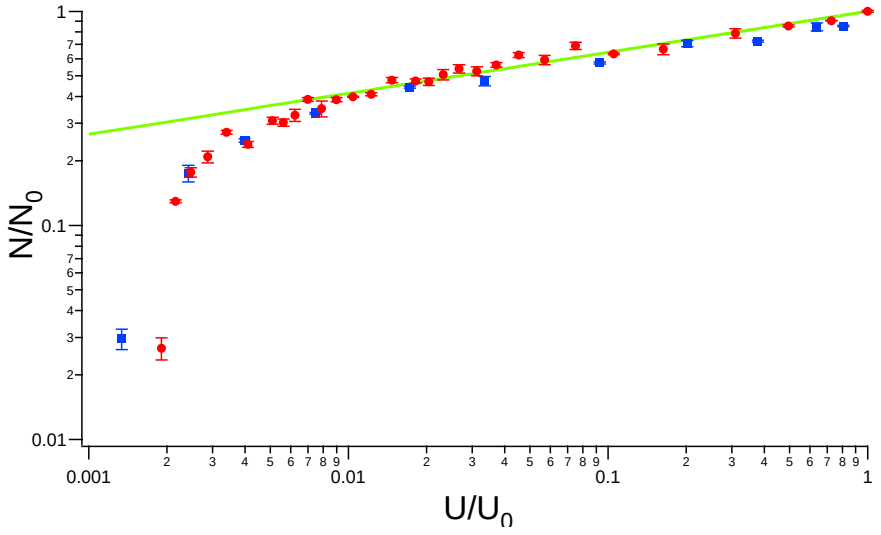

Figure 3.4: Atom number versus trap depth for evaporative cooling. The circles are obtained using a lowing curve for an energy independent collision cross section, while the blue squares are the measured values for a unitary gas lowering curve. The solid line indicates the scaling law prediction for $\chi = U/k_BT = 10$. The lowering time increases from right to left.

given in Figure 3.4 for two different lowering curves denoted by red circles and blue squares. In the case identified by the red circles, the lowering curve trajectory was constructed for an energy-independent collision cross section [79]. A unitary lowering curve, which will be developed in Section 3.4.3, was used to produce the data presented as blue squares. In both cases the lowering curve was optimized for $\chi = U/k_BT = 10$. The solid line displays the scaling law prediction of equation (3.19), also with $\chi = 10$. The prediction follows the data exceptionally well until approximately $U/U_0 = .007$, where the gas begins to become degenerate and the classical gas assumption used to develop the model in Section 3.4.1 breaks down. In addition, if a curve of the form $N/N_0 = (U/U_0)^p$ is fit to the data in the classical regime, the exponent is found to be $p = 0.21$. This is within 10% of the predicted value of $p = 0.191$ given by the theory for $\chi = 10$.

3.4.3 Unitary gas lowering curve

Forced evaporation is accomplished in an optical trap by lowing the intensity of the confining laser beam as a function of time, resulting in a time dependent potential. In order to achieve efficient evaporative cooling, the trajectory of the potential as a function of time must have a specific shape. The form of the appropriate shape can be obtained by considering the evaporation rate, $\dot{N}$.

An expression for the evaporation rate can be formulated through the use of the s-wave Boltzmann equation [80]. To lowest order in $\exp(-\chi)$, and neglecting background gas collisions, the evaporation rate can be shown to be [79]

$$\dot{N} = -2(\chi - 4)\exp(-\chi)\gamma_c N, \tag{3.25}$$

where γ_c is the elastic collision rate. Using equation (3.18), the evaporation rate, $\dot{N}$, can be changed into a differential equation in the trap potential, $\dot{U}$. After performing the substitution, equation (3.25) transforms to

$$\frac{\dot{U}}{U} = -\frac{4(\chi' - 3)(\chi - 4)}{3}\exp(-\chi)\gamma_c. \tag{3.26}$$

A solution to this equation can be obtained if an expression for γ_c is formulated. In general, the collision rate is given by $\gamma_c = n\, v_{rel}\, \sigma_c$, where n is the density, v_{rel} is the relative velocity of two colliding atoms, and σ_c is the collision cross section. The collision cross section for a unitary gas is energy dependent since it is inversely proportional to k^2. By utilizing the Boltzmann equation for an energy-dependent

cross section, σ_c can be shown to be [18, 81]

$$\sigma_c(U) = \frac{16\pi\hbar^2}{mU}, \tag{3.27}$$

where it has been assumed that $U \gg k_B T$, which is true for large χ.

The expression for σ_c given in equation (3.27) can also be derived using heuristic arguments. For a collision between two atoms of energy ϵ_1 and ϵ_2, energy conservation requires that $\epsilon_1 + \epsilon_2 = \epsilon_3 + \epsilon_4$, where ϵ_3 and ϵ_4 are the energies of the outgoing atoms. In order to escape from the trap during evaporation, the atom with energy ϵ_4 must gain energy during the collision, and obtain a magnitude $\epsilon_4 > U$. Correspondingly, the atom with energy ϵ_3 remains in the trap and loses energy during the collision. This energy loss is substantial, allowing ϵ_3 to be neglected in the energy conservation equation [81]. Since the atoms have the same mass, energy conservation gives $v_1^2 + v_2^2 = v_4^2$.

Momentum conservation leads to $\mathbf{v}_1 + \mathbf{v}_2 = \mathbf{v}_4$, assuming that $\mathbf{v}_3$ is negligible. Squaring both sides of this equation results in the cross term vanishing $\mathbf{v}_1 \cdot \mathbf{v}_2 \simeq 0$, after the consequences from energy conservation are included. Therefore, $v_{rel}^2 \simeq v_4^2 \simeq 2U/m$, since the kinetic energy of the evaporating atom will be on the order of the trap potential. Using $mv_{rel}/2 = \hbar k$ along with the expression for the cross section, $\sigma_c = 8\pi/k^2$, equation (3.27) is produced.

The collision rate given by $\gamma_c = n\, v_{rel}\, \sigma_c$ can only depend upon N and not the density, n, since it was shown in Section 3.4.1 that the mean square size of the trap doesn't change as the trap depth is lowered in a unitary gas. Therefore the volume occupied by the gas remains the same, and the density only decreases as the atom number decreases. Since it was shown that $v_{rel} \propto \sqrt{U}$ from the heuristic

derivation of the cross section, and that $\sigma_c \propto 1/U$ from equation (3.27), it follows from the scaling law provided by equation (3.19) that

$$\frac{\gamma_c}{\gamma_{c_0}} = \left(\frac{U}{U_0}\right)^{\frac{6-\chi'}{2(\chi'-3)}}, \tag{3.28}$$

where γ_{c_0} is the initial collision rate, which can be approximated using an energy-independent cross section to give $\gamma_{c_0} = (N_0/4\pi)8\hbar^2\bar{\omega}^3\chi/U_0^2$ [81]. The lowering curve for a unitary gas can be obtained by substituting equation (3.28) into the differential equation for the potential, given by equation (3.26). Solving the resulting equation for $U(t)$ yields

$$U(t) = \left(1 - \frac{t}{\tau_u}\right)^{\frac{2(\chi'-3)}{(\chi'-6)}}, \tag{3.29}$$

which is defined between $0 \leq t \leq \tau_u$. The lowering time constant, τ_u, is also found to be

$$\frac{1}{\tau_u} = \frac{2}{3}(\chi - 4)(\chi' - 6)\exp(-\chi)\gamma_{c0}, \tag{3.30}$$

where if $\chi = 10$, $\tau_u = 0.77$ seconds for typical initial conditions N_0 and U_0. In practice, forced evaporation is provided by a reduction in power of the FORT laser beam. Equation (3.24) states that the relationship between the trap potential and the CO_2 beam power is $U \propto P$ since $\omega_x\omega_y \propto P$. Therefore by lowing the power in the beam in a trajectory defined by the square of equation (3.29), a degenerate strongly interacting Fermi gas can be efficiently created in a fraction of a second.

Chapter 4

New Experimental Apparatus

When I first talked to John about joining the group he was very excited about the fact that I had a substantial background in manufacturing, and in particular, machining. I didn't think these skills would be in high demand, especially in a group that deals mainly in optics. The reason became apparent, however, the first summer that I began working in the lab. In the lab space, one experimental apparatus already existed, termed the "old lab," which had been constructed over the years with primary contributions provided by Ken O'Hara, Stephen Granade, Michael Gehm, and Staci Hemmer [50, 77, 83]. The adjoining room to the old lab was occupied by a single optics table with a lonely dye laser on it. From these humble beginnings, John explained, a next generation, state of the art cooling and trapping apparatus needed to be built. I gladly accepted the challenge unknowing that it would be almost a subsequent two years before the first experiments would be completed on the "new" system. This chapter will detail the design and construction of the experimental apparatus that was built mainly by myself and lab partner Le Luo [84].

The experimental apparatus was built to trap neutral ^{6}Li using a combination of lasers and magnetic fields. Two separate laser systems are used to trap the atoms and cool them down to degeneracy. The first is a dye laser that produces light at a frequency very close to the resonant frequency of the ^{6}Li ground state.

The second is the CO_2 laser, which has a frequency that is far away from the ^{6}Li resonance. The layout of these laser systems is given in Section 4.3, along with a description of their uses. A dye laser is used in this experiment due to its inherent tunability in comparison to other types of lasers. In order for it to produce a single stable frequency, it must be "locked" to a reference frequency. Section 4.4 details the design of a new vacuum chamber that was used to create the lithium source needed to lock the laser. In order to avoid collisions with background atoms, the experiments are done inside of a vacuum chamber. The operation of the lithium source and the design and construction of the experimental chamber are discussed in Section 4.1 and Section 4.2 respectively. Finally, a detailed account of the design and construction of the magnet system is presented in Section 4.5.

4.1 Oven and Zeeman slower

In the cooling and trapping experiments presented in this thesis, a dilute gas of atoms is held in an optical dipole trap for many tens of seconds before the experiment is complete. Therefore, the experiments must be done in a vacuum chamber with an extremely good vacuum to prevent atoms from being expelled from the trap as a consequence of collisions with gas in the background [85]. This section will detail the design and construction of the oven region and Zeeman slower, which are are part of the vacuum chamber that was used to perform the experiments. These two components produce and decelerate the ^{6}Li atoms so that they can eventually be trapped in the main vacuum chamber, which will be detailed in Section 4.2.

4.1.1 Lithium source

It has been my experience while working on the experiments presented in this thesis that the ultra high vacuum in the main vacuum chamber is fairly easy to maintain, but very difficult to initially achieve. The apparatus that was built maintains a vacuum at roughly 2×10^{-11} Torr, which is roughly the same level of vacuum that is found, for instance, on the moon. At these extremely low pressures, gas molecules that have been trapped in the metal of the vacuum chamber begin to "outgas" or create a "virtual leak" that effectively raise the pressure. Therefore in order to achieve ultra high vacuum levels it is necessary to "bake out" the vacuum chamber when it is first constructed by bringing it up to roughly 300°C for a few days to expel all the trapped gas. This is a difficult and time consuming process, and due to restrictions on temperature for some of the components, is practically impossible to do after the apparatus is complete. So after an ultra high vacuum level is achieved, it is prudent to minimize the frequency at which the vacuum chamber is brought up to atmosphere and opened to the outside world. Therefore, a reliable and long lasting lithium source is necessary to minimize the number of times the chamber is opened.

The lithium source consists of a barrel and a nozzle that resembles a corn cob pipe and its dimensions are given in Figure 4.1. The dimensions in this schematic are slightly larger than the sizes that have appeared in previous theses [51] due to a redesign that was undertaken by Andrey Turlapov in 2006. The main modification is a slightly larger barrel to hold more lithium. An average oven can hold roughly 1.5 grams of ^{6}Li in the barrel and can last in excess of three years with this meager amount. This is mainly due to fact that the interior of the barrel and nozzle are lined with fine mesh that acts as a "wick" to recirculate lithium that is unable

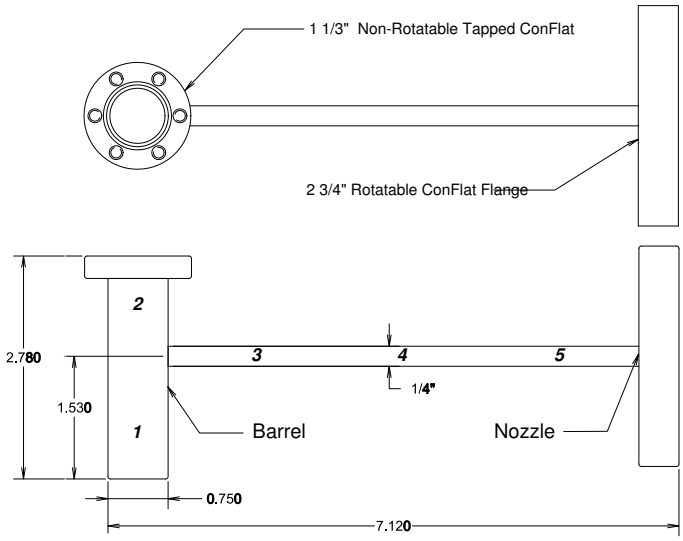

Figure 4.1: Schematic of the lithium source presenting the top and side views. ^{6}Li is stored in the barrel and exits through the nozzle. The italicized numbers indicate the five separate thermal regions of the oven. All dimensions are in inches.

to escape from the nozzle back into the barrel. Due to its long thin shape, the section that contains the wick acts as a collimator and only allows a thin stream of lithium to emerge into the rest of the vacuum chamber. The lithium that does not escape is recirculated back into the barrel by the mesh.

^{6}Li is an alkali metal and melts at the relatively low temperature of roughly 180°C [86]. But in order to generate enough flux from the nozzle, certain regions of the oven are brought up to temperatures in excess of 400°C. This is accomplished by wrapping nichrome wire (Omega PN NI80-020-50) around the oven in 5 independent sections. These sections are highlighted in Figure 4.1 by the italicized numbers. Nichrome wire has a large resistance and high melting point, therefore a large amount of heat can be generated by running current through the wire.

Independent control of the current in the 5 different regions allows a temperature profile to be created across the oven. Regions *1* and *2*, which are directly on the oven barrel, are usually kept at 380°C to 390°C so as not to exceed the maximum recommended temperature of 400°C for the 1 1/3 inch ConFlat (CF) flange at the top of the barrel. This flange is sealed with a nickel gasket, in comparison to the copper gaskets used for all other flanges, due to improved temperature cycling and chemical reactivity characteristics. Typically region *3* is held at the highest temperature of 415°C to 425°C and is considered the "source" of the lithium. After region *3*, the temperatures reduce in regions *4* and *5* to roughly 360°C and 280°C respectively. All of the temperature measurements are obtained through the use of thermocouples that are in contact with the oven in each of the five regions. The oven, thermocouples, and nichrome wire are all electrically isolated from each other by encasing each component in thermal cement (Omega CC High Temperature Cement) during the construction process.

4.1.2 Zeeman slower

It is known from kinetic theory that an atom of mass m at temperature T has a most probable velocity, v_{mp}, of $v_{mp} = \sqrt{2k_BT/m}$, where k_B is Boltzmann's constant. Based on this calculation, a ^{6}Li atom is traveling at a velocity of roughly 1400 meters per second as it leaves the oven nozzle. A typical magneto-optical trap (MOT) has a trap depth of roughly a Kelvin, which translates to a capture velocity of around 50 meters per second. So in order to trap the atoms that are coming out of the oven, they must be decelerated by a substantial amount. The deceleration can be facilitated by a resonant laser beam propagating in the opposite direction to the atoms that, on average, produces a force that slows the

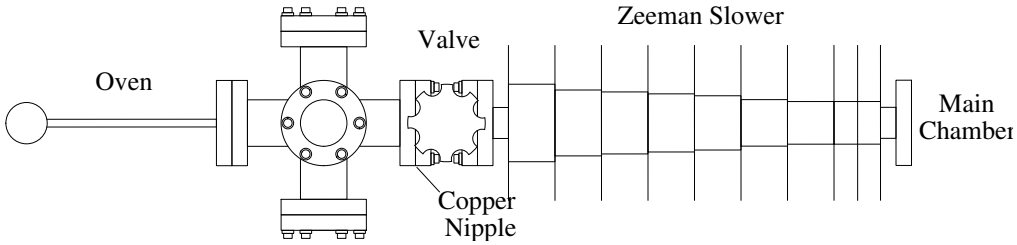

Figure 4.2: Top view of the oven, high vacuum valve, and Zeeman slower. Omitted is the sublimation pump attached to the top-most port, and the ion pump, which is attached directly underneath the middle port. The copper nipple, used to create differential pumping, is located between the valve and Zeeman slower.

atoms. But as the atoms slow down they observe a different frequency from the laser beam due to the Doppler shift and quickly fall out of resonance with the beam. One solution to this problem is to shift the laser frequency so that it is always on resonance with the atoms as they decelerate. A more practical solution is to Zeeman tune the energy levels of the atoms with a spatially varying magnetic field tailored in such a way so that as the atoms slow down, their energy levels continuously tune in resonance with the laser field. Such a device is known as a Zeeman slower. In this section the design and construction of the Zeeman slower used in the experiments is presented.

An illustration the Zeeman slower along with the oven is provided in Figure 4.2. The Zeeman slower consists of 9 separate coils of progressively smaller diameter with respect to the oven end. The right most flange after the slower is attached to the main chamber as shown later in Figure 4.4 in Section 4.2. The flange before the slower is attached to a high vacuum valve that can be closed, for instance, during a change of the oven. All of the ports on the entire apparatus are sealed together using copper gaskets except for the flange between the slower and the high vacuum valve. In place of a copper gasket is a 3/8 inch inner diameter, 6

inch long tube attached a copper plate, which is known as a "copper nipple." This is used to produce differential pumping between the right and left hand sides of the valve. The conductance of the copper nipple is exceptionally small, owing to its small diameter and long tube length. This allows a pressure differential to be created across the copper nipple, resulting in pressure difference of a factor of 200 when the oven is turned on. The differential pumping on the oven side is provided by a sublimation pump and ion pump that are attached to the cross between the oven and valve in Figure 4.2, but have been omitted for simplicity. The slowing laser beam is produced as shown in Figure 4.5 in Section 4.3 and enters the Zeeman slower from the chamber, goes through the center of the coils, and terminates at the back of the oven.

The spatially varying magnetic field is provided by the 9 coils that make up the Zeeman slower. In the previous experimental apparatus in the "old lab" all the coils had the same number of winds and separate power supplies were used to tailor the field [87, 88]. This leads to a device that is somewhat unwieldy, and requires a substantial amount of electronics to regulate the current in the separate coils. In addition, it is somewhat wasteful in power and requires water cooling to prevent it from overheating. In contrast, the slower constructed for this experiment has different diameter coils connected in series, which are all run off the *same* power supply. Therefore the variation in the magnetic field is provided by the geometry of the coils instead of a variation in current. This produces a very simple, compact device that is air cooled instead of water cooled, which is a substantial advantage.

A substantial amount of work for the design and construction of the Zeeman Slower was provided by Ingrid Kaldre and documented in her undergraduate

thesis [89]. The first step in the slower design is the determination the proper spatial variation for the magnetic field, so that the atoms remain on resonance with the slowing beam during deceleration. This is accomplished by equating the Zeeman energy shift for an atom in a particular magnetic field to the doppler shift experienced by the atom as it decelerates. With the help of the kinetic equations for a decelerating particle of mass m, an expression for the magnetic field as a function of distance can be shown to be

$$B(z) = \frac{2\pi\hbar}{\lambda\,\mu_B}\sqrt{v_i^2 - \frac{2\pi\hbar\,\Gamma}{\lambda\,m}z} \tag{4.1}$$

where λ is the frequency of the slowing light, v_i is the initial velocity of the atoms, $\Gamma/2$ is the spontaneous emission and absorbtion rate, μ_B is the Bohr magneton, and z is the distance traveled in the slower. The origin for z is the beginning of the largest coil in Figure 4.2, which is next to the valve.

The maximum deceleration of the atoms, $\pi\hbar\,\Gamma/m\lambda$, is a constant with a value of roughly 1.8×10^6 meters per second squared for ^{6}Li. Therefore, to slow atoms with a v_i equal to the most probable thermal velocity produced in the oven, v_{mp}, the slower needs to be rather long. If a shorter slower is desired, then the initial velocity of the atoms that are slowed must be smaller than v_{mp}. Since the velocity distribution coming out of the oven is Maxwell-Boltzmann [87], the result of designing the slower to decelerate atoms with a smaller v_i is a reduction in the flux of slow atoms produced by the slower. This leads to a tradeoff between slower length and atom flux. But a shorter slower also gains advantage in solid angle. In addition to a large forward velocity, the atoms also possess a finite transverse velocity, causing them to spread out over distance. When the atoms near the end

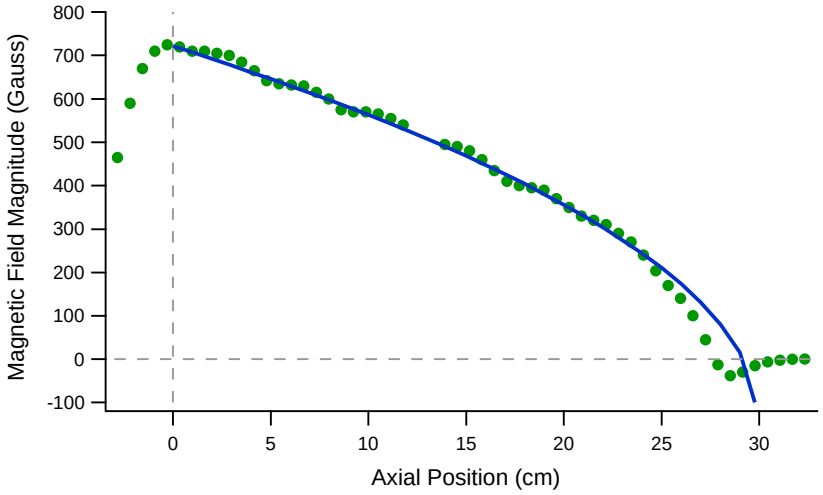

Figure 4.3: Plot of the axial magnetic field as a function of distance in the Zeeman slower. The solid line is the calculated optimal magnetic field for slowing atoms, while the solid circles are the measured field. The vertical dashed line marks the beginning of the largest coil and the horizontal dashed line highlights the point of zero field.

of the slower, they are traveling at the smallest velocity, accentuating this effect. In the end, the slow atoms have to be captured by the beams of the MOT, so a shorter slower actually produces a gain in capturable atoms, minimizing the effect of a loss in flux.

A plot of the magnetic field for the final slower configuration is presented in Figure 4.3. The solid line is the theoretical prediction from equation (4.1) and the solid circles are the field as measured with a Bell 620 Gaussmeter. It must be noted, however, that the slower was designed to produced the desired field at a current of 10 amps, but the test was performed at 1 amp. Since the magnetic field is linearly proportional to the current, the data was scaled up in the figure. For the high magnetic field values, the measurements oscillate about the theory, due to the discreteness of the coils and the gaps introduced by the cooling fins. But

towards the end of the slower, the measured magnetic field deviates substantially from the theory. This is due to the fact that the current in the last coil flows in the opposite direction with respect to the other coils, allowing the field to be brought rapidly to zero and bringing the atoms out of resonance with the slowing beam. This is necessary to prevent atoms from being pushed back into the slower during the additional 8 inches they must travel after the slower before reaching the MOT at the center of the chamber.

4.2 Main vacuum chamber

As the atoms leave the slower at roughly 30 to 40 meters per second, they enter the main vacuum chamber where they can be trapped by the MOT. The main vacuum chamber is a custom design built by MDC Vacuum Products in Hayward, CA. It consists of 14 ports to accommodate the MOT beams, CO_2 beam, camera beam, slowing beam, and RF antenna, along with an additional viewing port.

As illustrated in Figure 4.4, the main vacuum chamber has a pancake geometry. Except for the two vertical MOT beam ports, all the flanges are located around the circumference of the short cylinder. This allows for the magnets, which are mounted on the top and bottom of the cylinder, to be as close to the center of the chamber as possible. This is advantageous since the power, P, required to produce a particular bias field, B, at the center of the chamber with a coil of radius R and resistance Ω_R can be shown to be

$$P(B) = \frac{B^2 \left(d^2 + R^2\right)^3}{\mu_B^2 R^4} \Omega_R, \tag{4.2}$$

where d is half the distance between the coils and μ_B is the permeability of

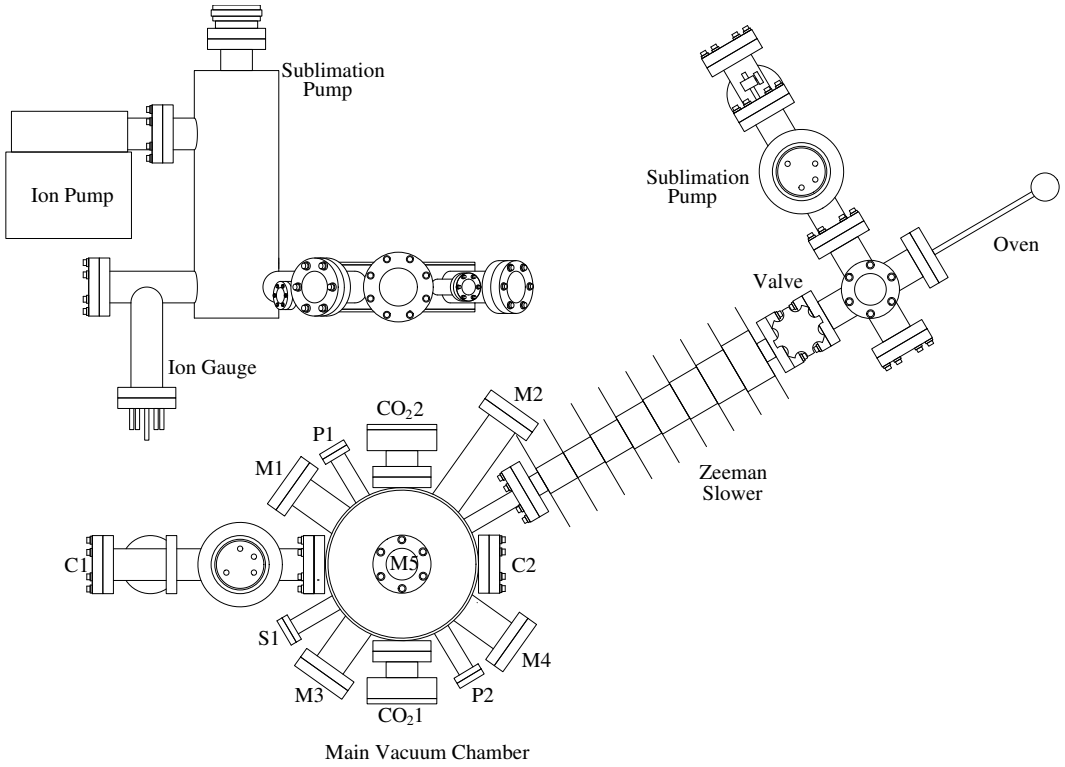

Figure 4.4: Schematic of the experimental vacuum chamber. Side view of the main vacuum chamber is given in the upper left had corner. Port definitions in top view are: MOT beam ports (M1-M5), camera beam ports (C1,C2), slowing beam port (S1), CO_2 beam port ($CO_2$1, $CO_2$2), and probe ports (P1, P2). The atoms travel from the oven, through the Zeeman slower, and into the center of the chamber where they are initially trapped by the MOT beams. A counter-propagating slowing beam enters through port S1 and terminates at the back of the oven.The ion pump is omitted in the top view for clarity.

free space [90]. Therefore, for a compact chamber the power consumption is substantially smaller, which makes cooling the magnet coils considerably easier and allows the magnets to operate at high field for a longer period of time. This advantage was exploited in the study of the entropy of a strongly interacting Fermi gas presented in Chapter 6 of this thesis.

The main vacuum chamber maintains a vacuum close to 2×10^{-11} Torr through the use of an ion pump and a sublimation pump. The ion pump is shown in the side view of the chamber in Figure 4.4, but omitted from the top view so that it doesn't obstruct the view of port C1. At these pressures the ion pump is mainly pumping the noble gases such as Helium and Argon that can slowly leak through the seals in the flanges. The sublimation pump, shown as the tall tube in the side view of Figure 4.4, pumps the remainder of the gas. Inside the sublimation pump are three titanium filaments suspended in the center of the tube. A sublimation pump works by passing a large amount of current through these filaments, causing them to glow like a light bulb until a monolayer of titanium is deposited on the inside to the tube. Titanium is a very reactive element, so if a gas molecule collides with a titanium atom it usually sticks to it, essentially taking it out of the vacuum. A sublimation pump will continue to operate as long as there is free titanium to react with, therefore it can only be used at very low pressures ($< 10^{-10}$ Torr) where there is little gas to absorb.

Since a sublimation pump relies only on surface area to work, it can have incredibly large pumping speeds of thousands of liters per second, compared to the 40 liters per second of the ion pump. But unfortunately during the design stage for the chamber it was not realized that the conductance of the vacuum port the sublimation pump is pumping through (1 1/2 inch diameter tube) is roughly

50 liters per second, which, limits its pumping speed to this value. Due to this handicap, the FORT lifetime is limited to typically 60 seconds due to background gas collisions with trapped atoms, but can be as long as 90 seconds after a new layer of titanium is deposited on the surface on the sublimation pump.

4.3 Optical beam setup

The degenerate atomic gases used in the experiments presented in this thesis are produced using all optical methods [42]. There are two main laser systems employed during experiments. The first creates all the near resonant beams necessary to slow atoms, trap them in the MOT, and image them with a CCD camera. A description of the layout and generation of these beams is presented in Section 4.3.1. At the heart of this system is a single stable dye laser, which produces enough power to generate all of the required near resonant beams. The second laser system consists of an off resonant CO_2 laser, which is responsible for the creation of the FORT, allowing the degenerate regime to be attained. A detailed description of the production and layout of the CO_2 laser system is given in Section 4.3.2.

4.3.1 Dye laser beams

In order to trap atoms in the MOT and image them in the FORT, it is necessary to generate numerous laser beams that are close in frequency to the D_2 resonance in ^{6}Li. These beams are generated by a Coherent 899 dye laser pumped by a Coherent Verdi V-10 solid state laser. The Verdi laser can output up to 10 Watts of power at 532 nm, although typically 5.5 Watts are used to pump the dye laser.

The gain medium used in the dye laser is created when 1.17 grams LD688 dye is dissolved in 1.1 liters of 2-phenoxyethanol, which usually lasts 9 months before it needs to be replaced. When the dye is fresh, up to 1.1 Watts of power can be expected at a single frequency near 671 nm. The dye is organic and is composed of long chains of hydrocarbon molecules. These molecules have a wide array of vibrational states that are very close in energy, allowing the dye laser to be tuned over a wide range of frequencies. Although the dye laser is inherently a broadband device, its frequency selective optics and stabilization circuitry allow frequency resolution down to 1 MHz to be obtained. This level of frequency selection is necessary for sensitive procedures such as imaging, since the natural linewidth of ^{6}Li is only 5.9 MHz [91].

Before atoms can be captured in the MOT, they must be slowed considerably by the Zeeman slower. As described in Section 4.1.2, in order to reduce the length of the Zeeman slower, the slowing beam can be red detuned from the D_2 resonance of ^{6}Li. Since the slowing beam is the most powerful resonant beam used in the experiments, with a power of over 100 mW, it would be wasteful to shift the frequency of this beam using an acousto-optic modulator (AO), which would reduce the power of the beam by roughly 40%. Therefore the beam that is used to lock the laser to a frequency standard, given by the dot-dashed line in Figure 4.5 and further discussed in Section 4.4, is *upshifted* by 220 MHz using the Locking Region AO. In this configuration the beam originating from the dye laser is *downshifted* from the D_2 resonance of ^{6}Li.

As shown in Figure 4.5, the output from the dye laser passes through a half waveplate that is used to rotate the polarization in order to divide the power for the slowing and MOT beams using a polarizing beam splitting cube (PBS1).

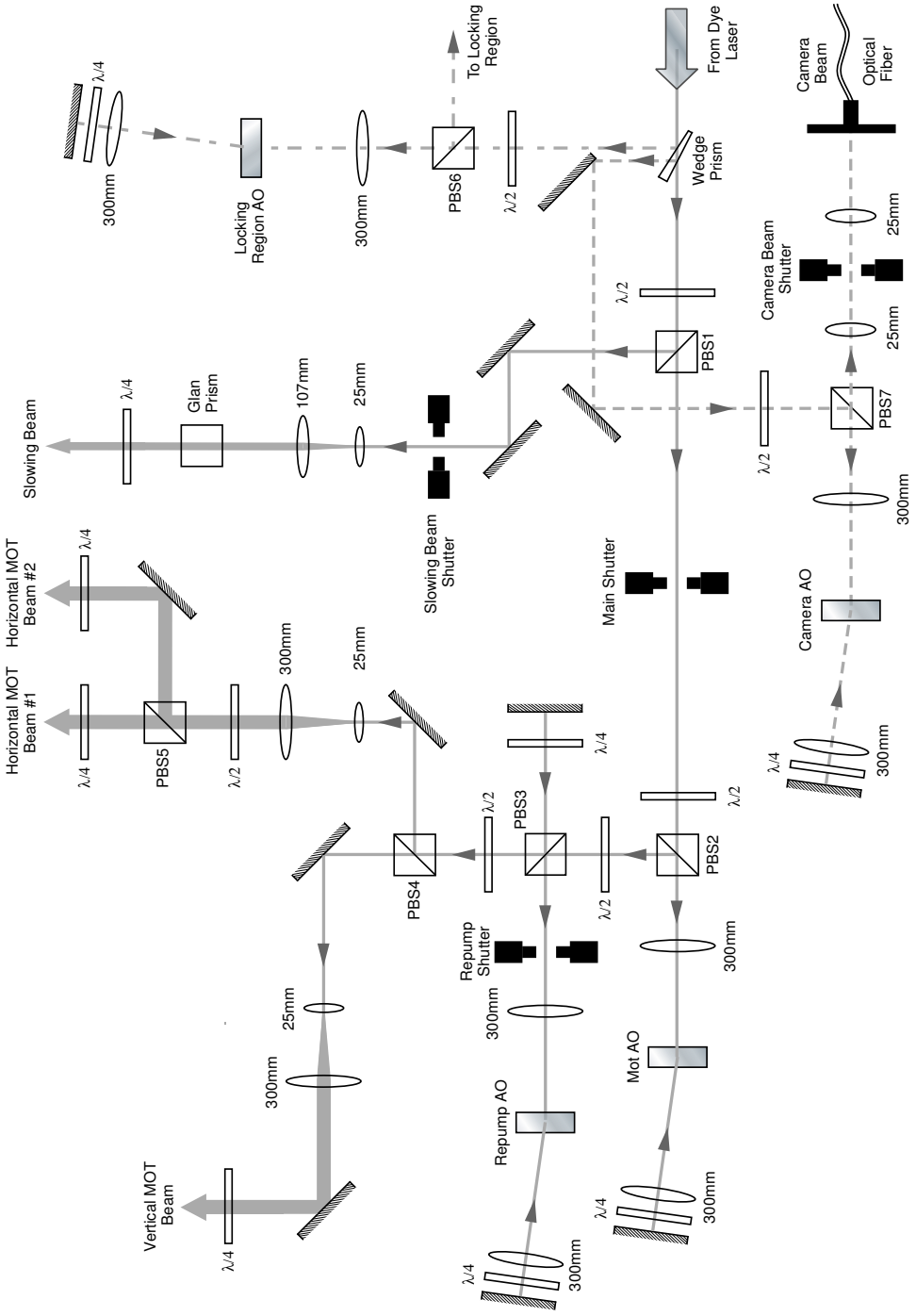

Figure 4.5: Optical layout for generating the MOT, slowing, locking region, and camera beams. The solid lines are MOT and slowing beams, the dashed line is the camera beam, and the dot-dashed is the locking region beam. The squares are polarizing beam splitting cubes. The schematic is not to scale.

After PBS1, the slowing beam passes through a high speed mechanical shutter before it is expanded to roughly 1.5 cm using two lenses. The shutter is used to completely extinguish the beam and prevent it from entering the chamber when it is no longer needed during the experimental sequence. The lenses after the shutter do not collimate the beam, however, since the loading of the MOT can be improved by a slowing beam that is convergent with a focus close to the nozzle of the oven. By having a convergent beam, a dipole force is created that attracts atoms to the slowing beam, improving the flux of slow atoms emerging from the Zeeman slower. Before entering the vacuum chamber, the slowing beam is circularly polarized through the use of a Glan prism and a quarter waveplate. Circular polarization is essential for the operation of the Zeeman slower since, by selection rules, it allows for a closed cooling cycle between the ground and excited states, which prohibits atoms from transitioning into a dark state [87].

Whereas the slowing beam is derived from the reflected beam originating from PBS1 after the input from the dye laser, the transmitted beam is used to create the MOT beams. As illustrated in Figure 4.5, this beam first travels through a high speed mechanical shutter before propagating through a half waveplate and entering a second polarizing beam splitting cube (PBS2). The waveplate is adjusted such that all the power is transmitted through this cube before being double passed through the MOT AO. A double pass arrangement allows the frequency of the beam to be upshifted twice as it passes through the AO. In the first pass, the beam is focussed onto the AO crystal using a 300 mm focal length lens. The beam then acquires a frequency shift of approximately 100 MHz and is deflected at an angle corresponding to the Bragg angle of the AO before being re-collimated using the second 300 mm focal length lens. The collimated

beam then passes through a quarter waveplate twice, producing a 90° rotation of the polarization after reflecting off a mirror. Following the same beam path back through the AO, the beam picks up a second frequency shift before being reflected by the polarizing beam splitting cube, since its polarization was rotated by 90°.

Typically, the frequency shift imparted by the MOT AO is 186 MHz. The natural linewidth of ^{6}Li is 5.87 MHz [50], so the frequency shift from the MOT AO detunes the MOT beams roughly 5 linewidths away from the D_2 resonance of ^{6}Li since the laser is locked roughly 220 MHz *below* the resonance. The ground state of ^{6}Li is split into a hyperfine doublet consisting of an $F = 1/2$ and $F = 3/2$ state. When the atoms are in the laser field of the MOT, they are excited from the $F = 3/2$ level of the $2\,^2S_{1/2}$ ground state up to the $2\,^2P_{3/2}$ excited state. In order to prohibit atoms from collecting in the $F = 1/2$ level when they return to the ground state, which is off resonance with the MOT beams, a repump beam is generated to transfer the atoms back to the $F = 3/2$ level. This beam is generated by the Repump AO after the MOT AO in Figure 4.5. A half waveplate and polarizing beam splitting cube (PBS3) are used to break off a fraction of the power from the MOT beam, upshifting it by 252 MHz before recombining it with the MOT beam again on PBS3.

After combining the two beams, the MOT and repump beams are sent through another half waveplate and polarizing beam splitting cube (PBS4). This allows the beams to be split into the two separate paths needed to create the horizontal and vertical MOT beams. The vertical MOT beam is derived from the transmitted beam through the cube. After PBS4, it passes through a collimating telescope in order to increase its diameter to roughly 3 cm. The larger diameter is necessary

to increase the number of atoms captured by the MOT beams. Before the vertical MOT beam enters the vacuum chamber, it is circularly polarized using a quarter waveplate.

Similarly, the horizontal MOT beam passes through a telescope, but is subsequently split into two equal pieces by PBS5 before being circularly polarized and entering the vacuum chamber. This allows independent control of the horizontal MOT beams, improving the stability of the MOT. After passing through the chamber, all three of the vertical and horizontal MOT beams are retro-reflected back on themselves. In the process of being retro-reflected, the beams pass through a quarter waveplate twice. This flips the handedness of the circular polarization before the beams re-enter the vacuum chamber, creating the three additional beams necessary for the operation of the MOT.

In addition to the slowing and MOT beams, the camera beam also needs to be generated out of the main beam from the dye laser. The camera beam propagates through the atoms during absorption imaging, allowing an image to be created. To create the camera beam, roughly 50 mW of power is removed from the main dye laser beam using a wedge prism as shown in Figure 4.5. This beam proceeds to travel through a half waveplate and polarizing beam splitting cube (PBS7) before double passing the Camera AO. After being upshifted in frequency by the AO, it is transmitted back through PBS7 before propagating through a high speed mechanical shutter and two lenses, which reduce the beam size to aid in coupling the beam into an optical fiber. The camera beam then travels through the fiber before emerging at the vacuum chamber for imaging. The imaging procedure will be further discussed in detail in Section 4.7.

4.3.2 CO_2 beam

After the atoms are trapped initially in the MOT, they are subsequently transferred to the FORT where they can be cooled to ultra-cold temperatures. Since the trapping potential produced by the FORT is proportional to the laser beam intensity, it is necessary to focus a laser beam with a very large power down to approximately 50 μm in order to produce a large potential depth. The laser frequency and stability are also critical in the FORT, since any scattered photons will heat the atoms and limit the ultimate temperature that can be attained. An ultra-stable CO_2 laser is ideally suited for such an application since it can produce over 100 Watts of power at a wavelength of 10.6 μm, which is roughly a factor of 16 away from the resonant frequency of ^{6}Li at 671 nm. In our experiments, a Coherent GEM-100 CO_2 laser that produces approximately 120 Watts of power is used to create the FORT.

The beam conditioning optics for the CO_2 laser are far less complicated than for the dye laser, and a schematic of the beam setup is given in Figure 4.6. As the beam leaves the laser, it initially hits two mirrors before entering an IntraAction Corp AGM-4010BJ1 AO. This is a high power germanium AO that is cooled using a mixture of distilled water and DowFrost. The quality of the beam after it leaves the AO is very sensitive to the crystal temperature. It was found that the increased path length, which allows the beam to expand due to diffraction, decreases the abberation of the beam after it passes through the AO since the larger beam size reduces the effect of thermal lensing [50].

In the case on the dye laser beams, an AO was used to upshift the frequency of the beams to become resonant with the atoms. Since a CO_2 laser is so far off resonance, the upshift in frequency has little effect on the atoms. But another

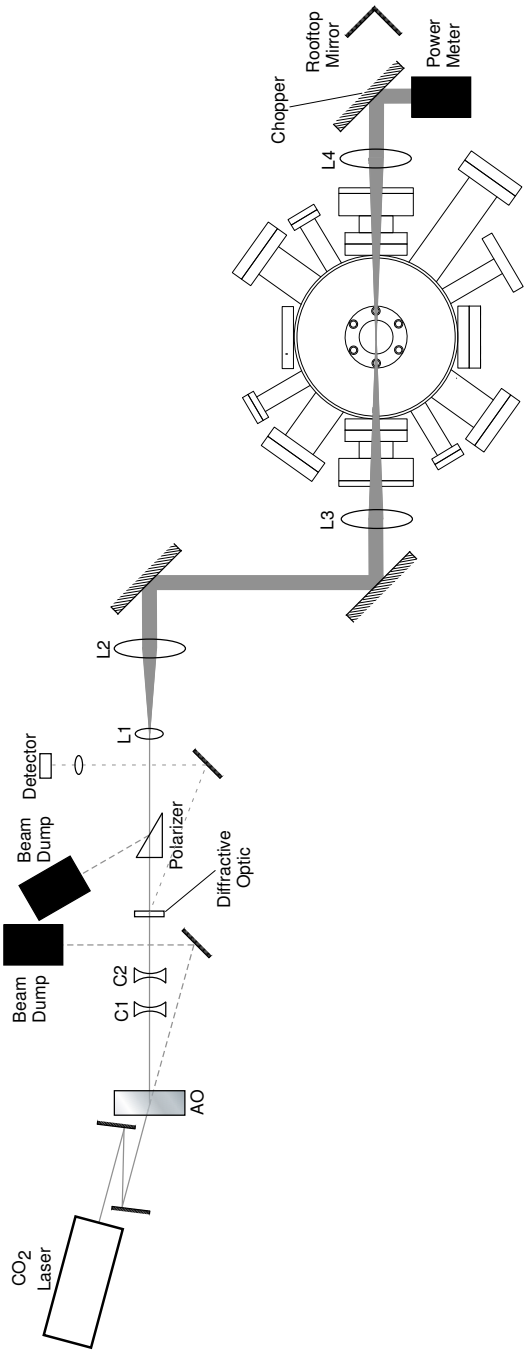

Figure 4.6: Optical layout for generating the CO_2 laser beams. The CO_2 beam passes through various beam conditioning optics before being brought to a focus at the center of the chamber, creating the FORT. The schematic is not to scale.

advantage of an AO is its ability to turn on and off very quickly. A typical beam extinguishing time for the IntraAction AO is less than 500 ns for our beam diameters. This allows the beam to be turned on and off extremely quickly, allowing dynamics in the microsecond time scale to be measured.

When the AO is off, all of the power in the CO_2 beam passes undeflected through the AO before hitting a pickoff mirror that steers it into a water cooled beam dump. This beam is given as the dashed line after the AO in Figure 4.6. When RF power is supplied to the AO, approximately 70% of the power emerges from the crystal in the 1st order beam. This beam is elliptical in shape owing to thermal lensing that arises due to thermal gradients in the AO crystal. To correct for this and return the beam to a circular shape, two cylindrical lenses that act vertically are placed directly after the AO. These lenses, as well as all the other optics in the CO_2 beam path, are made out of zinc-selenide. The glass lenses typically employed for visible wavelengths absorb strongly at 10.6 μm, and so cannot be used with a CO_2 laser.

After the cylindrical telescope, the CO_2 beam passes through a thin film polarizer. This optic will prohibit a retroreflected beam from propagating back into the CO_2 laser, causing considerable damage. A retroreflected beam is used to increase FORT loading and optical trap depth by increasing the intensity at the CO_2 beam focus by a factor of 2. If the chopper mirror after the main vacuum chamber in Figure 4.6 is lifted, the forward propagating beam will be reflected by a rooftop mirror instead of terminating at a beam dump. The rooftop mirror will flip the polarization by 90° and return the beam along its original path when properly oriented. When this retroreflected beam hits the front face of the polarizer, it is deflected into a water cooled beam dump instead of being transmitted

as a result of the polarization flip from the rooftop mirror.

An additional way of increasing the optical trap depth of the FORT is to increase the size of the CO_2 beam before it is focused at the center of the chamber. For a diffraction limited lens, the beam waist at the focus is inversely proportional to the diameter, d, of the incoming beam. Since the trap depth, U_0, is inversely proportional to the square of the beam waist, the relation $U_0 \propto d^2$ results. Therefore a deeper trap depth is produced by having a larger diameter beam at the final focusing lens before the chamber, given by lens L3 in Figure 4.6. To facilitate the expansion of the CO_2 beam, lenses L1 and L2 in Figure 4.6 create a collimating telescope that increases the beam size by a factor of 10 before reaching lens L3. This lens is positioned such that its focal point is at the center of the main vacuum chamber, creating the FORT. After passing through the vacuum chamber, the beam reaches lens L4, which is identical to lens L3 and acts to re-collimate the beam. The collimated beam can then be retroreflected using the rooftop mirror during FORT loading, or can be directed into a power meter by lowing the chopper mirror.

Since the CO_2 beam will be strongly absorbed while propagating through glass, zinc-selenide windows are used for the beam CO_2 beam path through the chamber. Commercially, ultra-high vacuum zinc-selenide windows are very expensive since they are not commonly used and are rather difficult to construct. Because of this, our lab has designed and constructed custom zinc-selenide windows to be used on the main chamber [84]. The design consists of two concentric seals, which are created when a pliable metal ring is compressed by the single crystal zinc-selenide window. An ion pump is used to evacuate the space between the seals, producing a vacuum for that region in the 10^{-7} to 10^{-8} Torr range. Since a region of high

vacuum exists between the seals, an ultra-high vacuum (10^{-11} Torr) is allowed to be maintained in the main chamber after the second seal. By constructing these windows in-house, a considerable monetary expense is avoided, and repairs can be expedited if the need arises.

4.4 Locking region

All of the beams that originate from the dye laser are required to have exceptional frequency stability. Therefore it is necessary to "lock" the frequency of the laser to a reference frequency to prevent it from drifting. In order to obtain a reference frequency, an atomic beam of ^{6}Li is generated in a vacuum chamber known as the "locking region". By intersecting this atomic beam with a laser beam at the D_2 resonant frequency, a signal is generated that can be used to stabilize the laser.

A schematic representation of the locking region is given in Figure 4.7. It consists of an oven that produces an atomic beam of ^{6}Li that is intersected orthogonally by a laser beam traveling through ports P1 and P2. As the dye laser frequency is scanned over the D_2 transition frequency for ^{6}Li, the atoms absorb light from the laser beam and re-radiate it in all directions. Some of that light is collected by a lens that is above the top viewport and positioned 2 focal lengths away from the atomic beam. After traveling through an iris to filter out stray background light, the light from the lens is collected into a fiber optic cable that is 2 focal lengths away from the lens to create 1:1 imaging. The light then travels through the fiber optic cable and into a photomultiplier tube (PMT) to be converted into a voltage.

In order to lock the laser, a small fraction of the power coming out of the dye

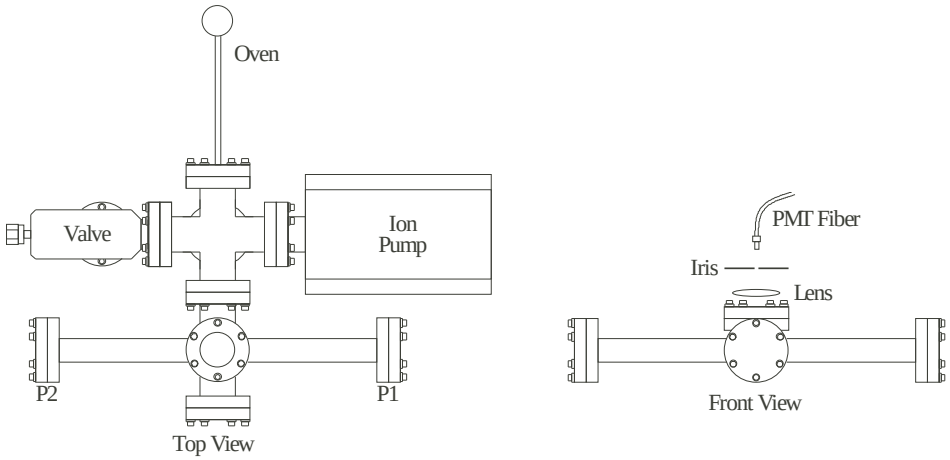

Figure 4.7: Schematic of the locking region. The top view (left) gives an overview of the entire apparatus. A stream of ^{6}Li originates from the oven, passes through the five-way cross, and then enters the region where it is intersected by a resonant laser beam generated by the dye laser. The front view (right) details the components used for atomic florescence acquisition. Scattered light from the atomic beam is collected by the lens and passes through and iris before being focused on the PMT fiber.

laser is split off using a wedge prism, shown as the dot-dashed line in Figure 4.5. This beam passes through a polarizing beamsplitter and then double-passes the Locking Region AO, upshifting the frequency by roughly 200 MHz. After the AO, roughly 1 mW of power is sent into the locking region through port P1. In addition to the 200 MHz shift given to the beam from the AO, is a 12 kHz dithering frequency. This dithering frequency introduces a modulation to the florescence signal produced in the locking region as the laser is scanned over the ^{6}Li D_2 transition frequency. The PMT that is monitoring the florescence sends a voltage to a lock-in amplifier and electronic servo system [92], which, in turn, produces an error signal that is sent to the dye laser control circuits to keep the laser locked to the ^{6}Li resonance.

4.5 Magnet system

It can be argued that one of the most powerful experimental tools that we have at our disposal is the magnetic field. We saw in Section 4.1 that the magnetic field produced by the Zeeman slower was essential for the production of atoms at a sufficiently small velocity to be captured by the MOT. Subsequently, the MOT itself requires a magnetic field gradient coupled with the laser field to produce a spatially varying force.

But more dramatically, by changing the magnitude of the bias field, a gas of ^{6}Li atoms can be converted from an ideal noninteracting gas into a strongly interacting superfluid just as presented in Chapter 2. Magnetic fields are very powerful tools in atomic, molecular, and optical physics because they can be used to vary energy level spacings in atoms as a result of the Zeeman effect. Perhaps only eclipsed by the laser in utility, they are essential for doing the experiments presented in this thesis. This section presents the details of the magnet system that was developed for the new experimental apparatus.

In addition to the Zeeman slower, there are two magnetic field configurations that are utilized during the experiment. The first is a gradient field that is needed for the MOT, and the other is the bias field that is used to tune the interactions between the atoms. Both configurations can be generated by a pair of symmetric coils placed a certain distance apart with identical radii. To create the gradient field for the MOT, the current in the two coils is run in opposite directions, creating a spherical quadrupole magnetic field with a point of zero magnetic field that lies halfway between the two coils. If the current is run in the same direction in both coils, a dipole field is generated, since the fields will add from each coil instead of subtract. A schematic of the two configurations is presented

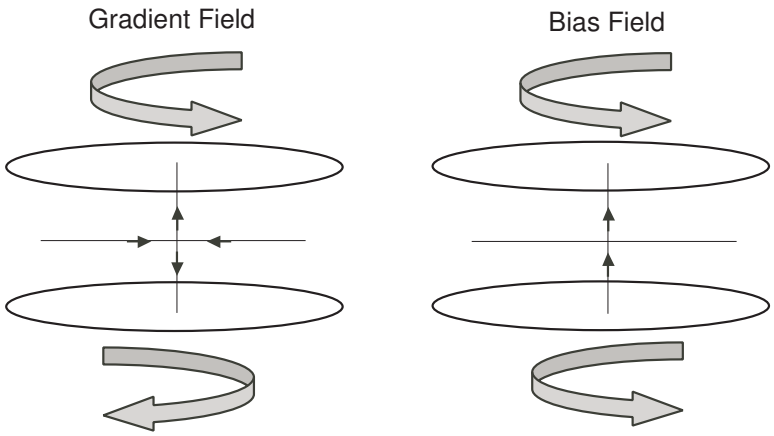

Figure 4.8: Schematic of the MOT gradient coil configuration (left) and bias field configuration (right). The block arrows indicate the direction of the current in the coils and the small arrows indicate the direction of the magnetic field along the axis of the coils and in the plane halfway between them.

in Figure 4.8. The discussion of the magnet system begins with an explanation of how the gradient configuration is achieved on the left side of the figure, followed by a presentation of the bias configuration on the right hand side.

4.5.1 Construction of magnet system

In the original experimental apparatus built in our lab [77, 83] a single pair of magnet coils generated not only the gradient field but also the bias field. This is possible since it is not necessary to have both fields operating simultaneously. After the FORT is loaded with the MOT in the gradient configuration, the current in one of the coils is reversed, resulting the bias field configuration. This adds a degree of technical complexity to the magnet system, since the electrical component that produces the switch must be able to withstand the large currents that are needed to reach the high fields necessary in the experiment. A less complicated design is to have separate coils to produce the individual fields. Not only

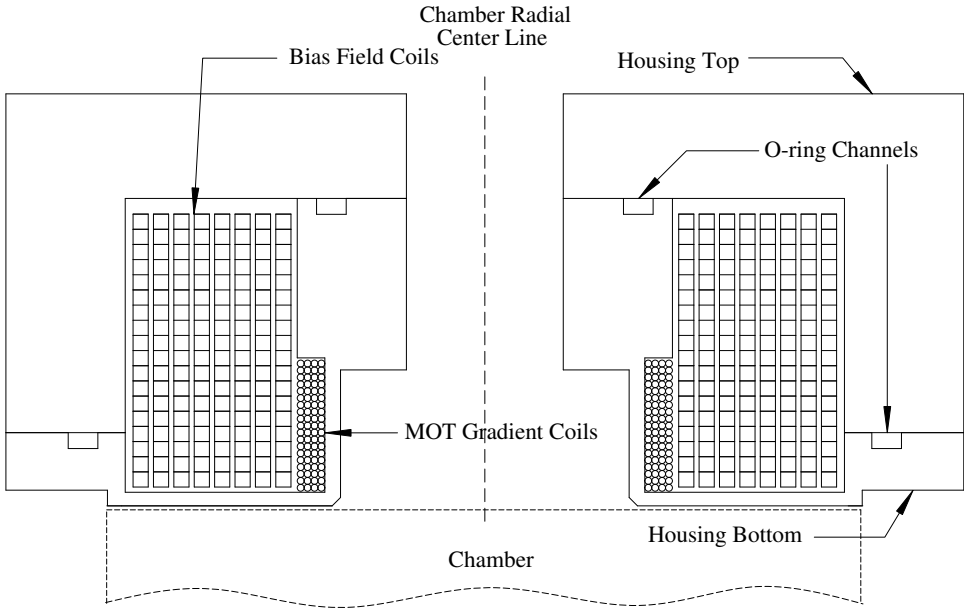

Figure 4.9: Scale drawing of the MOT coils (circles) and bias coils (squares) in their water-tight housing. Pictured is a cross sectional cut through the center of the coils. The large dashed line displays the center line of the chamber, while the small dashes outline a partial view of the chamber located below the magnets.

does this reduce the complexity of the experimental sequence, it also allows for an additional magnetic field source, which may be of use in future experiments. In this section, the design and construction of the magnet system used in the new experimental apparatus is presented.

Both the MOT gradient and bias field magnet coils have to be mounted on the outside of the main vacuum chamber, with the midpoint between both sets of coils being the center of the chamber. The best way to design such a magnet system is to have one magnet coil sitting inside the other. Since the MOT gradient magnet uses less power, it should be placed inside the much larger bias magnet. A scale drawing of the final design of the magnet system is shown in Figure 4.9. In this figure, the MOT and bias coils are shown in cross section inside of their Delrin

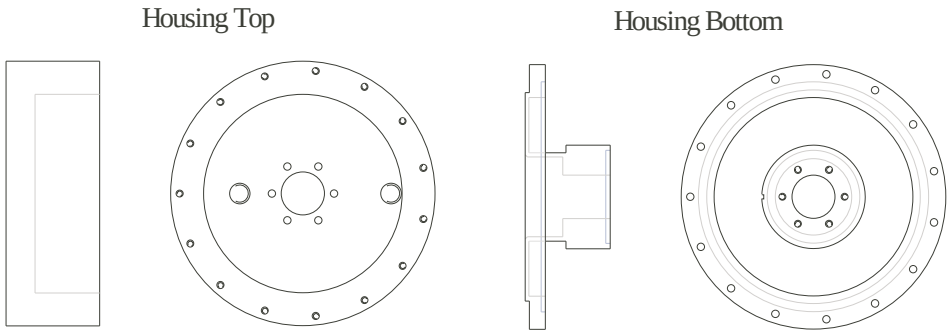

Figure 4.10: Scale drawing of the housing for the MOT and bias coils. Top and side views are given for the top (left) and bottom (right) sections of the housing.

housing. The MOT magnet is constructed from 14 gauge REA Super Hyslik 200 copper magnet wire and is represented by the small circles in Figure 4.9. The bias field coils are shown as the much larger squares and are constructed from 8 gauge REA Therm-Aimid square magnet wire. The insulation on both sets of wire is rated to withstand continuous use at 200°C, although the coils never attain such high temperatures due to efficient water cooling. The housing and magnets are designed to straddle the ports for the vertical MOT beams on the top and bottom of the main vacuum chamber. This is reflected in the need for the cutout in the housing bottom next to the MOT gradient magnets show in Figure 4.9.

The Delrin housing for the magnet coils serves two purposes. First, it acts as a spool for the MOT magnet wire, which aids in construction. But more importantly, the housing provides a waterproof enclosure for the magnets to be cooled in. The high field magnets produce roughly 1000 Watts of power at the Feshbach resonance at 834 Gauss, which will melt the coating of the wires if they are not cooled sufficiently. The housing bottom has two circular o-ring grooves machined into it, so when the housing top and bottom are screwed together, a

watertight seal is formed. A scale drawing of the housing for the coils is presented in Figure 4.10. The housing top has inlet and outlet ports to allow the flow of water in and out of the housing.

While the MOT magnets are wound directly onto the housing bottom, the bias field magnets are wound separately and then placed into the housing. A special Delrin form was created for this purpose, allowing the bias coils to be wound with the help of a lathe. Since these coils produce so much power, they need to be cooled efficiently. The coils are able to transfer more heat to the water if the surface area of the coils in contact with the water is increased. To facilitate this, a 0.05 inch thick starch based material is inserted between each successive layer of the coil. After the coil is completed and inserted in the housing, water is used to dissolve the starch based material, leaving vertical gaps between the rows of coils for water to flow through, as seen in Figure 4.9.

4.5.2 MOT gradient magnets

The MOT magnets are composed of 4 layers of wire with 19 turns in each layer. Each coil is wound directly onto the Delrin housing as displayed in Figure 4.9. By mounting a magnet coil on the top and bottom of the main vacuum chamber and running current in opposite directions, a spherical quadrupole magnetic field is produced at the center of the chamber as shown qualitatively in Figure 4.8. These magnets were designed by numerically solving the magnetic field magnitude and direction in space for a particular coil configuration using Mathematica. Each turn of the magnet is assumed to be an independent coil, and the contributions for all the coils are summed together to give the total field. The final design was chosen after considering various technical aspects such as the dimensions of the

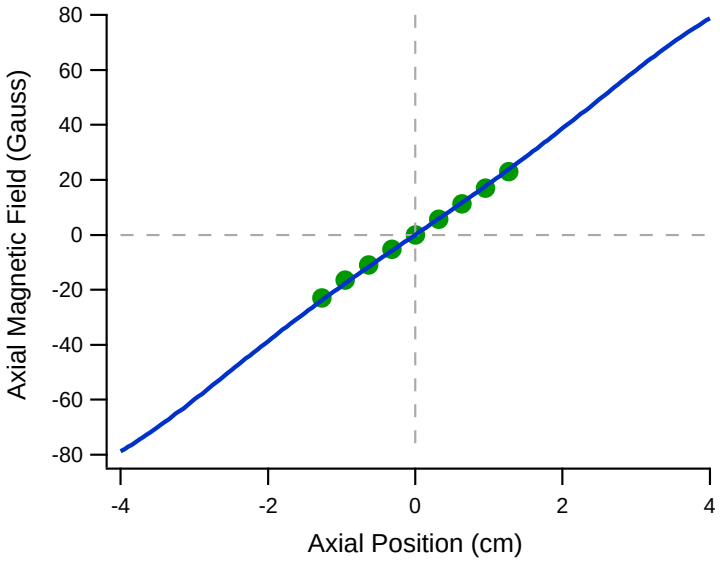

Figure 4.11: Plot of the axial magnetic field for the MOT gradient magnet versus position from the center of the chamber. The solid line is the theory and the closed circles are the experimental measurements for a current of 9 amps. Dashed lines accentuate the zero crossing.

main vacuum chamber, the amperage available in common power supplies, and the efficiency of heat transfer to prevent overheating.

To check the accuracy of the computer modeling and the quality of the construction, it is necessary to test the magnet coils after they are completed. On the main vacuum chamber the distance between the top and bottom walls, where the magnets will be mounted, is 2.6 inches. Therefore, the field inside the chamber can be simulated by placing the two magnets in their housings 2.6 inches apart and passing current in opposite directions through them. The center point between the two coils where the magnetic field vanishes, which coincides with the center of the main chamber, can be located using a Bell 620 Gaussmeter. By moving the probe of the Gaussmeter along the axis of the magnets, the magnitude of the magnetic field in the axial direction can be mapped out. A plot of

Table 4.1: Table of experimentally determined and theoretically calculated axial gradients for the MOT magnet. Gradient values are in Gauss per centimeter.

Coil Current	Exp. Gradient	Theo. Gradient	Difference
1 amp	1.97 G/cm	2.03 G/cm	3.0 %
3 amps	5.94 G/cm	6.10 G/cm	2.6 %
6 amps	11.8 G/cm	12.2 G/cm	3.3 %
9 amps	17.9 G/cm	18.3 G/cm	2.2 %

the theoretical magnetic field along with the experimentally determined points is given in Figure 4.11. For this experiment a coil current of 9 amps was used.

As seen in Figure 4.11 the variation in the magnetic field is nearly linear, especially in the region close to zero where the MOT will form. Therefore, the magnetic field gradient is well characterized by fitting a straight line to the data. A comparison of the theoretical and experimentally determined gradients for various coil currents is given in Table 4.5.2. This table, along with Figure 4.11, demonstrate that the mathematical modeling and the actual field differ only by a few percent. Based on the values presented in Table 4.5.2, a general formula for the axial magnetic field gradient in Gauss per centimeter is $|\, d\mathbf{B}/dz| = 2I$, where I is the current in amps and $\mathbf{B}$ is the magnetic field. Typically, a axial gradient of roughly 24 Gauss per centimeter is used to create the MOT by running 12 amps of current through each coil. All the gradient values given so far are in the axial direction. A linear gradient is also produced in the radial direction that has a magnitude half as much as in the axial direction and opposite in sign. This is due to the fact that the magnets have cylindrical symmetry and $\nabla \cdot \mathbf{B} = 0$.

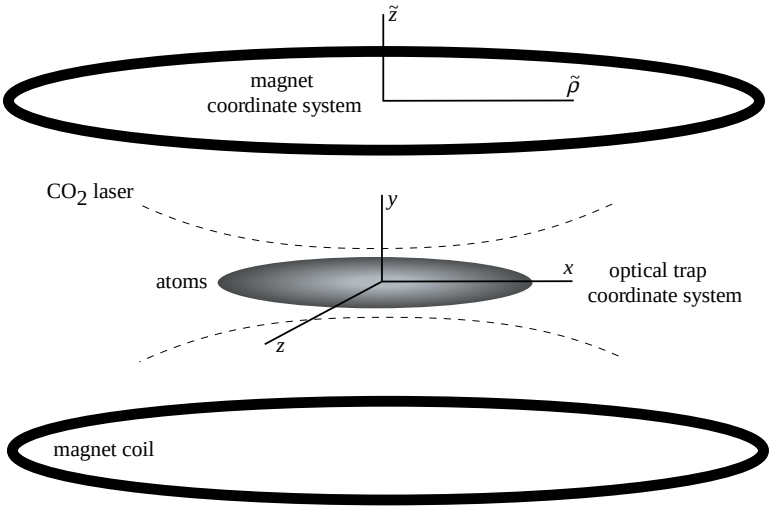

Figure 4.12: Illustration of the magnet and optical coordinate systems. The axial direction of the magnet, shown as the heavy lines in the figure, is defined as the $\tilde{z}$-direction, while the radial direction is denote by the coordinate $\tilde{\rho}$. The optical coordinate system, defined in Section 3.3.2, is also given.

4.5.3 High field magnets

Straddling the MOT magnets are the high magnetic field bias coils. As illustrated in Figure 4.9, the bias coils consist of 8 layers of coils with 18 turns per layer where each layer separated by 0.05 inches for cooling purposes. The purpose of the bias coils is to produce the magnetic fields needed to tune the scattering length between the atoms. They are designed to produce fields up to 5000 Gauss for 1 second, although the current configuration is limited to approximately 1250G[1].

The symmetry of the bias magnet configuration creates a natural coordinate system where the axial direction ($\tilde{z}$) is along the bore of the magnets and the radial direction ($\tilde{\rho}$) points radially outward. This coordinate system, along with

[1]By connecting 2 Agilent 6691A power supplies in series with each coil (4 total), it is possible to achieve 5000 Gauss for 1 second. However, in the current setup, one power supply is driving both coils, limiting the highest attainable field.

the coordinate system for the optical trap presented in Section 3.3.2, is illustrated in Figure 4.12. As shown in the figure, the axial direction of the magnetic field is actually perpendicular to the axial (long) direction of the optical trap. The magnet coordinate system will only be used for the derivations in this section to obtain an expression for the potential created by the magnetic field curvature, whereas the optical coordinate system is used throughout the remainder of the thesis.

In the axial and radial directions, the bias coils create a magnetic field that is parabolic in shape near the midpoint between the two coils, which corresponds to the center of the chamber. Similar to the MOT magnets, the magnetic field produced by the bias coils can be simulated numerically. A plot derived from a typical numerical simulation is given in Figure 4.13. This plot displays the magnitude of the magnetic field in the axial direction of the magnets ($\tilde{z}$) as a function of the distance between them. The minimum in the plot occurs at the center of the chamber, and in this particular simulation the field produced is 834G, which is the location of the Feshbach resonance.

Not only do the bias coils create the magnetic fields necessary to tune the atomic interactions, they also exert a force on the atoms due to the inhomogeneity of the field. Treating the atom as a magnetic dipole, the force exerted by the magnetic field can be written

$$\mathbf{F} = \boldsymbol{\nabla} \left(\boldsymbol{\mu}_B \cdot \mathbf{B} \right), \tag{4.3}$$

where $\boldsymbol{\mu}_B$ is the magnetic dipole moment [93]. Using the product rule, the expression for the force becomes $\mathbf{F} = \boldsymbol{\mu}_B \times (\boldsymbol{\nabla} \times \mathbf{B}) + (\boldsymbol{\mu}_B \cdot \boldsymbol{\nabla})\mathbf{B}$. Since $\boldsymbol{\nabla} \times \mathbf{B} = 0$

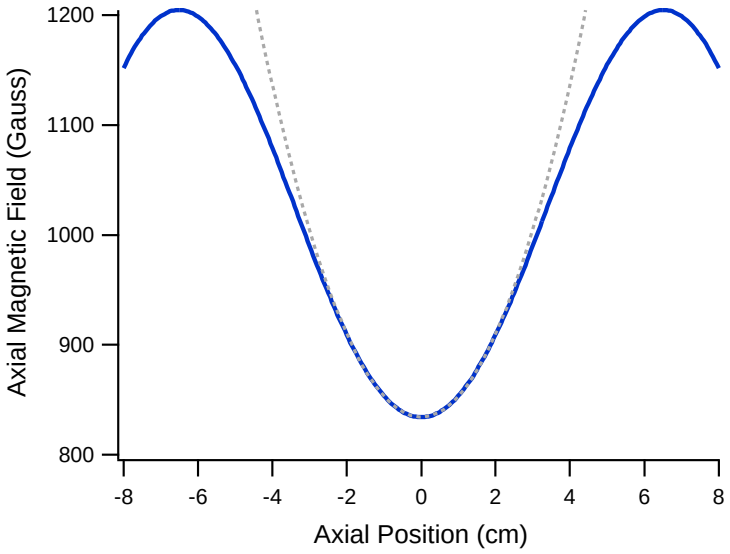

Figure 4.13: Plot of the magnitude of the axial magnetic field versus position from the center of the chamber for the bias coils. The solid line is the theory and the dotted line is a parabolic fit to the theory from -2 cm to 2 cm. The current in the theory is 86.75 amps corresponding to a minimum field of 834 Gauss.

in free space, equation (4.3) can be written in the alternative form

$$\mathbf{F} = (\boldsymbol{\mu}_B \cdot \boldsymbol{\nabla})\mathbf{B}. \tag{4.4}$$

As a result, the atoms will feel a force corresponding to the magnetic field curvature when the bias magnetic field is present. When the atoms are introduced to a large bias field, a torque is introduced that acts to align the magnetic dipoles in the direction of field. Therefore, $\boldsymbol{\mu}_B$ can be assumed to be in the direction of the magnetic field, $\boldsymbol{\mu}_B = \mu_B \hat{\hat{\mathbf{z}}}$, and only the axial component of the dot product in (4.4) will remain.

In order to calculate the force on an atom due to the magnetic field inhomogeneity, an expression for the spatial dependence of the magnetic field must

be found. A general formula for an arbitrary magnetic field can be constructed from Maxwell's equations in free space given by $\boldsymbol{\nabla} \cdot \mathbf{B} = 0$, $\boldsymbol{\nabla} \times \mathbf{B} = 0$, and additionally $\boldsymbol{\nabla}^2 \mathbf{B} = 0$. It can be shown that to second order in the coordinates, the most general form of the field that satisfies these equations in the bias field configuration is

$$\mathbf{B} = B_0 \left[1 + b_1 \left(\tilde{z}^2 - \tilde{\rho}^2/2\right)\right] \hat{\tilde{\mathbf{z}}} - B_0 b_1 \left(\tilde{\rho}\, \tilde{z}\right) \hat{\tilde{\boldsymbol{\rho}}}, \tag{4.5}$$

where B_0 is the magnitude of the bias field and b_1 is a constant that depends upon the geometry of the magnets. A cylindrical coordinate system has been assumed in equation (4.5) to reflect the symmetries of the magnets. This equation can also be found through the use of a multipole polynomial expansion of the vector potential [94]. Equation (4.5) is valid for describing magnetic fields close to the midpoint between the two magnets, which corresponds to the center of the chamber where the atoms are trapped. The dashed curve in Figure 4.13 demonstrates that a parabola well approximates the theoretical axial magnetic field between -2 and 2 cm, lending credence for our choice of $\mathbf{B}$. Using this this form of $\mathbf{B}$ in equation (4.3) or equation (4.4) produces the expression

$$\mathbf{F} = \mu_B B_0 b_1 \left(2\tilde{z}\, \hat{\tilde{\mathbf{z}}} - \tilde{\rho}\, \hat{\tilde{\boldsymbol{\rho}}}\right), \tag{4.6}$$

which is the equation for a harmonic oscillator in the radial direction ($\hat{\tilde{\boldsymbol{\rho}}}$) and a repulsive potential in the axial direction ($\hat{\tilde{\mathbf{z}}}$) of the magnets. Therefore, the bias field magnets create a harmonic trap in the radial plane of the magnets that must be accounted for, since it will modify the effective trap frequencies. This is especially important when experiments are done at very low trap depths, where

the confining potential due to the magnetic curvature in the $\tilde{\rho}$-direction is on the order of, and sometimes greater than, the optical potential in the x-direction.

The contribution of the magnetic field curvature to the overall trap frequencies can be estimated using the numerical simulation for the magnetic fields. A parabolic fit to the theoretical axial magnetic field, shown as the dotted line in Figure 4.13 and given by $B_{fit} = B_0(1 + b_1\tilde{z}^2)$, produces coefficients can be used to approximate the oscillator frequency. By equating the magnetic field potential to that of a harmonic oscillator

$$\frac{1}{2}\frac{\partial^2}{\partial\tilde{z}^2}(\boldsymbol{\mu}_B \cdot \mathbf{B})\tilde{z}^2 = \frac{1}{2}\, m\, \omega_{By}^2\, \tilde{z}^2, \tag{4.7}$$

the effective frequency due to the magnetic field curvature in the $\tilde{z}$-direction is found to be $\omega_{By} = \sqrt{2\,\mu_B\, B_0 b_1/m}$, where b_1 is determined from B_{fit}. In defining the frequencies for the magnetic potential, I will use the optical coordinate system shown in Figure 4.12 such that ω_{By} is in the axial direction of the magnets.

From the simulation done at 834 Gauss in Figure 4.13, the axial magnetic field frequency is determined to be $\omega_{By}(834\,G) = 2\pi \times 30.2$ Hertz. Since the frequencies in the radial plane of the magnets are reduced from the axial frequency by a factor of $\sqrt{2}$, the radial frequency is determined to be $\omega_{Bx}(834\,G) = \omega_{Bz}(834\,G) = 2\pi \times 21.4$ Hertz. These frequencies can be scaled to any other field, like 528 Gauss, by recognizing from the form of ω_{By} that the frequencies scale as the square root of the magnetic field. Therefore at the zero crossing of the scattering length the theoretical frequencies are $\omega_{By}(528\,G) = 2\pi \times 23.9$ Hertz and $\omega_{Bx,z}(528\,G) = 2\pi \times 16.9$ Hertz. Since the axial ($\tilde{z}$, ω_{By}) potential is repulsive, it will *decrease* the optical trap frequency (ω_y) in that direction, whereas the radial oscillator

will *increase* the optical trap frequencies (ω_x, ω_z). However, the optical trap is very tight in the $\tilde{z}$-direction, typically from hundreds of Hertz up to one or two thousand Hertz, so the magnetic potential has a negligible contribution in that direction since the total frequency comes in as the sum of the squares, $\omega^2_{total} = \omega^2_{magnetic} + \omega^2_{optical}$. Therefore, in practice, the only modification done to the optical trap frequencies is in the axial direction of the trap, producing the effective frequency $\omega_{x_{eff}} = \sqrt{\omega_x^2 + \omega_{Bx}^2}$.

4.5.4 Magnetic field calibration

After the magnets are installed on the experimental apparatus, it is prudent to experimentally validate the magnetic field magnitude. Most experiments require a magnetic field accuracy of ± 1 Gauss, so it is critical to not completely rely on the theoretical simulation to determine the magnetic field.

The evaporative cooling of a collection of atoms relies on collisions between atoms to reduce the energy contained in the gas as explained previously in Section 3.4. If the interactions between atoms are reduced, or removed entirely, a gas of hot atoms will have a difficult time thermalizing to a lower temperature through evaporative cooling. Since the energy contained in a harmonically trapped gas is proportional to the mean square size of the cloud [56], if evaporative cooling is attempted at different magnetic fields in the vicinity of 528 Gauss (where the scattering length is zero) a peak in the mean square size of the cloud will be observed.

To perform such an experiment, atoms from the MOT are loaded into the FORT and then allowed to evapoartively cool for 30 seconds without lowering the trap before they are imaged. This procedure is then repeated at several different

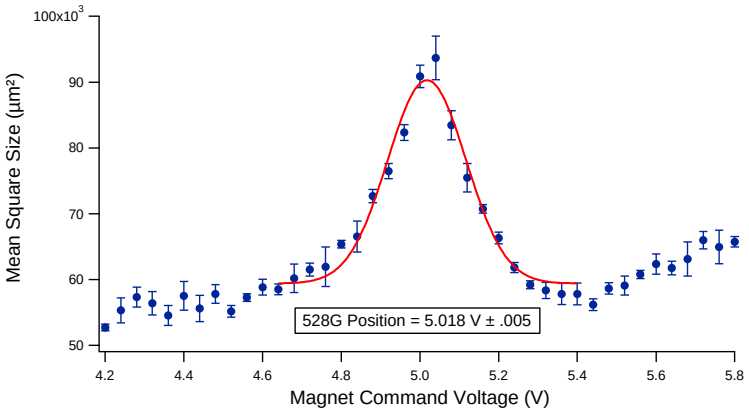

Figure 4.14: Plot of the mean square size of the cloud versus command voltage to the magnet power supplies. The solid circles are the experimental data points and the solid curve is a gaussian fit to the data. The peak in the fit corresponds the command voltage necessary to produce a field of 528 Gauss.

magnetic fields in the vicinity of the expected 528 Gauss position. Data produced form this experiment is presented in Figure 4.14. In this figure the mean square size of the cloud is plotted versus the command voltage sent to the magnet power supplies. The power supply for the magnets is controlled remotely using an analog command voltage signal between 0 and 10 volts that will produce from 0 to 220 amps of current. Since the current is linearly proportional to the magnitude of the magnetic field, the command voltage is also linearly proportional to the magnetic field.

The solid line in Figure 4.14 is a gaussian fit to the data with the peak corresponding to the command voltage necessary to produce a field of 528 Gauss, where the scattering length is zero and there are no interactions to evaporatively cool the gas. Since there is a linear relationship between the command voltage and the magnetic field, the command voltage necessary to produce any other field

follows the very simple formula

$$V(B) = \frac{5.018}{528} B \tag{4.8}$$

where V is the command voltage in Volts and B is the desired magnetic field in Gauss. This formula guarantees that a magnetic field of 0 Gauss will be produced at a 0 command voltage (magnets off).

4.5.5 Trim coils

In addition to the MOT and bias field coils, there are three additional magnetic field coils present on the main vacuum chamber. These coils are mounted directly on the windows of ports M1, M3, and M4 in Figure 4.4. Due to space constraints there is no coil attached to port M2. These coils consist of 29 turns of 20 gauge wire in 16 layers wound directly onto custom Delrin spools. They are mounted directly onto the MOT port windows and each coil is designed to produce a 5 Gauss bias field at the center of the chamber for 4 amps of current.

These coils are used to slightly adjust the position of the zero field point produced my the MOT magnets in the horizontal plane between the magnets. By producing a small bias field, the position of zero magnetic field can be adjusted. The center of the MOT will form at the point of zero field, so this is an effective way of moving the MOT around in space. This is important because due to slight drifts of the CO_2 beam from day to day, the alignment of the MOT and FORT may not be optimal. It is much easier to correct for the misalignment by adjusting the current in a magnet coil and moving the MOT center, rather than tweaking the alignment of the CO_2 beam path. The position of the MOT

is adjusted vertically by reducing the current in one of the MOT coils using a potentiometer wired in parallel, rather than adding additional coils.

4.6 Radio-frequency antenna

When the atoms are loaded into the FORT from the MOT, they are in the two lowest hyperfine levels, $|1\rangle$ and $|2\rangle$, of the $2\,^2S_{1/2}$ ground state of ^{6}Li. Since the MOT beams are fairly well balanced, typically equal populations of states $|1\rangle$ and $|2\rangle$ are produced. To ensure that there exists a 50:50 mixture of states, a radio-frequency (RF) antenna is used to drive transitions between the two levels, which equalizes the populations through rate equation pumping.

The RF antenna is attached to port P1 in Figure 4.4. It was designed by James Joseph and consists of a rectangular loop of wire, where the plane of the loop is oriented vertically to produce an RF field perpendicular to the bias field created by the magnets. At zero field the energy levels of states $|1\rangle$ and $|2\rangle$ are degenerate, therefore an 8 Gauss magnetic field is produced by the bias magnets to split the energy levels between the two states by roughly 7.8 MHz. An RF pulse centered at this frequency, that is also modulated with noise at a bandwidth of 2 MHz, is then applied to the atoms for 100 milliseconds to equalize the populations. Normally an RF pulse will create a coherent mixture od states $|1\rangle$ and $|2\rangle$, but the relatively large amount of magnetic field inhomogeneity at 8 Gauss assures the coherence will quickly decay.

The RF signal is produced by and Agilent 33220A arbitrary waveform generator and subsequently amplified by a Mini-Circuits TIA-1000-1R8 amplifier. The output to the antenna is controlled by a Mini-Circuits 15542 ZAD-1 frequency

mixer, which we use as a switch to turn the antenna on and off. Before the signal reaches the antenna, it passes through a MFJ Deluxe Versa Tuner II RF tuner, which impedance matches the antenna for maximum power delivery.

Although the RF antenna was used exclusively for spin balance for all the experiments done in this thesis, it can also be used for spin *imbalance*. At high magnetic field, the energy level spacing between states $|1\rangle$ and $|2\rangle$ is roughly 76 MHz, which is a spacing of 13 natural linewidths, so that an optical pulse resonant with state $|2\rangle$ will only slightly perturb state $|1\rangle$. Therefore if the interactions between the two states are minimized at the appropriate magnetic field, one state can be selectively removed from the trap with a short optical pulse. The leftover pure state can then be used to create a mixture of any composition by applying an RF pulse of appropriate time duration. This allows for access to the study of spin imbalanced mixtures, which is the topic of substantial theoretical and experimental interest [37, 95].

4.7 CCD camera and imaging system

At the end of every experimental cycle, an image of the atom cloud is taken. All of the necessary information for the experiment is contained in the image. We employ on-resonance absorption imaging to generate figures of the atom cloud, which is a destructive process. In most experiments, the width of the cloud or its orientation is the desired quantity to be measured. This information can be extracted from the images as long as a high quality, low noise imaging system is used to capture the cloud images.

At the heart of the imaging system is an Andor Technology DV434-BV CCD

camera. The CCD detector on this camera consists of a 1024 × 1024 array of high resolution pixels measuring 13 μm on each side. A thermoelectric cooler maintains the array at -40°C during data acquisition to minimize the production of dark current on the CCD. It has a peak quantum efficiency of 95%, allowing very sensitive imaging to be done under low light conditions.

Software is provided with this camera that allows the CCD array to be partitioned into separate regions, which extends its data acquisition capabilities to many different modes. In the so called Fast Kinetics mode, the CCD array is split vertically into multiple sections of identical size, and data is allowed to be transferred between the different sections. For example, during experiments a "signal shot" is taken to image the atoms, but the image is not of very good quality due to noise in the background and imperfections in the camera beam. Therefore a "reference shot" is taken typically 30 ms later, when there are no atoms present, which should contain all the same background noise and imperfections since it was taken so close to the signal shot. These two images are subtracted to yield a high quality image of the atoms on top of a very low background. A typical signal, reference, and processed image is given in Figure 4.15.

Unfortunately the time duration between acquiring these two images is much too short for the entire CCD array to be read out since it takes the camera 1 μs to process a pixel after an image is taken. Since the CCD contains 1024 × 1024 pixels, it takes over a second to process the entire array. But an entire horizontal row of pixels can be shifted down on the CCD array in only 16 μs. So by partitioning the array into three vertical sections of 340 pixels, one section of pixels can be transferred to the other section in under 6 ms. Therefore by masking the bottom 2/3 of the CCD array from the camera beam with a razor blade and

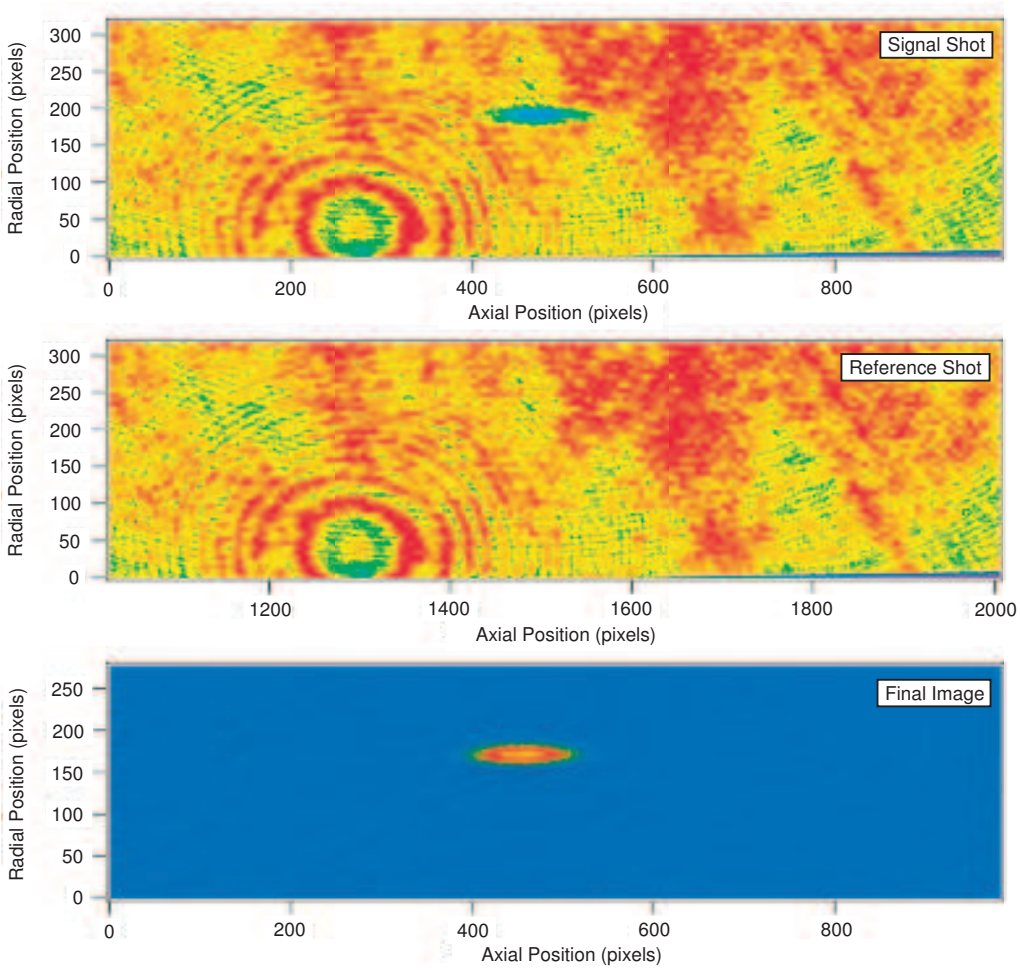

Figure 4.15: False color absorption images of the atomic cloud. The top and middle figures are the signal and reference shots, respectively. These raw images illustrate the distribution of photons on the CCD array and demonstrate the level of variation in the probe beam intensity. In the signal shot atoms are present, while in the reference shot they are absent. The bottom image is the final processed image, which results when the signal and reference shots are subtracted.

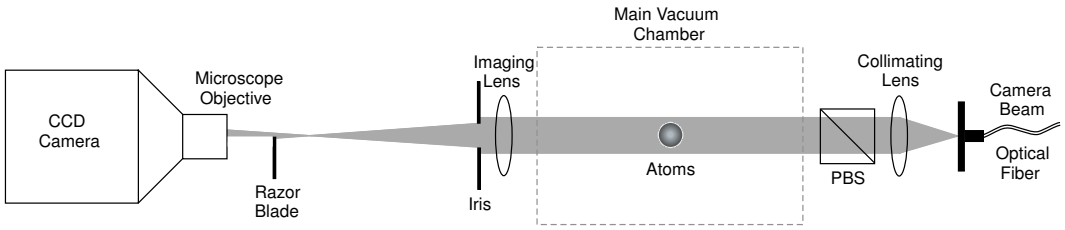

Figure 4.16: Schematic representation of the camera beam path. The camera beam originates at the fiber optic cable and propagates through the atoms to the CCD camera. A razor blade is used to mask 2/3 of the CCD array when images are taken in Fast Kinetics mode. The figure is not to scale.

only illuminating the top 1/3, the signal shot can be taken and then immediately shifted into the masked area to preserve the information in the pixels. Then the reference shot can be taken a short time later and also shifted into the masked area. At that point the experimental cycle has been completed and the time scale involved in reading out the array is no longer critical.

The generation of the camera beam was discussed in Section 4.3.1 and illustrated in Figure 4.5. The camera beam is used to illuminate the atoms during absorption imaging. Before a camera beam pulse reaches the atoms, it is first passed through a fiber optic cable. The reason for this is twofold. The cable is used to easily transport the camera beam from a location on the optics table where it is created, over to the chamber where it can be used for imaging. An added benefit of the fiber is that it "cleans up" the mode of the laser beam, producing a smooth gaussian beam at the exit of the fiber in a fixed, stable direction. This is advantageous since it minimizes the intensity fluctuations across the sample of atoms, producing a better quality image.

A schematic of the camera beam path after it exits the fiber is given in Figure 4.16. The beam is divergent as it leaves the fiber and is collimated using a

aspheric lens. The collimated beam is approximately 2.5 cm in diameter and typically contains 6 mW of power. Optimal image quality has been found by using a 5 μs pulse. Before entering the vacuum chamber, the camera beam passes through a polarizing beam splitting cube to assure that all vertical polarization has been removed from the beam. After interacting with the atoms, the beam leaves the chamber and propagates through an imaging lens. This lens, and the microscope objective attached to the CCD camera, provide the magnification for the imaging system. But before reaching the microscope objective, the beam passes through an iris and impinges on a razor blade. The iris is used to restrict the diameter of the camera beam after the imaging lens, reducing spherical abberation. The razor blade is used to mask 2/3 of the CCD array from the camera beam, which is necessary when the camera is used in Fast Kinetics mode.

4.8 Typical experimental sequence

In the preceding sections, the tools and equipment used to trap and cool ^{6}Li atoms have been introduced. In this section, the sequence of steps used to create a degenerate, strongly interacting gas is presented. Section 4.8.1 begins by giving an account of the techniques used to initially trap the atoms, and then cool them to degeneracy and beyond. This is followed by Section 4.8.2, which details the experiments used to characterize the trap frequencies once a degenerate sample has been created. It will be shown that the trap frequencies, ω_x, ω_y, and ω_z can be determined through a parametric resonance technique, or through a measurement of the collective modes.

4.8.1 Production of a strongly interacting Fermi gas

The experiments that can be done using a strongly interacting Fermi gas vary in the type and complexity, but the initial preparation sequence is roughly identical for all experiments. The sequence begins by allowing the MOT to load for 10 seconds before attempting to load the FORT. The FORT is always present during the MOT loading stage, since the CO_2 beam has little effect on the MOT loading. The chopper mirror in Figure 4.6 is raised out of the CO_2 beam path, allowing the beam to be retroreflected by the rooftop mirror, increasing the intensity at the beam focus.

The FORT loading consists of a progression of steps that cools the atoms in the MOT and then pumps them into the ground state. In the "cooling phase" the frequency of the MOT beams are switched to 1/2 linewidth below the atomic resonance while the intensity of the beams are simultaneously decreased. Bringing the beams closer to resonance increases the amount of Doppler cooling produced by the MOT beams and allows temperatures in the vicinity of 140 μK to be achieved. The cooling phase lasts 50 ms and is followed by the "optical pumping" phase wherein the atoms are transferred from the $F = 3/2$ to the $F = 1/2$ level of the ^{6}Li ground state. This is accomplished by turning off the repump beam and allowing the atoms to optically pump into the ground state for 200 μs. After the optical pumping phase, the MOT beams are switched off, leaving the sole CO_2 beam to confine the atoms. This procedure loads approximately 2 million atoms into the FORT.

After the MOT beams are extinguished, the MOT magnets that produce the magnetic field gradient are also turned off. After a delay of 500 μs to allow the gradient field to dissipate, a signal is sent to the bias magnet power supply

to provide enough current to produce a field of 8 Gauss for RF spin balance. Due to the RC time constant of the power supply and the inductance of the magnets, a delay of 800 ms occurs between a field being commanded and a steady state magnetic field being generated. This delay exists whenever a field switch is instigated, regardless of the beginning and ending field points. Once 8 Gauss is reached, a 100 ms noisy RF pulse centered at 7.83 MHz is applied to the atoms to ensure that a 50:50 mixture of the two lowest hyperfine ground states endures in the FORT.

After RF spin balance is complete, the magnetic field is ramped to the Feshbach at 834 Gauss in 800 ms. Once the desired field is reached, the atoms are held in the forward and retrorefected CO_2 beams for an additional 500 ms before the chopper mirror is lowered, adiabatically extinguishing the retrorefected beam as the atoms evaporate. The collection of atoms is then allowed to freely evaporate for a few seconds in the single beam FORT before forced evaporation commences. The single beam FORT has a much weaker potential than the double beam FORT, but much less position noise, allowing ultra-cold temperatures to be achieved. After free evaporation, approximately 1 million atoms remain in the FORT at a temperature of roughly 50 μK.

The remainder of the cooling results as a consequence of forced evaporation. Using the AO in the CO_2 beam path, the power of the CO_2 beam is lowered following the trajectory given in Section 3.4.3 to a final trap depth that is approximately 1000 times smaller than full trap depth. Lowering the trap usually can be accomplished in only 1.5 seconds. Collisions between the atoms result in some atoms being ejected from the trap, removing energy. Cooling results from this process as the remaining atoms left in the trap rethermalize to a lower tem-

perature. After reaching the lowest trap depth, the power is raised in the CO_2 beam as the trap is adiabatically recompressed to a user-defined final value. This process typically results in a degenerate sample of approximately 1.6×10^5 atoms that can now be used to conduct experiments.

If a noninteracting sample is desired, the foregoing procedure can be followed, with a few minor changes. Since the collision rate vanishes at 528 Gauss where the scattering length goes to zero, evaporative cooling is impossible at this field. But at 300 Gauss, a sufficiently large negative scattering length exists that can facilitate efficient evaporative cooling. Therefore free and forced evaporation occur at that field, and only after recompression is the field switched to 528 Gauss. However, the duration of forced evaporation is up to an order of magnitude longer at 300 Gauss versus 834 Gauss, where the collision cross section is unitary limited, due to the smaller collision rate [79, 81]. It is also difficult to attain the lowest temperatures at 300 Gauss, so the cooling methods are far from equivalent. But cooling must be done at a magnetic field below the zero crossing, since a degenerate sample created at 834 Gauss will be destroyed due to the adiabatic formation of molecules [44] and subsequent molecular relaxation [96] during a magnetic field sweep down to 528 Gauss.

4.8.2 Measurement of trap oscillation frequencies

Once a degenerate gas is prepared, it can be manipulated in many different ways depending upon what experiment needs to be done. For almost all experiments it is necessary to know the oscillation frequencies of the atoms in the trap. For example, these frequencies set the scale for the size and energy of the trapped gas and also dictate at what frequency it will oscillate when brought out of equi-

librium. Therefore it is crucial to accurately characterize the trap by obtaining the trap frequencies. The trap frequencies can be measured through parametric resonance, breathing modes, and through radial sloshing modes. Each method has advantages and drawbacks, which will be discussed in the following sections.

Parametric resonance

The most accurate and model independent way to measure the trap frequencies is through parametric resonance. Parametric resonance occurs in a mechanical system when the spring constant of an oscillator is periodically modulated. When the modulation frequency is twice the natural frequency, a resonance occurs that couples energy into the system [97]. The harmonic trap potential for the atoms can be modeled in an equivalent way. By amplitude modulating the CO_2 laser beam, the trap oscillation frequencies can be periodically modified, resulting in energy being coupled into the cloud, causing it to heat. Therefore, by measuring the cloud size as a function of modulation frequency, the trap frequencies can be determined.

To perform this experiment, the gas is evaporatively cooled at approximately 300 Gauss and then recompressed to the desired final trap depth. After recompression, the trap depth is modulated at a particular frequency by modulating the power of the CO_2 beam using the AO. Following the trap modulation, the magnetic field is ramped to the zero crossing at 528 Gauss and the cloud is imaged. By repeating this procedure for different modulation frequencies, plots such as Figure 4.17 and Figure 4.18 can be produced. The plot in Figure 4.17 is for the radial frequencies (ω_y, ω_z) of the cigar shaped optical trap, which are in the tight confinement direction. The coordinate system used for the frequencies is

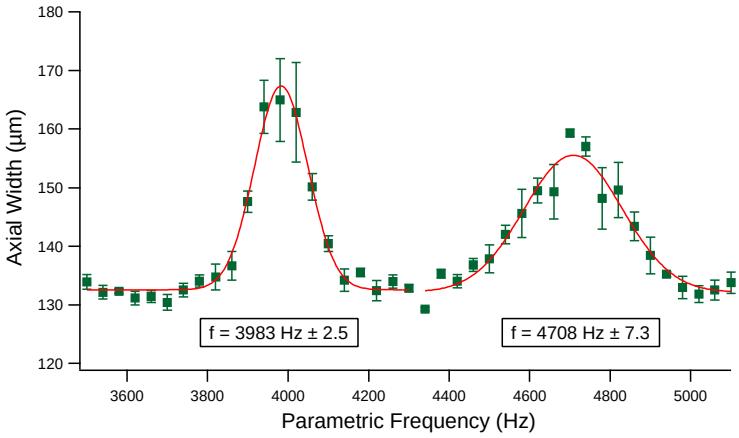

Figure 4.17: Plot of the axial (x) width of the cloud versus parametric drive frequency. The solid circles are the experimental data and the curves are gaussian fits to the data. This data set provides the parametric frequencies for the radial (tight) confinement direction of the optical trap. The data was taken for an optical trap depth equal to 20% of the maximum depth.

the same as defined in Figure 4.12. This particular data set is for an optical trap depth equal to 20% of the maximum depth. The peaks in the measured axial width indicate the frequencies at which energy was coupled into the gas through parametric resonance. There are two peaks in the data due to the slight ellipticity in the beam. To couple in the energy, a parametric modulation signal with an amplitude of 5 mV peak-to-peak was first put through a 15 dB attenuator, then summed with a DC signal that determines the optical trap depth through the AO. This sine wave is applied for a duration of 1 second to allow for a reasonable energy input.

A interesting thing to notice about Figure 4.17 is that a width measurement in the *axial* direction of the cigar shaped optical trap, which is along the Rayleigh length, is used for parametric resonance in the *radial* direction. The technical reason behind this stems from the fact that the axial direction can be imaged

without expanding the cloud, making the widths easier to measure due to the higher absorbtion. But it is not inherently obvious that the energy coupled into the gas through parametric resonance in the radial direction would result in an increase in the axial direction of the cloud. In fact if the parametric resonance was done at 528 Gauss where the gas in noninteracting, there would be no cross-relaxation between the different directions in the trap and a radial excitation would not produce a change in the axial width. Therefore the modulation of the trap is done at 300 Gauss, where the gas is weakly interacting, so energy can be transferred between all three directions. This also allows for the observation of the second peak in Figure 4.17, which would be impossible to measure in a noninteracting gas since it is in the same direction of the camera, and therefore a change in size in that direction cannot be imaged.

An experiment to determine the axial parametric frequency, ω_x, can be performed in a similar manner to the radial frequencies. In Figure 4.18 the data for the axial parametric frequency is presented for the same 20% trap. In this case the parametric modulation signal has an amplitude of 22 mV peak-to-peak and is applied for 4 seconds. The parametric amplitude and time duration are much larger than the radial data set, due to the difficulty of coupling in energy at the much lower axial frequency. The same peak in the axial width is observed, which is fit with a gaussian function to determine the frequency.

Parametric resonance provides a very accurate measurement of the trap oscillation frequencies in all three principle directions. Unfortunately, data acquisition for this experiment is very time consuming, and can take up to 5 hours to complete. Each trap depth has a unique combination of modulation parameters, which must be found using trial and error. In the next section a different method

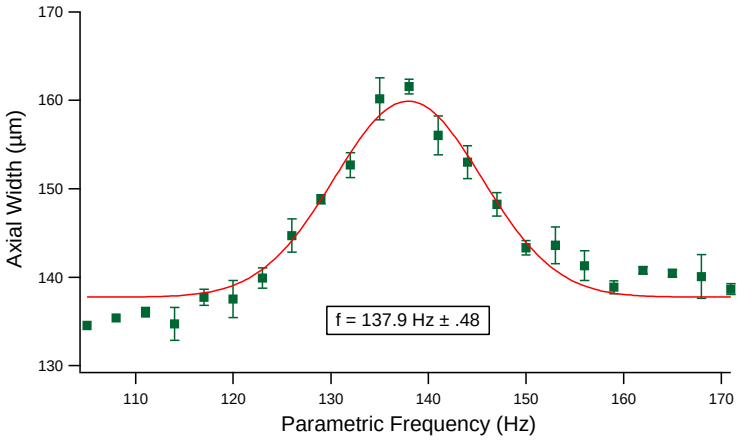

Figure 4.18: Plot of the axial (x) width of the cloud versus parametric drive frequency. The solid circles are the experimental data and the curves are gaussian fits to the data. This data set provides the parametric frequencies for the axial confinement direction of the optical trap. The data was taken for an optical trap depth equal to 20% of the maximum depth.

is presented for obtaining the trap frequencies that reduces the experimental time to approximately 30 minutes, which allows for the oscillation frequencies to be checked on a daily basis, if desired.

Radial and axial breathing modes

An additional tool that is available to measure the trap frequencies is the breathing mode [63, 98]. A breathing mode is a collective oscillation of the atoms in the trap where the cloud appears to rhythmically expand and contract at a specific frequency. The oscillation can be produced in either the radial or the axial direction of the optical trap. A radial breathing mode can be excited by the release and recapture method [51], where the trapping potential is extinguished for a very short period of time allowing the gas to slightly expand. When the trap is reinstated, the expanded cloud is out of equilibrium with the trapping potential,

causing it to oscillate.

An axial breathing mode can be excited in two different ways. The first uses the same release and recapture method employed for the radial breathing mode, except in the axial case the gas is allowed to expand for a duration up to an order of magnitude longer, which imparts a substantial amount of energy to cloud. At first this produces the expected radial breathing mode, which quickly damps out. But when the large amount of energy is transferred to the axial direction through cross-relaxation, the result is an explosion of the axial width, which produces a large amplitude axial breathing mode. This is the equivalent of hitting the gas with a hammer and exciting all the breathing modes of the gas simultaneously. The second method, which excites an oscillation that is more of a perturbation, involves recompressing the gas after forced evaporation very quickly, typically less than 150 milliseconds. This recompression is slow compared to the radial trap frequencies, but is fast compared to the axial frequency. Therefore the radial oscillation is not excited, but the axial breathing mode is produced with a typical amplitude modulation of 5%.

The oscillation frequencies of the breathing modes are not equal to the trap frequencies, but are proportional to them. In the hydrodynamic regime in the vicinity of the Feshbach resonance at 834 Gauss, a strongly interacting Fermi gas is well described by the equations of ideal hydrodynamics [40]. By treating the collective oscillations as a perturbation in these equations, a solution for the breathing mode frequencies can be obtained. The frequency can be shown to depend upon the form of the equation of state, and for a Fermi gas in a cylindrically symmetric cigar shaped trap the radial and the axial breathing mode frequencies are $\omega = \sqrt{10/3}\,\omega_\perp$ and $\omega = \sqrt{12/5}\,\omega_x$ respectively [99]. I have

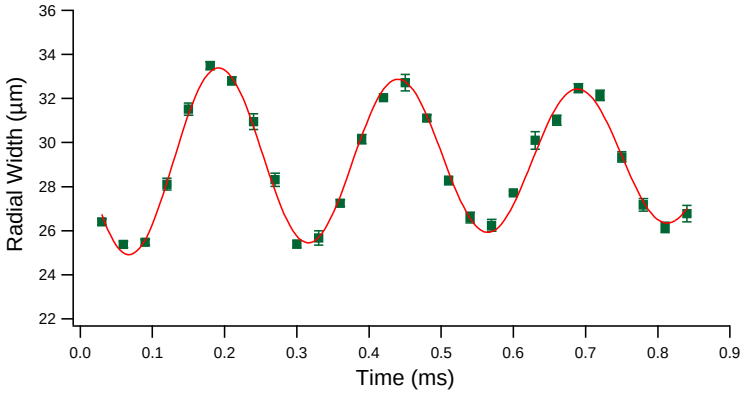

Figure 4.19: Plot of the radial breathing mode oscillation of a strongly interacting Fermi gas. The data was taken for an optical trap depth equal to 20% of the maximum depth. The solid circles are the data while the solid curve is a fit to the data of a damped sine wave. The measured frequency of oscillation is 4024 Hz $\pm$ 19, which corresponds to a $\omega_\perp$ of $2\pi \times 2203$ Hz.

defined the geometric mean of the two radial frequencies as $\omega_\perp = \sqrt{\omega_y \omega_z}$ and identified the axial frequency as ω_x.

An example of a radial breathing mode at 834 Gauss is given in Figure 4.19. The data in the figure was taken at an optical trap depth equal to 20% of the maximum depth, the same condition as in parametric resonance (Figure 4.17). In this data set the trap was extinguished for 20 microseconds in order to create the oscillation. A fit to the data yields a hydrodynamic frequency of $\omega = 2\pi \times 4024$ Hz corresponding to $\omega_\perp = 2\pi \times 2203$ Hz based on the hydrodynamic theory. Taking the geometric mean of the radial frequencies measured during parametric resonance results in $\omega_\perp = 2\pi \times 2165$ Hz, a difference of only 1.7% from the frequency obtained from the radial breathing mode. This value for the frequency was obtained by neglecting nonlinear effects in the trapping potential such as anharmonicity and a deviation from cylindrical symmetry. By including these effects, closer agreement can be found between parametric resonance and the

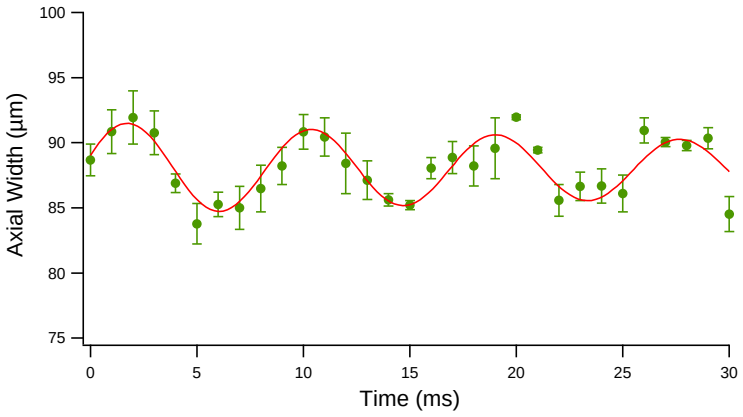

Figure 4.20: Plot of the axial breathing mode oscillation of a strongly interacting Fermi gas. The data was taken for an optical trap depth equal to 20% of the maximum depth. The solid circles are the data while the solid curve is a fit to the data of a damped sine wave. The measured frequency is 112.6 Hz $\pm$ 0.9, which corresponds to a ω_x of $2\pi \times 72.7$ Hz.

radial breathing mode [63, 65]. Therefore the radial breathing mode is a very quick and accurate method of obtaining a value for $\omega_\perp$. But unfortunately this method is not sensitive to the absolute frequency of ω_y and ω_z, only $\omega_\perp$. Therefore if it is necessary to know these frequencies individually, parametric resonance must be performed.

As described above, the axial breathing mode can be excited by recompressing the trap quickly with respect to the axial trap frequency. An example of data acquired through this procedure is given in Figure 4.20. The data in the figure was taken at 834 Gauss and with an optical trap depth equal to 20% of the maximum depth, the same condition as in parametric resonance (Figure 4.18). A fit to the experimental data gives a hydrodynamic frequency of $\omega = 2\pi \times 112.6$ Hz. Converting this frequency into the axial trap oscillation frequency yields $\omega_x = 2\pi \times 72.7$ Hz since the two frequencies are related by $\omega_{fit} = \sqrt{12/5}\,\omega_x$. The frequency obtained through parametric resonance can be shown to be $\omega_x =$

$2\pi \times 71.1$ Hz after the contribution to the total frequency due to ω_{Bx}, which is magnetic field dependent, is adjusted from the parametric resonance field of 300 Gauss to the breathing mode field of 834 Gauss. This difference in frequency between the two methods is only 2.2%, but can be improved if anharmonicity is taken into account. Therefore the axial breathing mode is an efficient way of obtaining the axial trap frequency.

Radial sloshing mode

An additional way to measure the radial trap oscillation frequencies is trough the radial sloshing mode. A sloshing mode is a rigid body oscillation that results if the optical trap center is abruptly shifted. After the trap center has been shifted, the atom cloud is out of equilibrium with the new trap location, and proceeds to oscillate about the new equilibrium position, "sloshing" back and forth. This can be accomplished experimentally by suddenly shifting the CO_2 beam position in the radial direction using the AO. This is also the same method used to create a rotation in the gas, and a detailed description of the procedure is provided in Section 5.3.1.

A plot of such an experiment is given in Figure 4.21. Similar to all the previous experiments presented in Section 4.8.2, this experiment was done at an optical trap depth equal to 20% of the maximum depth and at 834 Gauss. In this particular experiment the trap potential was shifted in the y-direction of the trap, which corresponds to the axial direction of the magnetic field. Therefore, the measured frequency will be ω_y and should be equal to one of the radial parametric frequencies given in Figure 4.17. A fit of a damped sine wave to the experimental data yields a sloshing frequency of $\omega_y = 2\pi \times 2381$ Hz. This is only 1.1% away

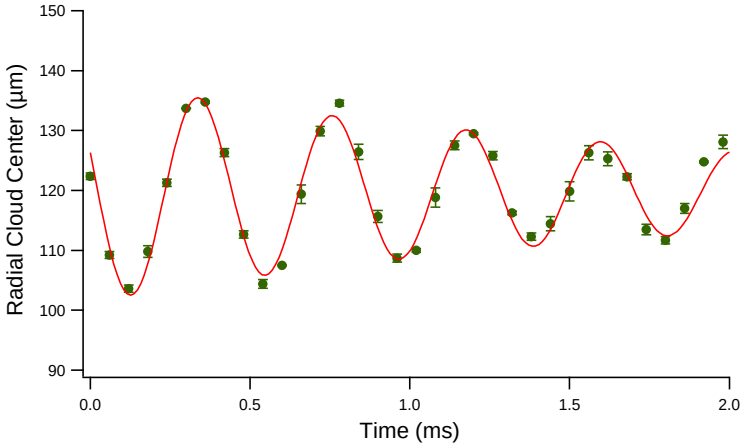

Figure 4.21: Plot of the radial sloshing mode of a strongly interacting Fermi gas. The data was taken for an optical trap depth equal to 20% of the maximum depth. The solid circles are the data while the solid curve is a fit to the data of a damped sine wave. The measured frequency of oscillation is 2381 Hz ± 11.

from the second parametric peak in Figure 4.17, allowing the direction of the parametric peaks to be discerned.

Chapter 5

Rotation and Expansion of a Unitary Fermi Gas

One of the things that I have always enjoyed about studying quantum mechanics is that it never fails to surprise me. In particular, it always interests me to learn about the rich dynamics demonstrated by quantum systems that are quite unlike their classical counterparts, and in some cases, are completely counterintuitive. Many such examples can be found in superfluids and, in particular, the situation that occurs when a superfluid is put into rotation. For example, if a cylindrical container of normal fluid is put under rotation at a constant rate, v_n, it will begin to rotate uniformly at the same speed as its container after an initial spin up time. The fluid in this configuration therefore has vorticity since the fluid close to the edges of the container has a greater translational velocity than the fluid near the center. It is also said to be *rotational* since every particle in the fluid is rotating at the same angular velocity. As a result, the requirement for vorticity can be written as $\nabla \times v \neq 0$, since the curl of a uniformly rotating velocity field is nonzero.

When uniform rotation is attempted in a superfluid, however, a completely different scenario develops that is quite unlike its classical counterpart. The particles in a superfluid can all be described by the same wavefunction, and the gradient of the phase of the wavefunction determines the superfluid velocity, $v_s = \nabla\psi$, where

ψ is the phase [4]. Since $\nabla \times (\nabla\psi) = 0$ for all scalar functions ψ, all superfluids are *irrotational* since their vorticity is by definition zero. For an irrotational superfluid, rotation can only be introduced in the form of quantized vortices [21]. In general, irrotational flow is only required to occur in the flow of a superfluid, with no restriction given to a normal fluid.

In this Chapter, the astonishing result of a *normal* fluid demonstrating irrotational flow when put under rotation is presented. A hydrodynamic theory for the rotation and expansion of a strongly interacting Fermi gas is introduced in Section 5.1. This theory is valid for a strongly interacting Fermi superfluid at zero temperature in the absence of viscosity. It is used to predict the value of the angle and aspect ratio of the cloud during the expansion. The hydrodynamic theory is compared to a ballistic theory that is derived in Section 5.2, and the differences between them are highlighted. In Section 5.3 a detailed description of the methods involved for experimentally creating and analyzing a cloud that is rotating and expanding simultaneously is presented. After analyzing the data, it is shown that a strongly interacting Fermi gas exhibits irrotational flow in not only the superfluid regime, but also in the normal fluid regime. These observations are further bolstered through measurements of the moment of inertia, which is discussed in Section 5.4.

5.1 Hydrodynamic theory

A superfluid can be considered a perfect fluid since it has a vanishing viscosity at zero temperature and can flow without dissipation. Therefore the governing dynamics of a superfluid are best described using the Euler equation for ideal

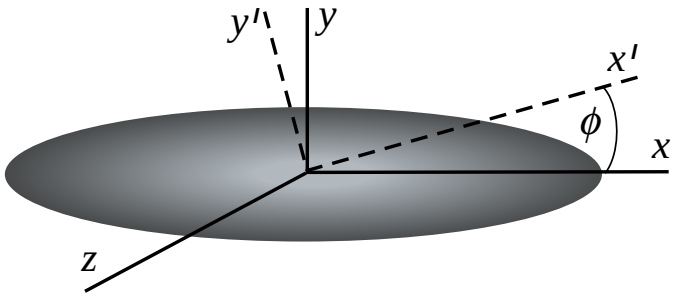

Figure 5.1: Coordinate system used throughout this chapter where the axial direction is defined as the x-direction. The primed coordinates denote a rotation of an angle ϕ about the z-axis.

hydrodynamics, along with the equation of continuity. Using these two equations the stream velocity, $\mathbf{v}(\mathbf{r}, t)$, and the number density, $n(\mathbf{r}, t)$, can be fully described as a function of position, $\mathbf{r}$, and time, t.

This section details the hydrodynamic theory that was developed to describe how a strongly interacting Fermi superfluid at zero temperature expands when it is released from a trap with finite angular velocity. A theory of this form was first pioneered by Stringari and collaborators for Bose-Einstein condensates [100,101], and subsequently was experimentally verified [102,103]. What separates the present work from what has been previously done is the extension of the theory to include the equation of state for a strongly interacting Fermi gas, and the inclusion of terms to account for rigid body rotation as well as irrotational flow during expansion.

The coordinate system that will be used throughout this section is presented in Figure 5.1. The axial (long) direction is defined as the x-axis and the radial (short) directions are the y-axis and z-axis. All rotations are assumed to occur in the x-y plane producing angular momentum about the z-axis. The coordinate

system in Figure 5.1 follows the geometry of the optical trap that confines the atoms, and is the most natural coordinate system to use for the theory since the angle of rotation of the principal axes of the cloud, ϕ, can be defined with respect to the x-axis. The development of the hydrodynamic theory begins by deriving the equations for hydrodynamic expansion in the absence of rotation in Section 5.1.1. In Section 5.1.2 the effects of rotation are included in the theory and equations for the physical observables of the angle and aspect ratio are given.

5.1.1 Expansion without rotation

A strongly interacting Fermi gas in the superfluid regime obeys the equations of ideal hydrodynamics [18]. Therefore a complete description of the expansion dynamics can be obtained through the use of the Euler equation and the equation of continuity. Before we get to the case of a gas that is rotating as well as expanding, it is instructive to look at the simpler case of the hydrodynamic expansion of a gas that is released from a trap without rotation. This will lend familiarity with the equations of motion and solution procedures without the added complexity that comes with the incorporation of rotation. The Euler equation for a gas in an external potential V_{ext} takes the form

$$\frac{\partial \mathbf{v}}{\partial t} + (\mathbf{v} \cdot \boldsymbol{\nabla})\, \mathbf{v} = -\frac{1}{mn} \boldsymbol{\nabla} P - \frac{1}{m} \boldsymbol{\nabla} V_{ext} \tag{5.1}$$

where $\mathbf{v}$ is the stream velocity, n is the density, m is the particle mass, and P is the pressure. This equation can be interpreted as providing force balance for a gas in an external potential. Assuming the gas follows a polytropic equation of state, the pressure can be written as a power law in the density, i.e. $P \propto n^{\gamma+1}$

were γ is a constant. Using this assumption, the first term on the right hand side of equation (5.1) becomes $\frac{1}{m}\nabla c n^{\gamma}$, where c is a constant. Plugging this expression into equation (5.1) produces

$$\frac{\partial \mathbf{v}}{\partial t} + \boldsymbol{\nabla}\left(\frac{v^2}{2} + \frac{V_{ext}}{m} + \frac{c\, n^{\gamma}}{m}\right) - \mathbf{v} \times (\boldsymbol{\nabla} \times \mathbf{v}) = 0, \tag{5.2}$$

where the fact that $\boldsymbol{\nabla}(v^2/2) = \mathbf{v} \times (\boldsymbol{\nabla} \times \mathbf{v}) + (\mathbf{v} \cdot \boldsymbol{\nabla})\, \mathbf{v}$ has been used to simplify the expression.

Many of the interesting dynamics exhibited by trapped gases can be modeled using equation (5.2) such as breathing modes [63, 66] and scissors modes [68]. In order to find a solution that satisfies equation (5.2), an ansatz for $\mathbf{v}(\mathbf{r}, t)$ and $n(\mathbf{r}, t)$ must be formulated. In a later part of this thesis we will be most interested in applying the equations of hydrodynamics to the limiting case of a zero temperature Fermi gas in the strongly interacting regime. In this approximation the constants in equation (5.2) become $c = (1+\beta)\,\frac{\hbar^2(3\pi^2)^{2/3}}{2m}$ and $\gamma = 2/3$. The term β is the unitary gas parameter and accounts for the energy shift due to the mean field.

In deriving the correct form for $n(\mathbf{r}, t)$, it is instructive to look at the stationary solutions of equation (5.2). A stationary solution for the case of no rotation corresponds to the situation of a static density in the trap with no velocity flow. Therefore, a stationary solution can be found by setting $\mathbf{v}$ equal to zero and assuming the external potential is a harmonic trap, $V_{ext} = \frac{m}{2}(\omega_x^2 x^2 + \omega_y^2 y^2 + \omega_z^2 z^2)$, where ω_x, ω_y, and ω_z are the harmonic trap frequencies. This leads to the equation

$$\boldsymbol{\nabla}\left(\frac{1}{2}\left(\omega_x^2 x^2 + \omega_y^2 y^2 + \omega_z^2 z^2\right) + (1+\beta)\,\frac{\hbar^2(3\pi^2)^{2/3}}{2m^2} n^{2/3} - \frac{\mu}{m}\right) = 0, \tag{5.3}$$

where we have added a constant $\frac{\mu}{m}$ since the gradient of this constant is equal to zero. By setting the quantity in parenthesis equal to zero, an equation for the density

$$n(\mathbf{r}) = \frac{1}{3\pi^2}\left(\frac{2m\mu}{(1+\beta)\,\hbar^2}\right)^{3/2}\left(1 - \frac{m\omega_x^2}{2\mu}x^2 - \frac{m\omega_y^2}{2\mu}y^2 - \frac{m\omega_z^2}{2\mu}z^2\right)^{3/2}, \qquad (5.4)$$

is obtained. Equation (5.4) describes the density of a zero-temperature Thomas-Fermi distribution, where the coordinates, $x_i = x, y, z$, range from $-2\mu/(m\omega_{x_i}^2) \leq x_i^2 \leq 2\mu/(m\omega_{x_i}^2)$.

An expression for μ, which can be interpreted as the chemical potential, can be obtained by integrating the density in equation (5.4) over the physical size of the trap, which will yield the total number of atoms, N. Writing the integral in spherical coordinates produces

$$N = \int n(\mathbf{r})\, d^3\mathbf{r} = \frac{32}{3\pi\,\omega_x\,\omega_y\,\omega_z}\left(\frac{\mu^2}{(1+\beta)\,\hbar^2}\right)^{3/2}\int_0^1 d\tilde{r}\,\left(1-\tilde{r}^2\right)^{3/2}\tilde{r}^2. \qquad (5.5)$$

The integral over $\tilde{r}$ equals $\pi/32$ so we can rearrange equation (5.5) and solve for μ to obtain

$$\mu = \sqrt{1+\beta}\,\hbar\,\overline{\omega}\,(3N)^{1/3} \equiv \sqrt{1+\beta}\,E_F, \qquad (5.6)$$

where I have defined $\overline{\omega} \equiv (\omega_x\,\omega_y\,\omega_z)^{1/3}$, which is the geometric mean of the trap frequencies, and $E_F \equiv \hbar\,\overline{\omega}\,(3N)^{1/3}$. Not surprisingly, equation (5.6) states that the chemical potential at the center of the trap is equal to the Fermi energy, E_F, if the interactions are turned off ($\beta = 0$). Using equation (5.6), the desired static density in equation (5.4) can be written in terms of various constants, the atom number N, and the trap frequencies ω_x, ω_y, and ω_z.

Now the the static form of the density has been determined, a time dependent form needs to be defined. After the trap is extinguished during an expansion experiment, the density becomes a dynamic quantity, so we need to re-write equation (5.4) with time dependent coefficients as

$$n(\mathbf{r},t) = n_0(t)\left(1 - \frac{x^2}{\sigma_x^2(t)} - \frac{y^2}{\sigma_y^2(t)} - \frac{z^2}{\sigma_z^2(t)}\right)^{3/2}. \tag{5.7}$$

We can identify $n_0(t)$ as the time dependent density at the center of the trap, along with $\sigma_x(t)$, $\sigma_y(t)$, and $\sigma_z(t)$ as the time dependent Thomas-Fermi radii. This makes physical sense since the density at the center of the trap, n_0, will decrease as the expansion progresses. Likewise the widths of the cloud, σ_x, σ_y, and σ_z, are increasing functions of time after the trap is extinguished, so it makes sense to make them time dependent parameters. In addition to the ansatz for the density, we need to have initial conditions for the time dependent coefficients. The initial conditions on the density at the center of the trap along with the Thomas-Fermi radii can be obtained from their static values given in equation (5.4) and expressed as

$$n_0(0) = \frac{1}{3\pi^2}\left(\frac{2mE_F}{\sqrt{1+\beta}\hbar^2}\right)^{3/2} \tag{5.8}$$

$$\sigma_i^2(0) = \frac{2\sqrt{1+\beta}E_F}{m\omega_i^2}, \tag{5.9}$$

where $i = x$, y, and z.

Along with an anstaz for the density, it is also necessary to have an ansatz for the velocity field in order to describe the expansion dynamics. The simplest velocity field to try is one that is first order in the coordinates and doesn't involve

cross terms. This will work for release from a harmonic trap, since this type of potential is also second order in the coordinates. However, it will be shown in later in Section 5.1.2 that the cross terms, such as xy, are essential for modeling the rotation of the gas during expansion. Using the aforementioned criteria, a reasonable form for the velocity field is

$$\mathbf{v}(\mathbf{r},t) = \frac{1}{2}\boldsymbol{\nabla}\left(\alpha_x(t)\,x^2 + \alpha_y(t)\,y^2 + \alpha_z(t)\,z^2\right), \tag{5.10}$$

which, by construction, is a purely irrotational velocity field since the curl of this equation is zero. The three time dependent parameters $\alpha_x(t)$, $\alpha_y(t)$, and $\alpha_z(t)$ will be used to descibe the dynamics of the velocity field after the trap is extinguished. By inserting the ansatz for the density and velocity field presented in equations (5.7) and (5.10) into the Euler equation and the equation of continuity, a system of seven coupled partial differential equations can be constructed. A solution to these equations can be obtained by simultaneously solving all seven numerically.

In order to solve for the expansion dynamics, the trapping potential needs to be extinguished. This can be accomplished by setting V_{ext} equal to zero in the Euler equation given by equation (5.2). This yields the simplified expression

$$\frac{\partial \mathbf{v}}{\partial t} + \boldsymbol{\nabla}\left(\frac{v^2}{2} + \frac{c\,n^{2/3}}{m}\right) - \mathbf{v}\times(\boldsymbol{\nabla}\times\mathbf{v}) = 0, \tag{5.11}$$

where the term $\mathbf{v}\times(\boldsymbol{\nabla}\times\mathbf{v}) = 0$ since the assumed velocity field from equation (5.10) is purely irrotational ($\boldsymbol{\nabla}\times\mathbf{v} = 0$). Equation (5.11), along with the equation of continuity

$$\frac{\partial n}{\partial t} + \boldsymbol{\nabla}\cdot(n\mathbf{v}) = 0 \tag{5.12}$$

can be used to completely model the expansion dynamics. A system of equations can be constructed by inserting the ansazts $n(\mathbf{r},t)$ and $\mathbf{v}(\mathbf{r},t)$, equations (5.7) and (5.10) respectively, into equations (5.11) and (5.12). Substitution into the Euler equation yields the vector expression

$$\sum_j \left(\dot{\alpha_j} + \alpha_j^2 - \frac{2c}{m\sigma_j^2} n_0^{2/3} \right) j\, \hat{\mathbf{x}}_j = 0 \tag{5.13}$$

where the sum has three terms for the $j = x,\ y,$ and z directions. The $\hat{\mathbf{x}}_j$ in equation (5.13) are the unit vectors for each respective direction. Since the dynamics in each direction will evolve independently, three differential equations can be obtained from equation (5.13) by setting each vector component equal to zero separately. This produces the system of equations

$$\dot{\alpha_x} + \alpha_x^2 - \frac{2\mu_0}{m\sigma_x^2} = 0 \tag{5.14}$$

$$\dot{\alpha_y} + \alpha_y^2 - \frac{2\mu_0}{m\sigma_y^2} = 0 \tag{5.15}$$

$$\dot{\alpha_z} + \alpha_z^2 - \frac{2\mu_0}{m\sigma_z^2} = 0 \tag{5.16}$$

were the fact that the time dependent chemical potential at the center of the trap, $\mu_0(t) = cn_0^{2/3}(t)$, has been used to create equations that are as simple as possible. These differential equations describe the time evolution of the velocity field. Before the trap is turned off and the gas begins to expand, the stream velocity is zero. Therefore, the initial conditions on the parameters that describe the velocity field are $\alpha_x(0) = \alpha_y(0) = \alpha_z(0) = 0$. Equations (5.14) through (5.16) constitute three of the seven equations that need to be solved for to characterize the expansion dynamics.

The other four equations can be obtained by substitution of $n(\mathbf{r},t)$ and $\mathbf{v}(\mathbf{r},t)$ into the equation of continuity defined by equation (5.12). The equation of continuity is a scalar equation, so after substitution of $n(\mathbf{r},t)$ and $\mathbf{v}(\mathbf{r},t)$ there are no vector components to independently set equal to zero, as was done for the Euler equation. But all the terms that do result from the continuity equation will be multiplied by either 1, x^2, y^2, or z^2. Therefore by setting powers of the coordinates equal to zero separately, we can formulate the remaining differential equations. After performing the algebra, the result can be shown to be

$$\dot{\mu_0} + \frac{2}{3}\,\mu_0\,(\alpha_x + \alpha_y + \alpha_z) = 0 \tag{5.17}$$

$$\dot{\sigma_x} - \sigma_x \alpha_x = 0 \tag{5.18}$$

$$\dot{\sigma_y} - \sigma_y \alpha_y = 0 \tag{5.19}$$

$$\dot{\sigma_z} - \sigma_z \alpha_z = 0. \tag{5.20}$$

An interesting observation that can be made about these equations is how weakly dependent the dynamics are on the equation of state. The chemical potential that has been used is of the form $\mu = cn^{\gamma}$, with $\gamma = 2/3$. With an equation of this type, the constant c can completely be scaled out by changing variables to $\tilde{\mu}(t) = \mu_0(t)/\mu_0(0)$ and $\tilde{\sigma_i}(t) = \sigma_i(t)/\sigma_i(0)$. This change of variables simply scales the time dependent chemical potential and cloud radii by their initial values. In addition, the constant γ only shows up in equation (5.17) as the prefactor 2/3 in the second term in the equation. Using these substitutions the seven equations

of motion in the $i = x, y, z$ directions can be shown to be

$$\dot{\tilde{\mu}} + \gamma\,\tilde{\mu}\,(\alpha_x + \alpha_y + \alpha_z) = 0 \tag{5.21}$$

$$\dot{\tilde{\sigma}}_i - \tilde{\sigma}_i \alpha_i = 0 \tag{5.22}$$

$$\dot{\alpha}_i + \alpha_i^2 - \frac{\tilde{\mu}}{\tilde{\sigma}_i{}^2}\,\omega_i^2 = 0 \tag{5.23}$$

where the initial conditions for $\tilde{\mu}$ and $\tilde{\sigma}_i$ are defined to be

$$\tilde{\mu}(0) = \tilde{\sigma}_i(0) = 1. \tag{5.24}$$

It is apparent by looking at these equations that the dynamics are completely driven by the trap frequencies, which determine the initial size of the gas in the trap and also dictate the expansion time scale. Actually, it can be shown that the above equations describe a gas that expands by a scale transformation [104]. This means that the time dependent Thomas-Fermi radii are related to their initial sizes by $\sigma_i(t) = b_i(t)\sigma_i(0)$, where the formulas that determine the $b_i(t)$ depend only on the trap frequencies.

By simultaneously solving equations (5.21) through (5.23) numerically, a solution for the evolution of the Thomas-Fermi radii, $\sigma_i(t)$, with time can be found. This is advantageous since the radii of the cloud are directly measurable quantities during an experiment. Since our trapping potential creates a highly elongated cigar-shaped cloud, a useful quantity to define is the aspect ratio, which is the ratio of the Thomas-Fermi radius in the short direction, σ_y, to the long direction, σ_x, $\lambda = \sigma_y/\sigma_x$. A plot of the measured aspect ratio upon expansion in the absence of rotation is given in Figure 5.2. Since the trap is highly cigar-shaped, the aspect

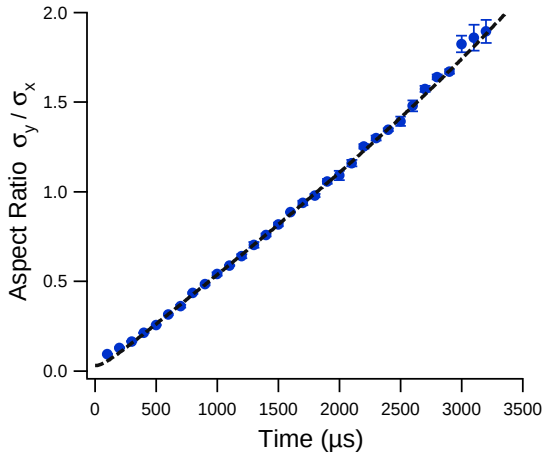

Figure 5.2: Aspect ratio plotted as a function of time for a strongly interacting Fermi gas close to the ground state with no rotation. The solid blue circles are data and the black dashed curve is the solution to the equations presented in this chapter with the appropriate initial conditions.

ratio starts off small and monotonically increases with time. As the aspect ration passes unity, the cloud becomes longer in the radial direction than it initially was in the axial direction. This is a hallmark of hydrodynamic expansion and is an example of elliptic flow [18]. As is evidenced by the plot, the fit of the data to the theory is exceptionally good.

5.1.2 Expansion with rotation

The previous section focused on the hydrodynamic expansion of a strongly interacting Fermi gas that was not initially rotating. This section will focus on how those dynamics change if the gas is released with an initial angular velocity Ω_0.

For rotation in the laboratory frame, the Euler equation and the equation of continuity will have the same form as equations (5.11) and (5.12) that were used for the case of no rotation. Therefore to incorporate rotation into the equations

of motion it is necessary to modify the ansatz for the stream velocity, $\mathbf{v}(\mathbf{r},t)$, and the density, $n(\mathbf{r},t)$. The specific case of a gas rotating in the x-y plane about the z axis can be considered without loss of generality. In this case the stream velocity is easily modified by including cross terms (xy) to account for the rotation. After release from a harmonic trap, both rotational and irrotational dynamics may result. Therefore an irrotational velocity field, $v_{irr}(x,y,t) = \alpha(t)\nabla xy$, and a rotation part, $v_{rot}(x,y,t) = \mathbf{\Omega}(t) \times \mathbf{r}$ need to be included in $\mathbf{v}(\mathbf{r},t)$. This changes the velocity field in equation (5.10) to

$$\mathbf{v}(\mathbf{r},t) = \frac{1}{2}\,\boldsymbol{\nabla}\left(\alpha_x(t)\,x^2 + \alpha_y(t)\,y^2 + \alpha_z(t)\,z^2 + 2\alpha(t)\,xy\right) + \mathbf{\Omega}(t) \times \mathbf{r}, \qquad (5.25)$$

where $\mathbf{\Omega}(t) = \Omega(t)\hat{z}$ for rotation in the x-y plane. This is the most general form for a velocity field that can support rotation, while still remaining linear in the coordinates.

It can be shown for steady state conditions that in the frame where the principal axes of the cloud are rotating at $\mathbf{\Omega}$, the spatial density maintains it's static shape, with modified frequencies [100]. Therefore it is reasonable to assume that the spatial density in the lab frame will have the same form as equation (5.7), with an additional cross term xy to account for the rotation

$$n(\mathbf{r},t) = n_0(t)\left(1 - \frac{x^2}{\sigma_x^2(t)} - \frac{y^2}{\sigma_y^2(t)} - \frac{z^2}{\sigma_z^2(t)} - a(t)\,xy\right)^{3/2}. \qquad (5.26)$$

Now that we have the trial functions for $\mathbf{v}(\mathbf{r},t)$ and $n(\mathbf{r},t)$, equations (5.25) and (5.26), we can follow the same procedure detailed in Section 5.1.1 to find the equations of motion for the ten time dependent coefficients $\alpha_i(t)$, $\sigma_i(t)$, $n_0(t)$, $a(t)$, $\alpha(t)$, and $\Omega(t)$. It is somewhat unnecessary to solve for the density at the

center of the trap, $n_0(t)$, as a function of time since in the end we are interested in creating expressions for the experimental observables, such as the angle of the principle axes of the cloud and the aspect ratio. It will be shown that these expressions do not depend upon $n_0(t)$. Therefore in order to make the equations somewhat more tractable, we can change variables from $n_0(t)$ to $\mu_0(t)$ using the relation $\mu_0(t) = cn_0^\gamma(t)$, where $\gamma = 2/3$ for a zero temperature gas.

The first step is to use the equation of continuity to get the first half of the equations we need. Inserting $\mathbf{v}(\mathbf{r}, t)$ and $n(\mathbf{r}, t)$ from equations (5.25) and (5.26) into the equation of continuity given by equation (5.12) from Section 5.1.1, an expression of the form

$$C_0(t) + C_1(t)x^2 + C_2(t)y^2 + C_3(t)z^2 + C_4(t)xy = 0 \tag{5.27}$$

is produced. In this equation the $C_i(t)$ terms contain all the time dependent coefficients from $\mathbf{v}(\mathbf{r}, t)$ and $n(\mathbf{r}, t)$ that need to be determined. Similar to what was done in Section 5.1.1, by setting each of the $C_i(t)$ terms to zero separately produces five differential equations

$$\dot{\mu}_0 + \gamma\,\mu_0\,(\alpha_x + \alpha_y + \alpha_z) = 0 \tag{5.28}$$

$$\dot{a} + \frac{2(\alpha - \Omega)}{\sigma_x^2} + \frac{2(\alpha + \Omega)}{\sigma_y^2} + a\,(\alpha_x + \alpha_y) = 0 \tag{5.29}$$

$$\dot{\sigma}_x - \sigma_x\alpha_x - \frac{1}{2}\,\sigma_x^3\,a\,(\alpha + \Omega) = 0 \tag{5.30}$$

$$\dot{\sigma}_y - \sigma_y\alpha_y - \frac{1}{2}\,\sigma_y^3\,a\,(\alpha - \Omega) = 0 \tag{5.31}$$

$$\dot{\sigma}_z - \sigma_z\alpha_z = 0, \tag{5.32}$$

which describe how the parameters in $n(\mathbf{r}, t)$ evolve with time.

Each one of these five differential equations needs to be accompanied by an initial condition. In the experiment that this theory will model, as described later in Section 5.3.1, the excitation of the rotation is accomplished by a sudden rotation of the trapping potential. This sudden rotation does not allow the size of the cloud to change from its initial dimensions, as it would during a steady state rotation [100]. Therefore, at $t = 0$ the spatial density in equation (5.26) must describe the undeformed density in the trap, if the gas is released at $\phi = 0$. This allows us to set $a(0) = 0$ and the $\sigma_i(0)$ values equal to their static Thomas-Fermi lengths given by equation (5.9). The initial condition for the chemical potential is just the unperturbed value at the center of the trap, $\mu_0(0) = \sqrt{1+\beta}E_F$, which is only dependent upon the trap frequencies and the atom number.

To obtain the second half of the equations needed to describe the rotation and expansion dynamics, the Euler equation derived in Section 5.1.1 can be employed. In this case, however, the term $\mathbf{v} \times (\boldsymbol{\nabla} \times \mathbf{v})$ in the Euler equation does not vanish since the velocity field of equation (5.25) contains a rotational component. If the trial functions, $\mathbf{v}(\mathbf{r}, t)$ and $n(\mathbf{r}, t)$, are inserted into the Euler equation given by equation (5.11), a vector expression of the form

$$[\, C_{xx}(t)x + C_{xy}(t)y \,]\, \hat{x} + [\, C_{yx}(t)x + C_{yy}(t)y \,]\, \hat{y} + C_{zz}(t)z\, \hat{z} = 0 \tag{5.33}$$

results. All of the time dependence in this equation is contained in the $C_{ii}(t)$ terms. In a similar fashion to what was done with equation (5.27), which resulted from the equation of continuity, by setting each one of the $C_{ii}(t)$ terms equal to

zero separately yields the five differential equations

$$\dot{\Omega} + \Omega\ (\alpha_x + \alpha_y) = 0 \tag{5.34}$$

$$\dot{\alpha} + \alpha\ (\alpha_x + \alpha_y) - \frac{\mu_0}{m}\, a = 0 \tag{5.35}$$

$$\dot{\alpha_x} + \alpha_x^2 + \left(\alpha^2 - \Omega^2\right) - \frac{2\mu_0}{m\sigma_x^2} = 0 \tag{5.36}$$

$$\dot{\alpha_y} + \alpha_y^2 + \left(\alpha^2 - \Omega^2\right) - \frac{2\mu_0}{m\sigma_y^2} = 0 \tag{5.37}$$

$$\dot{\alpha_z} + \alpha_z^2 - \frac{2\mu_0}{m\sigma_z^2} = 0, \tag{5.38}$$

which describe how the components of $\mathbf{v}(\mathbf{r}, t)$ evolve with time. These five equations must be accompanied by the appropriate initial conditions. Initially the cloud is only rotating and has a zero expansion velocity, so we can set $\alpha_x(0) = \alpha_y(0) = \alpha_z(0) = 0$. Depending upon what condition we are interested in simulating, the initial condition on the angular velocity can be $\Omega(0) = \Omega_0$ and $\alpha(0) = 0$ for pure rotational flow, or $\Omega(0) = 0$ and $\alpha(0) = \Omega_0$ for pure irrotational flow, or anything else in between.

An interesting consequence of equations (5.34) through (5.38) is that the initial conditions given to $\alpha(0)$ and $\Omega(0)$ have little effect on the resulting dynamics. The time evolution of the rotational part of the velocity field, $\Omega(t)$, is determined by equation (5.34). The solution to this equation is an exponential, so as long as the sum of α_x and α_y is always positive, $\Omega(t)$ will *always* exponentially decay. Due to the fact that we have a highly elongated cigar-shaped trap, the decay time is very rapid since α_y becomes on the order of ω_y soon after the cloud is released from the trap. As $\Omega(t)$ decays away, $\alpha(t)$ increases since the cloud will continue to rotate, making the gas more irrotational as time goes on. So for the conditions

we can create in our trap, the simulations give the essentially the same dynamics whether the gas is in initially purely rotational or purely irrotational, which is very surprising indeed.

Equations (5.28) through (5.32) and equations (5.34) through (5.38) constitute ten simultaneous differential equations that describe the dynamics of the cloud as it rotates and expands upon release from the trap. All of the equations need to be solved together numerically. Once a solution to the ten coefficients is found as a function of time, they can be used to predict any experimental observable, including the angle of the principal axes and the aspect ratio.

The angle of the principal axes can be found by using the transformation $x = x'\cos\phi - y'\sin\phi$, $y = y'\cos\phi + x'\sin\phi$, and $z = z'$ to go from the coordinates in the laboratory frame to the coordinates in the primed frame, which is rotating with the cloud as shown in Figure 5.1. In this transformation the angle ϕ is the angle of the principal axes of the cloud, as viewed in the laboratory frame. Applying this transformation to equation (5.26) for $n(\mathbf{r}, t)$ creates a density distribution in the rotating frame of the form

$$n(\mathbf{r}', t) = n_0(t)\left(1 - \frac{x'^2}{\sigma_x'^2(t)} - \frac{y'^2}{\sigma_y'^2(t)} - \frac{z'^2}{\sigma_z'^2(t)} - a'(t)\,x'y'\right)^{3/2}, \tag{5.39}$$

where the primed parameters are made up of complicated expressions composed of the parameters in the laboratory frame σ_x, σ_y, σ_z, and a, as well as functions of the angle ϕ.

In the rotating reference frame the density can not have any cross terms such as $x'\,y'$ since the ellipticity of the cloud is conserved during the expansion and it should have the same form as the density in a static trap given by equation (5.7).

Due to this restriction, it is necessary to set $a'(t) = 0$ in equation (5.39). Since the parameter $a'(t)$ contains functions of the angle ϕ, which defines the orientation of the principal axes in the lab frame, an expression for ϕ can be found when $a'(t)$ is set equal to zero. After this is done, the resulting equation can be shown to be

$$\tan(2\phi) = -a\,\frac{\sigma_x^2\,\sigma_y^2}{\sigma_x^2 - \sigma_y^2}. \tag{5.40}$$

Now that the $x'y'$ terms have been removed from equation (5.39) by the condition of equation (5.40), the aspect ratio of the cloud in the rotated frame can be found simply through the ratio $\lambda = \sigma'_y/\sigma'_x$. Despite its simple appearance, this actually represents a complicated function. After performing a substantial amount of algebra, the aspect ratio is found to be

$$\lambda = \left[\frac{\left(\sigma_x^2 + \sigma_y^2\right) - \sqrt{\left(\sigma_x^2 - \sigma_y^2\right)^2 + a^2\,\sigma_x^4\,\sigma_y^4}}{\left(\sigma_x^2 + \sigma_y^2\right) + \sqrt{\left(\sigma_x^2 - \sigma_y^2\right)^2 + a^2\,\sigma_x^4\,\sigma_y^4}}\right]^{1/2}. \tag{5.41}$$

In Section 5.3 these two parameters, ϕ and λ, will be plotted as a function of time and compared against the experimentally observed quantities. But before the experimental results are presented, the difference between hydrodynamic and ballistic expansion is explored in Section 5.2.

5.2 Ballistic rotation and expansion

In Section 5.1 a hydrodynamic theory was presented to model the dynamics of a strongly interacting Fermi gas during expansion. But if the gas is in the non-interacting regime, the expansion dynamics will be quite different. In this case

the gas should expand ballistically, and in the presence of rotation, should never demonstrate an inversion of its aspect ratio, which will be shown to be a hallmark of hydrodynamic flow in Section 5.3.2. Therefore it is instructive to formulate a theory for the expansion and rotation in the ballistic regime to compare to the hydrodynamic regime in order to elucidate the difference between the two types of dynamics.

To construct a theory for ballistic expansion, we first start with the phase space density in the rotating frame, $w'(\mathbf{r}', \mathbf{p}')$, for a trapped gas in terms of the positions $\mathbf{r}'$ and linear momenta $\mathbf{p}'$ in the rotating frame (see Figure 5.1 in Section 5.1). Integrating the phase space density over the momentum coordinates yields the actual spatial density, $n(\mathbf{r}', t)$. The derivation of $n(\mathbf{r}', t)$ for a ballistic gas is detailed in Section 5.2.1. Once an expression for the spatial density is constructed, it will be shown that the spatial dependence of $n(\mathbf{r}', t)$ contains x'^2, y'^2, z'^2, and $x'y'$ terms for a rotation in the $x-y$ plane. Since the cloud maintains an elliptical shape throughout the rotation, the $x'y'$ cross term cannot appear in the frame rotating with the cloud. In Section 5.2.2 it will be shown that the elimination of the $x'y'$ cross term in the rotating frame leads to expressions that determine how the angle and aspect ratio of the cloud evolve with time.

5.2.1 Derivation of the spatial density $n(\mathbf{r}, t)$

A theory can be constructed for the ballistic expansion of a Fermi gas in the noninteracting regime starting from the phase space density of a trapped gas in the rotating frame, $w'(\mathbf{r}', \mathbf{p}')$, for all positions $\mathbf{r}'$ and linear momenta $\mathbf{p}'$. The initial phase space density before expansion, $w'_0(\mathbf{r}'_0, \mathbf{p}'_0)$, can be written in terms

of the initial Hamiltonian, $H_0'(\mathbf{r}_0', \mathbf{p}_0')$, as

$$w_0'(\mathbf{r}_0', \mathbf{p}_0') = \frac{1}{(2\pi\hbar)^3} \int d\varepsilon\, f(\varepsilon)\, \delta\left[\varepsilon - H_0'(\mathbf{r}_0', \mathbf{p}_0')\right] \tag{5.42}$$

where δ is the Dirac delta function, $f(\varepsilon) = \left(e^{(\varepsilon-\mu)/k_BT} + 1\right)^{-1}$ is the occupation number , and the integral runs over all energies ε. The Hamiltonian in the rotating frame, H', can be related to the Hamiltonian in the laboratory frame through the relation $H' = H - \mathbf{\Omega} \cdot \mathbf{L}$, where $\mathbf{\Omega}$ is the angular velocity and $\mathbf{L}$ is the angular momentum in the laboratory frame [105]. The angular momentum is defined as $\mathbf{L} = \mathbf{r} \times \mathbf{p}$, so the initial Hamiltonian in the rotating frame can be written in the coordinates of the laboratory frame as

$$H_0'(\mathbf{r}_0, \mathbf{p}_0) = H_0(\mathbf{r}_0, \mathbf{p}_0) - \mathbf{p}_0 \cdot (\mathbf{\Omega}_0 \times \mathbf{r}_0), \tag{5.43}$$

where an identity of the scalar triple product has been used. The initial Hamiltonian consists of a kinetic energy term, $p_0^2/2m$, and a term for the potential. Assuming a harmonic potential, H_0' can be written in the form

$$H_0'(\mathbf{r}_0, \mathbf{p}_0) = \frac{(\mathbf{p}_0 - m\mathbf{\Omega}_0 \times \mathbf{r}_0)^2}{2m} - \frac{m}{2}(\mathbf{\Omega}_0 \times \mathbf{r}_0)^2 + \frac{m}{2}\sum_i \omega_i^2 x_{i_0}^2, \tag{5.44}$$

where the index i runs over the three directions x, y, and z and the ω_i are the harmonic trap frequencies. The term proportional to $(\mathbf{\Omega}_0 \times \mathbf{r}_0)^2$ in the Hamiltonian is the fictitious centrifugal potential. Physically, this term acts to weaken the frequencies of the harmonic oscillator potential under steady state conditions. Therefore the trap frequencies, ω_i, in equation (5.44) can be replaced by the modified frequencies $\tilde{\omega}_{x,y}^2 = \omega_{x,y}^2 - \Omega_0^2$ and $\tilde{\omega}_z^2 = \omega_z^2$ for a rotation in the x-y plane.

This substitution leads to the simplified expression

$$H_0'(\mathbf{r}_0, \mathbf{p}_0) = \frac{(\mathbf{p}_0 - m\boldsymbol{\Omega}_0 \times \mathbf{r}_0)^2}{2m} + \frac{m}{2}\sum_i \tilde{\omega}_i^2 x_{i_0}^2. \tag{5.45}$$

The atoms in a ballistic gas are noninteracting. Therefore, the momentum of an atom during expansion following the removal of the trapping potential will be identical to the initial momentum, $\mathbf{p} = \mathbf{p}_0$. This means that after the trap is extinguished, the atoms will follow straight line trajectories defined by $\mathbf{r_0} = \mathbf{r} - \frac{\mathbf{p}}{m}t$. Substituting this expression into equation (5.46) produces

$$H_0'(\mathbf{r}, \mathbf{p}, t) = \frac{\left[\mathbf{p} - \boldsymbol{\Omega}_0 \times (m\,\mathbf{r} - \mathbf{p}\,t)\right]^2}{2m} + \frac{m}{2}\sum_i \tilde{\omega}_i^2 \left(x_i - \frac{p_i}{m}t\right)^2, \tag{5.46}$$

which can be used in equation (5.42) to calculate the phase space density in the rotating frame using the coordinates in the laboratory frame. In order to derive expressions for the aspect ratio and angle as a function of time, the phase space density needs to be integrated over the momentum to produce the spatial density

$$n'(\mathbf{r}, t) = \frac{1}{(2\pi\hbar)^3}\int d\varepsilon\, f(\varepsilon) \int d^3\mathbf{p}\, \delta\left[\varepsilon - H_0'(\mathbf{r}, \mathbf{p}, t)\right], \tag{5.47}$$

where the momentum integral runs over all momenta and the fact that the momentum in both reference frames is identical, $\mathbf{p} = \mathbf{p}'$, has been used [105].

The best way to solve for the spatial density in equation (5.47) is to multiply out all the terms in the Hamiltonian given by equation (5.46) and group together all the terms quadratic in $\mathbf{r}$ and $\mathbf{p}$. The procedure is tedious and involves a couple of changes of variable, but after all the algebra equation (5.47) can be shown to

reduce to

$$n'(\mathbf{r},t) = \frac{1}{(2\pi\hbar)^3}\Lambda(t)\int d\varepsilon\, f(\varepsilon)\int dp\, p^2\,\delta\left[\varepsilon - p^2 - \frac{m}{2}\varphi(x,y,z)\right] \tag{5.48}$$

where

$$\Lambda(t) = \frac{4\pi\,(2m)^{3/2}}{\sqrt{\left(1+\Omega_0^2t^2+\tilde{\omega}_x^2t^2\right)\left(1+\Omega_0^2t^2+\tilde{\omega}_y^2t^2\right)\left(1+\tilde{\omega}_z^2t^2\right)}} \tag{5.49}$$

and

$$\begin{aligned}\varphi(x,y,z) &= \frac{\left(x^2+2xy\Omega_0t\right)\left(\Omega_0^2+\tilde{\omega}_x^2\right)-y^2\Omega_0^2}{1+\Omega_0^2t^2+\tilde{\omega}_x^2t^2} \\ &\quad + \frac{\left(y^2-2xy\Omega_0t\right)\left(\Omega_0^2+\tilde{\omega}_y^2\right)-x^2\Omega_0^2}{1+\Omega_0^2t^2+\tilde{\omega}_y^2t^2} + \frac{\tilde{\omega}_z^2z^2}{1+\tilde{\omega}_z^2t^2}.\end{aligned} \tag{5.50}$$

The expression $\varphi(x,y,z)$ contains all the position dependence found in $n'(\mathbf{r},t)$, and encompasses all the information needed to derive formulas for the angle and aspect ratio. The momentum integral in equation (5.48) can be solved using the delta function identity

$$\delta\left[\varepsilon - p^2 - \frac{m}{2}\varphi(x,y,z)\right] = \frac{\delta\left(p-\sqrt{\varepsilon-\frac{m}{2}\varphi(x,y,z)}\right)}{\sqrt{\varepsilon-\frac{m}{2}\varphi(x,y,z)}}, \tag{5.51}$$

which subsequently reduces equation (5.48) to

$$n'(\mathbf{r},t) = \frac{1}{(2\pi\hbar)^3}\Lambda(t)\int d\varepsilon\, f(\varepsilon)\left(\varepsilon - \frac{m}{2}\varphi(x,y,z)\right)^{1/2}. \tag{5.52}$$

To solve this equation we need to know the form of the occupation number, $f(\varepsilon)$. Since we want to compare the ballistic theory to the hydrodynamic theory, which was done under the approximation of zero temperature, we can use that same

assumption here. In the ground state for a Fermi system all the energy levels are filled up to the Fermi energy, so the density of states is just a Heaviside step function, $f(\varepsilon) = U[\varepsilon - E_F]$, up to the Fermi energy [106]. Evaluating the integral of equation (5.52) then produces the final form of the spatial density in the rotating frame as

$$n'(\mathbf{r},t) = \frac{1}{3\pi^2}\left(\frac{2m}{\hbar^2}\right)^{3/2} \frac{\left(E_F - \frac{m}{2}\varphi(x,y,z)\right)^{3/2}}{\sqrt{\left(1+\Omega_0^2t^2+\tilde{\omega}_x^2t^2\right)\left(1+\Omega_0^2t^2+\tilde{\omega}_y^2t^2\right)\left(1+\tilde{\omega}_z^2t^2\right)}}, \tag{5.53}$$

which reduces to equation (5.4), the previously derived static density in the trap before expansion, for $\Omega_0 = t = 0$ in the case where there are no interactions ($\beta = 0$).

5.2.2 Angle and aspect ratio for ballistic rotation

Now that we have an expression for the spatial density as a function of time, we need to extract formulas for the aspect ratio and the angle of the principle axes of the cloud. The derivation that we have done so far is for the density in the rotating frame expressed in the coordinates of the laboratory frame. If the principal axes of the cloud are rotated by and angle ϕ, we can employ the usual transformations $x = x'\cos\phi - y'\sin\phi$, $y = y'\cos\phi + x'\sin\phi$, and $z = z'$ to change coordinates from the laboratory frame into the rotating frame. This is exactly the same procedure followed in Section 5.1.2 to formulate expressions for the angle ϕ and aspect ratio λ.

In the rotating frame the spatial density should maintain the general form of equation (5.7) for all time t. Therefore all $x'\,y'$ cross terms must be eliminated from equation (5.53) after the substitution. Since all the position dependence

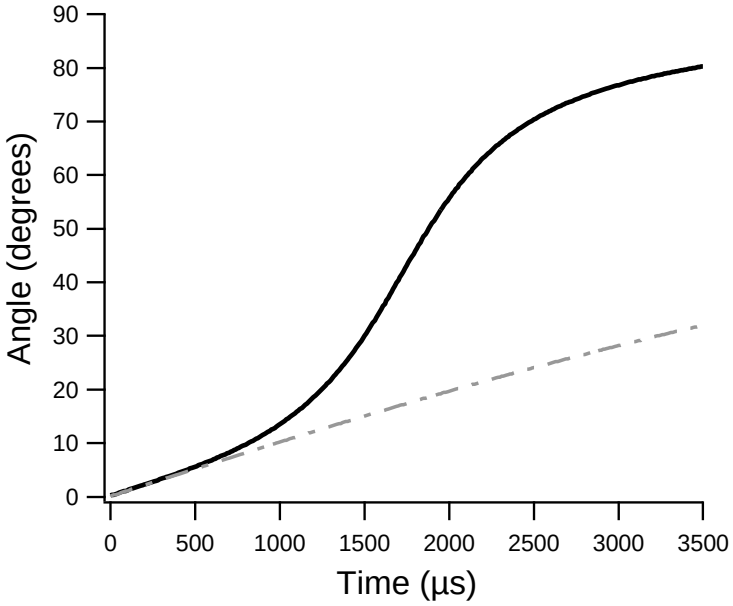

Figure 5.3: Angle of the principle axes are plotted as a function of time for a hydrodynamic and ballistic gas. A prediction from the hydrodynamic theory is given by the solid black line. The ballistic case is represented by the dashed-dot grey line. Both cases have the same initial conditions.

of $n'(\mathbf{r}, t)$ is contained in $\varphi(x, y, z)$, the change of coordinates can be performed exclusively on equation (5.50), with all the $x'y'$ terms subsequently set equal to zero. When this procedure is complete the incredibly simple formula

$$\tan\phi = \Omega_0 t \tag{5.54}$$

results for the angle of the principle axes of the cloud as a function of time.

Similar to the hydrodynamic case, the angle ϕ for the ballistic gas begins a zero for $t = 0$ and asymptotically approaches 90° as $t \to \infty$. But that is where the similarities end. It is impossible for such an expression as equation (5.54) to exhibit the rich dynamics observed in the hydrodynamic case. This

can be clearly seen in Figure 5.3 were the hydrodynamic and ballistic theories are plotted together for the same initial conditions. The ballistic theory doesn't replicate the fast rise in the angle demonstrated by the hydrodynamic theory and observed during experiments. In fact the angular velocity for the ballistic case

$$\dot{\phi} = \frac{\Omega_0}{1 + \Omega_0^2 t^2} \tag{5.55}$$

starts off as Ω_0 and monotonically approaches zero as $t \to \infty$ in stark contrast to the hydrodynamic case that exhibits a maximum in angular velocity as the aspect ratio approaches unity.

After setting all the cross terms $x'\,y'$ in $\varphi\,(x', y', z')$ equal to zero, the resulting expression is quadratic in x', y', and z' and has the same form for the static spatial density of equation (5.7), namely

$$n(\mathbf{r}', t) = n_0(t) \left(1 - \frac{x'^2}{\sigma_x'^2(t)} - \frac{y'^2}{\sigma_y'^2(t)} - \frac{z'^2}{\sigma_z'^2(t)} \right)^{3/2}. \tag{5.56}$$

Therefore, the cloud radii in the rotating frame, $\sigma_i'(t)$, can be extracted from the resultant expression. Using these widths, the aspect ratio $\lambda = \sigma_y'/\sigma_x'$ can be constructed. After a substantial amount of algebra, an expression for aspect ratio can be shown to be

$$\lambda = \frac{\tilde{\omega}_x}{\tilde{\omega}_y} \left[\frac{1 + \left(\Omega_0^2 + \tilde{\omega}_y^2\right) t^2}{1 + \left(\Omega_0^2 + \tilde{\omega}_x^2\right) t^2} \right]^{1/2}. \tag{5.57}$$

There are two situations that must be considered when using equation (5.57) to model the aspect ratio of a rotating cloud expanding ballistically. It was mentioned earlier that as a result of the fictitious centrifugal potential term in the rotation Hamiltonian, the trap frequencies are modified to read $\tilde{\omega}_{x,y}^2 = \omega_{x,y}^2 - \Omega_0^2$.

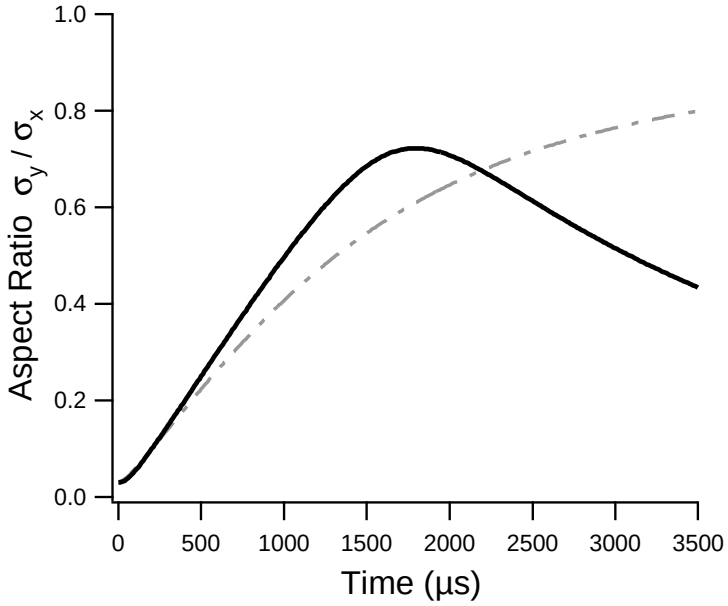

Figure 5.4: Aspect ratio of the principle axes are plotted as a function of time for a hydrodynamic and ballistic gas. A prediction from the hydrodynamic theory is given by the solid black line. The ballistic case is represented by the dashed-dot grey line. Both cases have the same initial conditions.

This is only true if the cloud is allowed to rotate in the trap for a long period of time before release, resulting in steady state conditions. In the hydrodynamic experiments presented in Section 5.3.2, the gas is not allowed to reach equilibrium before release, negating the effect of the centrifugal potential on the trap frequencies. Since it is desired that the ballistic theory model the same conditions as the hydrodynamic theory, the expression for the aspect ratio reduces to

$$\lambda = \frac{\omega_x}{\omega_y} \left[\frac{1 + \left(\Omega_0^2 + \omega_y^2\right) t^2}{1 + \left(\Omega_0^2 + \omega_x^2\right) t^2} \right]^{1/2} . \tag{5.58}$$

Just as in the hydrodynamic case, the aspect ratio begins at $\omega_x/\omega_y \ll 1$, since $\omega_y \gg \omega_x$ for a highly cigar shaped cloud. By taking into account the

fact that $\omega_y \gg \Omega_0$ for all initial angular velocities, as $t \to \infty$ equation (5.57) reduces to $\lambda \to \frac{\omega_x}{\sqrt{\Omega_0^2+\omega_x^2}}$. In this case λ is always less than unity for finite Ω_0, just as in the hydrodynamic case. But unlike a hydrodynamic gas, a ballistic gas monotonically approaches this value and never shows an inversion of the aspect ratio as observed in Figure 5.4. It will be shown in Section 5.3.2 that an inversion of the aspect ratio is a hallmark of rotational gas hydrodynamics and irrotational flow. Therefore, by monitoring the aspect ratio of the cloud during the rotation and expansion, the difference between hydrodynamic and ballistic dynamics can easily be distinguished.

5.3 Creating and analyzing rotating gases

A hydrodynamic theory for the rotation and expansion of a strongly interacting Fermi gas was presented in Section 5.1. In that section, predictions for the angle and aspect ratio of an expanding and rotating gas as a function of time were given. To lend credence to those predictions, experiments were performed on gases of various temperatures. Section 5.3.1 presents the experimental method used to produce a gas that is rotating with an initial angular velocity Ω_0 prior to release from the trap. This is followed by a description of how the angle and aspect ratio are extracted from the cloud images in Section 5.3.2.

5.3.1 Rotating a strongly interacting Fermi gas

Under normal conditions, the atoms used for experiments are trapped within the static potential created at the focus of the CO_2 laser beam and are not rotating. One of the easiest ways to excite a rotation and impart some angular momentum

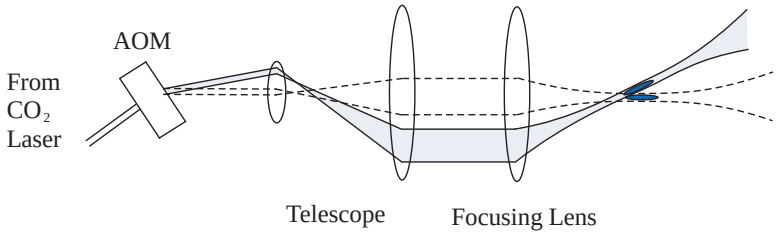

Figure 5.5: Rotation of a trapped gas using an acousto-optic (AO) modulator. A small change in the driving frequency of the AO causes a slight angle change in the transmitted beam (solid line), which results primarily in a rotation of the focussed beam.

to gas is to rotate the potential that is confining the atoms. A schematic of such a process is given in Figure 5.5. As shown in the figure, the trapping beam passes through an acousto-optic (AO) modulator and can be deflected by changing the driving frequency supplied to the AO. An AO consists of a crystal attached to a piezoelectric transducer that drives the crystal, in our case at 40 MHz, creating sound waves in the crystal. The sound waves create a varying index of refraction from which a laser beam traveling through the crystal scatters off, similar to Bragg diffraction. The angle at which the scattered light leaves the crystal is proportional to the driving frequency. By changing this frequency a deflection of the CO_2 laser beam is produced. As this deflected beam travels through the CO_2 laser optical system, the deflection results primarily in a rotation of the beam at the focus of the lens after the telescope, creating a potential for the atoms that is rotated with respect to the static position.

If the AO frequency is changed suddenly on a time scale that is fast compared to the trap frequencies, the atoms will find themselves in a configuration that is out of equilibrium with the rotated potential. This will cause a torque on the cloud, causing a rotation. In the ideal case of a pure rotation of the trapping potential,

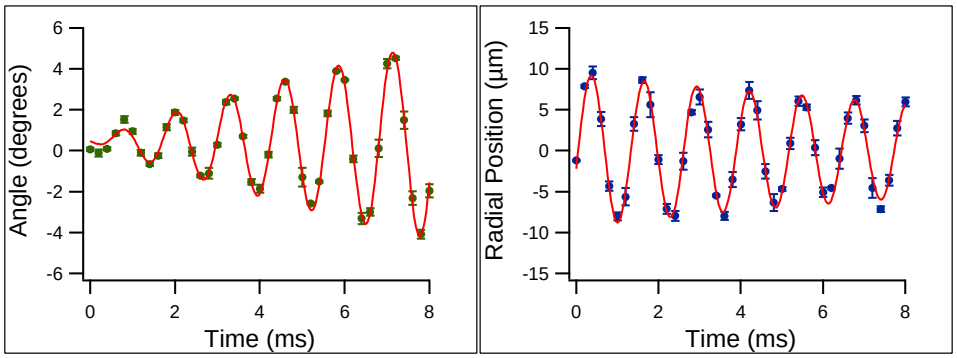

Figure 5.6: Plots of the coupled scissors mode (left) and rigid body translational mode (right) that are excited when the CO_2 beam is suddenly deflected. The solid lines are fits to the data using a sine function with an exponential decay.

the atom cloud will oscillate about the new rotated equilibrium position in what is known as a "scissors mode" [107, 108]. The rotation about the equilibrium position is harmonic, resulting in an angular velocity of the cloud that continually varies between zero and a maximum value, Ω_{max}, which depends upon how hard the cloud is "kicked". Therefore the cloud can be released from the trap with an arbitrary initial angular velocity, Ω_0, up to the maximum angular velocity characteristic of the scissors mode.

In reality, however, the deflection of the CO_2 beam with the AO doesn't cause a pure rotation of the beam at the location of the trap. A transverse translation of the beam accompanies the rotation as shown schematically in Figure 5.5. This sets up a rigid body "sloshing" mode in conjunction with the scissors mode. In the actual experiment we observe a coupling between these two modes as demonstrated in Figure 5.6. As evidenced in the figure, there appears to be an exchange of energy between the two modes since the decay of the sloshing mode has the same time constant as the build up of the scissors mode. Rather than being a problem, this is actually advantageous for the experiment at hand. Since

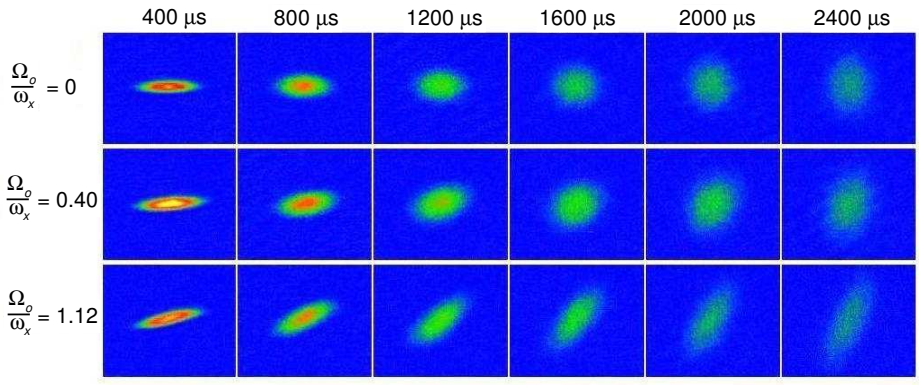

Figure 5.7: Expansion of a rotating, strongly interacting Fermi gas for different initial angular velocities, Ω_0. ω_x is the trap frequency in the axial (long) direction.

the maximum amplitude of the scissors mode increases with time, a small Ω_0 can be imparted to the cloud by releasing it soon after the initial CO_2 beam deflection, or a large Ω_0 can be created by holding it for a longer period. In this way we have a great amount of control over the initial angular velocity of the cloud.

In order to observe expansion of the gas in the hydrodynamic regime, the gas is cooled to degeneracy at 834G where the s-wave scattering length is infinite due to the broad Feshbach resonance as demonstarted in Section 2.5. After the gas has been cooled to roughly $E = 0.56\,E_F$, which is close to the ground state value of $E = 0.50\,E_F$, the cloud is set oscillating by changing the frequency of the AO by typically 0.25%. Once the cloud is released, it evolves according to the hydrodynamic equations derived in Section 5.1.

The images for the expansion are quite dramatic, and are substantially different from the case of no rotation, as displayed in Figure 5.7. The top panel in the Figure shows how the gas expands with no initial angular velocity and displays the hallmark anisotropic expansion previously observed [18]. However, when there is

a finite Ω_0, the expansion in the radial direction is suppressed as the aspect ratio approaches unity and the angular velocity begins to speed up. For example, at 1600 μs the cloud is roughly circular and the aspect ratio is close to unity in the rotation free case ($\Omega_0 = 0$). However if $\Omega_0 = 1.12\,\omega_x$, the cloud is still highly elliptical in shape, demonstrating a suppression of the aspect ratio. Additionally, the rapid acceleration of the principle axes of the cloud can be observed by comparing the angle of the cloud at 1200 μs and 2000 μs for $\Omega_0 = 0.40\,\omega_x$. At 1200 μs the angle of the long axis of the cloud is approximately $\phi = 30°$, whereas at 2000 μs $\phi = 60°$. It will be shown in Section 5.4 that all of these observations are a consequence of the conservation of angular momentum in a rotating, expanding gas.

5.3.2 Measuring the angle and aspect ratio

In order to extract the aspect ratio and angle data from images similar to Figure 5.7, a two dimensional gaussian function of the form $A\exp\left[-ax^2 - bxy - cy^2\right]$ is used to fit the density profiles. By following the same procedure of transforming into the rotating frame outlined in Section 5.1 where $x \to x'$ and $y \to y'$, expressions for the angle ϕ and aspect ratio $\lambda = \sigma_x/\sigma_y$ based upon the fit function are found to be

$$\tan(2\phi) = -\frac{b}{a-c} \tag{5.59}$$

for the angle and

$$\lambda = \left[\frac{(a+c) + \sqrt{(a-c)^2 + b^2}}{(a+c) - \sqrt{(a-c)^2 + b^2}}\right]^{1/2} \tag{5.60}$$

for the aspect ratio, which, not surprisingly, are very similar to the theoretical expressions for the angle and aspect ratio found in equations (5.40) and (5.41).

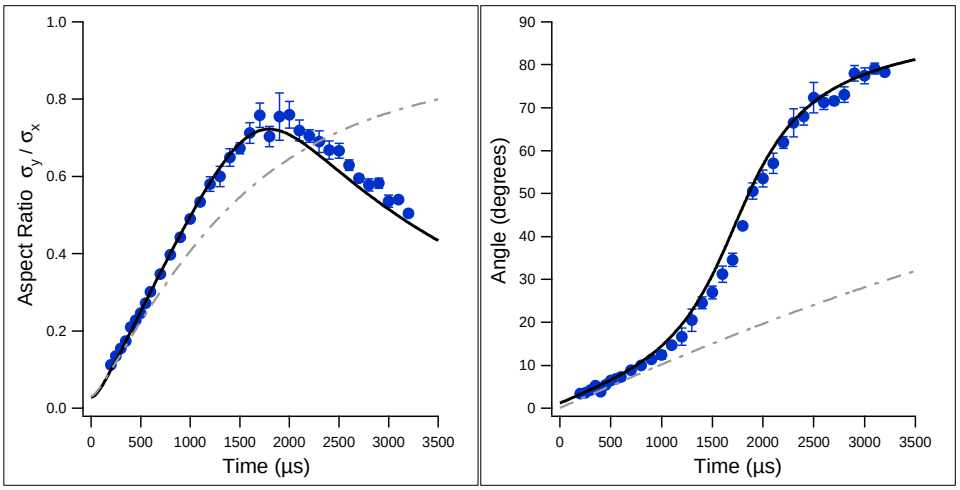

Figure 5.8: Aspect ratio (left) and angle (right) of a rotating, strongly interacting Fermi gas as a function of time. The solid circles are the experimental data, the solid line is the hydrodynamic theory, and the dashed-dot line is the ballistic theory. The initial angular velocity is $\Omega_0 = 0.40\,\omega_x$.

A typical experimental sequence involves taking three repetitions of the same data point to obtain error bars, and taking all the data points in random order. By performing the experiments in this manner, plots of the data can be generated similar to Figure 5.8. In this Figure the hydrodynamic theory developed in Section 5.1.2 and the ballistic theory developed in Section 5.2 for the angle and aspect ratio is presented along with typical experimental data. In the hydrodynamic theory, pure irrotational flow is assumed for the initial velocity. Both hydrodynamic and ballistic theories have the same initial conditions as the experiment, which corresponds to the middle row of the expansion images in Figure 5.7 where $\Omega_0/\omega_x = 0.40$.

It is clear from Figure 5.8 that the gas behaves hydrodynamically as opposed to ballistically. This is most evident in the plot for the angle where the data unmistakably follows the hydrodynamic theory and departs considerably from the

ballistic theory. Behavior such as this is to be expected, since at these low energies the gas should be almost completely superfluid [26, 39, 109], and thus should act like an ideal irrotational fluid as opposed to a noninteracting gas. Similar behavior has been observed in the rotation and expansion of a superfluid Bose gas [102,103], which has also been shown to be hydrodynamic. But contrary to observations of Fermi gases, when the temperature is raised in a rotating Bose gas it will expand ballistically, since the gas is weakly interacting and is no longer irrotational at temperatures above the critical temperature. Therefore the hydrodynamic expansion and rotation of a Bose-Einstein condensate is a very good test for superfluidity in that system, since the only way to get an irrotational velocity field is through the existence of a condensate.

However, in the Fermi case, when the gas is brought above the superfluid transition energy, $E = 0.94\,E_F$ [39], it can still be hydrodynamic [18, 63]. This is due to the fact that the gas is in the strongly interacting regime, where the dynamics can be explained by low viscosity collisional hydrodynamics as opposed to superfluid hydrodynamics. But if irrotational flow is observed in the normal fluid regime, the viscosity must be exceptionally small to support it, due to the large amount of shear generated by irrotational flow [110]. Therefore a normal gas isn't expected to demonstrate the same dynamics observed for a superfluid gas in Figure 5.8. But when a high temperature experiment, where the energy of the gas is well into the normal regime at $E = 2.10\,E_F$, is done under the same conditions as Figure 5.8, the cloud exhibits almost identical dynamics to the superfluid gas.

A comparison between the two cases is clearly seen in Figure 5.9 where the open circles representing the hot data are almost all on top of the closed circles indicating the cold data. This indicates that a strongly interacting Fermi gas

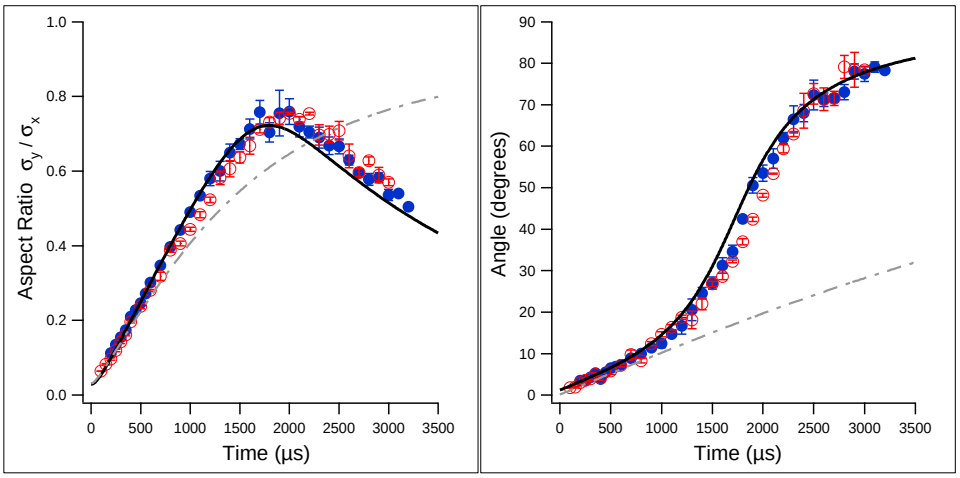

Figure 5.9: Aspect ratio (left) and angle (right) of a rotating, strongly interacting Fermi gas as a function of time. The solid circles are the experimental data at $E = 0.56E_F$,the open circles are the data at $E = 2.10E_F$, the solid line is the hydrodynamic theory, and the dashed-dot line is the ballistic theory.

can demonstrate nearly zero-viscosity hydrodynamics at energies up to twice the superfluid transition energy, which is quite a remarkable property. This observation has important implications for other strongly interacting collisional Fermi systems in nature, such as the quark-gluon plasma. It is known that quark-gluon plasmas, as created recently in heavy ion accelerators, exhibit minimum viscosity hydrodynamics and elliptic flow [19, 111]. It is therefore possible that irrotational flow will alter the signature of quark-gluon plasmas that are created with finite angular momentum.

5.4 Moment of inertia

The experimental results presented in Section 5.3 dramatically demonstrate the consequences of irrotational flow. The inversion of the aspect ratio of the cloud

and corresponding angular acceleration are only found in a hydrodynamic system, and are absent in the ballistic predictions. These dynamics arise as a consequence of the quenched moment of inertia that originates only for a gas of atoms exhibiting irrotational flow. In Section 5.4.1 the theoretical framework for a calculation of the moment of inertia is introduced, along with a presentation of experimental data in Section 5.4.2. The results obtained from the moment of inertia measurements provide further evidence for the existence of irrotational flow not only in superfluid Fermi gases where it is to be expected, but also in normal strongly interacting Fermi gases as well.

5.4.1 Moment of inertia for irrotational flow

A dramatic consequence of irrotational flow is the quenching of the moment of inertia. For a rotating gas of atoms a fundamental prediction of irrotational hydrodynamics is

$$\frac{I}{I_{rig}} = \delta^2 \equiv \frac{\langle x'^2 - y'^2 \rangle^2}{\langle x'^2 + y'^2 \rangle^2}. \tag{5.61}$$

In this equation I is the moment of inertia and I_{rig} is the corresponding rigid body value. Physically, I_{rig} is the moment of inertial that would be measured if the cloud rotated rigidly. The primed coordinates represent the principal axes that are rotating with the cloud as shown in Figure 5.10. The spatial anisotropy of the atom cloud in the $x' - y'$ plane is described by the parameter δ, which is also called the deformation parameter. The expectation values in equation (5.61) have their normal meanings

$$\langle x'^2 \pm y'^2 \rangle = \frac{1}{N} \int d\mathbf{r}'\, n(\mathbf{r}') \left(x'^2 \pm y'^2 \right), \tag{5.62}$$

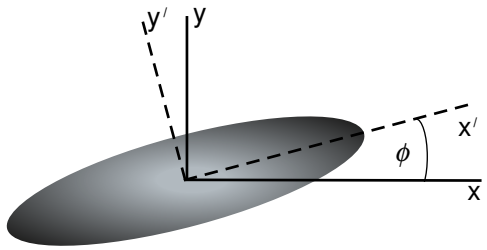

Figure 5.10: Illustration of the principal axes of the cloud in the laboratory and rotating coordinate systems. The unprimed coordinates are in the lab frame, while the primed coordinates are in the rotating frame.

which is equivalent to the sum or difference of the mean square cloud sizes in the x' and y' directions.

An important physical consequence of the rotation and expansion can be concluded from the moment of inertia given by equation (5.61). For any rotating system it is unphysical for the moment of inertia to vanish. Therefore, the numerator in equation (5.61) must remain finite throughout the rotation and expansion of the atom cloud. When the gas is released from the trap while rotating, it begins to expand as if no rotation was present. This behavior can be observed in the aspect ratio plot provided in Figure 5.11. But as the aspect ratio increases and approaches unity, it reaches a maximum and begins to invert. The maximum value of the aspect ratio is dependent upon the initial angular velocity of the cloud, as shown in Figure 5.11. If the aspect ratio were allowed to reach unity, the mean square size of the cloud in the x' and y' directions would become equal. This would cause the moment of inertia, I, in equation (5.61) to become zero. Correspondingly, in order to conserve angular momentum as I vanishes, the angular velocity and rotational energy would become infinite. Therefore in order to conserve energy and angular momentum, an inversion of the aspect ratio must

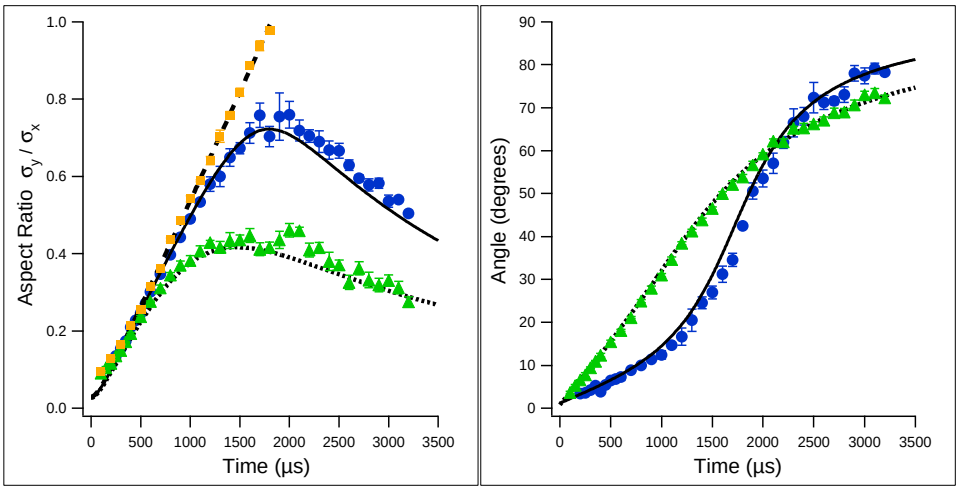

Figure 5.11: Aspect Ratio (left) and Angle (right) of a rotating, strongly interacting Fermi gas as a function of time. The solid circles are the experimental data at $E = 0.56E_F$ and $\Omega_0 = 0.40\,\omega_x$, while the triangles are for $E = 0.56E_F$ and $\Omega_0 = 1.12\,\omega_x$. The solid and dotted lines are the corresponding hydrodynamic theories. The solid squares and dashed line are for the case of no rotation.

occur, which is a hallmark and consequence of irrotational flow.

It can be shown that the moment of inertia in equation (5.61) is usually only valid for a hydrodynamic gas rotating under *steady state* conditions [112]. In our experiments the density and stream velocity are continuously changing, therefore the moment of inertia is inherently a *dynamic* quantity. Because of this, it is necessary to justify the conclusion that the moment of inertia is in fact quenched in the experiments and that equation (5.61) is valid for all times during the expansion.

To prove this result, it is easiest to work in the laboratory coordinate system. This requires a transformation of equation (5.61) from the rotating frame into the laboratory frame. This can be done using the usual transformations $x' = y\sin\phi + x\cos\phi$ and $y' = y\cos\phi - x\sin\phi$. Substituting these expressions into the

numerator and denominator of equation (5.61) produces

$$\langle x'^2 + y'^2 \rangle = \langle x^2 + y^2 \rangle \tag{5.63}$$

$$\langle x'^2 - y'^2 \rangle = \langle x^2 - y^2 \rangle \cos 2\phi + 2\langle xy \rangle \sin 2\phi \tag{5.64}$$

indicating that the polar moment is the same in both reference frames, but the difference moment is markedly different. The angle ϕ is defined previously by equation (5.40) and can be written in terms of the time dependent coefficients in the laboratory frame σ_x, σ_y, σ_z, and a, which dictate how the density, $n(\mathbf{r}, t) = n_0(t)\left(1 - x^2/\sigma_x^2(t) - y^2/\sigma_y^2(t) - z^2/\sigma_z^2(t) - a(t)\,xy\right)^{3/2}$, evolves with time as given in equation (5.26). By using this form of the density in the expectation values of equation (5.62), σ_x, σ_y, σ_z, and a can be written in terms of the expectation values of the coordinates in the laboratory frame. Therefore the time dependent coefficients provide a bridge between expressions for the angle ϕ and the expressions for the expectation values in the laboratory frame. After the time dependent coefficients are eliminated from both expressions, the equations

$$\cos 2\phi = \frac{\langle x^2 - y^2 \rangle}{\sqrt{\langle x^2 - y^2 \rangle^2 + 4\langle xy \rangle^2}} \tag{5.65}$$

$$\sin 2\phi = \frac{2\langle xy \rangle}{\sqrt{\langle x^2 - y^2 \rangle^2 + 4\langle xy \rangle^2}} \tag{5.66}$$

can be shown to result. Note that $\cos^2 2\phi + \sin^2 2\phi = 1$, as it should. By using these two expressions in equation (5.64) a relationship between the expectation values in the laboratory and rotating reference frames is established. When equations (5.63) and (5.64) are substituted into the formula for the deformation parameter, equation (5.61), the desired form for the moment of inertia in the

laboratory coordinates is produced and is given by

$$\frac{I}{I_{rig}} = \delta^2 \equiv \frac{\langle x^2 - y^2\rangle^2 + 4\langle xy\rangle^2}{\langle x^2 + y^2\rangle^2}. \tag{5.67}$$

It must now be shown that this expression is true in general, and not just for the specific case of steady state rotation.

Equation (5.67) can be derived for a dynamic moment of inertia starting from the definition of angular momentum. A cloud with its principal axes rotating at an angular velocity of $\dot{\phi}$ in the $x-y$ plane has an angular momentum

$$\langle J_z\rangle = I\,\dot{\phi}, \tag{5.68}$$

where J_z is the angular momentum of the cloud (taken to be in the $\hat{\mathbf{z}}$ direction) and I is the effective moment of inertia. The angular momentum of an atom cloud rotating in the laboratory $x-y$ plane is simply $\langle J_z\rangle = mN\langle x\,v_y - y\,v_x\rangle$, where m is the atom mass and N is the number of atoms in the cloud. Taking the irrotational part of the ansatz for the velocity field given in equation (5.25) as $\mathbf{v}(\mathbf{r},t) = 1/2\,\boldsymbol{\nabla}\,(\alpha_x(t)\,x^2 + \alpha_y(t)\,y^2 + \alpha_z(t)\,z^2 + 2\alpha(t)\,xy)$, the velocity components become $v_x = \alpha_x\,x + \alpha\,y$ and $v_y = \alpha_y\,y + \alpha\,x$, where the α terms are time dependent coefficients of the stream velocity. Incorporating these expressions into equation (5.68) yields

$$I\,\dot{\phi} = mN\langle\alpha\,x^2 - (\alpha_x - \alpha_y)\,xy - \alpha\,y^2\rangle. \tag{5.69}$$

The best way to simplify equation (5.69) is to write it in terms of the time dependent coefficients σ_x, σ_y, σ_z, and a of the density in the laboratory frame. The expectation values in equation (5.69) denote integrals of the coordinates with

the density, as given by equation (5.62). By using the expression for the density of a zero temperature gas given by equation (5.26) and performing the integrals, the mean square cloud sizes and cross term can be shown to be

$$\langle x^2 \rangle = \frac{\sigma_x^2}{8} \frac{1}{1 - a^2\,\sigma_x^2\,\sigma_y^2/4} \tag{5.70}$$

$$\langle y^2 \rangle = \frac{\sigma_y^2}{8} \frac{1}{1 - a^2\,\sigma_x^2\,\sigma_y^2/4} \tag{5.71}$$

$$\langle xy \rangle = -\frac{\sigma_x^2\,\sigma_y^2}{16} \frac{a}{1 - a^2\,\sigma_x^2\,\sigma_y^2/4}. \tag{5.72}$$

These are the same expressions used to simplify equations (5.65) and (5.66). Using these results in equation (5.69) changes the expression for the angular momentum to

$$I\,\dot{\phi} = \frac{mN}{16} \frac{1}{1 - a^2\,\sigma_x^2\,\sigma_y^2/4} \left[a\,\sigma_x^2\,\sigma_y^2\,(\alpha_x - \alpha_y) + 2\alpha\left(\sigma_x^2 - \sigma_y^2\right)\right]. \tag{5.73}$$

Since this equation eventually needs to be expressed in terms of the mean square sizes to compare it to the deformation parameter, δ, it can be written in the more suggestive form

$$\frac{I}{I_{rig}}\,\dot{\phi} = \frac{1}{2} \frac{1}{\sigma_x^2 + \sigma_y^2} \left[a\,\sigma_x^2\,\sigma_y^2\,(\alpha_x - \alpha_y) + 2\alpha\left(\sigma_x^2 - \sigma_y^2\right)\right] \tag{5.74}$$

using equations (5.70) and (5.71). This equation takes advantage of the fact that the classical rigid body moment of inertia can be written as $I_{rig} = mN\langle x^2 + y^2 \rangle$.

In order to simplify equation (5.74), an expression for $\dot{\phi}$ is needed. An equation for the angle of the cloud, ϕ, is provided in equation (5.40). Taking the derivative of this expression and using the equations derived from the equation of continuity

(equations (5.29) - (5.31)) produces the angular velocity

$$\dot{\phi} = \frac{1}{2} \frac{\sigma_x^2 + \sigma_y^2}{\left(\sigma_x^2 - \sigma_y^2\right)^2 + a^2\,\sigma_x^4\,\sigma_y^4} \left[a\,\sigma_x^2\,\sigma_y^2\,(\alpha_x - \alpha_y) + 2\alpha\left(\sigma_x^2 - \sigma_y^2\right)\right]. \tag{5.75}$$

Inserting this expression into equation (5.74) yields

$$\frac{I}{I_{rig}} = \frac{\left(\sigma_x^2 - \sigma_y^2\right)^2 + a^2\,\sigma_x^4\,\sigma_y^4}{\left(\sigma_x^2 + \sigma_y^2\right)^2} \tag{5.76}$$

Utilizing the expectation values provided in equations (5.70) through (5.72) in this expression leads to the desired result

$$\frac{I}{I_{rig}} = \frac{\langle x^2 - y^2\rangle^2 + 4\langle xy\rangle^2}{\langle x^2 + y^2\rangle^2} = \delta^2 \equiv \frac{\langle x'^2 - y'^2\rangle^2}{\langle x'^2 + y'^2\rangle^2}, \tag{5.77}$$

which is valid for any steady flow that can be described by the equations of motion derived in Section 5.1.2.

5.4.2 Measurement of the moment of inertia

Although the moment of inertia as defined by equation (5.77) is valid throughout the expansion dynamics, in general it is defined for steady state conditions [99]. Therefore, I will refer to it as the effective moment of inertia from this point forward. The identity $I/I_{rig} = \delta^2$ from equation (5.77) can be experimentally validated using angular momentum conservation. When the gas is released from the trap, the expansion dynamics evolve in the absence of external forces[1] so the

[1]Actually, the atom cloud is released from the optical trap into the magnetic bowl produced by the bias field magnets. The forces from the magnetic bowl do apply a torque on the cloud, but simulations indicate this changes the angular momentum by less than 10% over the time scales of interest.

angular momentum is conserved throughout the rotation. As defined in equation (5.68), the magnitude of the angular momentum for an atom cloud rotating in the $x-y$ plane can be written as $\langle J_z \rangle = I\,\dot{\phi}$. When the cloud is initially released from the optical trap, the angular momentum is $\langle J_z \rangle_0 = I_0\,\Omega_0$, which is conserved. Therefore by measuring I_0 and Ω_0 at the beginning of the rotation, and subsequently measuring $\dot{\phi}$ and I_{rig}, the moment of inertia is found to be

$$\frac{I}{I_{rig}} = \frac{I_0 \Omega_0}{I_{rig}\dot{\phi}}. \tag{5.78}$$

When the cloud is released from the optical trap, the initial moment of inertia, I_0, is nearly equal to the rigid body value [101, 103]. At the beginning of the expansion, a highly cigar-shaped cloud has a small aspect ratio, $\lambda \simeq \sigma_y/\sigma_x$, resulting in rotational and irrotational velocity fields that are almost identical. The initial stream velocity for irrotational flow is $\mathbf{v} = \Omega_0 y\,\hat{\mathbf{x}} + \Omega_0 x\,\hat{\mathbf{y}}$, while for rotational flow, $\mathbf{v} = -\Omega_0 y\,\hat{\mathbf{x}} + \Omega_0 x\,\hat{\mathbf{y}}$. These two expressions differ only in the $\hat{\mathbf{x}}$ direction, which becomes negligible as σ_y/σ_x goes to zero. Since for our cloud σ_x is much greater than σ_y, upon release from the trap the initial moment of inertia is $I_0 \simeq mN\langle x^2 \rangle_0$ to within 0.3% accuracy. Therefore I_0 can be found by measuring $\langle x^2 \rangle_0$, which is easily determined from the cloud images.

The angular velocity of the cloud can be obtained from the time derivative of a polynomial fit to the angle versus time data. At the beginning of the rotation, the angular velocity is roughly constant since the stream velocity is nearly identical to a rotational velocity field due to the geometry of the cigar-shaped trap. Consequently, the initial angle versus time data in plots like Figure 5.11 can be fit by a straight line. The slope of this line yields the initial angular velocity Ω_0.

The angular velocity at a later time during the rotation, $\dot{\phi}$, can also be obtained by a polynomial fit to the data. The most significant time to measure the moment of inertia is at its minimum value, where the consequences of irrotational flow are at a maximum and the moment of inertia is strongly suppressed. This occurs when $\dot{\phi}$ is at a maximum and the angle versus time data exhibits the greatest slope. The region of maximum slope in the angle versus time data for plots similar to Figure 5.11 can be well fit with a polynomial. By taking the derivative of the polynomial, the magnitude of the maximum velocity, $\dot{\phi}_{max}$, can be found. The rigid body moment of inertia, $I_{rig} = mN\langle x^2 + y^2 \rangle$, can be found by measuring the mean square cloud sizes from the images at the same time in which $\dot{\phi}_{max}$ occurs. Therefore, the minimum effective moment of inertia can be calculated from the expression

$$\frac{I_{min}}{I_{rig}} = \frac{I_0 \Omega_0}{I_{rig} \dot{\phi}_{max}}. \tag{5.79}$$

The minimum moment of inertia as measured through the use of equation (5.79) is equal to δ^2 only for a rotating cloud undergoing irrotational flow. If the velocity field contains a rotational component, the relationship between the moment of inertia and δ^2 is no longer valid. Since the value of δ^2 is only dependent upon the geometry of the cloud as given in equation (5.77), it can also be measured by analyzing the cloud images. Therefore the relationship between I/I_{rig} and δ^2 given in equation (5.61) can actually be experimentally tested. If a linear relationship is found to exist between I/I_{rig} and δ^2, then the flow inside the rotating gas must be described by an irrotational velocity field. A plot of the measured I_{min}/I_{rig} versus δ^2 is shown in Figure 5.12. The data in this figure was taken under various experimental conditions. The solid circles in the figure were taken at energies below the superfluid transition energy $E_c = 0.94\, E_F$, while the

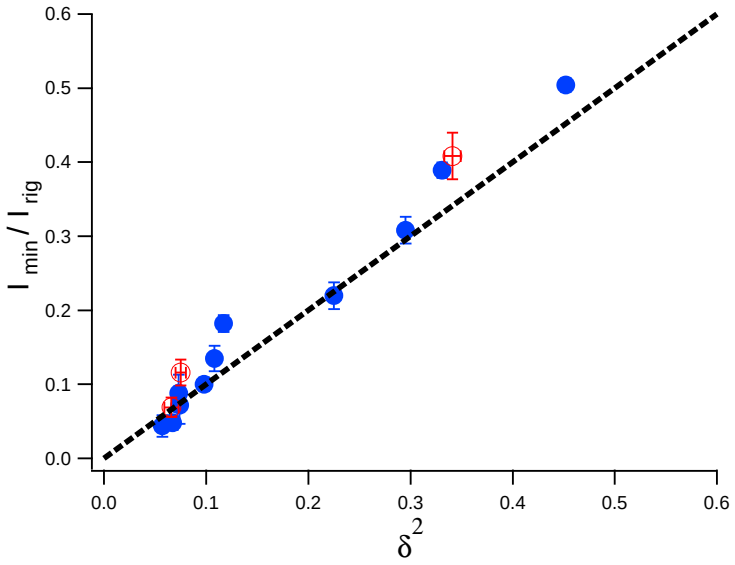

Figure 5.12: Plot of the minimum moment of inertia versus the square of the deformation parameter. The solid circles are for data taken below the superfluid transition energy of $E_c = 0.94E_F$, while the open circles are taken above E_c. The dashed line is the theoretical prediction $I_{min}/I_{rig} = \delta^2$.

open circles denote the data that was taken above E_c from 1.1 to 2.1 E_F. The dashed line is the identity $I/I_{rig} = \delta^2$, providing further evidence that the cold data, as well as the high temperature data, exhibits almost perfect irrotational flow.

A different perspective on the data is obtained by looking at I_{min}/I_{rig} as a function of the initial angular velocity. Figure 5.13 presents the plot of the measured minimum moment of inertia versus Ω_0/ω_x. The smallest values of I_{min}/I_{rig} are generated at the lowest initial angular velocities since the angular acceleration of the cloud is greatest under these conditions. The theory for I_{min}/I_{rig}, illustrated as a solid line in the Figure, is calculated numerically from the same hydrodynamic theory used to find the angle and aspect ratio of the cloud during rotation. Quenching of the moment of inertia to values as small as 5% of the rigid

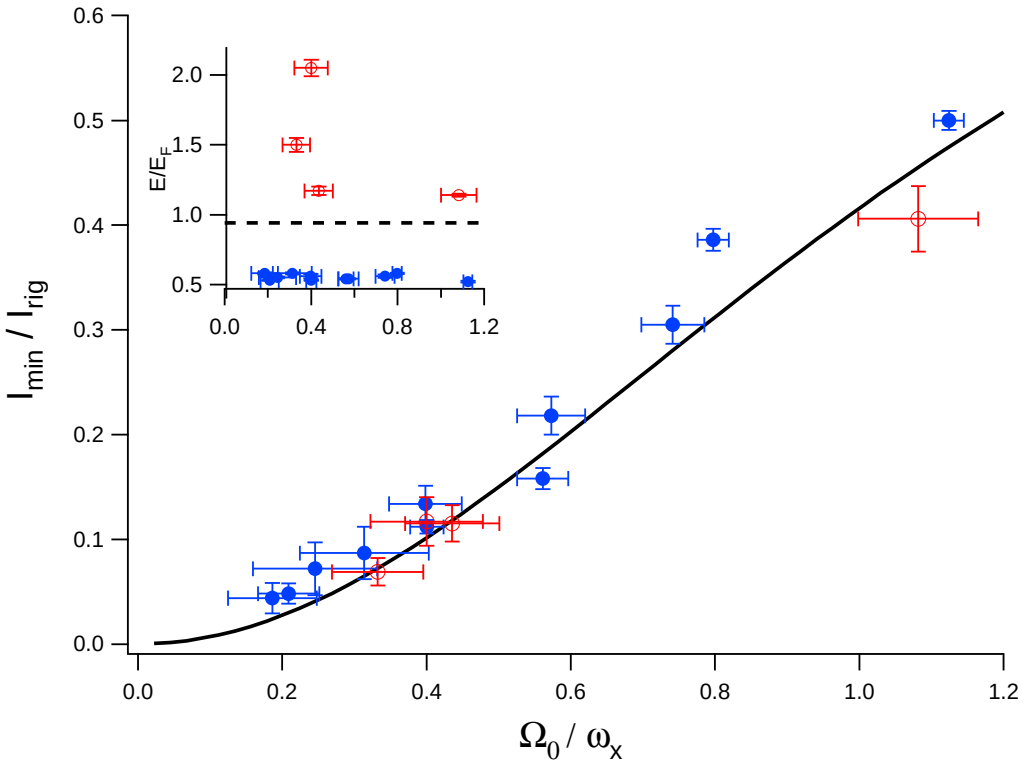

Figure 5.13: Quenching of the minimum moment of inertia versus the initial angular velocity in units of I_{rig} and ω_x respectively. The solid circles are for data taken below the superfluid transition energy of $E_c = 0.94E_F$, while the open circles are taken above E_c. The solid line is the theoretical prediction for irrotational flow. The inset shows the energy for each data point with a dashed line for E_c.

body value is observed for the coldest clouds, indicated by solid circles in the Figure. Similar to Figure 5.12, the high temperature data is also in good agreement with the theory and demonstrates the same suppression of the moment of inertia that the low temperature data exhibits.

The suppression of the moment of inertia and observation of irrotational flow in the normal, strongly interacting fluid at high temperature can be attributed to low viscosity hydrodynamics, as touched on in Section 5.3. For a zero viscosity fluid, equation (5.34), which describes the rate of change of the rotational part of the velocity field, $\mathbf{\Omega} \times \mathbf{r}$, was derived in Section 5.1.2 and obeys the differential equation $\dot{\Omega} + \Omega\ (\alpha_x + \alpha_y) = 0$. As a consequence, Ω must decay rapidly in a zero viscosity system since after release the stream velocity increases and α_y becomes on the order of ω_y, the radial optical trap frequency. Therefore, even if the cloud starts out with a pure rotational velocity field at the beginning of the rotation, the flow will quickly become irrotational as the expansion progresses. To preserve the rotational part of the velocity field, an additional dissipative term must be added to equation (5.34), which, as we will see in the next Chapter, appears as a result of viscosity. Therefore, in order to explain the results presented in this section the viscosity of a normal, strongly interacting Fermi gas must be exceptionally small. A quantitative measure of how small the viscosity must be can be obtained by accounting for viscosity in the hydrodynamic equations. A simple hydrodynamic model for viscosity is presented in the following chapter.

Chapter 6

Quantum Viscosity

Viscosity can be described as internal friction acting inside a flowing fluid. Like all dissipative forces, viscosity introduces a measure of irreversibility into the motion of the fluid. In this chapter a simple hydrodynamic model for viscosity is added to the ideal equations of motion developed in Chapter 5. By comparing the results of the model to experimental data, an estimate of the viscosity of a strongly interacting Fermi gas can be obtained.

In a zero temperature unitary Fermi gas, the interparticle spacing, which is proportional to the inverse of the Fermi wavevector, k_f^{-1}, sets the only length scale as the scattering length, a_s, approaches infinity. The shear viscosity, η, has units of momentum/area. Therefore a natural expression for the viscosity is $\eta \propto \hbar k_f/(1/k_f^2) \propto \hbar\, n$, where n is the local density. Using a proportionality constant ξ_η, which only depends upon the local reduced temperature, T/T_F, an expression for the viscosity can be written as

$$\eta = \xi_\eta \hbar\, n. \tag{6.1}$$

Due to the fact that $\hbar$ is explicitly contained in this expression, equation (6.1) has come to be known as quantum viscosity. The magnitude of the dimensionless coefficient $\xi_\eta\,(T/T_F)$ can be used to characterize the viscous nature of a fluid. If

this coefficient is comparable to or smaller than unity, the system is considered to be in the quantum viscosity regime [113]. The value of ξ_η can also be used to judge the degree to which a fluid is ideal. For a normal fluid, the coefficient is much larger than unity, whereas an exotic near-ideal quantum fluid will have a value of ξ_η that is on the order of unity or smaller. Therefore, a fluid can be considered more "perfect" for progressively smaller values of ξ_η.

A limit on how perfect a fluid can be has been conjectured using string theory methods [41]. It has been shown that for a wide class of strongly interacting quantum fields, the ratio of the shear viscosity η to the entropy density s has a minimum value. The string theory prediction is

$$\frac{\eta}{s} \geq \frac{1}{4\pi}\frac{\hbar}{k_B}, \tag{6.2}$$

where $\hbar$ is Plank's constant and k_B is Boltzmann's constant. It has been postulated that the lower bound in equation (6.2) may apply to ultra-cold gases, making them a near-ideal fluid [20, 41]. In Section 5.3 it was demonstrated that a superfluid, as well as normal strongly interacting Fermi gas, must have an exceptionally small value of viscosity in order to exhibit almost perfect irrotational flow and follow the predictions of ideal hydrodynamics. This behavior motivates the prospect that a strongly interacting Fermi gas may be a near-ideal fluid with a viscosity close to the quantum viscosity limit.

In order to test this conjecture, it is necessary to measure the viscosity and entropy of a strongly interacting Fermi gas. By including dissipative terms in the ideal equations of hydrodynamics developed in Section 5.1, a model for the trap averaged value of ξ_η can be obtained, leading to an estimate of η. This

viscosity model is developed in Section 6.1. In order to obtain a value for the entropy density, an experiment was performed to determine the entropy, S, as a function of energy, E, of a strongly interacting Fermi gas [39]. The details of this experiment and a presentation of the results are given in Section 6.2. Using the results for η and S, the string theory limit for ultracold atoms can be tested. The outcome of this procedure is given in Section 6.3, providing an estimate of the degree to which a strongly interacting Fermi gas can be considered a perfect fluid.

6.1 Hydrodynamic equations with viscosity

In Section 5.1 a hydrodynamic theory was presented for the rotation and expansion of a strongly interacting Fermi gas. The theory was constructed assuming zero-viscosity hydrodynamics, which is directly applicable to an ideal, zero temperature superfluid Fermi gas. In the case of finite viscosity, additional dissipative terms must be added to the equations of motion to account for the irreversible nature of the flow. In Section 6.1.1 a simple hydrodynamic model for viscosity is introduced into the ideal Euler equation using the pressure tensor. Based on this model, equations of motion that include viscosity are derived in Section 6.1.2, which allow the angle and aspect ratio of a viscous rotating and expanding cloud to be predicted. The section ends with a discussion on the limitations of the simple viscosity model.

6.1.1 Euler equation revisited

The inclusion of viscosity into the equations of motion is relatively easy since it results in an additional force being added to the Euler equation, leaving the equation of continuity unaltered. Therefore the five equations produced in Section 5.1.2 from the equation of continuity will be exactly the same if viscosity is considered. However, the new shear viscosity force adds an additional level of complexity to the Euler equation, limiting the analysis to a trap average of the shear force in order to find analytic expressions for the equations of motion. In the presence of viscosity the Euler equation reads

$$\frac{\partial \mathbf{v}}{\partial t} + \boldsymbol{\nabla}\left(\frac{v^2}{2} + \frac{V_{ext}}{m} + \frac{cn^{\gamma}}{m}\right) - \mathbf{v} \times (\boldsymbol{\nabla} \times \mathbf{v}) = \frac{1}{mn}\,\boldsymbol{\nabla}\overrightarrow{P} \tag{6.3}$$

where the pressure tensor $\overrightarrow{P}$ takes the form [57]

$$\overrightarrow{P_{ij}} = \eta\left(\frac{\partial v_i}{\partial x_j} + \frac{\partial v_j}{\partial x_i} - \frac{2}{3}\,\delta_{ij}\,\boldsymbol{\nabla}\cdot\mathbf{v}\right) + \delta_{ij}\,\zeta\,\boldsymbol{\nabla}\cdot\mathbf{v} \tag{6.4}$$

and ζ is the bulk viscosity. It can be shown that the bulk viscosity vanishes in a normal strongly interacting gas, while two of the three bulk viscosities are identically zero in a superfluid gas [114]. For simplicity, ζ will neglected in this treatment and all dissipation will be considered to arise from the shear viscosity η. For the sake of consistency, the same ansatz for the density and stream velocity used in Section 5.1.2 will also be used in this analysis. Using equation (5.25) for the velocity field

$$\mathbf{v}(\mathbf{r},t) = \frac{1}{2}\,\boldsymbol{\nabla}\left(\alpha_x(t)\,x^2 + \alpha_y(t)\,y^2 + \alpha_z(t)\,z^2 + 2\alpha(t)\,xy\right) + \boldsymbol{\Omega}(t) \times \mathbf{r}, \tag{6.5}$$

the right hand side of equation (6.3) assumes the form

$$\begin{aligned}\frac{1}{mn}\boldsymbol{\nabla}\overrightarrow{P} &= \frac{2}{mn}\left[(\alpha_x-\bar{\alpha})\,\frac{\partial\eta}{\partial x}+\alpha\frac{\partial\eta}{\partial y}\right]\hat{\mathbf{x}} \\ &\quad+\frac{2}{mn}\left[(\alpha_y-\bar{\alpha})\,\frac{\partial\eta}{\partial y}+\alpha\frac{\partial\eta}{\partial x}\right]\hat{\mathbf{y}}+\frac{2}{mn}\left[(\alpha_z-\bar{\alpha})\,\frac{\partial\eta}{\partial z}\right]\hat{\mathbf{z}} \quad (6.6)\end{aligned}$$

where $\bar{\alpha}=(\alpha_x+\alpha_y+\alpha_z)/3$. It is interesting to note that the components of $\boldsymbol{\Omega}(t)$ do not appear in this equation due to that fact that a rigid rotation produces no shear. In the case of zero viscosity, five equations of motion were created by setting the coefficients of x, y, and z equal to zero separately in each of the $\hat{\mathbf{x}}$, $\hat{\mathbf{y}}$, and $\hat{\mathbf{z}}$ directions. This will not be possible if viscosity is included, mainly due to the fact that each term in equation (6.6) is divided by the density, $n(\mathbf{r})$, which is position dependent. The solution, therefore, is to do a trap average of the viscosity by multiplying both sides of equation (6.3) by $n(\mathbf{r})$, and integrating over the volume of the trap. This procedure and its consequences will be discussed in more detail below.

In the previous ideal case without viscosity in Section 5.1.2, an equation of the form $[C_{xx}\,x+C_{xy}\,y\,]\hat{\mathbf{x}}+[\,C_{yx}\,x+C_{yy}\,y\,]\hat{\mathbf{y}}+C_{zz}\,z\,\hat{\mathbf{z}}=0$ was produced from the left hand side of the Euler equation given by equation (6.3). When viscosity is included, the expression becomes more complex since the right hand side of the Euler equation is a complicated function of the coordinates and time. After multiplying both sides of equation (6.3) by the density, an expression of the form

$$\begin{aligned}&n(\mathbf{r})\,[[\,C_{xx}\,x+C_{xy}\,y\,]\,\hat{\mathbf{x}}+[\,C_{yx}\,x+C_{yy}\,y\,]\,\hat{\mathbf{y}}+C_{zz}\,z\,\hat{\mathbf{z}}]= \\ &\left[D_{xx}\,\frac{\partial\eta}{\partial x}+D_{xy}\,\frac{\partial\eta}{\partial y}\right]\hat{\mathbf{x}}+\left[D_{yx}\,\frac{\partial\eta}{\partial y}+D_{yy}\,\frac{\partial\eta}{\partial x}\right]\hat{\mathbf{y}}+\left[D_{zz}\,\frac{\partial\eta}{\partial z}\right]\hat{\mathbf{z}} \quad (6.7)\end{aligned}$$

is created, where the constants C_i and D_i are exclusively functions of time and contain all the terms that will eventually be used to construct the equations of motion. Five separate equations will ultimately be obtained from equation (6.7) by setting the expressions in the $\hat{\mathbf{x}}$, $\hat{\mathbf{y}}$, and $\hat{\mathbf{z}}$ directions equal to zero independently. For the sake of brevity, I will focus on the solution method in detail for the equation in the $\hat{\mathbf{x}}$ direction only, and simply state the solutions for the other directions.

The $\hat{\mathbf{x}}$ component of the Euler equation from equation (6.7) can be written in explicit form as

$$\begin{aligned} &n(\mathbf{r})\left(\dot{\alpha}-\dot{\Omega}+(\alpha_x+\alpha_y)(\alpha-\Omega)-\frac{\mu_0}{m}\,a\right)y+ \\ &n(\mathbf{r})\left(\dot{\alpha_x}+\alpha_x^2+\left(\alpha^2-\Omega^2\right)-\frac{2\mu_0}{m\sigma_x^2}\right)x=\frac{2}{m}\left[(\alpha_x-\bar{\alpha})\,\frac{\partial\eta}{\partial x}+\alpha\frac{\partial\eta}{\partial y}\right]. \end{aligned} \tag{6.8}$$

Previously, in the absence of viscosity ($\eta = 0$), the two expressions on the left side of equation (6.8) were set to zero independently, and constituted two of the five equations of motion. With finite viscosity, this procedure is not possible since equation (6.8) can no longer be separated into powers of x and y, as was done in Section 5.1.2 to create individual equations, due to the term $n(\mathbf{r})$. Instead, two independent equations can be constructed by performing a trap average of equation (6.8). This is accomplished by multiplying equation (6.8) by either x or y and integrating over the volume of the trap.

On the left hand side of equation (6.8) all of the position dependence is contained in the terms $x\,n(\mathbf{r})$ and $y\,n(\mathbf{r})$. Therefore if this equation is multiplied by

x or y and integrated over the volume of the trap, the usual mean square sizes

$$\frac{1}{N}\int d\mathbf{r}\, n(\mathbf{r})\, x^2 = \langle x^2\rangle = \frac{\sigma_x^2}{8}\frac{1}{1-a^2\sigma_x^2\sigma_y^2/4} \tag{6.9}$$

$$\frac{1}{N}\int d\mathbf{r}\, n(\mathbf{r})\, y^2 = \langle y^2\rangle = \frac{\sigma_y^2}{8}\frac{1}{1-a^2\sigma_x^2\sigma_y^2/4} \tag{6.10}$$

$$\frac{1}{N}\int d\mathbf{r}\, n(\mathbf{r})\, xy = \langle xy\rangle = -\frac{\sigma_x^2\sigma_y^2}{16}\frac{a}{1-a^2\sigma_x^2\sigma_y^2/4} \tag{6.11}$$

will be created. In order to express the mean square sizes in equations (6.9) through (6.11) in terms of the cloud widths, the density ansatz of Chapter 5,

$$n(\mathbf{r},t) = n_0(t)\left(1-\frac{x^2}{\sigma_x^2(t)}-\frac{y^2}{\sigma_y^2(t)}-\frac{z^2}{\sigma_z^2(t)}-a(t)\,xy\right)^{3/2}, \tag{6.12}$$

is used. Although the left hand side of equation (6.8) yields rather simple expressions after performing the integrals, the right hand side of the equation will produce a slightly more complex expression. When the right hand side is multiplied by x or y and integrated over the volume of the trap, a term of the form $\int d\mathbf{r}\, x\,\frac{\partial\eta}{\partial x}$ or $\int d\mathbf{r}\, y\,\frac{\partial\eta}{\partial y}$, respectively, will result. Integrating such an expression by parts produces the relation

$$\int d\mathbf{r}\, x\,\frac{\partial\eta}{\partial x} = \int d\mathbf{r}\, y\,\frac{\partial\eta}{\partial y} = -\int d\mathbf{r}\,\eta\,. \tag{6.13}$$

The same procedure of multiplying the right hand side of equation (6.8) by x or y that produced the expressions in equation (6.13) will also yield the cross terms $\int d\mathbf{r}\, x\,\frac{\partial\eta}{\partial y}$ or $\int d\mathbf{r}\, y\,\frac{\partial\eta}{\partial x}$. Integrating an expression of this type by parts yields

$$\int d\mathbf{r}\, x\,\frac{\partial\eta}{\partial y} = \int dx\, dz\, x\int dy\,\frac{\partial\eta}{\partial y} = \int dx\, dz\, x\,\eta = 0. \tag{6.14}$$

Therefore, unlike the left hand side of equation (6.8), all cross terms on the right hand side of the equation will vanish. Combining the results from equations (6.9) through (6.14), the Euler equation in the $\hat{\mathbf{x}}$ direction can be simplified to

$$\mathcal{F}_1(t)\langle xy\rangle + \mathcal{F}_2(t)\langle x^2\rangle = -\frac{2\left(\alpha_x - \bar{\alpha}\right)}{Nm}\int d\mathbf{r}\,\eta \tag{6.15}$$

when both sides of equation (6.8) are multiplied by x and integrated over the volume of the trap. The functions $\mathcal{F}_1(t)$ and $\mathcal{F}_2(t)$ in equation (6.15) are defined by

$$\dot{\alpha} - \dot{\Omega} + (\alpha_x + \alpha_y)(\alpha - \Omega) - \frac{\mu_0}{m}\,a = \mathcal{F}_1(t) \tag{6.16}$$

$$\dot{\alpha_x} + \alpha_x^2 + \left(\alpha^2 - \Omega^2\right) - \frac{2\mu_0}{m\sigma_x^2} = \mathcal{F}_2(t), \tag{6.17}$$

which are two of the zero viscosity equations of motion from Section 5.1.2. When both sides are multiplied by y and integrated, the formula

$$\mathcal{F}_1(t)\langle y^2\rangle + \mathcal{F}_2(t)\langle xy\rangle = -\frac{2\alpha}{Nm}\int d\mathbf{r}\,\eta. \tag{6.18}$$

is produced instead. Equations (6.15) and (6.18) constitute two of the five equations that can be generated from the Euler equation. Two other similar equations can be obtained by performing the same procedure for the terms in the $\hat{\mathbf{y}}$ direction, and the final equation is attained by multiplying the expression in the $\hat{\mathbf{z}}$ direction by z and integrating.

6.1.2 Development of the equations of motion

As stated at the beginning of this chapter, quantum viscosity in the unitary regime can be shown to be proportional to the density of atoms in the trap as expressed by $\eta = \xi_\eta \hbar\, n(\mathbf{r})$. In this form the viscosity is inherently a local variable, since it depends upon the local value of the density. In general, the constant ξ_η is a function of the local reduced temperature $T/T_F(n)$, which is conserved if the expansion is nearly isentropic, expressed as

$$\frac{T}{T_F\left[n(\mathbf{r})\right]} = \frac{T_0}{T_F\left[n_0(\tilde{\mathbf{r}}_0)\right]}\,. \tag{6.19}$$

In this expression, $\tilde{\mathbf{r}}_0$ denotes the initial coordinates of the cloud before the trap is extinguished and the expansion begins. Another quantity that is conserved during the expansion in the atom number

$$\int d\mathbf{r}\, n(\mathbf{r}) = N = \int d\tilde{\mathbf{r}}_0\, n_0(\tilde{\mathbf{r}}_0)\,. \tag{6.20}$$

The integral over the viscosity can be written in terms of an integral of the parameter ξ_η using $\eta = \xi_\eta \hbar\, n(\mathbf{r})$, yielding

$$\int d\mathbf{r}\, \eta = \hbar \int d\mathbf{r}\, n(\mathbf{r})\, \xi_\eta \left[\frac{T}{T_F[n(\mathbf{r})]}\right]\,. \tag{6.21}$$

Using the fact that the temperature and atom number are conserved during the expansion, the integral of η over the volume of the trap can be related to the initial trap average of ξ_η by

$$\int d\mathbf{r}\, \eta = \hbar \int d\tilde{\mathbf{r}}_0\, n_0(\tilde{\mathbf{r}}_0)\, \xi_\eta \left[\frac{T_0}{T_F[n_0(\tilde{\mathbf{r}}_0)]}\right] = N\hbar\, \langle \xi_\eta \rangle_0\,. \tag{6.22}$$

This relation allows the initial trap average of ξ_η, $\langle \xi_\eta \rangle_0$, to be included in the equations of motion, permitting the consequences of quantum viscosity to be estimated in a strongly interacting Fermi gas. A perfect fluid should have an exceptionally small value of $\langle \xi_\eta \rangle_0$, while a less ideal fluid will have an increasingly larger magnitude. By including the trap average of ξ_η in the equations of motion, the angle and aspect ratio for a viscous gas can be predicted as a function of $\langle \xi_\eta \rangle_0$ and compared to experimental data. By requiring the experimental data to overlap with the predicted angle and aspect ratio, an estimate for $\langle \xi_\eta \rangle_0$ can be obtained.

In order to construct a theory to estimate $\langle \xi_\eta \rangle_0$, the equations of motion must be written in terms of the time dependent coefficients σ_x, σ_y, σ_z, and a instead of the mean square sizes. Equations (6.15) and (6.18) can be put into the appropriate form by introducing the relation for ξ_η given by equation (6.22) and by using the appropriate form of the mean square sizes given in equations (6.9) through (6.11). Putting all of these equations together produces

$$\mathcal{F}_2(t) - \mathcal{F}_1(t)\frac{\sigma_y^2\, a}{2} = -\frac{16\,\hbar\,(\alpha_x - \bar{\alpha})\,(1 - a^2\sigma_x^2\sigma_y^2/4)}{m\sigma_x^2}\,\langle \xi_\eta \rangle_0 \tag{6.23}$$

$$\mathcal{F}_1(t) - \mathcal{F}_2(t)\frac{\sigma_x^2\, a}{2} = -\frac{16\,\alpha\,\hbar(1 - a^2\sigma_x^2\sigma_y^2/4)}{m\sigma_y^2}\,\langle \xi_\eta \rangle_0 \tag{6.24}$$

for the equations of motion.

The parameter $\langle \xi_\eta \rangle_0$ will vary depending upon the initial energy per particle, E_i, of the gas. The initial energy per particle can be obtained through the mean square size through the unitary gas identity $E_i = 3m\omega_x^2\langle x^2 \rangle_0$ as presented in Section 2.3.2. This equation represents the *initial* energy per particle of the gas before expansion. This energy can easily be measured by performing an

experiment under the same conditions without rotation. Since the widths of the cloud will also scale with energy, it is optimal to normalize them by their initial sizes. The initial density of the gas will be equal to equation (6.12) with $a = 0$, producing an initial mean square size in the x-direction of $\langle x^2 \rangle_0 = \sigma_{x_0}^2/8$, where σ_{x_0} is the initial width of the cloud in the x-direction. Therefore, the cloud widths can be written in terms of the initial energy per particle as

$$\sigma_{x_0}^2 = \frac{8E_i}{3m\omega_x^2}. \tag{6.25}$$

Using this expression, the normalized widths can be written as

$$\tilde{\sigma}_x^2 = \frac{\sigma_x^2}{\sigma_{x_0}^2} = \frac{3m\omega_x^2\sigma_x^2}{8E_i}. \tag{6.26}$$

A similar expression can be obtained for $\tilde{\sigma}_y^2$ and $\tilde{\sigma}_z^2$ by substituting ω_y^2 or ω_z^2, respectively, for ω_x^2 in equation (6.26). By including expressions of the form of (6.26) into the equations of motion given by equations (6.23) and (6.24), the expressions

$$\mathcal{F}_2(t) - \mathcal{F}_1(t)\frac{4a\,\tilde{\sigma}_y^2}{3m\omega_y^2}E_i = -\frac{6\,\hbar\,\omega_x^2\,(\alpha_x - \bar{\alpha})}{E_i\,\tilde{\sigma}_x^2}\left(1 - \frac{16a^2\,\tilde{\sigma}_x^2\,\tilde{\sigma}_y^2}{9m^2\omega_x^2\,\omega_y^2}E_i^2\right)\langle\xi_\eta\rangle_0 \tag{6.27}$$

and

$$\mathcal{F}_1(t) - \mathcal{F}_2(t)\frac{4a\,\tilde{\sigma}_x^2}{3m\omega_x^2}E_i = -\frac{6\,\hbar\,\omega_y^2\,\alpha}{E_i\,\tilde{\sigma}_y^2}\left(1 - \frac{16a^2\,\tilde{\sigma}_x^2\,\tilde{\sigma}_y^2}{9m^2\omega_x^2\omega_y^2}E_i^2\right)\langle\xi_\eta\rangle_0 \tag{6.28}$$

can be shown to result. Writing the equations in this form is advantageous since the dynamics can be fully described by specifying the initial energy per particle

E_i, viscosity coefficient $\langle\xi_\eta\rangle_0$, trap frequencies ω_i, and the initial angular velocity. All of the other initial conditions are either unity ($\tilde{\sigma}_x$, $\tilde{\sigma}_y$, $\tilde{\sigma}_z$) or zero (α_x, α_y, α_z, a), simplifying a numerical simulation of the dynamics.

The same methods developed to derive equations (6.27) and (6.28) from the $\hat{\mathbf{x}}$ direction of the Euler equation can be used to obtain the remaining three equations of motion for the $\hat{\mathbf{y}}$ and $\hat{\mathbf{z}}$ directions. When this is done the resulting equations can be shown to be

$$\tilde{\mathcal{F}}_2(t) - \tilde{\mathcal{F}}_1(t)\,\lambda_0^2\,\tilde{a}\,\tilde{\sigma}_y^2 = -6\,\frac{\omega_x^2\,(\alpha_x-\bar{\alpha})}{\bar{\omega}\,\tilde{\sigma}_x^2\,(3N)^{1/3}}\,\left(1-\lambda_0^2\,\tilde{a}^2\,\tilde{\sigma}_x^2\,\tilde{\sigma}_y^2\right)\frac{E_F}{E_i}\langle\xi_\eta\rangle_0 \tag{6.29}$$

$$\tilde{\mathcal{F}}_1(t) - \tilde{\mathcal{F}}_2(t)\,\tilde{a}\,\tilde{\sigma}_x^2 = -6\,\frac{\omega_y^2\,\alpha}{\bar{\omega}\,\tilde{\sigma}_y^2\,(3N)^{1/3}}\,\left(1-\lambda_0^2\,\tilde{a}^2\,\tilde{\sigma}_x^2\,\tilde{\sigma}_y^2\right)\frac{E_F}{E_i}\langle\xi_\eta\rangle_0 \tag{6.30}$$

$$\tilde{\mathcal{F}}_4(t) - \tilde{\mathcal{F}}_3(t)\,\tilde{a}\,\tilde{\sigma}_x^2 = -6\,\frac{\omega_y^2\,(\alpha_y-\bar{\alpha})}{\bar{\omega}\,\tilde{\sigma}_y^2\,(3N)^{1/3}}\,\left(1-\lambda_0^2\,\tilde{a}^2\,\tilde{\sigma}_x^2\,\tilde{\sigma}_y^2\right)\frac{E_F}{E_i}\langle\xi_\eta\rangle_0 \tag{6.31}$$

$$\tilde{\mathcal{F}}_3(t) - \tilde{\mathcal{F}}_4(t)\,\lambda_0^2\,\tilde{a}\,\tilde{\sigma}_y^2 = -6\,\frac{\omega_x^2\alpha}{\bar{\omega}\,\tilde{\sigma}_x^2\,(3N)^{1/3}}\,\left(1-\lambda_0^2\,\tilde{a}^2\,\tilde{\sigma}_x^2\,\tilde{\sigma}_y^2\right)\frac{E_F}{E_i}\langle\xi_\eta\rangle_0 \tag{6.32}$$

$$\tilde{\mathcal{F}}_5(t) = -6\,\frac{\omega_z^2\,(\alpha_z-\bar{\alpha})}{\bar{\omega}\,\tilde{\sigma}_z^2\,(3N)^{1/3}}\,\frac{E_F}{E_i}\langle\xi_\eta\rangle_0, \tag{6.33}$$

where the normalization $a = \frac{3m\omega_x^2}{4E_i}\,\tilde{a}$ was undertaken and $\lambda_0 = \omega_x/\omega_y \ll 1$ is the initial aspect ratio. The normalized parameter $\tilde{\mathcal{F}}_i(t)$ equations take the form

$$\dot{\alpha} - \dot{\Omega} + (\alpha_x+\alpha_y)(\alpha-\Omega) - \tilde{a}\,\omega_x^2\,\tilde{\mu} = \tilde{\mathcal{F}}_1(t) \tag{6.34}$$

$$\dot{\alpha_x} + \alpha_x^2 + \left(\alpha^2-\Omega^2\right) - \frac{\omega_x^2}{\tilde{\sigma}_x^2}\tilde{\mu} = \tilde{\mathcal{F}}_2(t) \tag{6.35}$$

$$\dot{\alpha} + \dot{\Omega} + (\alpha_x+\alpha_y)(\alpha+\Omega) - \tilde{a}\,\omega_x^2\,\tilde{\mu} = \tilde{\mathcal{F}}_3(t) \tag{6.36}$$

$$\dot{\alpha_y} + \alpha_y^2 + \left(\alpha^2-\Omega^2\right) - \frac{\omega_y^2}{\tilde{\sigma}_y^2}\tilde{\mu} = \tilde{\mathcal{F}}_4(t) \tag{6.37}$$

$$\dot{\alpha_z} + \alpha_z^2 - \frac{\omega_z^2}{\tilde{\sigma}_z^2}\tilde{\mu} = \tilde{\mathcal{F}}_5(t) \tag{6.38}$$

where the normalization of the chemical potential to its initial value, $\mu = \frac{4}{3} E_i \, \tilde{\mu}$, has been made. This choice of normalization is justified since it can shown that when the density ansatz of equation (6.12) is used, the initial chemical potential at the center of the trap is $\mu_0 = c n_0^{2/3} = \frac{4}{3} E_i$, since a zero temperature shape is assumed for the density. This theory will be used to model expansion dynamics at finite temperatures, so μ is essentially being used as a energy scale in the equations. The gas is assumed to roughly maintain a zero temperature shape as the temperature increases, but the cloud radii increase from their ground state values and the density at the center of the trap decreases. Using a normalization of this type leads to the initial value of the chemical potential equaling unity $\tilde{\mu}(0) = 1$.

In the equations of motion given by equations (6.29) through (6.38), an understanding of the role that the viscosity has on the dynamics is obscured by the complexity of the expressions. Therefore it is beneficial to put them in a more transparent form. By adding and subtracting equations (6.29) through (6.32) successively, the following simplified equations can be shown to result

$$\dot{\Omega} + \Omega(\alpha_x + \alpha_y) = \frac{3\omega_x^2}{\bar{\omega}\,(3N)^{1/3}} \left[(\alpha_x - \alpha_y)\tilde{a} + \alpha \frac{\tilde{\sigma}_x^2 - \lambda_0^2\,\tilde{\sigma}_y^2}{\lambda_0^2\,\tilde{\sigma}_x^2\,\tilde{\sigma}_y^2} \right] \frac{E_F}{E_i} \langle \xi_\eta \rangle_0 \tag{6.39}$$

$$\dot{\alpha} + \alpha(\alpha_x + \alpha_y) = \tilde{a}\,\omega_x^2\,\tilde{\mu} - \frac{3\omega_x^2}{\bar{\omega}\,(3N)^{1/3}} \left[\bar{\alpha}'\,\tilde{a} + \alpha \frac{\tilde{\sigma}_x^2 + \lambda_0^2\,\tilde{\sigma}_y^2}{\lambda_0^2\,\tilde{\sigma}_x^2\,\tilde{\sigma}_y^2} \right] \frac{E_F}{E_i} \langle \xi_\eta \rangle_0 \tag{6.40}$$

$$\left[\dot{\alpha_x} + \alpha_x^2 + \left(\alpha^2 - \Omega^2\right)\right] \frac{\tilde{\sigma}_x^2}{\omega_x^2} = \tilde{\mu} - 6 \frac{(\alpha_x - \bar{\alpha} + \alpha\,\tilde{\sigma}_x^2\,\tilde{a})}{\bar{\omega}\,(3N)^{1/3}} \frac{E_F}{E_i} \langle \xi_\eta \rangle_0 \tag{6.41}$$

$$\left[\dot{\alpha_y} + \alpha_y^2 + \left(\alpha^2 - \Omega^2\right)\right] \frac{\tilde{\sigma}_y^2}{\omega_y^2} = \tilde{\mu} - 6 \frac{\left(\alpha_y - \bar{\alpha} + \alpha\,\lambda_0^2\,\tilde{\sigma}_y^2\,\tilde{a}\right)}{\bar{\omega}\,(3N)^{1/3}} \frac{E_F}{E_i} \langle \xi_\eta \rangle_0 \tag{6.42}$$

$$\left[\dot{\alpha_z} + \alpha_z^2\right] \frac{\tilde{\sigma}_z^2}{\omega_z^2} = \tilde{\mu} - 6 \frac{(\alpha_z - \bar{\alpha})}{\bar{\omega}\,(3N)^{1/3}} \frac{E_F}{E_i} \langle \xi_\eta \rangle_0 \tag{6.43}$$

where $\bar{\alpha}' = \alpha_x + \alpha_y - 2\bar{\alpha}$. When the equations of motion are written in this form,

it is clear that for vanishing viscosity ($\langle \xi_\eta \rangle_0 = 0$) they will reduce to the same equations derived in Section 5.1.2, except in normalized variables.

Equations (6.39) through (6.43) may look a bit overwhelming at first glance, but a physical interpretation of the equations can be inferred by looking at a few salient features. First, the scaling of the viscosity represented in these equations makes physical sense. In a simple classical collisional model, the viscosity is proportional to the particle momenta, p, mean free path, l, and number density, n, leading to $\eta \propto p\, l\, n$. All of the viscosity terms in equations (6.39) through (6.43) are inversely proportional to the initial energy of the gas E_i/E_F. This is consistent with the simple model for viscosity since the gas will become more dilute as the energy increases, decreasing n and reducing the magnitude of the viscosity. Additionally, all of the viscosity terms contain the α_i coefficients that describe the magnitude of the stream velocity v. A simple model for the shear force, F_η, due to viscosity states that $F_\eta \propto \eta\, v$. Therefore, the shear force driving the dynamics should be proportional to the stream velocity, which is also reflected in equations (6.39) through (6.43).

Due to the choice of normalization for the time dependent parameters, the initial conditions in the $i = x, y, z$ directions can be expressed as

$$\tilde{\sigma}_i(0) = \tilde{\mu}_0(0) = 1 \tag{6.44}$$

$$\alpha_i(0) = \tilde{a}(0) = 0 \tag{6.45}$$

with the initial condition on the angular velocity being $\alpha = \Omega_0$ and $\Omega = 0$ for pure *irrotational* flow and $\alpha = 0$ and $\Omega = \Omega_0$ for pure *rotational* flow. This makes modeling the dynamics exceptionally easy since the only input parameters

are the trap frequencies, ω_i, the initial energy per particle of the gas E_i/E_F, the viscosity coefficient $\langle\xi_\eta\rangle_0$, and the initial angular velocity Ω_0. The ground state equations of Section 5.1.2 can be recovered by setting $E_i/E_F = 0.48$ [36] and $\langle\xi_\eta\rangle_0 = 0$, necessitating only a determination of the trap frequencies and initial angular velocity to simulate the dynamics.

The five expressions given in equations (6.39) through (6.43) were obtained through the use of the Euler equation with the addition of viscosity. The remaining five differential equations can be found using the equation of continuity. Since the equation of continuity describes the conservation of flow regardless of the forces acting on the fluid, the expressions stemming from the equation of continuity will be unchanged from the ones derived in Section 5.1.2. Writing these equations in the normalized coordinates yields

$$\dot{\tilde{\mu}} + \frac{2}{3}\,\tilde{\mu}\,(\alpha_x + \alpha_y + \alpha_z) = 0 \tag{6.46}$$

$$\dot{\tilde{a}} + \frac{(\alpha - \Omega)}{\tilde{\sigma}_x^2} + \frac{(\alpha + \Omega)}{\lambda_0^2\,\tilde{\sigma}_y^2} + \tilde{a}\,(\alpha_x + \alpha_y) = 0 \tag{6.47}$$

$$\dot{\tilde{\sigma}}_x - \tilde{\sigma}_x\alpha_x - \tilde{\sigma}_x^3\,\tilde{a}\,(\alpha + \Omega) = 0 \tag{6.48}$$

$$\dot{\tilde{\sigma}}_y - \tilde{\sigma}_y\alpha_y - \lambda_0^2\,\tilde{\sigma}_y^3\,\tilde{a}\,(\alpha - \Omega) = 0 \tag{6.49}$$

$$\dot{\tilde{\sigma}}_z - \tilde{\sigma}_z\alpha_z = 0. \tag{6.50}$$

Since the aspect ratio $\lambda_0 \ll 1$, it is fairly easy to tell which terms in the equations of motion will dominate the dynamics.

It is interesting to note how weakly dependent the equations of motion are on the equation of state. This was seen previously in Chapter 5 for the equations of motion in the absence of viscosity. An underlying assumption used in the Euler equation is that the chemical potential can be expressed as $\mu = cn^\gamma$. The

equations of motion presented in this section are independent of the constant c, and the index γ only appears as the factor of 2/3 in equation (6.46).

Previously in Section 5.1.2, expressions for the angle and aspect ratio were given as a function of the parameters a and σ_i. Since normalizations were introduced in this section that change the definitions of these time dependent parameters, the expressions for the angle and aspect ratio have to be modified also. In the new normalized variables, the expression for the angle ϕ of the principal axes becomes

$$\tan 2\phi = -2\tilde{a}\frac{\lambda_0^2\,\tilde{\sigma}_x^2\tilde{\sigma}_y^2}{\tilde{\sigma}_x^2 - \lambda_0^2\,\tilde{\sigma}_y^2}\,, \tag{6.51}$$

while the aspect ratio converts to

$$\lambda = \left[\frac{\left(\tilde{\sigma}_x^2 + \lambda_0^2\,\tilde{\sigma}_y^2\right) - \sqrt{\left(\tilde{\sigma}_x^2 - \lambda_0^2\,\tilde{\sigma}_y^2\right)^2 + 4\lambda_0^4\,\tilde{a}^2\,\tilde{\sigma}_x^4\,\tilde{\sigma}_y^4}}{\left(\tilde{\sigma}_x^2 + \lambda_0^2\,\tilde{\sigma}_y^2\right) + \sqrt{\left(\tilde{\sigma}_x^2 - \lambda_0^2\,\tilde{\sigma}_y^2\right)^2 + 4\lambda_0^4\,\tilde{a}^2\,\tilde{\sigma}_x^4\,\tilde{\sigma}_y^4}}\right]^{1/2}. \tag{6.52}$$

At the beginning of the expansion $a(0) = 0$ and $\tilde{\sigma}_x(0) = \tilde{\sigma}_y(0) = 1$, so the aspect ratio can easily be shown to reduce to $\lambda(0) = \lambda_0 = \omega_x/\omega_y$ as it should.

A prediction for the angle and aspect ratio as a function of time can be simulated by solving equations (6.39) through (6.43) and equations (6.46) through (6.50) numerically. A result of the simulation is displayed in Figure 6.1. In each plot, the ideal $\langle\xi_\eta\rangle_0 = 0$ simulation is given as a solid line for the angle and aspect ratio. Two additional curves that include the effects of viscosity are given for $\langle\xi_\eta\rangle_0 = 1$ and 2. The harmonic trap ground state energy of $E_i/E_F = 0.48$ is used in all the curves, and the initial velocity is $\Omega_0 = 0.4\,\omega_x$, which is the same condition used for the experiments presented in Section 5.3. Since the ratio of the viscosity coefficient, $\langle\xi_\eta\rangle_0$, to the initial energy per particle, E_i, enter into all

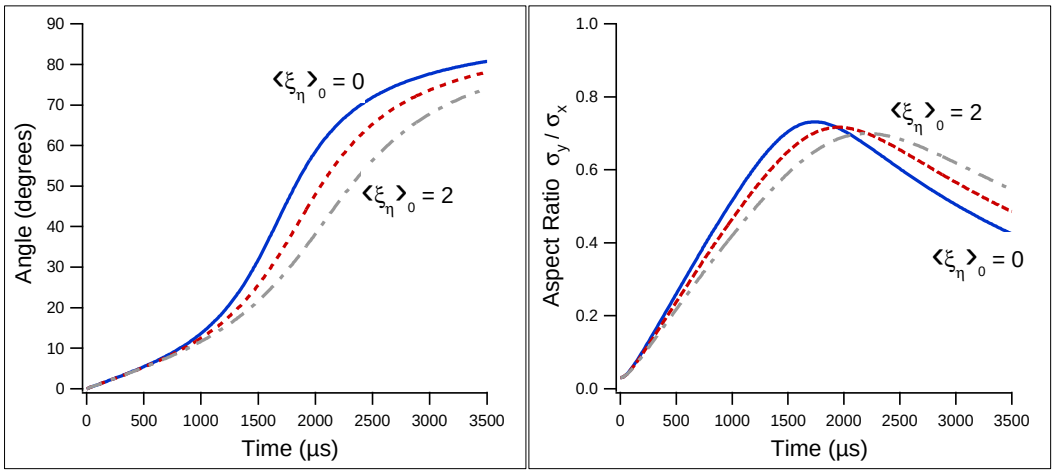

Figure 6.1: Plot of the angle and aspect ratio for different values of $\langle \xi_\eta \rangle_0$. The solid line in the figure is for the ideal case of $\langle \xi_\eta \rangle_0 = 0$. The dashed and dot-dashed lines are for $\langle \xi_\eta \rangle_0 = 1$ and $\langle \xi_\eta \rangle_0 = 2$, respectively. The initial angular velocity is $\Omega_0 = 0.4\,\omega_x$ and the energy per particle is $E_i/E_F = 0.48$, corresponding to the ground state.

the equations of motion in an identical way, the curves presented in Figure 6.1 will demonstrate the same behavior if the viscosity coefficient and initial energy are increased or decreased by the same factor. For example, the theoretical curve for $E_i/E_F = 1/2$ and $\langle \xi_\eta \rangle_0 = 1$ will be identical to the curve for $E_i/E_F = 1$ and $\langle \xi_\eta \rangle_0 = 2$. Therefore if a higher energy gas exhibits dynamics that deviate substantially from the ideal predictions, the viscosity must be becoming exceptionally large.

As shown in Figure 6.1, when the viscosity increases, the peak in the aspect ratio shifts later in time and the slope of the angle curve becomes more flat, indicating that the maximum angular velocity during the expansion is suppressed. This makes intuitive sense since the dissipative forces acting in a viscous fluid would act to dampen the motion, prohibiting the flow from rotating as quickly as it could in the ideal case. This behavior is reflected in the plot of the aspect ratio,

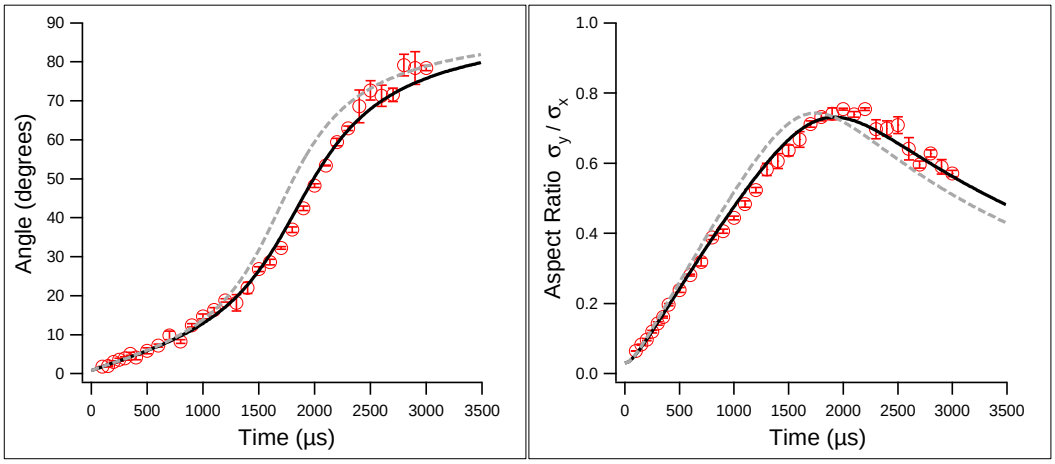

Figure 6.2: Plot of the angle and aspect ratio illustrating the effect of viscosity on the resulting dynamics. The dashed curve represents the ideal theory for $\langle \xi_\eta \rangle_0 = 0$, while the solid line was simulated under the conditions of $\langle \xi_\eta \rangle_0 = 4.4$ and $E_i/E_F = 2.1$. The initial energy used in the simulation is the same energy measured for the experimental data, indicated by open circles.

where the maximum aspect ratio is suppressed as the magnitude of the viscosity increases.

The effects of viscosity on experimental data can be clearly seen in Figure 6.2. The experimental data in the figure has a measured initial energy of $E_i/E_F = 2.1$. Displayed with the data are a dashed line modeled with $\langle \xi_\eta \rangle_0 = 0$ for the ideal case, and a solid line simulated with $\langle \xi_\eta \rangle_0 = 4.4$. This later value was obtained by a least squares fit of the theory to the data, which will be described later in Section 6.3.1. As illustrated in Figure 6.2, the finite viscosity theory distinctly follows the data much closer than the ideal theory, providing evidence that the simple viscosity model can account for the effects observed in the rotation and expansion of a viscous gas.

6.1.3 Viscosity model limitations

The simple hydrodynamic quantum viscosity model presented in this chapter allows the effects of viscosity to be included in the equations of motion, but like all theories it does have its limitations. The deficiencies stem from the assumptions needed to create such a simple model, as well as the validity of using a hydrodynamic model to describe the gas at the outer edges of the atom cloud, as discussed below.

One of the more transparent shortcomings of the model is in the density ansatz given by equation (6.12). At time $t = 0$ the time dependent parameter a vanishes and the expression for the density reduces to that of a zero temperature Thomas-Fermi distribution. Using a density of this form is rigorously valid for a gas in the ground state, but a finite temperature gas will have a density distribution that follows a slightly different shape. Therefore care must be taken when applying this model to gases with energies far above the ground state. In order to derive the density in equation (6.12), a chemical potential of the form $\mu = cn^{\gamma}$ was used, where c and γ are constants. While deriving the equations of motion it was found that they were independent of c, and only weakly dependent upon γ (see equation (6.46)). Therefore, the resultant expansion dynamics should not drastically depend upon the form of the density used to fit the initial distribution, especially since the hydrodynamics are mainly determined by the initial aspect ratio in the trap, λ_0, and the trap frequencies, ω_i, which remain fixed as the energy of the gas is increased.

An additional limitation for the simple model is the validity of defining a trap average of the viscosity through the parameter $\langle \xi_\eta \rangle_0$. This parameter was defined in equation (6.22) as $\int d\mathbf{r}\, \eta = N\hbar \langle \xi_\eta \rangle_0$, where the integral is taken over

the volume of the trap. The quantum viscosity η is a hydrodynamic variable and therefore only applies to a fluid in the hydrodynamic regime. Towards the edges of the trap, especially at higher energies, the gas ceases to be hydrodynamic and a viscous description of the gas is no longer applicable. In order to be rigorous, the integral over the volume of the trap should be truncated to only include the regions of the gas that are truly hydrodynamic [115, 116]. This restriction was not incorporated into the model developed in this chapter.

6.2 Entropy measurement

In addition to the viscosity model developed in Section 6.1, a value for the entropy is needed to calculate the ratio η/s. This section will describe an experiment undertaken to measure the entropy of a unitary gas as a function of energy.

A strongly interacting Fermi gas is a complicated many-body system. The complexity of the interactions between particles makes calculations of the basic thermodynamic properties rather difficult. To calculate the entropy, for example, the most recent pseudogap, NSR, and quantum Monte Carlo techniques must be used [35,36,117]. On the other hand, a noninteracting Fermi gas is a rather simple system to study. The expressions for the thermodynamic variables E, S, and T are accessible by simply knowing the occupation number, $f(\epsilon)$, and density of states, $D(\epsilon)$ for atoms in the trap with energy ϵ. In contrast, the only parameter that is easily measured in the strongly interacting regime is the energy, which is related to the mean square cloud size through the use of the virial theorem [56].

The difficulty of determining the thermodynamics in the strongly interacting regime can be alleviated if a method for an isentropic passage to the noninteracting

regime is developed. In such an isentropic process, the entropy would be conserved and the value measured in the noninteracting regime would equal the value in the strongly interacting regime. In our system, an isentropic magnetic field sweep allows the entropy, and thus the thermodynamics, to be connected in the two regimes. Since the energy can be calculated in a model independent way, this allows the entropy of a strongly interacting Fermi gas to be determined as a function of energy in a rigorous, model independent way.

This section presents the results of the entropy experiment. In Section 6.2.1 the experimental procedures involved in the entropy experiment are given. This is followed by a presentation of the results of the experiment in Section 6.2.2, providing measurements of the entropy as a function of energy. These measurements are critical for an accurate estimate of the ratio η/s.

6.2.1 Experimental procedures for entropy measurement

One of the primary motivations behind measuring the entropy of a strongly interacting Fermi gas is that it allows access to the thermometry of the gas. If the entropy, S, is measured as a function of total energy, E, the temperature of the gas can be determined through the fundamental relation $T = \partial E/\partial S$. This is of fundamental importance since a model independent experimental determination of the temperature of a unitary gas has been elusive until the following study was completed.

The energy of a strongly interacting Fermi gas can be determined from the mean square cloud size as discussed in Section 2.3.2. This is an incredibly useful result since thermometry is very difficult in a complicated many-body system such as a strongly interacting superfluid. In most experiments it is instructive to

measure the properties of the gas in the superfluid as well as normal fluid regimes, requiring a parameter to characterize the state of the gas. A measurement to the total energy through the mean square cloud size provides a model independent method of producing such a parameter.

The entropy experiment was done at a magnetic field of 840 Gauss, which is slightly above the broad Feshbach resonance at 834 Gauss. At this field the gas is still strongly interacting [58], allowing the relationship

$$E_{840} = 3m\omega_x^2 \langle x^2 \rangle_{840} \, (1 - \kappa) \tag{6.53}$$

to be used for the total energy per particle of the gas, E_{840}, at 840 Gauss. The correction factor $1-\kappa$ arises from anharmonicity[1] in the shallow trapping potential ($U_0 \simeq 10E_F$) used in the experiments. The total energy can be normalized to the Fermi energy of a noninteracting gas at the center of the trap, $E_F = \hbar\bar{\omega}(3N)^{1/3}$, where $\bar{\omega} = (\omega_x\omega_y\omega_z)^{1/3}$. Making use of the definition $3m\omega_x^2 x_F^2 = E_F$, equation (6.53) can be written as

$$\frac{E_{840}}{E_F} = \frac{\langle x^2 \rangle_{840}}{x_F^2} \, (1 - \kappa) \, , \tag{6.54}$$

where x_F^2 is the mean square size of a noninteracting gas in the x-direction. The extent of the anharmonic correction given by the correction factor $1 - \kappa$ depends upon the amount of energy contained in the gas. As the gas is heated it becomes larger in the trap, an the effects of anharmonicity increase. For the experiments used to measure the entropy, it is found that κ varies from 3% in the lowest energy

[1] If the trap potential is approximated by a gaussian, $U = U_0\{1 - \exp[-m\bar{\omega}^2 r^2/(2U_0)]\}$, the correction factor becomes $\kappa = 5m\omega_x^2\langle x^4 \rangle / \left(8U_0\langle x^2 \rangle\right)$. For energies above E_F, where the spatial distribution in the trap is nearly Gaussian, one readily obtains $\langle x^4 \rangle = 3\langle x^2 \rangle^2$ and $\kappa = (5E_F/8U_0) \, \langle x^2 \rangle / x_F^2$.

data to 13% at the highest.

For a typical experiment, $N \simeq 1.3 \times 10^5$ atoms are produced in the optical trap characterized by radial frequencies $\omega_y = 2\pi \times 764$ Hz and $\omega_z = 2\pi \times 665$ Hz. The axial trap frequency is $\omega_x = 2\pi \times 30.1$ Hz at 840 Gauss and $\omega_x = 2\pi \times 33.2$ Hz at 1200 Gauss. The axial frequency is different at the two magnetic fields due to the small change in the trapping potential arising from the magnetic field curvature. This frequency change is negligible in the radial directions. These parameters are used in conjunction with a measurement of the mean square cloud size in the axial direction at 840 Gauss, $\langle x^2 \rangle_{840}$, to obtain the total energy of a strongly interacting Fermi gas through equation (6.54).

The entropy in the strongly interacting regime at 840 Gauss can be measured through the use of and adiabatic sweep of the magnetic field to 1200 Gauss, where the gas is weakly interacting and the entropy can be estimated from the mean square cloud size in the axial direction, $\langle x^2 \rangle_{1200}$. Since the magnetic field sweep is adiabatic, the entropy of the weakly interacting gas at 1200 Gauss will be equal to the entropy of the strongly interacting gas at 840 Gauss. At a particular magnetic field, the magnitude of the interactions in the gas can be characterized by the parameter $k_F a_s$, where $k_F = (2mE_F/\hbar^2)^{1/2}$ is the Fermi wavevector. The smaller the value of $k_F a_s$, the more weakly interacting a gas is considered to be. At a magnetic field of 1200 Gauss the s-wave scattering length is reduced to $a_s = -2900$ bohr [58], which is close to the background scattering length of ^{6}Li of -2240 bohr [118, 119]. The trap depth used is this experiment, $U_0 \simeq 10E_F$, is relatively shallow resulting in an interaction parameter of $k_F a_s = -0.75$. By comparison, $k_F a_s$ is infinite at the Feshbach resonance where the scattering length diverges. Since $k_F a_s$ is small at 1200 Gauss, the gas is very weakly interacting.

Additionally, the cloud is also observed to expand ballistically at this field, even at the lowest temperatures. Since ballistic expansion only occurs in a weakly interacting gas, this shows that the interactions are small and that the gas is normal as opposed to superfluid.

To calculate the entropy, the atoms at 1200 Gauss can be approximated by a noninteracting gas in a Gaussian potential since the interactions at that field are almost negligible. The occupation number for a Fermi gas at a given energy level ϵ and chemical potential μ is

$$f(\epsilon) = \frac{1}{e^{(\epsilon-\mu)/k_B T} + 1}. \tag{6.55}$$

The chemical potential can be found as a function of T/T_F by normalizing to the atom number, N, by integrating $f(\epsilon)$ with the density of states for a gaussian potential, $\mathcal{D}(\epsilon)$, over all energies ϵ. A similar integral can be used to find the spatial density, $n(\mathbf{r})$, which is needed to calculate the mean square size, $\langle x^2 \rangle$, as a function of T/T_F. The entropy per particle, $S(T/T_F)$, is obtained by integrating the entropy per orbital $s(\epsilon)$ for a noninteracting gas with the density of states

$$S(T/T_F) = 2\int d\epsilon\, \mathcal{D}(\epsilon)\, s(\epsilon) = -2k_B \int_0^\infty d\epsilon\, \mathcal{D}(\epsilon)\, \left[f \ln f + (1-f)\ln(1-f)\right], \tag{6.56}$$

where the factor of 2 comes from the fact that there are two spin states per energy level. Since both $\langle x^2 \rangle$ and S can be calculated as a function of T/T_F, the relationship $S\left(\langle x^2 \rangle\right)$ can be numerically calculated to associate the entropy of the gas at 1200 Gauss to the measured mean square size. Since the sweep from 840 to 1200 Gauss is adiabatic, the calculated noninteracting Fermi gas entropy will also be equal to the entropy in the strongly interacting regime.

6.2.2 Entropy experiment results

In order to measure the Entropy as a function of energy, $S(E)$, the mean square size is measured in separate experiments at 840 and 1200 Gauss under the same conditions. Starting with and energy close to the ground state, the gas can be heated using the release and recapture method described in Section 4.8.2 for exciting breathing modes. By letting the gas expand for a variable duration before the trap is reinstated, the final energy of the gas can be precisely controlled. A measurement of $\langle x^2 \rangle_{840}$ will give the energy in the unitary regime through the use of equation (6.54). Likewise, a measurement of $\langle x^2 \rangle_{1200}$ will yield the strongly interacting entropy S as described in Section 6.2.1.

A plot of the ratio of the measured mean square sizes at 1200 and 840 Gauss is given in Figure 6.3. Since there exists an attractive mean field at magnetic fields near the Feshbach resonance centered at 834 Gauss, an atom cloud at that field will be smaller than the same cloud in the noninteracting regime. Therefore, the ratio in the figure is substantially above unity for energies close to the ground state. As the energy is increased, the ratio asymptotically approaches unity as the mean field energy becomes small in comparison to the thermal energy. The abrupt change in slope of the data at an energy close to 0.9 E/E_F can be interpreted as a transition from superfluid to normal fluid behavior. Further details about this transition can be found in reference [84].

The data in Figure 6.3 can be converted into an entropy measurement using the procedure described in Section 6.2.1. Figure 6.4 displays the resulting entropy per particle of a strongly interacting gas in units of k_B. The entropy is plotted against the energy per particle in the unitary regime in units of E_F. Also shown in the figure is the expected entropy for a noninteracting ideal gas. It is clearly

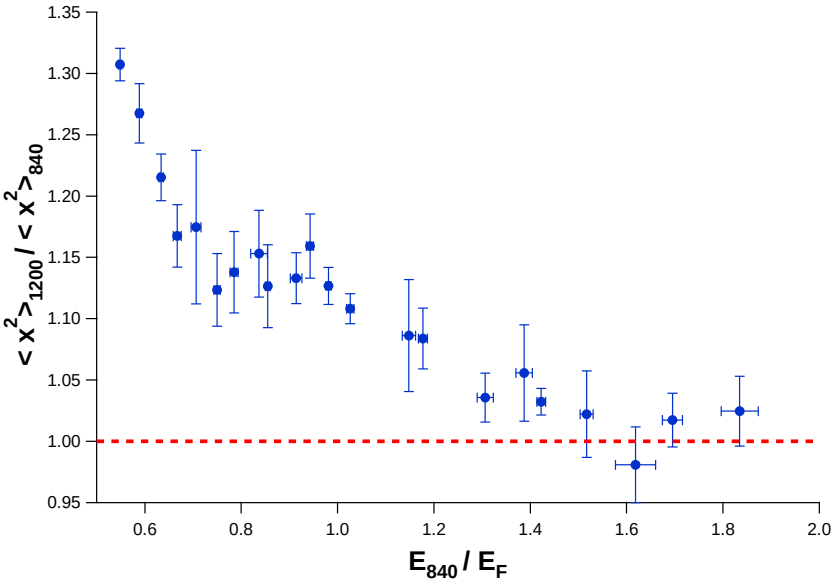

Figure 6.3: Size ratio of a noninteracting Fermi gas, $\langle x^2 \rangle_{1200}$, to a unitary Fermi gas, $\langle x^2 \rangle_{840}$, as a function of the energy in the strongly interacting regime. The dashed line indicates where the ratio becomes unity.

seen that for a particular value of S, at low values of E the energy of a strongly interacting gas is much smaller than for an ideal gas, reflecting the results seen in Figure 6.3. The calculated ideal gas entropy also asymptotically approaches the measured strongly interacting entropy at high energy. This is also reflected in Figure 6.3 by the ratio of mean square sizes approaching unity at high energy. The high energy behavior can be understood by the mean field energy becoming dwarfed by the thermal energy, leading to the cloud sizes becoming almost equal in the two regimes. It is interesting to note that this occurs at approximately $E = 2.0\,E_F$, which close to the point where the dynamics of the rotating gas experiment of Section 5.3 begin to depart from ideal hydrodynamics.

The additional dotted and dashed curves in Figure 6.4 present two theoretical curves for the entropy of a strongly interacting Fermi gas. The dotted curve is

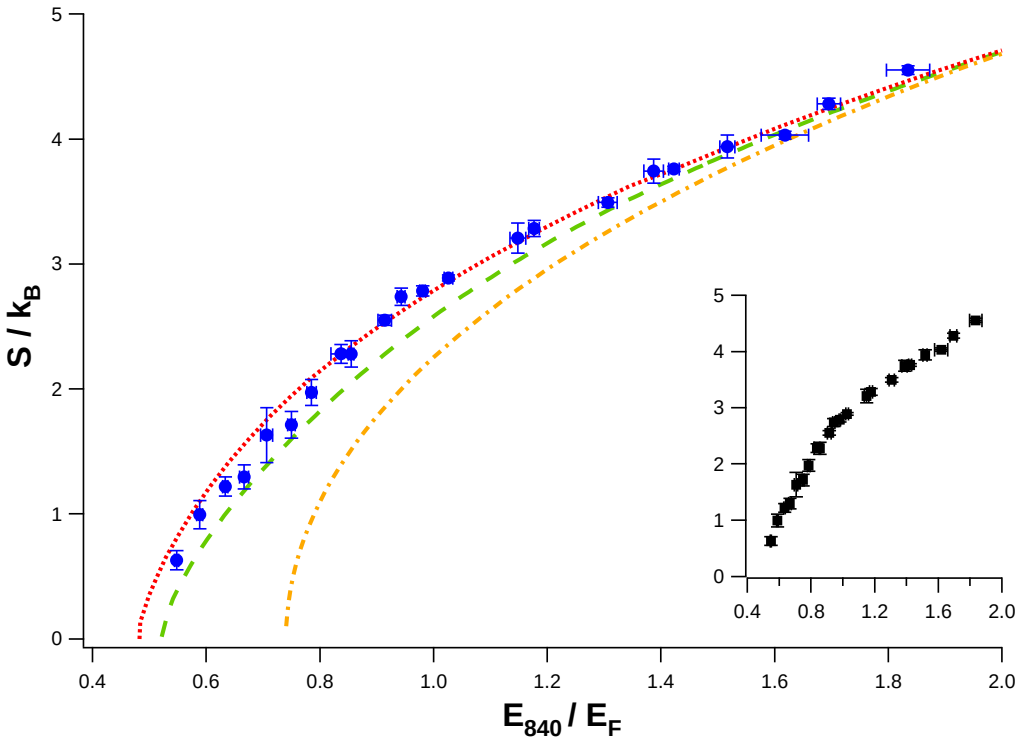

Figure 6.4: Plot of the entropy per particle of a strongly interacting fermi gas as a function of energy per particle at 840 Gauss. The solid dots represent the data, while the dotted line gives a quantum Monte Carlo result and the dashed line is a prediction based on pseudogap theory. The dot-dashed line below the data is the entropy expected for a noninteracting ideal gas. The inset displays the data in the absence of the theoretical curves.

based on a quantum Monte Carlo simulation [35], while the dashed curve gives the prediction based on pseudogap theory [117]. The quantum Monte Carlo result follows the measurements more closely than the pseudogap theory, especially at low energies. In addition to the theories presented in Figure 6.4, a comparison to the experiment has been made using a theory based upon NSR theory [36]. A calculation for the entropy as a function of energy presented in that work is in excellent agreement with the data in Figure 6.4, further bolstering the validity of the experimental results.

As well as providing a test-bed for many-body theories, the measurement of the entropy as a function of energy also provides a method of temperature measurement in the unitary regime. By parameterizing the data in Figure 6.4, the temperature as a function of energy can be found through the thermodynamic identity $\partial S/\partial E = 1/T$. An inset is provided in Figure 6.4, which displays the entropy data in the absence of any theoretical curves. A change in the slope can clearly be seen in the data found in the inset, indicating a change in the properties of the gas above and below a critical energy value. This critical energy can be interpreted as the superfluid transition energy [39]. By parameterizing the data with a different power law above and below the critical energy, the temperature can be obtained by taking the derivative of the resultant curves. After this procedure is followed, a superfluid transition temperature of $T_c/T_F = 0.29 \pm 0.03$ with a corresponding critical energy of $E_c/E_F = 0.94 \pm 0.05$ is found to result [39].

6.3 Viscosity estimate

As discussed at the beginning of this chapter, there is a conjectured fundamental limit for the ratio of the viscosity to the entropy density, η/s, predicted using string theory methods. The minimum value is determined to be $1/4\pi$ in units of $\hbar/k_B$ and is expected to result only for a perfect fluid. In this section, an estimate of η/s is attempted using the viscosity model in Section 6.1 along with the entropy data in Section 6.2. The ratio of the viscosity to the entropy density can be related to the parameters in those sections by integrating the numerator and denominator over the volume of the trap yielding

$$\frac{\eta}{s} \simeq \frac{\int d\mathbf{r}\, \eta}{\int d\mathbf{r}\, s} = \frac{\hbar}{k_B} \frac{\langle \xi_\eta \rangle_0}{S/k_B}, \tag{6.57}$$

where S is the entropy per particle. An estimate for the coefficient $\langle \xi_\eta \rangle_0$ can be obtained by fitting experimental expansion data with the viscosity model developed in Section 6.1. Dividing this value by the entropy per particle measured in Section 6.2 will give an estimate for the magnitude of η/s.

6.3.1 Determining $\langle \xi_\eta \rangle_0$

The first step in evaluating η/s is obtaining an estimate of the coefficient $\langle \xi_\eta \rangle_0$. The simple hydrodynamic model for viscosity developed in Section 6.1 is fully described through a knowledge of the trap frequencies ω_i, the total atom number N, the initial energy per particle E_i/E_F, the initial angular velocity Ω_0, and the viscosity coefficient $\langle \xi_\eta \rangle_0$. The trap frequencies can be determined using the parametric resonance technique described in Section 4.8.2, and the atom number along with the initial energy can be measured using the cloud images. In addition,

the procedure for obtaining Ω_0 from the angle versus time data is provided in Section 5.4.2, leaving $\langle\xi_\eta\rangle_0$ as the only free parameter in the model that can not be measured directly. However, a least-squares fit of the model to the angle versus time data or the aspect ratio data can provide an estimate for $\langle\xi_\eta\rangle_0$.

A least squares fit to the experimental data can be achieved by calculating the square of the deviation between the model and data through the function $\chi^2 = \sum_i(\phi_i - f_i(\langle\xi_\eta\rangle_0))^2/\sigma_i^2$, where ϕ_i is a data point for the angle of the cloud at a particular time and $f_i(\langle\xi_\eta\rangle_0)$ is the value of the theoretical model for a given value of $\langle\xi_\eta\rangle_0$ at the same point in time. The variance for each data point, σ_i^2, is assumed to be uniform for all data points in the analysis. This restriction is employed because it was found that the data points at the beginning and end of the expansion, which are relatively insensitive to $\langle\xi_\eta\rangle_0$, typically have very small error bars and unduly influence the least squares fit resulting in a curve that does not reliably represent the entire data set when determining $\langle\xi_\eta\rangle_0$.

By finding the value of $\langle\xi_\eta\rangle_0$ that minimizes χ^2, an estimate for the viscosity coefficient can be found. The result of this procedure is displayed in Figure 6.5 for gases of varying initial energies. Displayed in this figure is preliminary data for four experiments at energies above the superfluid transition energy of $E_c/E_F = 0.94$ [39], and a single data point near the ground state. It should be noted that a correction factor to the trap frequencies was used to obtain the data displayed in the figure. The frequencies measured using parametric resonance are $\omega_x = 2\pi \times 71.1$ Hz, $\omega_y = 2\pi \times 2354$ Hz, and $\omega_z = 2\pi \times 1992$ Hz. When the optical trap is rotated using the AO, the frequencies in the rotated configuration at *steady state* are observed to decrease by 6.5%. This could be due to a reduction in the efficiency of the AO at the "kicked" frequency leading to a loss of power, or the

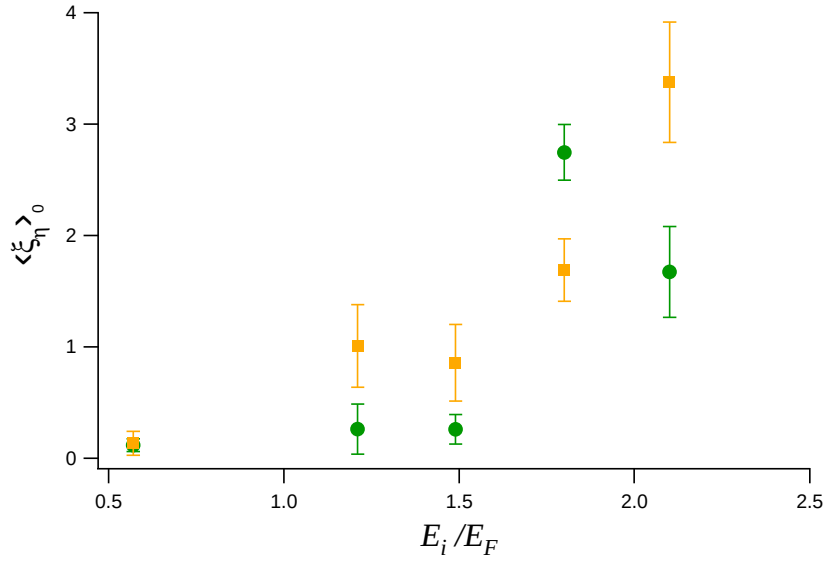

Figure 6.5: Plot of $\langle \xi_\eta \rangle_0$ versus initial energy for a rotating, strongly interacting Fermi gas. The solid circles in the plot are obtained by using a least squares fit to the experimental data of the angle of the cloud, ϕ, as a function of time. The solid squares are determined from a fit to the aspect ratio data.

power could be lost as a result of the beam clipping on an optical element. To correct for systematic errors resulting from an incorrect determination of the trap frequencies, a least squares fit is used to optimize the frequencies for a data set close to the ground state near $E_i/E_F = 0.48$ [36] where the viscosity should be negligible. In this data set, the viscosity is set to zero and the superfluid expansion model is used to fit the angle and aspect ratio data with the trap frequencies as free parameters. Least squares fits to the angle and aspect ratio yield two separate frequencies, which differ by 1%, so an average is used for the true trap frequencies. This results in a reduction of the trap frequencies by 7% and leads to a value of $\langle \xi_\eta \rangle_0 \simeq 0.1$ at the lowest energy when refit with the finite viscosity theory at the new frequencies. Without this correction, the $\langle \xi_\eta \rangle_0$ values would be erroneously inflated as the viscosity is used as a remedy for the incorrect frequencies.

Displayed in Figure 6.5 at each energy are two data points. The solid circles represent a least squares fit to the angle versus time data, while the solid squares are obtained through a fit to the aspect ratio data. The error bars indicate the variation in the fitting procedure only, and are obtained by assuming that each term in the χ^2 sum is roughly unity, leading to a normalized χ^2 that is equal to the number of data points. The error bars represent the change in $\langle \xi_\eta \rangle_0$ when the normalized χ^2 from the fit increases by unity. As the energy of the gas increases, the values of $\langle \xi_\eta \rangle_0$ also increase as the effects of viscosity begin to become more pronounced. The data is limited to a maximum energy of $E_i/E_F = 2.1$ due to signal to noise limitations imposed by the diluteness of the cloud. The large discrepancy between the $\langle \xi_\eta \rangle_0$ values found between the two methods at higher energies can be attributed to the difficulty of performing the experiments at higher energies where the data is difficult to obtain due to the decreased signal strength.

6.3.2 Estimate of η/s

An estimate of η/s can easily be obtained from the $\langle \xi_\eta \rangle_0$ data in Figure 6.5 by dividing it by the entropy per particle, S/k_B, as dictated by equation (6.57). The entropy data in Section 6.2 is presented as a function of E/E_F, and can be parameterized by a different power law in two separate regions above and below the superfluid transition energy at $E_c/E_F = .94$ [39]. Below the transition the power law is found to be $S_<(E) = 4.5k_B[(E - E_0)/E_F]^{0.59}$, while above the transition the expression becomes $S_>(E) = 4.0k_B[(E - E_0)/E_F]^{0.45}$. For the expansion experiment, the harmonic approximation of $E_0/E_F = 0.48$ can be used in these expressions, allowing the entropy of the gas at a particular energy to be calculated for each data point in Figure 6.5. The value of η/s is subsequently

estimated in units of $\hbar/k_B$ by $\langle\xi_\eta\rangle_0/(S/k_B)$ through the use of equation (6.57).

The result of a calculation of η/s is displayed in Figure 6.6. The data, given as solid circles and solid squares, is accompanied by three other estimates as well as a dashed horizontal line representing the conjectured minimum value of $1/4\pi$ predicted using string theory methods. A current theoretical estimate of η/s for the quark-gluon plasma is between 0.16 and 0.24, which is illustrated by a solid grey horizontal line in Figure 6.6. The dot-dashed line in the figure gives a representation of η/s calculated from the damping rate in collective mode experiments [20]. In those experiments, a hydrodynamic theory that included viscosity was used to relate the damping rate of a radial breathing mode (See Section 4.8.2) to $\langle\xi_\eta\rangle_0$, and hence to the ratio η/s using the same underlying assumption found in this chapter, namely $\eta = \xi_\eta \hbar\, n$. Therefore, the results of the collective mode experiment share a lot in common with the rotating gas experiment estimates, since both data sets are based on hydrodynamic theories built using the same assumptions. Although the data presented in reference [20] does not all lie on a straight line, the dot-dashed line in Figure 6.6 does portray the general trend exhibited by the data.

The data in Figure 6.6 is obtained by fits to either the angle data (circles) or aspect ratio data (squares) as discussed in Section 6.3.1. The ground state data point close to $E_i/E_F = 0.50$ was used to correct for a potential frequency overestimate, and the error bars only represent the quality of the $\langle\xi_\eta\rangle_0$ least squares fit. The data is preliminary, and more experiments are needed to minimize systematic errors and improve the discrepancy between the η/s estimate found using the two methods. But the data is useful in estimating the degree to which a strongly interacting Fermi gas can be considered a perfect fluid.

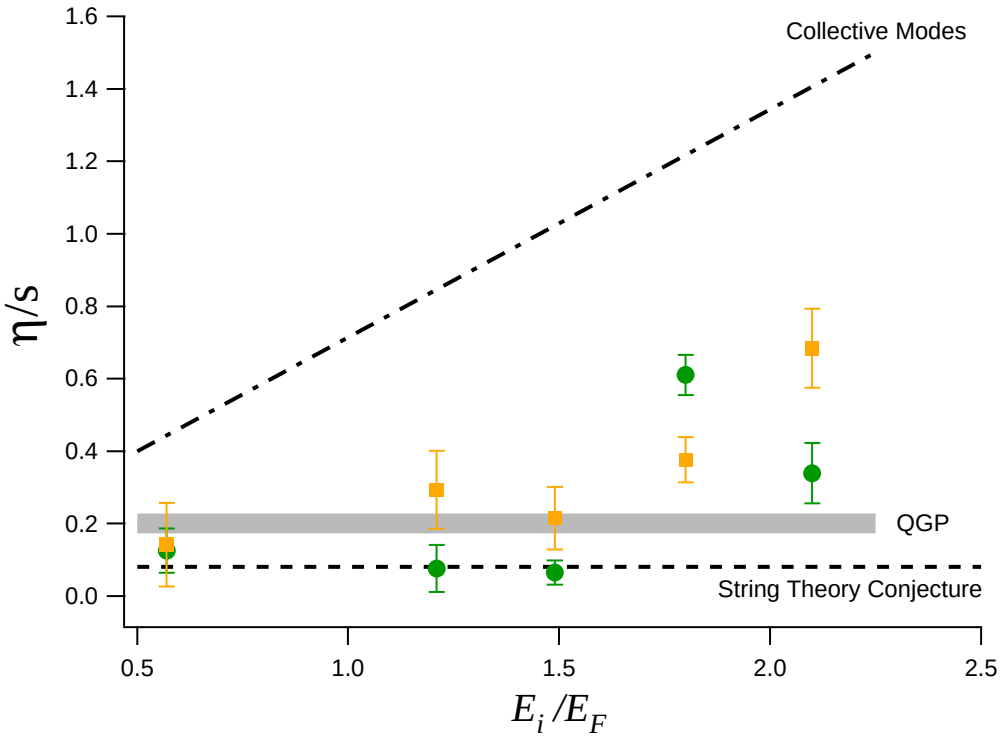

Figure 6.6: Plot of η/s versus initial energy in units of $\hbar/k_B$. The solid circles represent the data obtained from equation (6.57) using a value of $\langle \xi_\eta \rangle_0$ obtained from a least squares fit to the angle data, while the solid squares are fits to the aspect ratio data. The dashed horizontal line gives the minimum viscosity limit of $1/4\pi$ as conjectured using string theory methods, while the grey heavy solid line displays the estimate for a quark-gluon plasma. The dot-dashed line illustrates the ratio calculated from collective mode experiments in reference [20].

As illustrated in Figure 6.6, as the energy is increased, the value of η/s increases also, similar to what was seen in the collective mode experiments. In those experiments it was unclear whether the damping rate could be attributed entirely to viscous damping or if another effect, such as anharmonicity, could provide a substantial contribution. If extraneous effects do contribute, they would result in a larger calculated η/s. Since the data presented in Figure 6.6 for the rotating gas experiment is obtained from a gas that is freely expanding, it is immune to such effects. This can explain why all the data displayed in Figure 6.6 lies below or near the estimate from the collective mode experiment.

Regardless of the absolute magnitude of the individual points in the η/s data, it is important to note that up to an initial energy of $E_i/E_F = 2.1$, all the data is calculated to be below unity. In fact, the data points obtained from a fit to the angle at an energy of $E_i/E_F = 1.2$ and $E_i/E_F = 1.49$ lie below the theoretical prediction for the quark-gluon plasma and hover around the string theory conjecture. This is of particular interest since the gas is *normal* at these energies and is no longer superfluid. This demonstrates that a strongly interacting Fermi gas in the superfluid *and* normal regimes has an exceptionally small viscosity that may rival all other systems in nature. The advantage of creating such a minimal viscosity system in an ultracold gas is found in the unprecedented flexibility afforded for manipulating such a system, enabling future experiments to be performed to probe the properties of this unique, strongly interacting quantum system.

Chapter 7

Conclusions

This dissertation presented the results of experiments which probed the hydrodynamic and thermodynamic properties of a strongly interacting Fermi gas. These studies were made possible through the use of a newly constructed experimental apparatus. The experimental results contributed to the increasing body of knowledge relating to strongly interacting systems, which have an impact on many areas of physics such as in quark-gluon plasmas, high temperature superconductors, and nuclear matter. A study of the hydrodynamics of a strongly interacting Fermi gas in the superfluid and normal fluid regimes demonstrated that the viscosity of a normal unitary gas must be exceptionally small, and may approach the fundamental limit predicted using string theory methods [40]. An experimental measurement of the entropy versus energy of a unitary gas allowed thermometry to be performed in the strongly interacting regime in model independent way for the first time [39].

A lasting contribution to the lab that was undertaken and described in detail in Chapter 4 was the construction of a new experimental apparatus. The addition of a second, more improved apparatus doubles the production of the lab, and allows experiments of a dramatically different nature to be conducted in parallel. Due to their specialized nature, most experiments require unique modifications to be made to the experimental system. By having two independent machines,

vastly different experiments can be performed simultaneously, allowing more experiments to be done in a shorter time. Being able to implement new experiments quickly is definitely an advantage in this highly competitive field.

7.1 Chapter summaries

This dissertation began with an introduction in Chapter 1 that gave the motivations behind studying strongly interacting Fermi gases and details the significance of the work presented in this thesis. In that chapter connections were made between the strongly interacting gas that we study, and other strongly interacting systems in nature. The main results presented in this dissertation were introduced and an overview of the organization of the thesis was given.

One of the most important aspects of our quantum system, the tuning of the atomic energy levels with magnetic field, was presented in Chapter 2. The tuning of the energy levels dramatically effects the collisional properties through the presence of a Feshbach resonance. In Chapter 2 a derivation of the collision cross section for binary s-wave collisions in the vicinity of a Feshbach resonance is given. The consequences of unitarity, which results from the divergence of the s-wave scattering length at a Feshbach resonance, on the equation of state of a Fermi gas are presented along with a definition of the universal parameter β. The chapter ends with a brief discussion of recent unitary Fermi gas experiments that are related to the experiments presented in this thesis.

Chapter 3 developed the general cooling and trapping methods employed in our lab. After discussing how the atoms are initially prepared, the chapter mainly focused on the physics behind the the two atom traps used in our lab, the MOT

and the FORT, and the method of evaporative cooling that is used to reduce the temperature of the atom clouds. A newly devised method of evaporative cooling based upon a energy dependent collision cross section is presented along with experimental evidence for its validity.

A very detailed account of the design and construction of the new experimental apparatus was given in Chapter 4. The chapter began by explaining how atoms are produced by an atom source and slowed to velocities that allow them to be captured in a MOT inside of the main vacuum chamber. It continued with a discussion of the myriad of laser beams that are used to slow, trap, and image the atoms. Next came a presentation of the magnet system that helps trap the atoms and tune their interactions. After brief sections about the RF spin balance and imaging techniques, the chapter ended with an account of the steps involved in a typical experimental sequence and provided typical data from collective mode and parametric resonance experiments used to determine the trap frequencies.

An account of the original experiments performed in this dissertation began in Chapter 5 with the rotation and expansion experiment of a unitary Fermi gas. At the beginning of the chapter a hydrodynamic theory of the rotation and expansion process was given, followed by a derivation of a ballistic theory that was used for comparison. After the theory was developed, the experimental data was compared to the theory and almost perfect agreement was demonstrated at low temperatures, and surprisingly, at high temperatures also. The consequences of these results, along with the outcome of a measurement of the moment of inertia, are presented at the end of the chapter.

Intimately related to the rotation and expansion experiment is the quantum viscosity estimate presented in Chapter 6. This chapter began with an inclusion

of quantum viscosity in the equations of motion of a rotating and expanding gas, enabling an estimate of its magnitude. This is followed by an account of the entropy experiment, in which the entropy of a strongly interacting gas was measured as a function of energy. At the end of the chapter, the quantum viscosity estimate and entropy measurement were using in conjunction to probe the lower bound of the ratio of the viscosity to entropy density ratio conjectured using string theory methods.

7.2 Future experimental apparatus upgrades

One of the major accomplishments presented in this thesis is the construction of a new experimental apparatus that allows experiments to be performed on strongly interacting Fermi gases. The construction of the machine took upwards of two years to complete and required a substantial amount of design and fabrication. In its current state at the publication of this thesis, a wide range of experiments on ultra-cold gases can be performed using the apparatus. Although the apparatus has a wide range of capabilities, in order to undertake more specialized experiments, some important modifications must be initiated.

The most glaring inadequacies of the current experimental setup is its inability to perform fast magnetic field sweeps. As discussed in Section 4.5, due to capacitances in the power supplies that drive the magnet coils and inductances in the coils themselves, the time constant for a magnetic field sweep is currently 0.8 seconds. This is beneficial for some experiments, like the entropy experiment presented in Section 6.2, since the time scale of the sweep is slow in comparison to the oscillation period of the atoms in the trap, making the sweep adiabatic.

But there are a few experiments, especially molecular projection experiments, in which a fast magnetic field sweep would be beneficial. A fast magnetic field sweep could also allow the noninteracting regime at 528 Gauss to be reached directly from the Feshbach resonance at 834 Gauss without heating the gas through molecular relaxation that occurs at intermediate fields. Such an improvement would allow substantially colder temperatures to be reached in a noninteracting gas, as compared to the current procedure of evaporative cooling at a weakly interacting magnetic field below 528 Gauss.

Although it is difficult to forecast every modification that must be made to the experimental apparatus, one alteration that has already begun concerns the CO_2 beam path. As discussed in Section 4.3.2, currently the CO_2 beam is retroreflected using a rooftop mirror after it passes through the main vacuum chamber in order to increase the intensity at the beam focus to aid in loading. The rooftop mirror flips the polarization of the retroreflected beam, allowing it to be diverted into a water cooled beam dump by a thin film polarizer instead of propagating back into the laser and causing significant damage. By rotating the polarization by 90° before the retroreflected beam re-enters the main vacuum chamber, the rooftop mirror also prevents a standing wave from being produced in the trapping potential. But in future reduced dimensional studies, a standing wave is *desired*. Therefore, an alternative method of rotating the polarization to prevent feedback into the CO_2 laser before the main vacuum chamber must be undertaken, and a regular flat mirror that maintains the polarization must be used to retroreflect the beam. A scheme of this type has the added benefit leaving all current experimental methods unperturbed. As long as atoms can be loaded reliably into a standing wave trap without substantial heating, all of the traditional experiments can still

be performed simply by lowering the blocker mirror after the atoms are loaded, cutting off the retroreflected beam and leaving the single forward propagating beam to create a gaussian potential for the atoms to be held in.

7.3 Outlook

Future breakthroughs in the field of strongly interacting Fermi gases are increasingly possible as the techniques and methodologies involved in creating the atomic samples mature. When motivations for the study of unitary gases are given to the general public, they usually involve high temperature superconductors and a discussion of levitating trains and power lines that can deliver electricity without any loss due to heating. Although these are grand visions of what can be accomplished by studying strongly interacting systems, It will be a substantial amount of time before any practical applications will emerge as a consequence of the basic research that is being undertaken today. But currently there are research avenues available that can possibly advance our knowledge of strongly interacting systems, bringing us closer to our eventual goals.

A potentially fruitful area research that was mentioned in Section 7.2 is in the production of unitary gases in reduced dimensions. Almost all of the research that has been conducted thus far in the field pertains to systems that are inherently three dimensional. Interesting effects, which are too numerous to mention here, can occur if a gas is restricted to one or two dimensions. These regimes can be realized through the use of optical lattices, which can be implemented using current technology.

Appendix A

Numerical simulations

This appendix presents the mathematica computer code used to numerically integrate the equations of motion detailed in Section 6.1.2. The output of the program provides predictions for the angle and aspect ratio of an expanding cloud.

The program begins with a definition of the trap frequencies, total number of atoms, and the initial conditions on the angular velocity as well as the viscosity coefficient. The first simulation is for the hydrodynamic expansion of a trapped gas without rotation. The basis for this model was developed in Section 5.1.1. The succeeding simulation includes the effect of rotation and is based off the equations of motion derived in Section 5.1.2. The final program includes the effects of viscosity that were introduced through a simple model in Section 6.1.2. At the end of the program two plots are provided to emphasize the effect viscosity has on the resulting dynamics.

Rotation Expansion Notebook

- **This notebook will calculate the angle and aspect ratio associated with an expanding gas that has an initial angular velocity.**

Constants. EoEF is the initial energy of the gas in units of the Fermi energy and Num is the total number of atoms, not the number per spin state.

```
EoEF = .5;
Num = 150000;
γ = 2 / 3;
```

Trap Frequencies. The first set of frequencies are for the optical trap, while the second set is for the magnetic bowl.

```
wy = 2 π * 2354;
wx = 2 π * 71.1;
wz = 2 π * 1992;

wmy = 2 π * 21.5 * √2;
wmx = 2 π * 21.5;
wmz = 2 π * 21.5;

wbar = (wx wy wz)^(1/3);
λ = wx / wy;
EF = wbar (3 Num)^(1/3);
```

Initial Conditions. Ω is the initial angular velocity of the cloud. Set $\alpha[0]=\Omega$ for pure initial irrotational flow and $\Phi[0]=\Omega$ for pure initial rotational flow.

```
Ω = 178;
```

Viscosity section. f is the viscosity coefficient given in the dissertation as $<\xi_\eta>_0$.

```
f = 1;
```

Hydrodynamic Expansion: No Rotation

The following is a list of the 7 coupled ODE's for no rotation.

$$\begin{aligned}
\text{DifEq} = \Big\{ & \mu'[t] + \frac{2}{3}\,(\alpha x[t] + \alpha y[t] + \alpha z[t])\,\mu[t] == 0, \\
& \sigma x'[t] - \sigma x[t]\,\alpha x[t] == 0, \\
& \sigma y'[t] - \sigma y[t]\,\alpha y[t] == 0,\ \sigma z'[t] - \sigma z[t]\,\alpha z[t] == 0, \\
& \alpha x'[t] + \alpha x[t]\text{^}2 - \frac{\mu[t]}{\sigma x[t]\text{^}2}\,wx^2 + wmx^2 == 0, \\
& \alpha y'[t] + \alpha y[t]\text{^}2 - \frac{\mu[t]}{\sigma y[t]\text{^}2}\,wy^2 - wmy^2 == 0, \\
& \alpha z'[t] + \alpha z[t]\text{^}2 - \frac{\mu[t]}{\sigma z[t]\text{^}2}\,wz^2 + wmz^2 == 0\Big\};
\end{aligned}$$

This will numerically solve the above equations given the initial conditions.

```
EqSet = NDSolve[{DifEq[[1]], DifEq[[2]],
    DifEq[[3]], DifEq[[4]], DifEq[[5]], DifEq[[6]],
    DifEq[[7]], μ[0] == 1, σx[0] == 1, σy[0] == 1,
    σz[0] == 1, αx[0] == 0, αy[0] == 0, αz[0] == 0},
   {μ, σx, σy, σz, αx, αy, αz}, {t, 0, .012}];
```

Make lists of all the solutions out to the appropriate time scale.

```
μT = Table[μ[t] /. EqSet[[1, 1]], {t, 0, .012, .00001}];
σxT = Table[σx[t] /. EqSet[[1, 2]], {t, 0, .012, .00001}];
σyT = Table[σy[t] /. EqSet[[1, 3]], {t, 0, .012, .00001}];
σzT = Table[σz[t] /. EqSet[[1, 4]], {t, 0, .012, .00001}];
αxT = Table[αx[t] /. EqSet[[1, 5]], {t, 0, .012, .00001}];
αyT = Table[αy[t] /. EqSet[[1, 6]], {t, 0, .012, .00001}];
αzT = Table[αz[t] /. EqSet[[1, 7]], {t, 0, .012, .00001}];
```

Plot the aspect ratio for hydrodynamic expansion. This is simply the ratio of the time dependent widths.

```
NoARatio =
  Table[{(t - 1) * .01, σyT[[t]] wx / σxT[[t]] wy}, {t, 1, 1201}];
NoARatioPlot = ListPlot[NoARatio,
   PlotRange → {{0, 3.5}, {0, 3}}];
```

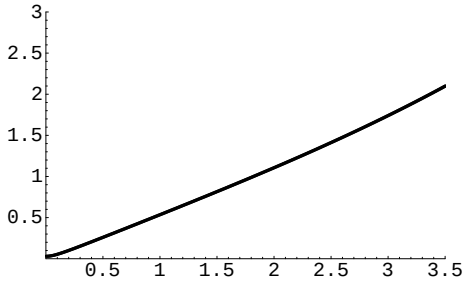

Rotation and Expansion: NoViscosity

The following is a list of the 10 coupled ODE's without viscosity.

```
DifEq = {μ'[t] + γ (αx[t] + αy[t] + αz[t]) μ[t] == 0,
  σx'[t] - σx[t] αx[t] - σx[t]^3 a[t] (α[t] + Φ[t]) == 0,
  σy'[t] - σy[t] αy[t] - σy[t]^3 λ^2 a[t] (α[t] - Φ[t]) == 0,
  σz'[t] - σz[t] αz[t] == 0, a'[t] + (α[t] - Φ[t]) / σx[t]^2 +
    (α[t] + Φ[t]) / (λ^2 σy[t]^2) + a[t] (αx[t] + αy[t]) == 0,
  Φ'[t] + (αx[t] + αy[t]) Φ[t] == 0,
  α'[t] + (αx[t] + αy[t]) α[t] == wx^2 μ[t] a[t],
  (αx'[t] + αx[t]^2 + α[t]^2 - Φ[t]^2 + wmx^2) σx[t]^2 / wx^2 == μ[t],
```

$$\left(\alpha y'[t] + \alpha y[t]^2 + \alpha[t]^2 - \Phi[t]^2 - wmy^2\right) \frac{\sigma y[t]^2}{wy^2} == \mu[t],$$

$$\left(\alpha z'[t] + \alpha z[t]^2 + wmz^2\right) \frac{\sigma z[t]^2}{wz^2} == \mu[t]\Big\};$$

The following command will numerically solve the above equations given an initial angular velocity of Ω right before the trap is turned off. Use α[0]=Ω and Φ[0]=0, for pure irrotational flow or use α[0]=0 and Φ[0]=Ω, for pure rotational flow.

```
EqSet = NDSolve[{DifEq[[1]], DifEq[[2]], DifEq[[3]],
    DifEq[[4]], DifEq[[5]], DifEq[[6]], DifEq[[7]],
    DifEq[[8]], DifEq[[9]], DifEq[[10]], μ[0] == 1,
    σx[0] == 1, σy[0] == 1, σz[0] == 1, α[0] == Ω, Φ[0] == 0,
    a[0] == 0, αx[0] == 0, αy[0] == 0, αz[0] == 0},
   {μ, a, σx, σy, σz, α, Φ, αx, αy, αz},
   {t, 0, .0035}, SolveDelayed → True];
```

Make lists of all the solutions out to the appropriate time scale.

```
μT = Table[μ[t] /. EqSet[[1, 1]], {t, 0, .0035, .00001}];
aT = Table[a[t] /. EqSet[[1, 2]], {t, 0, .0035, .00001}];
σxT = Table[σx[t] /. EqSet[[1, 3]], {t, 0, .0035, .00001}];
σyT = Table[σy[t] /. EqSet[[1, 4]], {t, 0, .0035, .00001}];
σzT = Table[σz[t] /. EqSet[[1, 5]], {t, 0, .0035, .00001}];
αT = Table[α[t] /. EqSet[[1, 6]], {t, 0, .0035, .00001}];
ΦT = Table[Φ[t] /. EqSet[[1, 7]], {t, 0, .0035, .00001}];
αxT = Table[αx[t] /. EqSet[[1, 8]], {t, 0, .0035, .00001}];
αyT = Table[αy[t] /. EqSet[[1, 9]], {t, 0, .0035, .00001}];
αzT =
  Table[αz[t] /. EqSet[[1, 10]], {t, 0, .0035, .00001}];
```

Plot the angle of the cloud.

```
Theta0 = Table[
    {(t - 1) * .01, 1/2 ArcTan[σxT[[t]]^2 - λ^2 σyT[[t]]^2, -2
        aT[[t]] λ^2 σxT[[t]]^2 σyT[[t]]^2] 180/π}, {t, 1, 351}];
Theta0Plot = ListPlot[Theta0, PlotRange →
    {{0, 3.5}, {0, 90}}];
```

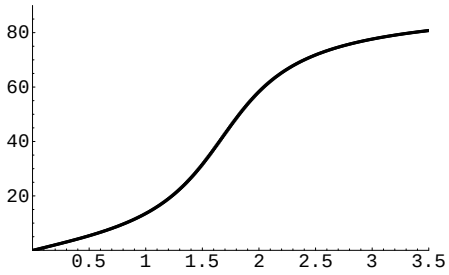

Plot the aspect ratio.

```
X0 = Table[√((σxT[[t]]^2 - λ^2 σyT[[t]]^2)^2 +
      4 λ^4 aT[[t]]^2 σxT[[t]]^4 σyT[[t]]^4), {t, 1, 351}];
AR0 = Table[{(t - 1) * .01,
    √((σxT[[t]]^2 + λ^2 σyT[[t]]^2 - X0[[t]])/(σxT[[t]]^2 + λ^2 σyT[[t]]^2 + X0[[t]]))}, {t, 1, 351}];
AR0Plot = ListPlot[AR0, PlotRange → {{0, 3.5}, {0, 1.0}}];
```

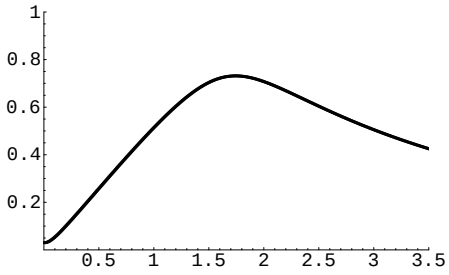

Rotation and Expansion: Viscosity Included

The following is a list of the 10 coupled ODE's with the effects of viscosity included.

$$\begin{aligned}
\text{DifEq} = \Big\{ & \mu'[t] + \gamma\,(\alpha x[t] + \alpha y[t] + \alpha z[t])\,\mu[t] == 0, \\
& \sigma x'[t] - \sigma x[t]\,\alpha x[t] - \sigma x[t]\text{^}3\,a[t]\,(\alpha[t] + \Phi[t]) == 0, \\
& \sigma y'[t] - \sigma y[t]\,\alpha y[t] - \sigma y[t]^3\,\lambda^2\,a[t]\,(\alpha[t] - \Phi[t]) == 0, \\
& \sigma z'[t] - \sigma z[t]\,\alpha z[t] == 0,\ a'[t] + \frac{(\alpha[t] - \Phi[t])}{\sigma x[t]^2} + \\
& \quad \frac{(\alpha[t] + \Phi[t])}{\lambda^2\,\sigma y[t]^2} + a[t]\,(\alpha x[t] + \alpha y[t]) == 0, \\
& \Phi'[t] + (\alpha x[t] + \alpha y[t])\,\Phi[t] == \frac{3\,wx^2}{EF} \\
& \quad \left((\alpha x[t] - \alpha y[t])\,a[t] + \alpha[t]\,\frac{\sigma x[t]^2 - \lambda^2\,\sigma y[t]^2}{\lambda^2\,\sigma x[t]^2\,\sigma y[t]^2} \right) \frac{f}{EoEF}, \\
& \alpha'[t] + (\alpha x[t] + \alpha y[t])\,\alpha[t] == wx^2\,\mu[t]\,a[t] - \\
& \quad \frac{3\,wx^2}{EF} \left(\frac{1}{3}\,(\alpha x[t] + \alpha y[t] - 2\,\alpha z[t])\,a[t] + \right. \\
& \qquad \left. \alpha[t]\,\frac{\sigma x[t]^2 + \lambda^2\,\sigma y[t]^2}{\lambda^2\,\sigma x[t]^2\,\sigma y[t]^2} \right) \frac{f}{EoEF}, \\
& (\alpha x'[t] + \alpha x[t]^2 + \alpha[t]^2 - \Phi[t]^2 + wmx^2)\,\frac{\sigma x[t]^2}{wx^2} == \\
& \quad \mu[t] - \frac{1}{EF}\,(6\,(\alpha x[t] - (\alpha x[t] + \alpha y[t] + \alpha z[t])\,/\,3 + \\
& \qquad \alpha[t]\,\sigma x[t]^2\,a[t]))\,\frac{f}{EoEF}, \\
& (\alpha y'[t] + \alpha y[t]^2 + \alpha[t]^2 - \Phi[t]^2 - wmy^2)\,\frac{\sigma y[t]^2}{wy^2} == \\
& \quad \mu[t] - \frac{1}{EF}\,(6\,(\alpha y[t] - (\alpha x[t] + \alpha y[t] + \alpha z[t])\,/\,3 + \\
& \qquad \alpha[t]\,\lambda^2\,\sigma y[t]^2\,a[t]))\,\frac{f}{EoEF}, \\
& (\alpha z'[t] + \alpha z[t]\text{^}2 + wmz^2)\,\frac{\sigma z[t]^2}{wz^2} == \mu[t] - \\
& \quad \frac{6\,(\alpha z[t] - (\alpha x[t] + \alpha y[t] + \alpha z[t])\,/\,3)}{EF}\,\frac{f}{EoEF} \Big\};
\end{aligned}$$

The following command will numerically solve the above equations given an initial angular velocity of Ω. Use $\alpha[0]=\Omega$ and $\Phi[0]=0$, for pure irrotational flow or use $\alpha[0]=0$ and $\Phi[0]=\Omega$, for pure rotational flow.

```
EqSet = NDSolve[{DifEq[[1]], DifEq[[2]], DifEq[[3]],
    DifEq[[4]], DifEq[[5]], DifEq[[6]], DifEq[[7]],
    DifEq[[8]], DifEq[[9]], DifEq[[10]], μ[0] == 1,
    σx[0] == 1, σy[0] == 1, σz[0] == 1, α[0] == Ω, Φ[0] == 0,
    a[0] == 0, αx[0] == 0, αy[0] == 0, αz[0] == 0},
   {μ, a, σx, σy, σz, α, Φ, αx, αy, αz},
   {t, 0, .0035}, SolveDelayed → True];
```

Make lists of all the solutions out to the appropriate time scale.

```
μT = Table[μ[t] /. EqSet[[1, 1]], {t, 0, .0035, .00001}];
aT = Table[a[t] /. EqSet[[1, 2]], {t, 0, .0035, .00001}];
σxT = Table[σx[t] /. EqSet[[1, 3]], {t, 0, .0035, .00001}];
σyT = Table[σy[t] /. EqSet[[1, 4]], {t, 0, .0035, .00001}];
σzT = Table[σz[t] /. EqSet[[1, 5]], {t, 0, .0035, .00001}];
αT = Table[α[t] /. EqSet[[1, 6]], {t, 0, .0035, .00001}];
ΦT = Table[Φ[t] /. EqSet[[1, 7]], {t, 0, .0035, .00001}];
αxT = Table[αx[t] /. EqSet[[1, 8]], {t, 0, .0035, .00001}];
αyT = Table[αy[t] /. EqSet[[1, 9]], {t, 0, .0035, .00001}];
αzT =
  Table[αz[t] /. EqSet[[1, 10]], {t, 0, .0035, .00001}];
```

Plot the angle of the cloud.

$$\texttt{Theta} = \texttt{Table}\Big[\Big\{(\texttt{t}-1)*.01,\ \frac{1}{2}\,\texttt{ArcTan}[\sigma\texttt{xT}[[\texttt{t}]]^2-\lambda^2\,\sigma\texttt{yT}[[\texttt{t}]]^2,\ -2\,\texttt{aT}[[\texttt{t}]]\,\lambda^2\,\sigma\texttt{xT}[[\texttt{t}]]^2\,\sigma\texttt{yT}[[\texttt{t}]]^2]\,\frac{180}{\pi}\Big\},\ \{\texttt{t},\ 1,\ 351\}\Big];$$

```
ThetaPlot =
  ListPlot[Theta, PlotRange → {{0, 3.5}, {0, 90}},
   PlotStyle → {RGBColor[1, 0, 0]}];
```

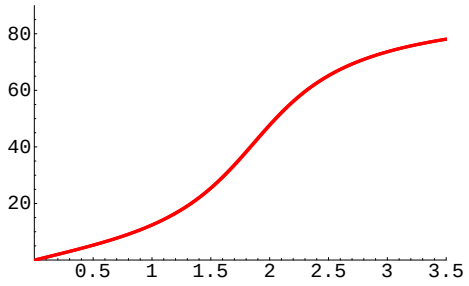

Plot the aspect ratio.

```
X0 = Table[√((σxT[[t]]^2 - λ^2 σyT[[t]]^2)^2 +
      4 λ^4 aT[[t]]^2 σxT[[t]]^4 σyT[[t]]^4), {t, 1, 351}];

AR = Table[{(t - 1) * .01,
   √((σxT[[t]]^2 + λ^2 σyT[[t]]^2 - X0[[t]])/(σxT[[t]]^2 + λ^2 σyT[[t]]^2 + X0[[t]]))}, {t, 1, 351}];

ARPlot = ListPlot[AR, PlotRange → {{0, 3.5}, {0, 1.0}},
   PlotStyle → {RGBColor[1, 0, 0]}];
```

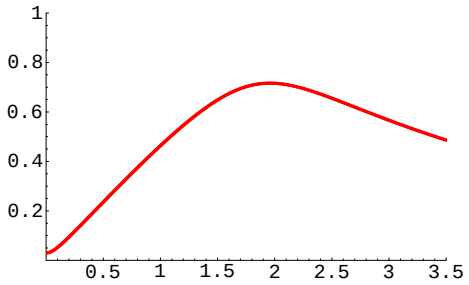

Comparisons

Now let's look at a comparison of the two theories. In both plots the zero viscosity theory is to the left of the finite viscosity prediction.

Aspect Ratio: Red → Viscosity, Black → No Viscosity

```
Show[AR0Plot, ARPlot];
```

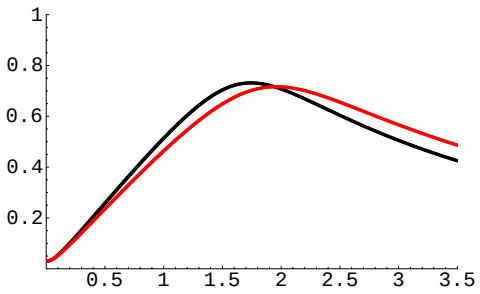

Angle: Red → Viscosity, Black → No Viscosity

```
Show[Theta0Plot, ThetaPlot];
```

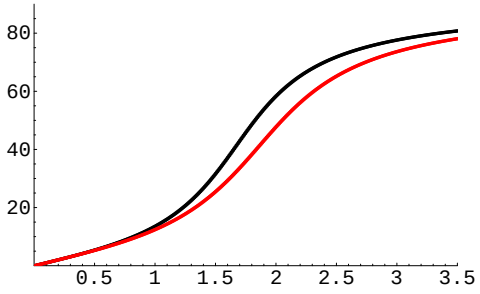

Bibliography

[1] A. L. Migdall, J. V. Prodan, W. D. Phillips, T. H. Bergeman, and H. J. Metcalf. First observation of magnetically trapped neutral atoms. *Phys. Rev. Lett.*, 54:2596, 1985.

[2] H. J. Metcalf and P. van der Straten. *Laser Cooling and Trapping*. Springer, New York, 1999.

[3] C. E. Wieman, D. E. Pritchard, and D. J. Wineland. Atom cooling, trapping, and quantum manipulation. *Rev. Mod. Phys.*, 71:S253, 1999.

[4] L. Pitaevskii and S. Stringari. *Bose-Einstein Condensation*. Clarendon Press, Oxford, 2003.

[5] M. H. Anderson, J. R. Ensher, M. R. Matthews, C. E. Wieman, and E. A. Cornell. Observation of Bose-Einstein condensation in a dilute atomic vapor. *Science*, 269:198, 1995.

[6] K. B. Davis, M. O. Mewes, M. R. Andrews, N. J. van Druten, D. S. Durfee, D. M. Kurn, and W. Ketterle. Bose-Einstein condensation in a gas of sodium atoms. *Phys. Rev. Lett.*, 75:3969, 1995.

[7] C. C. Bradley, C. A. Sackett, J. J. Tollett, and R. G. Hulet. Evidence of Bose-Einstein condensation in an atomic gas with attractive interactions. *Phys. Rev. Lett.*, 75:1687, 1995.

[8] B. DeMarco and D. S. Jin. Onset of Fermi degeneracy in a trapped atomic gas. *Science*, 285:1703, 1999.

[9] L. N. Cooper. Bound electron pairs in a degenerate Fermi gas. *Phys. Rev.*, 104:1189, 1956.

[10] M. Holland, S. J. J. M. F. Kokkelmans, M. L. Chiofalo, and R. Walser. Resonance superfluidity in a quantum degenerate Fermi gas. *Phys. Rev. Lett.*, 87:120406, 2001.

[11] S. J. J. M. F. Kokkelmans, J. N. Milstein, M. L. Chiofalo, R. Walser, and M. J. Holland. Resonance superfluidity: Renormalization of resonance scattering theory. *Phys. Rev. A*, 65:053617, 2002.

[12] T. Köhler, K. Góral, and P. S. Julienne. Production of cold molecules via magnetically tunable Feshbach resonances. *Rev. Mod. Phy.*, 78:1311, 2006.

[13] T. L. Ho. Universal thermodynamics of degenerate quantum gases in the unitarity limit. *Phys. Rev. Lett.*, 92:090402, 2004.

[14] W. N. Cottingham and D. A. Greenwood. *An introduction to the Standard Model of particle physics*. University Press, Cambridge, 1998.

[15] K. A. Olive. The quark-hadron transition in cosmology and astrophysics. *Science*, 251:1194, 1991.

[16] B. Müller. Physics of the quark-gluon plasma. nucl-th/9211010, November 1992.

[17] U. Heinz. The quark-gluon plasma at RHIC. *Nucl. Phys. A*, 721:30, 2003.

[18] K. M. O'Hara, S. L. Hemmer, M. E. Gehm, S. R. Granade, and J. E. Thomas. Observation of a strongly interacting degenerate Fermi gas of atoms. *Science*, 298:2179, 2002.

[19] E. Shuryak. Why does the quark-gluon plasma at RHIC behave as a nearly ideal fluid? *Prog. Part. Nucl. Phys.*, 53:273, 2004.

[20] A. Turlapov, J. Kinast, B. Clancy, L. Luo, J. Joseph, and J. E. Thomas. Is a gas of strongly interacting atomic fermions a nearly perfect fluid? *Jour. Low Temp. Phys.*, 150:567, 2008.

[21] D. R. Tilley and J. Tilley. *Superfluidity and Superconductivity*. Institude of Physics Publishing, Philadelphia, 3rd edition, 1990.

[22] J. G. Bednorz and K. Mueller. Possible high-T_c superconductivity in the Ba-La-Cu-O system. *Z. Physik B*, 64:189, 1986.

[23] J. Bardeen, L. N. Cooper, and J. R. Schrieffer. Theory of superconductivity. *Phys. Rev.*, 108(5):1175, 1957.

[24] J. Kinnunen, M. Rodríguez, and P. Törmä. Pairing gap and in-gap excitations in trapped fermionic superfluids. *Science*, 305:1131, 2004.

[25] A. Perali, P. Pieri, and G.C. Strinati. Quantitative comparison between theoretical predictions and experimental results for the BCS-BEC crossover. *Phys. Rev. Lett.*, 93:100404, 2004.

[26] Joseph Kinast, Andrey Turlapov, John E. Thomas, Qijin Chen, Jelena Stajic, and Kathryn Levin. Heat capacity of a strongly interacting Fermi gas. *Science*, 307:1296–1299, 2005.

[27] P. Massignan, G. M. Bruun, and H. Smith. Viscous relaxation and collective oscillations in a trapped Fermi gas near the unitarity limit. *Phys. Rev. A*, 71:033607, 2005.

[28] H. Hu, X. J. Liu, and P. D. Drummond. Temperature of a trapped unitary Fermi gas at finite entropy. *Phys. Rev. A*, 73:023617, 2006.

[29] A. Bulgac, J. E. Drut, and P. Magierski. Spin 1/2 fermions in the unitary regime: A superfluid of a new type. *Phys. Rev. Lett.*, 96:090404, 2006.

[30] Q. Chen, J. Stajic, S. Tan, and K. Levin. BCS-BEC crossover: From high temperature superconductors to ultracold superfluids. *Physics Reports*, 412:1, 2005.

[31] J. Carlson, S.-Y. Chang, V. R. Pandharipande, and K. E. Schmidt. Superfluid Fermi gases with large scattering length. *Phys. Rev. Lett.*, 91:050401, 2003.

[32] G. F. Bertsch, MBX Challenge Problem in Many-Body Physics, http://www.phys.washington.edu/∼mbx/george.html (1998).

[33] H. Heiselberg. Fermi systems with long scattering lengths. *Phys. Rev. A*, 63:043606, 2001.

[34] G. E. Astrakharchik, J. Boronat, J. Casulleras, and S. Giorgini. Equation of state of a Fermi gas in the BEC-BCS crossover: A quantum monte carlo study. *Phys. Rev. Lett.*, 93:200404, 2004.

[35] A. Bulgac, J. E. Drut, and P. Magierski. Thermodynamics of a trapped unitary Fermi gas. *Phys. Rev. Lett.*, 99:120401, 2007.

[36] H. Hu, P. D. Drummond, and X. J. Liu. Universal thermodynamics of a strongly interacting Fermi gases. *Nature Physics*, 3:469, 2007.

[37] G. B. Partridge, W. Li, R. I Kamar, Y. Liao, and R. G. Hulet. Pairing and phase separation in a polarized Fermi gas. *Science*, 311:503, 2006.

[38] J. T. Stewart, J. P. Gaebler, C. A. Regal, and D. S. Jin. Potential energy of a ^{40}K Fermi gas in the BCS-BEC crossover. *Phys. Rev. Lett.*, 97:220406, 2006.

[39] L. Luo, B. Clancy, J. Joseph, J.Kinast, and J. E. Thomas. Measurement of the entropy and critical temperature of a strongly interacting Fermi gas. *Phys. Rev. Lett.*, 98:080402, 2007.

[40] B. Clancy, L. Luo, and J. E. Thomas. Observation of nearly perfect irrotational flow in normal and superfluid strongly interacting Fermi gases. *Phys. Rev. Lett.*, 99:140401, 2007.

[41] P. K. Kovtun, D. T. Son, and A. O. Starinets. Viscosity in strongly interacting quantum field theories from black hole physics. *Phys. Rev. Lett.*, 94:111601, 2005.

[42] S. R. Granade, M. E. Gehm, K. M. O'Hara, and J. E. Thomas. All-optical production of a degenerate Fermi gas. *Phys. Rev. Lett.*, 88(12):120405, 2002.

[43] A. Einstein. Quantentheorie des einatomigen idealen gases. Zweite abhandlung. *Sitzungberichte, Preussische Akademie der Wissenschaften*, page 3, 1925.

[44] C. A. Regal, C. Ticknor, J. L. Bohn, and D. S. Jin. Creation of ultracold molecules from a Fermi gas of atoms. *Nature*, 424:47, 2003.

[45] M. Greiner, C. A. Regal, and D. S. Jin. Emergence of a molecular Bose-Einstein condensate from a Fermi gas. *Nature*, 426:537, 2003.

[46] M. E. Gehm, S. L. Hemmer, S. R. Granade, K. M. O'Hara, and J. E. Thomas. Mechanical stability of a strongly interacting Fermi gas of atoms. *Phys. Rev. A*, 68:011401(R), 2003.

[47] E. J. Mueller and G. Baym. Finite-temperature collapse of a Bose gas with attractive interactions. *Phys. Rev. A*, 62:053605, 2000.

[48] R. Shankar. *Principles of Quantum Mechanics*. Springer, New York, 2nd edition, 1994.

[49] C. Cohen-Tannoudji, B. Diu, and F. Laloë. *Quantum Mechanics*, volume Two. John Wiley & Sons, New York, 1977.

[50] M. E. Gehm. *Preparation of an Optically-trapped Degenerate Fermi gas of ^{6}Li: Finding the Route to Degeneracy*. PhD thesis, Duke University, 2003.

[51] J. M. Kinast. *Thermodynamics and superfluidity of a strongly interacting Fermi gas*. PhD thesis, Duke University, 2006.

[52] D. A. Butts and D. S. Rokhsar. Trapped Fermi gases. *Phys. Rev. A*, 55:4346, 1997.

[53] G. A. Baker Jr. Neutron matter model. *Phys. Rev. C*, 60:054311, 1999.

[54] J. Joseph, B. Clancy, L. Luo, J. Kinast, A. Turlapov, and J. E. Thomas. Measurement of sound velocity in a Fermi gas near a Feshbach resonance. *Phys. Rev. Lett.*, 98:170401, 2007.

[55] S. Y. Chang, V. R. Pandharipande, J. Carlson, and K. E. Schmidt. Quantum Monte-Carlo studies of superfluid Fermi gases. *Phys. Rev. A*, 70:043602, 2004.

[56] J. E. Thomas, J. Kinast, and A. Turlapov. Virial theorem and universality in a unitary Fermi gas. *Phys. Rev. Lett.*, 95:120402, 2005.

[57] L. D. Landau and E. M. Lifshitz. *Fluid Mechanics*. Pergamon Press, New York, 2nd edition, 1975.

[58] M. Bartenstein, A. Altmeyer, S. Riedl, R. Geursen, S. Jochim, C. Chin, J. H. Denschlag, R. Grimm, A. Simoni, E. Tiesinga, C.J. Williams, and P.S. Julienne. Precise determination of ^{6}Li cold collision parameters by radio-frequency spectroscopy on weakly bound molecules. *Phys. Rev. Lett.*, 94:103201, 2005.

[59] K. M. O'Hara, S. L. Hemmer, S. R. Granade, M. E. Gehm, J. E. Thomas, V. Venturi, E. Tiesinga, and C. J. Williams. Measurement of the zero crossing in a Feshbach resonance of fermionic ^{6}Li. *Phys. Rev. A*, 66:041401(R), 2002.

[60] C. A. Regal, M. Greiner, and D. S. Jin. Observation of resonance condensation of fermionic atom pairs. *Phys. Rev. Lett.*, 92:040403, 2004.

[61] M. W. Zwierlein, C. A. Stan, C. H. Schunck, S. M. F. Raupach, A. J. Kerman, and W. Ketterle. Condensation of pairs of fermionic atoms near a Feshbach resonance. *Phys. Rev. Lett.*, 92:120403, 2004.

[62] M. W. Zwierlein, C. H. Schunck, C. A. Stan, S. M. F. Raupach, and W. Ketterle. Formation dynamics of a fermion pair condensate. *Phys. Rev. Lett.*, 94:180401, 2005.

[63] J. Kinast, S. L. Hemmer, M.E. Gehm, A. Turlapov, and J. E. Thomas. Evidence for superfluidity in a resonantly interacting Fermi gas. *Phys. Rev. Lett.*, 92:150402, 2004.

[64] M. W. Zwierlein, J. R. Abo-Shaeer, A. Schirotzek, C. H. Schunck, and W. Ketterle. Vortices and superfluidity in a strongly interacting Fermi gas. *Nature*, 435:1047, 2005.

[65] J. Kinast, A. Turlapov, and J. E. Thomas. Breakdown of hydrodynamics in the radial breathing mode of a strongly interacting Fermi gas. *Phys. Rev. A*, 70:051401(R), 2004.

[66] M. Bartenstein, A. Altmeyer, S. Riedl, S. Jochim, C. Chin, J. Hecker Denschlag, and R. Grimm. Collective excitations of a degenerate gas at the BEC-BCS crossover. *Phys. Rev. Lett.*, 92:203201, 2004.

[67] A. Altmeyer, S. Riedl, M. J. Wright, C. Kohstall, J. Hecker Denschlag, and R. Grimm. Dynamics of a strongly interacting Fermi gas: The radial quadrupole mode. *Phys. Rev. A*, 76:033610, 2007.

[68] M. J. Wright, S. Riedl, A. Altmeyer, C. Kohstall, E. R. Sánchez Guajardo, J. Hecker Denschlag, and R. Grimm. Finite-temperature collective dynamics of a Fermi gas in the BEC-BCS crossover. *Phys. Rev. Lett.*, 99:150403, 2007.

[69] J. K. Chin, D. E. Miller, Y. Liu, C. Stan, W. Setiawan, C. Sanner, K. Xu, and W. Ketterle. Evidence for superfluidity of ultracold fermions in an optical lattice. *Nature*, 443:961, 2006.

[70] K. Günter, T. Stöferle, H. Moritz, M. Köhl, and T. Esslinger. p-wave interactions in low-dimensional fermionic gases. *Phys. Rev. Lett.*, 95:230401, 2005.

[71] J. P. Martikainen and P. Törmä. Quasi-two-dimensional superfluid fermionic gases. *Phys. Rev. Lett.*, 95:170407, 2005.

[72] A. L. Migdall, J. V. Prodan, W. D. Phillips, T. H. Bergeman, and H. J. Metcalf. First observation of magnetically trapped neutral atoms. *Phys. Rev. Lett.*, 54(24):2596, 1985.

[73] E. L. Raab, M. Prentiss, A. Cable, S. Chu, and D. E. Prichard. Trapping of neutral sodium atoms with radiation pressure. *Phys. Rev. Lett.*, 59(23):2631, 1987.

[74] H. J. Lee, C. S. Adams, M. Kasevich, and S. Chu. Raman cooling of atoms in an optical dipole trap. *Phys. Rev. Lett.*, 76:2658, 1996.

[75] M. D. Barrett, J. A. Sauer, and M. S. Chapman. All-Optical formation of an atomic Bose-Einstein condensate. *Phys. Rev. Lett.*, 87:010404, 2001.

[76] J. D. Miller, R. A. Cline, and D. J. Heinzen. Far-off-resonance optical trapping of atoms. *Phys. Rev. A*, 47:R4567, 1993.

[77] S. R. Granade. *All-optical Production of a Degenerate Gas of ^{6}Li: Characterization of Degeneracy*. PhD thesis, Duke University, 2002.

[78] A. Yariv. *Quantum Electronics*. John Wiley and Sons, New York, 2nd edition, 1975.

[79] K. M. O'Hara, M. E. Gehm, S. R. Granade, and J. E. Thomas. Scaling laws for evaporative cooling in time-dependent optical traps. *Phys. Rev. A*, 64:051403(R), 2001.

[80] O. J. Luiten, M. W. Reynolds, and J. T. M. Walraven. Kinetic theory of the evaporative cooling of a trapped gas. *Phys. Rev. A*, 53:381, 1996.

[81] L. Luo, B. Clancy, J. Joseph, J.Kinast, A. Turlapov, and J. E. Thomas. Evaporative cooling of unitary Fermi gas mixtures in optical traps. *New Journal of Physics*, 8:213, 2006.

[82] L. Windholz, M. Musso, G. Zerza, and H. Jäger. Precise Stark-effect investigations of the lithium D1 and D2 lines. *Phys. Rev. A*, 46:5812, 1992.

[83] K. M. O'Hara. *Optical Trapping and Evaporative Cooling of Fermionic Atoms*. PhD thesis, Duke University, 2000.

[84] L. Luo. *Thermodynamics and superfluid critical parameters of a strongly interacting Fermi gas*. PhD thesis, Duke University, 2008.

[85] S. Bali, K. M. O'Hara, M. E. Gehm, S. R. Granade, and J. E. Thomas. Quantum-diffractive background gas collisions in atom-trap heating and loss. *Phys. Rev. A*, 60:R29, 1999.

[86] R. C. Weast, M. J. Astle, and W. H. Beyer, editors. *CRC Handbook of Chemistry and Physics*. CRC Press, Boca Raton, 1983.

[87] C. A. Baird. Design and characterization of a multi-coil Zeeman slower. Master's thesis, Duke University, 1996.

[88] Margaret Harris. Design and construction of an improved zeeman slower. Undergraduate, Duke University, 2003.

[89] I. Kaldre. A compact, air-cooled zeeman slower as a cold atom source. Undergraduate, Duke University, 2006.

[90] P. A. Tipler. *Physics for Scientists and Engineers*. Worth Publishers, Inc., 3rd edition, 1991.

[91] W. I. McAlexander, E. R. I. Abraham, and R. G. Hulet. Radiative lifetime of the $2p$ state of lithium. *Phys. Rev. A*, 54:R5, 1996.

[92] J. R. Gardner. *Ultra-High Resolution Atom Imaging in a Light-Shift Gradient*. PhD thesis, Duke University, 1995.

[93] D. J. Griffiths. *Introduction to Electrodynamics*. Prentice Hall, Upper Saddle River, NJ, 2nd edition, 1989.

[94] T. Bergeman, G. Erez, and H. J. Metcalf. Magnetostatic trapping fields for neutral atoms. *Phys. Rev. A*, 35(4):1535, 1987.

[95] M. W. Zwierlein, A. Schirotzek, C. H. Schunck, and W. Ketterle. Fermionic superfluidity with imbalanced spin populations. *Science*, 311:492, 2006.

[96] T. Bourdel, L. Khaykovich, J. Cubizolles, J. Zhang, F. Chevy, M. Teichmann, L. Tarruell, S. J. J. M. F. Kokkelmans, and C. Salomon. Experimental study of the BEC-BCS crossover region in Lithium 6. *Phys. Rev. Lett.*, 93:050401, 2004.

[97] L. D. Landau and E. M. Lifshitz. *Mechanics*, volume One. Butterworth-Heineman, Boston, 3rd edition, 1981.

[98] M. Bartenstein, A. Altmeyer, S. Riedl, S. Jochim, C. Chin, J. Hecker Denschlag, and R. Grimm. Crossover from a molecular Bose-Einstein condensate to a degenerate Fermi gas. *Phys. Rev. Lett.*, 92:120401, 2004.

[99] M. Cozzini and S. Stringari. Fermi gases in slowly rotating traps: superfluid versus collisional hydrodynamics. *Phys. Rev. Lett.*, 91:070401, 2003.

[100] A. Recati, F. Zambelli, and S. Stringari. Overcritical rotation of a trapped Bose-Einstein condensate. *Phys. Rev. Lett.*, 86(3):377, 2001.

[101] M. Edwards, C. W. Clark, P. Pedri, L. Pitaevskii, and S. Stringari. Consequence of superfluidity on the expansion of a rotating Bose-Einstein condensate. *Phys. Rev. Lett.*, 88(7):070405, 2002.

[102] G. Hechenblaikner, E. Hodby, S. A. Hopkins, O. M. Maragó, and C. J. Foot. Direct observation of irrotational flow and evidence of superfluidity in a rotation Bose-Einstien condensate. *Phys. Rev. Lett.*, 88:070406, 2002.

[103] M. Modugno, G. Modugno, G. Roati, C. Fort, and M. Inguscio. Scissors mode of an expanding Bose-Einstein condensate. *Phys. Rev. A*, 67:023608, 2003.

[104] C. Menotti, P. Pedri, and S. Stringari. Expansion of an interacting Fermi gas. *Phys. Rev. Lett.*, 89(25):250402, 2002.

[105] D. Guéry-Odelin. Spinning up and down a Boltzmann gas. *Phys. Rev. A*, 62:033607, 2000.

[106] R. K. Pathria. *Statistical Mechanics*. Butterworth-Heinemann, Boston, 2nd edition, 1996.

[107] M. Cozzini and S. Stringari. Scissors mode and superfluidity of a trapped Bose-Einstein condensed gas. *Phys. Rev. Lett.*, 83(22):4452, 1999.

[108] D. Guéry-Odelin and S. Stringari. Fermi gases in slowly rotating traps: superfluid versus collisional dynamics. *Phys. Rev. Lett.*, 91(7):070401, 2003.

[109] J. Kinast, A. Turlapov, and J. E. Thomas. Damping of a unitary Fermi gas. *Phys. Rev. Lett.*, 94:170404, 2005.

[110] T. Schäfer. Ratio of shear viscosity to entropy density for trapped fermions in the unitarity limit. *Phys. Rev. A*, 76:063618, 2007.

[111] P. F. Kolb and U. Heinz. *Quark Gluon Plasma 3*, page 634. World Scientific, 2003.

[112] F. Zambelli and S. Stringari. Moment of inertia and quadrupole response function of a trapped superfluid. *Phys. Rev. A*, 63:033602, 2001.

[113] B. Gelman, E. Shuryak, and I. Zahed. Ultracold strongly coupled gas: A near-ideal liquid. *Phys. Rev. A*, 72:043601, 2005.

[114] D. T. Son. Vanishing bulk viscosities and conformal invariance of the unitary Fermi gas. *Phys. Rev. Lett.*, 98:020604, 2007.

[115] G. M. Kavoulakis, C. J. Pethick, and H. Smith. Damping of hydrodynamic modes in a trapped Bose gas above the Bose-Einstein transition temperature. *Phys. Rev. A*, 57:2938, 1998.

[116] G. M. Bruun and H. Smith. Shear viscosity and damping for a Fermi gas in the unitary limit. *Phys. Rev. A*, 75:043612, 2007.

[117] Q. Chen, J. Stajic, and K. Levin. Thermodynamics of interacting fermions in atomic traps. *Phys. Rev. Lett.*, 95:260405, 2005.

[118] E. R. I. Abraham, W. I. McAlexander, J. M. Gerton, R. G. Hulet, R. Côté, and A. Dalgarno. Triplet s-wave resonance in ^{6}Li collisions and scattering lengths of ^{6}Li and ^{7}Li. *Phys. Rev. A*, 55(5):R3299, 1997.

[119] K. M. O'Hara, M. E. Gehm, S. R. Granade, S. Bali, and J. E. Thomas. Stable, strongly attractive, two-state mixture of lithium fermions in an optical trap. *Phys. Rev. Lett.*, 85:2092, 2000.

Biography

Bason Eric Clancy was born June 3, 1977 in San Leandro, California. After graduating from Arroyo High School in 1995 he enrolled in the Engineering Physics program at the Colorado School of Mines in Golden, CO. Four years later in May of 1999 he received his B.S. with high scholastic honors. In August of 1999 he began an M.S. program in Mechanical Engineering at Purdue University in West Lafayette, IN. While working toward his eventual graduation in December of 2001, he was awarded the William K. and Gail E. Cordier Fellowship in Mechanical Engineering. After taking a year off of academic work, he enrolled in the graduate school at Duke University in 2002, pursuing a Ph.D. in Physics. After joining John Thomas's research group in June 2003, he contributed to experiments investigating the hydrodynamic and thermodynamic properties of degenerate, strongly interacting Fermi gases. He received his M.A. in Physics in 2005 and was awarded the Fritz London Fellowship in 2007 before graduating with a Ph.D. in May 2008.

Publications

A. Turlapov, J. Kinast, B. Clancy, L. Luo, J. Joseph, and J. E. Thomas, "Is a gas of strongly interacting atomic fermions a nearly perfect fluid?," *Journal of Low Temperature Physics*, **150**, 567 (2008).

Bason Clancy, Le Luo, and John E. Thomas, "Observation of nearly perfect irrotational flow in normal and superfluid strongly interacting Fermi gases," *Physical Review Letters*, **99**, 140401 (2007).

J. Joseph, B. Clancy, L. Luo, J. Kinast, A. Turlapov, and J. E. Thomas, "Mea-

surement of sound velocity in a Fermi gas near a Feshbach resonance," *Physical Review Letters*, **98**, 170401 (2007).

L. Luo, B. Clancy, J. Joseph, J. Kinast, and J. E. Thomas, "Measurement of the entropy and critical temperature of a strongly interacting Fermi gas," *Physical Review Letters*, **98**, 080402 (2007).

L. Luo, B. Clancy, J. Joseph, J. Kinast, A. Turlapov, and J. E. Thomas, "Evaporative cooling of unitary Fermi gas mixtures in optical traps," *New Journal of Physics*, **8**, 213 (2006).

B. Clancy, Y. Shin, "A comprehensive chatter prediction model for face turning operation including tool wear effect," *International Journal of Machine Tools and Manufacture*, **42**, 1035 (2002).

Selected Presentations

B. Clancy, L. Luo, J. Kinast, J. Joseph, A. Turlapov, and J. E. Thomas, "Sound in a strongly interacting Fermi gas," *APS March Meeting 2006*, Baltimore, MD, presented by B. Clancy, March 2006.